Imperial College London

Single-molecule Protein Analysis Using Nanopores

Xiaoyi Wang

Department of Chemistry

Imperial College London

A thesis submitted in partial fulfilment of the requirement for the degree of Doctor of Philosophy

October 2023

Abstract

Nanopores have displayed immense potential as an analytical platform for label-free single-molecule biosensing, particularly evident in their successful application for direct long-read DNA sequencing. However, the analysis of proteins using nanopores presents unique challenges due to inherent limitations. This thesis aims to address these challenges and advance the performance of protein nanopore sensing.

The thesis commences by exploring the potential of nanopipettes in studying proteins and their interactions, with a specific focus on actin, a crucial protein in eukaryotic cells. Nanopipettes offer insights into the ATP-activated filamentation, urea-induced unfolding, and drug-induced structural alteration. However, direct analysis using nanopipettes still faces limitations in terms of spatiotemporal resolution and selectivity.

In the subsequent part of the thesis, molecular carriers including DNA and peptides are explored as powerful tools to enhance protein analysis through nanopores. To overcome the issue of carrier folding, a novel strategy of protein-binding-induced carrier dimerisation is developed, enabling precise detection of target proteins.

The use of cationic supercharged unstructured polypeptide (SUP) carriers proves highly beneficial in enhancing protein capture and detection, leading to significant improvements in nanopore measurements. The electrostatic attraction between the SUP carrier and the nanopore not only increases protein capture but also decelerates protein translocation through the pore. This approach successfully realises the size identification of small proteins and precise recognition of protein-protein interactions at the single-molecule level.

In summary, the integration of nanopipettes and molecular carriers show great promise for advancing single-molecule protein analysis. By overcoming the inherent limitations of protein nanopore sensing, these advancements have the potential to significantly impact the field of proteomics and contribute to precise early-stage diagnostics and therapeutics.

Declaration of Originality

I, the author, declare that the work presented in this thesis is original and performed by myself, otherwise it is clearly cited and acknowledged. This work has not previously been submitted in any form to satisfy any degree requirements at this or any other universities.

Xiaoyi Wang

October 2023

Copyright Declaration

The copyright of this thesis rests with the author. Unless otherwise indicated, its contents are licensed under a Creative Commons Attribution-NonCommercial 4.0 International Licence (CC BY-NC).

Under this licence, you may copy and redistribute the material in any medium or format. You may also create and distribute modified versions of the work. This is on the condition that: you credit the author and do not use it, or any derivative works, for a commercial purpose.

When reusing or sharing this work, ensure you make the licence terms clear to others by naming the licence and linking to the licence text. Where a work has been adapted, you should indicate that the work has been changed and describe those changes.

Please seek permission from the copyright holder for uses of this work that are not included in this licence or permitted under UK Copyright Law.

Acknowledgments

First, I would like to express my deepest appreciation to my supervisors, Prof. Joshua Edel and Dr. Alex Ivanov, whose guidance, expertise, and unwavering commitment to my PhD studies and research have been invaluable. Your stunning mentorship has not only shaped my academic journey but has also inspired me to strive for excellence in every aspect of my work and life.

I am also grateful to all my collaborators, who have provided fruitful contributions and insights to my research projects. This thesis would not be possible without your contributions. I would specifically acknowledge Dr. Mark Wilkinson, Prof. Keith Willison and Prof. Jake Baum for the actin work; Tina-Marie Thomas, Dr. Yu Zhou, Prof. Andreas Herrmann and Prof. Kai Liu for the SUP work.

To all the members in Edel/Ivanov group, thanks for providing a stimulating and collaborative environment. It is enjoyable and productive to work with these lovely people. To Longhua, Binoy, Paolo, Giulia and Alex DL, thanks for your guidance and help at my start in the group, and I wish all the best in your future career and life. To Alfie, Micol, Mike, Long, Aleksandra, Oliver, Caroline, Annie, Tony, Ben, Charlotte, Zoe, Javier, Jiayu, Liquan, and Xixian, thanks for all the joy you shared with me and I hope you have a bright future in your studies and work.

To Ren, my best mate in science, my best friend in life and my best partner in game, it is my best luck to meet you in my PhD stage and learn a lot from you both in research and in life. I wish you will soon find your best place and always double yolk in ten pulls. Shenglin, I am also lucky to meet you in the group and keep in close contact with you these years. Your passion on the science deeply inspired and encouraged me and I hope all the best in your academic career. For Yilin, さあ、行こう!

To Yaxian, it was my pleasure to work with you in the last stage of my PhD and it was always happy and joyful to be with you. We explored and enjoyed delicious food all over London. Your company has kept me always happy through these years. I would also express my special appreciation to Nezha, my cat, for the company of three years.

Finally, I am deeply indebted to my family for their unending support, encouragement, and love, especially my parents. Your belief in me has been my source of strength and motivation. Thank you for everything, my Mum and Dad!

In London

October 2023

Table of Contents

Abstract ..... [1]

Declaration of Originality ..... [2]

Copyright Declaration ..... [3]

Acknowledgments ..... [4]

Table of Contents ..... [6]

List of Figures ..... [11]

List of Tables ..... [34]

Abbreviation ..... [35]

Chapter 1

Introduction

1.1 Single-molecule science ..... [39]

1.2 Nanopore technology ..... [41]

1.2.1 Biological nanopores ..... [42]

1.2.2 Solid-state nanopores ..... [44]

1.3 Working principle of nanopore sensing ..... [48]

1.3.1 Ionic current detection ..... [48]

1.3.2 The effect of surface charge ..... [51]

1.3.3 Ionic current rectification ..... [54]

1.3.4 Electrophoretic and electroosmotic flow ..... [55]

1.3.5 Sensing of biomolecules using solid-state nanopores ..... [57]

1.4 Single-molecule protein and proteome analysis ..... [59]

1.4.1 Current development of proteomic analysis ..... [59]

1.4.2 Challenges of nanopore-based protein analyser ..... [61]
1.4.3 Surface-functionalised nanopores ..... [62]
1.4.4 Molecular carriers ..... [64]
1.4.5 Integrated nanopore technology ..... [67]
1.5 Objectives and thesis overview ..... [74]
1.6 References ..... [75]

Chapter 2

Methodology

2.1 Nanopore fabrication and characterisation ..... [90]
2.1.1 Nanopore fabrication ..... [90]
2.1.2 Nanopore characterisation by microscopes ..... [93]
2.1.3 Nanopore characterisation by conductance ..... [94]
2.1.4 Calculation of the diameter of nanopores ..... [96]
2.1.5 Calculation of the effective length of nanopores ..... [97]
2.2 Nanopore translocation of single molecules ..... [98]
2.2.1 Setup of nanopore experiments ..... [98]
2.2.2 Preparation of Ag/AgCl electrodes ..... [99]
2.2.3 Preparation of buffer solutions ..... [101]
2.2.4 Ionic current measurements ..... [102]
2.3 Data analysis ..... [103]
2.3.1 Single-molecule data processing ..... [103]
2.3.2 Extraction of individual events ..... [103]
2.3.3 Subpeak analysis ..... [109]
2.3.4 Statistical analysis ..... [110]
2.4 References ..... [112]

Chapter 3

Single-molecule nanopore sensing of actin dynamics and drug binding

3.1 Introduction ..... [115]

3.2 Methods and materials ..... [117]

3.2.1 Fabrication of nanopipettes ..... [117]

3.2.2 Preparation of actin samples ..... [118]

3.2.3 Nanopore measurements and data processing ..... [120]

3.2.4 Calculation of the actin unfolding free energy ..... [120]

3.2.5 Estimation of the zeta potential for folded and unfolded actin ..... [121]

3.2.6 Theoretic models of protein flux in nanopore translocations ..... [122]

3.2.7 Estimation of the protein size and shape ..... [122]

3.2.8 Kinetics measurements of actin binding with Swinholide A ..... [124]

3.3 Results and discussion ..... [125]

3.3.1 Experimental configuration and sensing principle ..... [125]

3.3.2 Discrimination of different actin species ..... [127]

3.3.3 Actin folding and unfolding landscape ..... [130]

3.3.4 Voltage dependence on actin conformation ..... [136]

3.3.5 Real-time sensing of actin polymerisation ..... [141]

3.3.6 Recognition of actin drug binding ..... [144]

3.4 Conclusions ..... [149]

3.5 References ..... [150]

Chapter 4

Single-molecule protein profiling using nanopores and dimeric aptamer-modified DNA carriers

4.1 Introduction ..... [156]
4.2 Methods and materials ..... [160]
4.2.1 Preparation of aptamer-modified DNA carriers ..... [160]
4.2.2 Fabrication of nanopipettes ..... [160]
4.2.3 Nanopore measurements and data processing ..... [161]
4.3 Results and discussion ..... [162]
4.3.1 Experimental setup and sensing principle ..... [162]
4.3.2 Design and characterisation of aptamer-modified DNA carriers ..... [165]
4.3.3 DNA length recognition by charge classification ..... [169]
4.3.4 Thrombin detection by heterogenous dimerisation of DNA carriers ..... [173]
4.3.5 Detection of dimeric proteins by homogenous dimerisation of DNA carriers ... [180]
4.3.6 Direct observation of the activation and inhibition of c-Met dimerisation ..... [183]
4.4 Conclusions ..... [189]
4.5 References ..... [191]

Chapter 5

Nanopore detection using supercharged polypeptide molecular carriers

5.1 Introduction ..... [196]
5.2 Methods and materials ..... [199]
5.2.1 Molecular cloning of protein-SUP conjugates ..... [199]
5.2.2 Protein expression and purification ..... [201]
5.2.3 Fabrication of nanopipettes ..... [202]
5.2.4 Nanopore measurements and data processing ..... [203]
5.3 Results and discussion ..... [205]
5.3.1 Design and characterisation of supercharged polypeptides ..... [205]
5.3.2 Single-molecule protein sensing using nanopipettes ..... [207]
5.3.3 Comparison of native protein and its charged variants ..... [211]
5.3.4 Length and voltage dependence of cationic SUPs on nanopore translocation .. [214]

5.3.5 SUP carriers for improved protein detection ..... [219]
5.3.6 Nanopore sensing of protein-protein interactions using SUP carriers ..... [229]
5.4 Conclusions ..... [237]
5.5 References ..... [238]

Chapter 6

Conclusions and future work

6.1 Aims and achievements ..... [244]
6.2 Future work ..... [245]
6.2.1 Integration of tunnelling-based detector with nanopipettes ..... [246]
6.2.2 Proteomic analysis using molecular carriers ..... [251]
6.3 Conclusions ..... [253]
6.4 References ..... [254]

Appendices

Appendix I: Copyright permission ..... [256]
Appendix II: List of publications ..... [273]

List of Figures

Figure 1.1 The development of measurement techniques from large-scale entities to single molecules. (a) The evolution of measurement techniques has traversed a remarkable trajectory, progressing from studying entire organisms down to individual cells and even single molecules. As our scientific capabilities have surged, the focus has shifted towards detecting ever-smaller entities, leading to a radical reduction in sample sizes. This shift has brought us to an exciting juncture where single-molecule measurements are transitioning into the quantitative science. (b) Conventional sensors analyse an ensemble sample, providing an averaged signal that represents the combined behaviour of all the molecules in the sample. In contrast, single-molecule sensors have the remarkable capability to measure and analyse individual molecules one by one. This provides insights into the intrinsic heterogeneity present in the sample. Every molecule is treated as a unique entity, enabling the detection of variations, interactions, and behaviours that would otherwise be masked in ensemble measurements. Panel (a) adapted from reference, [3] Wiley. ..... [40]

Figure 1.2 Biological nanopores. Side view and top view of (a) α-Hemolysin (PDB: 7AHL), (b) MspA (PDB: 1UUN) and (c) Aerolysin (PDB: 5JZT). ..... [44]

Figure 1.3 Fabrication of solid-state nanopores. (a) Fabrication of sub-10 nm nanopores on a membrane using focused electron or ion-beam milling, in which the pore size and shape and be monitored by TEM during the fabrication process. TEM images showing SiO_2 nanopore formation using an electron beam. (b) Pore formation using controlled dielectric breakdown. The membrane material, such as SiN, HfO_2 and SiO_2, is immersed in an electrolyte (such as KCl, NaCl or LiCl) and exposed to an electric field with intensity comparable to the dielectric strength of the membrane. This leads to the generation of structural via tunnelling leakage current, resulting in the dielectric breakdown of the membrane and in the formation of a nanopore. Panel (a) adapted from reference, [43] Springer Nature Limited. Panel (b) adapted from reference, [44] Springer Nature Limited. ..... [45]

Figure 1.4 Nanopipette sensors. Nanopipettes offer a promising confined space that enables advances in electrochemical, optical, mass spectrometric measurements from microscale to

nanoscale. The pipettes can be used for non-invasive detection within single cells. Also, they can also be used to sense single particles or single biomolecules such as protein or DNA to reveal the hidden population properties and dynamics. ..... [47]

Figure 1.5 Working principle of nanopore sensing. (a) Two reservoirs filled with an electrolyte such as KCl, NaCl or LiCl are separated by a non-conductive membrane and connected via a single nanopore. Two electrodes, typically Ag/AgCl electrodes, are immersed in the two reservoirs and a constant bias is applied across the pore, resulting in a steady ionic current through the pore. Under the application of voltage, analytes such as DNA or proteins are captured by the local electric field and translocate through the nanopore. (b) Current-time trace showing the current blockade events of single-molecule translocation. By analysing the features of individual events such as the duration, amplitude, and noise level, the properties of the analytes such as size, shape and charge can be revealed. ..... [49]

Figure 1.6 Schematic of the electrical double layer in aqueous solution at the interface with a charged surface. Ion distribution as well as local potential distribution is characterised by Gouy-Chapman-Stern model. The decay length is estimated to be the Debye length, λ_{D}. ..... [52]

Figure 1.7 Ionic current rectification in nanopores. I-V curves of a nanopipette with a diameter of 15 nm at (a) 1 M KCl, 10 mM Tris-EDTA, pH 8.0 buffer, and (b) 0.1 M KCl, 10 mM Tris-EDTA, pH 8.0 buffer. ..... [54]

Figure 1.8 Electrophoretic and electroosmotic flow in nanopore sensing. (a) Current traces of avidin translocation under an application of positive and negative bias at varying pH values (pH 2-10). (b) Schematic of electrophoretic and electroosmotic velocities in protein translocation with varying protein and pore charges. Figures adapted from reference, [91] American Chemical Society. ..... [57]

Figure 1.9 Nanopore sensing of single biomolecules. (a) Differentiation of small nucleic acids using a nanopore with 3 nm in diameter and 7 nm in thickness. Specifically, 25-bp DNA, 22-bp RNA and tRNA are distinguished based on their current amplitudes. (b) Protein detection using an ultra-thin solid-state nanopore based on a freestanding HfO_2 membrane. The current traces are recoded using a high-bandwidth and low-noise system. Calmodulin is shown as an example. Panel (a) adapted from reference, [54] Springer Nature Limited. Panel (b) adapted from reference, [96] American Chemical Society. ..... [58]

Figure 1.10 Functionalised nanopores. (a) Schematic of a His-tagged protein translocated through a bi-NTA (shown in green) functionalised gold-coated nanopore. A zoomed-in view shows the His6-tag chelated with the Ni-NTA during translocating. A typical current trace, as seen in the bottom panel, shows the prolonged translocation events upon the specific binding of target molecules. (b) Real-time shape approximation of single proteins using a lipid coated nanopore. Proteins with different sizes and shapes can be obtained from the current modulations within individual translocation events. Panel (a) adapted from reference, [129] Springer Nature Limited. Panel (b) adapted from reference, [133] Springer Nature Limited. . [63]

Figure 1.11 Molecular carriers used in protein nanopore sensing. (a) Multiplexed detection of proteins using aptamer-modified DNA carriers. The analyte protein is recognised by the subpeak positioned within individual events, where the subpeak amplitude indicates the protein size. (b) Peptide nanopore sequencing assisted by a carrier DNA. Based on the nanopore sequencing system, the carrier DNA is controlled by the motor protein under a precise speed, resulting in a high-resolution reading of the conjugated peptide. (c) Antigen detection based on the dimerisation of gold nanoparticle carriers. The doublet signals suggest the translocation of particle dimers, which further indicate the presence of analyte proteins. Panel (a) adapted from reference, [135] Springer Nature Limited. Panel (b) adapted from reference, [120] AAAS. Panel (c) adapted from reference, [136] Wiley. ..... [66]

Figure 1.12 Hybrid nanopores. (a) Structure of α-Hemolysin conjugated with a carrier DNA. Under an applied voltage, the protein-dsDNA conjugate is electrophoretically driven through the solid-state nanopore, forming a stable hybrid pore. (b) Covalent linkage between the solid-state nanopore and the G20C portal protein. The solid-state nanopore is chemically functionalised thiol groups, which can form disulfide bridges with the cysteine residues of the G20C portal protein to ensure a stable hybrid nanopore. Panel (a) adapted from reference, [145] Springer Nature Limited. Panel (b) adapted from reference, [148] American Chemical Society. ..... [68]

Figure 1.13 Optical nanopore sensing. (a) Detecting the translocation of a fluorophore-labelled analyte through the nanopore. (b) Detecting the nanopore translocation of an analyte labelled with an indicator dye. Analyte translocation changes the fluorescence signal by modifying the transport of Ca^{2+} ions through the pore. (c) Detecting an analyte translocating through a plasmonic nanostructure. Analytes in close proximity to the nanostructure change the local

refractive index which changes the plasmon resonance frequency. (d) Detection by surface-enhanced Raman spectroscopy. (e) Protein detection using molecular-beacon-modified DNA carriers. The simultaneous detection of optical and electrical signals suggests the presence of target proteins. (f) A plasmonic bow-tie nanostructure is fabricated next to a nanopore, which is used for DNA sequencing. Panels (a)-(d) adapted from reference, [149] American Chemical Society. Panel (e) adapted from reference, [150] Springer Nature Limited. Panel (f) adapted from reference, [151] American Chemical Society. ..... [70]

Figure 1.14 Nanopore sensing integrated with scanning microscopy. (a) Principle of scanning ion conductance spectroscopy (SICS). Molecule capture followed by controlled translocation and corresponding conductance-distance spectrum. (b) Controlled translocation of a DNA ruler using SICS, where DNA is grafted upon a glass surface by biotin-streptavidin interactions. The subpeaks shown in the SICS result correspond to the positions and sizes of the DNA markers on the DNA backbone. (c) Localised protein detection using a nanopore AFM. The tip of AFM approaching to the surface creates a nanoconfined area that produces an energy barrier for biomolecular translocation before entering to the nanopore. Panels (a) and (b) adapted from reference, [73] Springer Nature Limited. Panel (c) adapted from reference, [155] Springer Nature Limited. ..... [71]

Figure 1.15 Nanopore field-effect transistors (FETs) and tunnelling junctions. (a) A nanopore sensor integrated with a FET component. Polypyrrole can serve as a gate to modulate molecule translocation through the nanopore. Recognition receptors can be dopped in the polymeric film to improve the selectivity of nanopore sensing. (b) Schematic of tunnelling sequencing embedded on a nanopore. The DNA molecule is led through a nanopore, which is modified with integrated emitter and collector tunnelling probes, alongside a back gate. As the DNA translocates through the pore, the changes in the tunnelling currents are expected to differentiate the nucleotide type. Panel (a) adapted from reference, [159] Springer Nature Limited. Panel (b) adapted from reference, [10] Springer Nature Limited. ..... [72]

Figure 2.1 Fabrication of single-barrel nanopipettes. Single-barrel quartz nanopipettes are fabricated using a laser-assisted puller following a two-line protocol. ..... [90]

Figure 2.2 Optical imaging of single-barrel nanopipettes. Single-barrel quartz nanopipettes fabricated after a two-line laser pulling with (a) Protocol 1 and (b) Protocol 2. Scale bar: (i) 200 µm; (ii) 20 µm. ..... [92]

Figure 2.3 SEM imaging of single-barrel nanopipettes. A single-barrel quartz nanopipette fabricated using Protocol 2 was shown with a side view (a) (scale bar: 20 µm) and a top view (b) (scale bar: 20 nm). ..... [94]

Figure 2.4 I-V characterisation of a nanopipette. I-t measurement of a typical nanopipette under the bias from -600 mV to 600 mV in (a) 1 M KCl Tris-EDTA buffer and (b) 100 mM KCl Tris-EDTA buffer. The I-V curve was obtained from the steady current at each voltage. (c) and (d) I-V curves of the nanopipette corresponding to (a) and (b), respectively, which can be used to calculate the conductance and the ionic current rectification of the nanopore. ..... [95]

Figure 2.5 Schematic representation of a nanopipette geometry. (a) The geometric model was used for the calculation of the diameter and effective length of nanopipettes. (b) SEM images of the nanopipettes show the taper and geometry (scale bar: 100 nm). The outer half cone angle was directly measured from these side-view images. The inner semi-angle was assumed is equal to the outer semi-angle when calculating the nanopore size. ..... [96]

Figure 2.6 Calculation of the effective length of nanopipettes. Plots of $R_{\mathrm{l}}/R_{\mathrm{int}}$ versus normalised length (l/r) showing the increase of resistance contribution with the distance for 20 different conical nanopipettes. The effective length was calculated at the region of 90% as marked in the plot. ..... [98]

Figure 2.7 Experimental setup for nanopore measurements. In a typical nanopore experiment, the nanopore separates the electrolyte solution into two chambers. Two Ag/AgCl electrodes are used to connect the circuit. Analytes are introduced into one of the chambers and translocate through the pore under the application of voltage. ..... [99]

Figure 2.8 Fabrication of Ag/AgCl electrodes. (a) Experimental setup for preparation of Ag/AgCl electrodes. A potentiostatic technique was used for the electrodeposition. Concretely, a potential of +2 V was applied at the working electrode where AgCl grew on the surface of the Ag wire. The same Ag wire was used as the reference electrode where hydrogen bubbles were

generated accordingly. (b) I-t curve showing an electrodeposition of AgCl in a 1 M KCl solution under a bias of 2 V. ..... [100]

Figure 2.9 Schematic of nanopipette-based ionic current measurements. Two Ag/AgCl electrodes were filled into the nanopipette (*trans* chamber) and the external bath (*cis* chamber), respectively. Voltage was applied across these two electrodes to drive molecule translocating through the nanopore. Inset is the SEM image of a nanopore (scale bar: 20 nm). Ionic current was recorded using a high-bandwidth amplifier (Chimera VC100) as shown aside. ..... [102]

Figure 2.10 Workflow of single-molecule data processing. A diagram showing a typically procedure to analyse nanopore translocation data using The Nanopore App. ..... [103]

Figure 2.11 Data import. Raw data of lambda DNA translocation (100 pM in 1 M KCl Tris-EDTA pH 8.0 buffer) recorded by Chimera VC100 under a bias of +500 mV was imported into The Nanopore App. ..... [104]

Figure 2.12 Data resampling and filtering. Imported data of lambda DNA translocation (100 pM in 1 M KCl Tris-EDTA pH 8.0 buffer) recorded by Chimera VC100 was resampled to 1 μs and low-pass filtered to 50 kHz in The Nanopore App. ..... [105]

Figure 2.13 Baseline tracking and data thresholding. (a) Current-time trace after being flipped to ensure the events are upward. (b) The baseline was tracked using a polynomial fitting with a step of 200 data points. (c) A threshold of 9 standard deviations of the baseline distribution was applied to determine the translocation events. (d) Poisson probability distribution of current points, where the baseline level was fitted with red line and the threshold was shown with black dashed line. ..... [106]

Figure 2.14 Single-molecule translocation event extraction. (a) Individual events were extracted after applying the lower and upper thresholds from the previous step. (b) Individual events were separated after removing the inter-event baseline. (c) Each event was fitted using the CUSUM+ algorithm to characterise its features. ..... [108]

Figure 2.15 Subpeak analysis of translocation events. (a) Events with at least one subpeak were isolated in this section. (b) The Nanopore App can automate the subpeak features from the

CUMSUM+ fitting. (c) Scatter plots of current vs. dwell time for the isolated events. (d) Aligned events with the normalised event width. Dashed line shows the average event shape. ....[109]

Figure 2.16 Statistical analysis of translocation events. (a) Histograms of dwell time, charge and peak current showing the molecular behaviours of lambda DNA during nanopore translocation. It should be noted that the histograms can be fitted using Gaussian distribution, while the distribution of dwell time can also be fitted by Ling distribution if needed. (b) Density scatter plots of peak current vs. dwell time and charge vs. dwell time. (c) The distribution of inter-event times fitted with an exponential decay curve. (d) The power spectral density (PSD) of the ionic current recordings. .....[110]

Figure 3.1 Purification and characterisation of actin and its activity. (a) A size exclusion chromatography profile of the purified actin. Monomeric actin eluted between elution fractions 60 mL and 80 mL. (b) SDS-PAGE analysis of the monomeric elution fractions. Gel 1 and 2 correspond to the elution fractions show in panel a, in which different columns represent different loading amounts. (c) A sample of the actin was labelled with pyrene and checked for activity using a pyrene fluorescence filamentation assay. Actin polymerised as normal under the presence of polymerisation enhancing factors (c and d) with a critical concentration of 0.6 μM. (e) actin did not form filaments in the nanopore buffer at the concentrations used in the nanopore experiments. .....[119]

Figure 3.2 SEM images of nanopipettes fabricated by a laser-assisted pulling protocol of quartz capillaries. Left: SEM images showing a conical shape at the tapered tip of nanocapillaries. Middle: deeper landscape of the tip of nanopipettes with a nanoscale pore in the centre. Right: close-up SEM images of the nanopore with a diameter of 25 ± 4 nm formed in the pipettes. .....[125]

Figure 3.3 Current-voltage curves of nanopipettes used in nanopore measurements. I-V curves obtained in 1 M KCl actin monomeric buffer (containing 20 mM Tris pH 8, 0.4 mM ADP, 0.1 mM $CaCl_2$, 0.01% DMSO and 10% glycerol). The nanopore conductance was estimated to be 37.0 ± 3.9 nS by linear fitting. .....[126]

Figure 3.4 Schematic of experimental set-up of protein detection using nanopipette-based nanopore. The nanopipette and external bath were filled with a monomeric ADP-actin calcium buffer. One Ag/AgCl working electrode was inserted into the pipette, and the other one

Ag/AgCl reference/ground electrode was fixed in the bath where the protein was introduced. Under external electric field, actin molecules in different states were translocated from the bath to the inside of the pipette through a conical nanopore at the pipette tip. Right insert: a typical SEM image showing that the nanopipette tapers down at the tip to form a nanopore with the diameter of 25 nm (scale bar 200 nm, top; 50 nm, bottom). .....[127]

Figure 3.5 Ionic current-time traces of 800 nM actin monomers. The nanopore experiments were conducted in 1 M KCl buffer containing 20 mM Tris pH 8, 0.4 mM ADP, 0.1 mM $CaCl_2$, 0.01% DMSO and 10% glycerol, recorded at 4.17 MHz, filtered to 50 kHz, and collected at different voltages. These traces show translocation spikes at positive voltages with a voltage dependence but no translocation events at negative voltages, demonstrating that EP driving forces dominate the actin transport. .....[128]

Figure 3.6 Nanopore detection of actin macromolecular states. (a) Top: protein structures (from left to right): G-actin monomer (42 kDa, PDB: 1NWK, 800 nM), drug-induced actin dimer (PDB: 1YXQ, 500 nM) and F-actin (up to 200 actin subunits, PDB: 3G37, 800 nM). Middle: representative current-time traces. Bottom: typical translocation events. Box and whisker plots showing the distribution of peak current (b) and dwell time (c) (median line and interquartile range). All data in this figure was recorded at 250 mV, sampled at 1 MHz and low-pass filtered at 50 kHz. .....[129]

Figure 3.7 Statistical analysis of actin macromolecular states. Scatterplots of current blockades vs. dwell times for different actin species (from left to right: G-actin monomer, drug-induced actin dimer, and F-actin) with the voltage application of 250 mV. .....[130]

Figure 3.8 Nanopore compatibility with actin unfolding conditions. (a) Current-time traces of 1 M KCl actin monomeric buffer containing 0 M and 6 M urea respectively at 250 mV. The trace for 6 M urea shows a decrease of ionic current due to the decrease of solution conductivity and remains stable after a long-time recording, indicative of a good compatibility of quartz nanopipettes with urea. (b) I-V curves of nanopipettes obtained in 1 M KCl actin monomeric buffer with 6 M urea. The grey shadow is the I-V curves tested in the buffer without urea. .....[131]

Figure 3.9 Discrimination of actin unfolding in a urea gradient using nanopipettes. (a) Normalised statistic of excluded volumes (calculated from $\Lambda \approx \Delta I_{\mathrm{b}} \cdot H_{\mathrm{eff}}^2/(\sigma\psi)$) from native

actin to denatured actin in increasing urea concentration. The orange boundary represents the fully folded actin state, and blue boundary determines the unfolded actin or other transient aggregates at low urea concentrations. The population shifts from a mostly native, folded state to a higher excluded volume, consistent with an unfolded state with larger hydrodynamic radius, as the urea concentration increases. Protein models for each state based on the crystal structures of G-actin (PDB: 1NWK) are shown in the inset. (b) The mean excluded volume plot exhibits a sigmoid increase when urea concentration increases, indicative of actin unfolding with an increase of hydrodynamic radius. (c) Mean dwell time decreases as the urea concentration increases. (d) Proportion of actin in different states (monomeric folded, unfolded or transient aggregated) plotted against urea concentrations shows a sigmoid curve, suggesting a two-state transition between folded (including a small fraction of aggregates) and unfolded actin. .....[132]

Figure 3.10 Changes of hydrodynamic radii ($\boldsymbol{R_H}$) of actin monomers during unfolding process. (a) Normalised distribution of fractional current blockade ($\Delta I/I_o$) in different urea concentrations. The orange boundary represents the fully folded actin state, and blue boundary determines the unfolded actin or other transient aggregates at low urea concentrations. The population shifts from a mostly native, folded state to a higher excluded volume, consistent with an unfolded state with larger hydrodynamic radii, as the urea concentration increases. (b) Top: schematic of conformational changes during actin unfolding. Bottom: plot of R_H vs. urea concentrations showing a two-state trend. .....[134]

Figure 3.11 Plots of free energy as a function of urea concentration along with a linear fitting. .....[135]

Figure 3.12 Voltage dependence upon actin translocation through nanopipettes. (a) Voltage-dependent ionic current traces show the translocation spikes of 800 nM folded actin in 0 M urea and unfolded actin in 6 M urea. Open currents (I_o) for each voltage were marked upon each baseline. (b) Effective velocity (H_{eff}/t_d) for both folded and unfolded actin shows a linearly voltage-dependent increase when increasing the applied voltage. (c) Normalised capture rates (J_C/C_0) shows an exponential function of applied voltages for both folded and unfolded actin. This nonlinear increase suggests a two-stage regime in which the entropic barriers restrict successful translocations at low voltages and electrophoretic forces dominate capture behaviours at higher voltages. (d) Normalised distributions of elapsed time between

successive captured events (δt) for actin transport in 0 M and 6 M urea buffers at 250 mV and 350 mV. Solid lines represent a single-exponential decay fit, from which the protein flux (J_C) is extracted for (c). (e) Plots of the ratio of the radius of gyration to hydrodynamic radius (R_G/R_H) illustrate that the actin shape is an oblate ellipsoid in 0 M urea buffer, but a prolate ellipsoid in 6 M urea buffer during nanopore translocation. With the voltage increases, the value of R_G/R_H increases both for folded and unfolded actin. This is unchanged at high voltages, indicating the protein was stretched under a high-strength localised electric field across the pipette tip. .....[137]

Figure 3.13 Discriminating folded and unfolded actin using nanopipettes performed in 1 M KCl with 0 M or 6 M urea. (a) Scatterplots of fractional current blockades vs dwell times for folded and unfolded actin at different voltages. (b) Distributions of fractional current blockades for both folded and unfolded actin at various voltages. (c) Statistic histograms of the excluded volume calculated from eq. 1 for folded and unfolded actin at different voltages from 150 mV to 350 mV. .....[138]

Figure 3.14 Plots of hydrodynamic radius (a) and excluded volume (b) vs. voltages for folded and unfolded actin. .....[140]

Figure 3.15 F-actin formation in real-time. (a) Time-dependent ionic current traces of actin filamentation. 1 µM actin was induced in the bath to form filaments and aggregation data was recorded in real-time. (b) Scatterplots of current blockades vs dwell times for F-actin formation at different time points corresponding to the I-t traces show in panel a. (c) Time-dependence of actin filament fraction (purple line) and normalised capture rate (green line) for 1 µM monomeric actin concentration. Each point was calculated every 10 min and averaged over a continuous 2 min trace. The threshold for the formation of actin oligomers and filaments was 150 pA (the mean of the second distribution in Figure 3.16). Three shadow areas and protein models (from left to right) represent actin monomers, oligomers and filaments, respectively. .....[141]

Figure 3.16 Statistical analysis of actin polymerisation. (a) Histograms of the peak current for actin filament formation at 0, 80 and 150 min at 150 mV, showing a distribution of multiple populations and an extension in higher peak currents. (b) Scatterplots of charge vs. dwell time for actin polymerisation at 0 and 150 min. .....[142]

Figure 3.17 I-V curves before and after measurement of actin filament formation (1 µM monomer concentration in ATP buffer). The slight increase of conductivity is indicative of water evaporation over time and no significant interactions between proteins and the nanopore surface. .....[143]

Figure 3.18 Latrunculin B and Swinholide A do not interact with the nanopipette surface. Current-time trances show no observable current changes for both drugs at 250 mV. .....[146]

Figure 3.19 Actin drug binding assays. (a) Left: protein models based on the X-ray crystallographic structures (actin with Latrunculin B bound, PDB: 1IJJ and actin with Swinholide A bound, PDB: 1YXQ). Right: typical current traces for actin bound to different filament inhibitors at 150, 200 and 250 mV. Ionic currents were recorded in monomeric buffer, 1 µM actin monomer and 10 µM filament inhibitor. (b) Scatterplots of current blockades vs. dwell times for both actin monomers and dimers in the same scale at 250 mV. (c) Normalised statistic of charge drops along with a Gaussian distribution fitting for actin and actin bound with two drugs. The charge drop is equivalent to the integral area of individual translocation events. (d) Voltage dependence upon normalised capture rates of actin monomers and actin bound with two drugs. .....[146]

Figure 3.20 Statistic information for (a) Actin bound with Latrunculin B, (b) Actin monomers and (c) Actin bound with Swinholide A. Left: distributions of dwell time. Middle: distributions of peak current. Right: 2-D Kernel plots of peak current vs. dwell time. All data were collected in 1 µM actin and 10 µM drug at 250 mV. .....[147]

Figure 3.21 Kinetics measurements of actin drug binding. (a) Top: typical current traces for drug binding kinetics collected at 200 mV. The first extract is the stable 1 µM actin monomer translocation trace. The second is the initial trace when 1 µM Swinholide A added, and the recording after 30 min is shown in the third trace. Bottom: histograms represent the current blockade distributions corresponding to each trace above. (b) Time-dependent curves for 1 µM actin dimerisation with 1, 0.5, and 0.2 µM Swinholide A. The dimer fraction of each point was calculated from the statistical data in 2 min, with a threshold of 75 pA. The curves were fitted by a model of three-component interactions with positive cooperativity. .....[148]

Figure 4.1 Nanopore-based protein detection using aptamer-protein-aptamer sandwich structures. (a) Schematic of the experimental setup of single-molecule detection process using

nanopipettes. The protein analyte binds to two aptamer-modified DNA carriers, generating a dimeric complex that signifies the presence of the target protein. The protein analytes, along with the DNA carriers, is positioned within the interior of the nanopipette (*trans* side), where a working Ag/AgCl electrode is situated. The external bath (*cis* side) is filled with the measuring buffer (100 mM KCl, 10 mM Tris-EDTA pH 8.0), accompanied by the reference Ag/AgCl electrode. (b) A typical current trace highlighting the occurrence of conductive current events under the application of a bias of -300 mV. (c) Proteins possessing two aptamer-binding sites, exemplified by thrombin (PDB: 5EW2), have the capability to establish a sandwich structure in conjunction with the specially engineered DNA carriers. Upon the successful formation of such structures, translocation events exhibit distinctive characteristics including double dwell time and charge, as well as the emergence of a discernible subpeak at the midpoint of the event. .....[159]

Figure 4.2 SEM and conductance characterisation of nanopipettes. The nanopipettes used in this work were fabricated from quartz capillaries (ID: 0.5 mm, OD: 1.0 mm) by a laser-assisted puller. (a) I-V curves were measured from 20 different pipettes in 100 mM KCl, 10 mM Tris-EDTA, pH 8.0 buffer, showing a current rectification feature. (b) Top-view SEM images of a typical nanopore (scale bar: 100 nm). .....[163]

Figure 4.3 Noise evaluation for nanopore measurements. The power spectral density (PSD) plots for the nanopipette system under a bias of (a) 0 mV and (b) -300 mV. .....[164]

Figure 4.4 DNA translocation direction in the nanopore sensing. DNA molecules translocated from the inside to the outside of the nanopipette under a negative bias showing conductive enhancement events, whereas no translocation events were observed at positive voltages. The traces were collected from 200 pM 4.3 kbp DNA in 100 mM KCl, 10 mM Tris-EDTA pH 8.0 buffer with a voltage of ±300 mV. .....[165]

Figure 4.5 Preparation of 4.3 kbp aptamer-modified DNA carriers. 4.3 kbp DNA carriers were cleaved from λ-DNA using a restriction enzyme, Hind III, followed by hybridisation and ligation the aptamer probe to the carrier. The aptamer probe includes a sequence complementary to the 12-base sticky overhand of the 4.3 kbp carrier, a polyT spacer, and a protein aptamer sequence. Detailed sequence information is shown in the table. The final products were characterised by gel electrophoresis in the inset. .....[165]

Figure 4.6 Characterisation of 4.3 kbp aptamer-modified DNA carriers. (a) Gel electrophoresis showing the fragments digested from λ-DNA using Hind III. The marked bands are the expected 4.3 kbp DNA fragments. (b) A typical absorption spectrum of the purified 4.3 kbp aptamer-modified DNA carriers showing its concentration and purity with a high 260/280 ratio. ... [167]

Figure 4.7 DNA translocation at varying applied voltages. Representative current traces at a gradient voltage showing the translocation of 4.3 kbp aptamer-modified DNA carrier in 100 KCl, 10 mM Tris-EDTA pH 8.0 measuring buffer. ..... [168]

Figure 4.8 Voltage dependence of nanopore translocation for 4.3 kbp aptamer-modified DNA carriers. Plots of (a) capture rate, (b) dwell time, (c) peak amplitude and (d) equivalent charge are shown along with the fitting curve. ..... [169]

Figure 4.9 Event definition using CUSUM+ algorithm. Typical events for 5 kbp and 10 kbp DNA in both folded and unfolded states are shown in blue lines. The boundaries for event definition are established through the fitting of the CUSUM+ analysis. The equivalent charge is subsequently calculated based on the peak area within the boundaries determined by the CUSUM+ algorithm. ..... [170]

Figure 4.10 Charge classification for 5 kbp and 10 kbp DNA. (a) A representative current trace of nanopore translocation for a mixture of 200 pM 5 kbp and 200 pM 10 kbp DNA. Typical events are shown corresponding to 5 kbp and 10 kbp DNA at folded and unfolded conformations. Density scatter plots of (b) peak amplitude against dwell time, and (c) charge against dwell time for the mixture of 5 kbp and 10 kbp DNA. (d) Distribution of the charge showing that 5 kbp and 10 kbp DNA are easy to discriminate by setting a threshold of charge. ..... [171]

Figure 4.11 Charge classification for 5 kbp and 10 kbp DNA. Histograms of (a) dwell time and (b) peak amplitude for the mixture of 5 kbp and 10 kbp DNA, along with the multiple Gaussian fittings. ..... [172]

Figure 4.12 Nanopore measurements of pure thrombin. Nanopore experiments were performed using 10 nM thrombin in 100 mM KCl measuring buffer under a bias of -300 mV, without translocation events detectable under this condition. ..... [174]

Figure 4.13 Representative current traces and events of thrombin detection. (a) A typical trace recorded using 100 pM thrombin and 100 pM DNA carrier in 100 mM KCl measuring buffer under a bias of -300 mV. (b) Monomeric events and (c) dimeric events with sandwich structure formed. .....[175]

Figure 4.14 Nanopore detection of thrombin using dimerisation of aptamer-modified DNA carriers. (a) Schematic of the structure of thrombin sandwiched by HD1 and HD22 modified DNA carriers (PDB: 5EW2). Inset: overlay of 100 dimeric events formed by the HD1-thrombin-HD22 sandwich structure. (b) Diagrams of nanopore translocation for unfolded and partially folded dimeric events. Nanopore experiments were performed using 100 pM thrombin with 100 pM of each carrier in 100 mM KCl measuring buffer under a bias of -300 mV. .....[176]

Figure 4.15 Statistics of carrier translocation with and without thrombin. Scatter plots of charge versus dwell time for (a) 100 pM HD1-modified carrier and 100 pM HD22-modified carrier; (b) 100 pM thrombin incubated with 100 pM HD1-modified carrier and 100 pM HD22-modified carrier. Nanopore experiments were performed in 100 mM KCl measuring buffer under a bias of -300 mV. .....[177]

Figure 4.16 Statistical analysis of thrombin detection using dimeric carriers. (a) Histogram of charge showing two populations which correspond to monomeric DNA carriers and dimeric DNA carriers, respectively. (b) Distributions of extracted dwell time and peak amplitude for subpeaks and DNA levels. (c) Scattering points of fractional width (defined as the ratio of subpeak width to the width of DNA level) against the fractional position where the subpeak maxima was located along the event for extracted dimeric events. (d) Binding assays of 100 pM of each carrier in the presence of thrombin ranging from 100 fM to 10 nM. The binding curve was fitted with a biphasic Hill model and the K_{d} value was determined to be about 12.2 pM. .....[178]

Figure 4.17 Nanopore detection of dimeric proteins using aptamer-modified DNA carrier. Schematic of the dimeric protein bound to two identical aptamer-modified DNA carriers for (a) VEGF and (b) PDGF. Representative current traces and typical dimeric events were collected with 100 pM protein concentration and 200 pM carrier concentration in 100 mM KCl measuring buffer under a bias of -300 mV. .....[181]

Figure 4.18 Nanopore measurements of pure VEGF and PDGF. Nanopore experiments were performed using 10 nM VEGF/PDGF in 100 mM KCl measuring buffer under a bias of -300 mV, without translocation events detectable under this condition. .....[182]

Figure 4.19 Statistical analysis of VEGF and PDGF detection using dimeric carriers. (a) Scatter plots of charge against dwell time for VEGF and PDGF, where the dimeric events over the charge threshold were highlighted with blue and orange colour, respectively. (b) Scattering points of normalised subpeak amplitude (defined as the ratio of subpeak amplitude to the height of DNA level) against the fractional position for extracted dimeric events, along with the statistical histograms. (c) Binding assays of 200 pM DNA carriers in the presence of VEGF and PDGF ranging from 10 fM to 10 nM. The binding curves were fitted with a biphasic Hill model and the K_{d} value was determined to be about 1.0 pM and 5.9 pM for VEGF and PDGF, respectively. .....[183]

Figure 4.20 Nanopore measurements of pure c-Met. Nanopore experiments were performed using (a) 10 nM c-Met, (b) 10 nM c-Met + 10 nM HGF, and (c) 10 nM c-Met + 10 nM HGF + 10 nM anti-HGF antibody in 100 mM KCl measuring buffer under a bias of -300 mV, without translocation events detectable under this condition. .....[185]

Figure 4.21 Nanopore detection of HGF-induced c-Met dimerisation using aptamer-modified DNA carrier. (a) Schematic and typical events for (i) monomeric c-Met receptors bound to the DNA carriers, (ii) HGF-induced c-Met dimers bound to two DNA carriers, and (iii) c-Met receptors and HGF under the inhibition of anti-HGF antibody. (b) Scatter plots of charge against dwell time for nonactivated c-Met monomers, activated c-Met dimers and inhibited c-Met monomers, where the dimeric events over the charge threshold were highlighted with purple colour, respectively. Representative events were collected with 200 pM protein concentration and 200 pM carrier concentration in 100 mM KCl measuring buffer under a bias of -300 mV. .....[186]

Figure 4.22 Subpeak analysis for translocation events of HGF-induced c-Met dimerisation. (a) The distribution of normalised subpeak amplitude and fractional position for dimeric events extracted from the translocation of HGF-induced c-Met dimers bound to DNA carriers. (b) Comparison of the distribution of normalised subpeak amplitude for the c-Met dimer,

thrombin, VEGF and PDGF. (c) A linear correlation was shown on mean normalised subpeak amplitude against the molecular weight. .....[187]

Figure 4.23 Nanopore detection of c-Met dimerisation in human serum. (a) Dimerisation ratio of c-Met in the presence of varying HGF concentrations (0, 2, 20, 200 pM). DNA carriers and c-Met concentration were fixed to be 200 pM and an excess concentration of 5 nM anti-HGF antibody were used to monitor the inhibitory effect. (b) Current baseline for the dilution of human serum to the measuring buffer (1: 5, 1: 10 and 1: 20). (c) Typical trace of DNA translocation in 1: 20 serum solution. Binding ratio of c-Met dimers to DNA carrier in 1: 20 serum solution. .....[189]

Figure 5.1 Schematic of nanopore detection using supercharged polypeptide carriers. Nanopore measurements of native proteins show fast translocation beyond the limits of traditional instruments, resulting in lower-than-expected capture rates and biased characteristic signals. With the assistance of SUP carriers, the protein capture rate is dramatically improved due to the introduction of a high net charge. In addition, translocation of such protein conjugates is substantially slowed down by the electrostatic attraction with the pore. Here, protein signals can be well distinguished from the SUP signals based on the difference in their excluded volume. .....[199]

Figure 5.2 Workflow of the Nanopore App for data analysis. (a) Data import and filter. In this step, nanopore data was loaded into the Nanopore App and then resampled and low-pass filtered dependent on the signal-to-noise ratio (e.g., 1 MHz sampling rate and 10 kHz low-pass filter). (b) Baseline tracking and threshold. The baseline was tracked to compensate for fluctuations in the current recordings. A histogram of all points was fitted by a Poisson distribution for the baseline, and a threshold (e.g., 7 σ) was used to classify events. (c) Peak selection. Events with a peak amplitude above the set threshold were selected. (d) Subpeak analysis. Multiple levels of an event were classified using cumulative sum (CUSUM) analysis, and subpeak amplitude and fractional position could be exported. .....[204]

Figure 5.3 Schematic for the preparation of SUPs via recombinant DNA technology. (a) Recursive directional ligation (RDL) was used for the molecular cloning of SUP plasmid. (b) The fused SUPs were expressed in an *E. coli* system. .....[205]

Figure 5.4 SDS-PAGE characterisation of SUP samples. Protein molecular weight markers were shown in each gel image with the protein products (a) eGFP; (b) eGFP-E36; (c) eGFP-K18, eGFP-K36, and eGFP-K72; (d) K72 and Sn-K72; (e) mIFP-K72; (f) K36-SfGFP-K36. It should be noted that the electrophoretic mobility of highly charged SUP samples is slightly different from that of folded proteins, which usually exhibit a larger apparent mass than standard mass markers. .....[206]

Figure 5.5 Mass spectra of SUP samples. (a) eGFP; (b) eGFP-E36; (c) eGFP-K18; (d) eGFP-K36; (e) eGFP-K72; (f) K36-SfGFP-K36. .....[207]

Figure 5.6 SEM and conductance characterisation of nanopipettes. The nanopipettes used in this work were fabricated from quartz capillaries (ID: 0.5 mm, OD: 1.0 mm) by a laser-assisted puller. (a) Top-view SEM images of the nanopores (scale bar: 20 nm). (b) I-V curves were measured in 1 M KCl, 10 mM Tris-EDTA, pH 8.0 buffer. The nanopore conductance was estimated to be 20.0 ± 1.6 nS fitted as a linear curve. (c) SEM images of the nanopipettes show the taper and geometry (scale bar: 100 nm). The outer half cone angle was directly measured from these side-view images. When calculating the nanopore size, the inner semi-angle was assumed to be equal to the outer semi-angle. .....[208]

Figure 5.7 Power spectral density (PSD) plots of the nanopore platform. PSD plots were measured in 1 M KCl, 10 mM Tris-EDTA, pH 8.0 buffer, under a voltage of 500 mV and processed by The Nanopore APP. .....[209]

Figure 5.8 Single-molecule nanopore sensing of proteins carried by SUPs. (a) Schematic of the experimental setup of single-protein detection using nanopipettes. A SEM image of a typical 13 nm nanopore formed at the tip of a quartz nanopipette (scale bar: 20 nm). (b) Structural illustration of enhanced green fluorescent protein (eGFP, 28.6 kDa, pI of 5.58), anionic eGFP-E36 (46.6 kDa, pI of 4.57) and cationic eGFP-K36 (46.6 kDa, pI of 9.83). Representative ionic current traces and typical translocation events (filtered at 5 kHz for visualisation) in 1 M KCl, 10 mM Tris-EDTA, pH 8.0 buffer for eGFP (5 nM, +500 mV), eGFP-E36 (5 nM, +500 mV) and eGFP-K36 (5 nM, -500 mV) were shown respectively. Data was recorded at 1 MHz and fur-ther processed with a 10 kHz low-pass filter for statistics. .....[210]

Figure 5.9 Capture rate of eGFP, eGFP-E36 and eGFP-K36. Distributions of the inter-event time (the time between two successive captured events) for (a) 750 nM eGFP, (b) 5 nM eGFP-E36,

and (c) 5 nM eGFP-K36 at an applied voltage of 500 mV in 1 M KCl, 10 mM Tris-EDTA, pH 8.0 buffer. Solid lines represent single-exponential fits, from which the protein capture rate was extracted. .....[211]

Figure 5.10 eGFP nanopore detection at a high concentration. 750 nM eGFP was used to obtain sufficient data for statistical analysis due to the low capture rate for native eGFP. Protein translocation was performed in 1 M KCl, 10 mM Tris-EDTA, pH 8.0 buffer at +500 mV. ...[212]

Figure 5.11 Nanopore translocation behaviours of different eGFP variants. (a) Normalised capture rate (event frequency/concentration) for eGFP, eGFP-E36, and eGFP-K36 at the same voltage magnitude (500 mV). T scores were used to test the statistical significance between eGFP and eGFP-SUPs; ***P<0.001 and ****P<0.0001. (b) Scatter plots of peak amplitude versus dwell time for eGFP (n = 845), eGFP-E36 (n = 1074), and eGFP-K36 (n = 871) at 500 mV. Box and whisker plots of (c) dwell time and (d) peak amplitude for eGFP, eGFP-E36, and eGFP-K36, along with associated statistics. .....[214]

Figure 5.12 Nanopore detection of eGFP-K18, eGFP-K36 and eGFP-K72. Representative traces for the translocation of (a) 10 nM eGFP-K18, (b) 10 nM eGFP-K36, and (c) 1 nM eGFP-K72. All the translocation experiments were performed in 1 M KCl, 10 mM Tris-EDTA, pH 8.0 buffer at -500 mV. Data was sampled at 1 MHz and digitally filtered using a Bessel low-pass filter at 10 kHz. .....[215]

Figure 5.13 Charge- and length-dependence of nanopore translocation for eGFP-SUPs. (a) Schematic of the cationic eGFP-SUPs translocated through a nanopore. Lysine is the key compound in the repeated sequence $(VPGKG)_n$, where n represents the net charge of the SUP. Application of a negative bias to the *trans* chamber captures cationic eGFP-SUPs by both EP and EO flows. A series of eGFP-SUPs with different charges and chain lengths (K18, K36, and K72) were shown. Ionic current was recorded in 1 M KCl, 10 mM Tris-EDTA pH 8.0 buffer. Data was sampled at 1 MHz and low-pass filtered at 10 kHz. (b) Concentration dependence of capture rate for eGFP, eGFP-K18, eGFP-K36, and eGFP-72 at -500 mV. Voltage dependence of (c) normalised capture rate, (d) dwell time, and (e) peak amplitude for eGFP, eGFP-K18, eGFP-K36, and eGFP-72. The error bars represent one standard deviation of at least three independent experimental repeats. .....[216]

Figure 5.14 Voltage dependence of capture rate for eGFP and eGFP-K18. Normalised capture rate of cationic eGFP-SUPs was plotted as a function of the applied voltage. In particular, eGFP and eGFP-K18 show an exponential increase with the voltage, which indicates its nanopore translocation is limited by an energy barrier. Longer molecules, eGFP-K36 and eGFP-K72, present a linear increase with voltage. .....[217]

Figure 5.15 Dependence of peak amplitude on molecular weight. Peak amplitude of eGFP variants as a function of molecular weight. The current amplitude shows an exponential increase in response to the increasing length of SUPs. This experiment was repeated at least three times for each protein at 500 mV. .....[218]

Figure 5.16 Nanopore detection of K72. (a) Protein model of K72 predicted by I-TASSER. [46] (b) Typical events and current-time traces of 1 nM K72 translocation recorded in 1 M KCl, 10 mM Tris-EDTA, pH 8.0 buffer at -500 mV. Data was sampled at 1 MHz and digitally filtered using a Bessel low-pass filter at 10 kHz. (c) Scatter plot of peak amplitude versus dwell time. (d) Distribution of the dwell time and peak amplitude for K72 translocation. .....[220]

Figure 5.17 Nanopore detection of λ-DNA. (a) Representative current-time traces of 100 pM λ-DNA translocation were recorded in 1 M KCl, 10 mM Tris-EDTA, pH 8.0 buffer at +500 mV. Data was sampled at 1 MHz and digitally filtered using a Bessel low-pass filter at 10 kHz. (b) Typical events of unfolded and folded DNA molecules. (c) Scatter plot of peak amplitude versus dwell time. (d) Distribution of the dwell time and peak amplitude for λ-DNA translocation showing multiple folding levels. .....[221]

Figure 5.18 Schematic of protein detection carried by K72 carriers. (a) Structure of the protein-SUP complex, where the protein of interest was attached at one end of K72. (b) Schematic illustration of a typical event of one protein-SUP molecule during nanopore translocation. The relationship between the excluded volume (Λ) and the blockade current (ΔI_b) can be estimated using **Equation 5.1**, indicating current blockade is proportional to the excluded volume of translocated molecules. A folded protein, therefore, has a greater excluded volume per unit length than that of an unfolded, linear SUP. Individual nanopore readouts are shown with the protein level as a higher current blockade and the SUP level as a lower current blockade but longer time residence. .....[222]

Figure 5.19 Size-dependent single-protein identification using cationic SUPs and subpeak analysis. (a) Structures of a series of proteins with different sizes, Sn (13.0 kDa), SfCherry (20.3 kDa), eGFP (28.6 kDa), and mIFP (35.2 kDa), fused in K72 carriers. (b) Representative ionic current traces (scale bar: 100 pA; 5 s) and typical individual translocation events (scale bar: 50 pA; 80 ms) for the corresponding structures were filtered to 5 kHz for better visualisation. Protein translocation was performed in 1 M KCl, 10 mM Tris-EDTA pH 8.0 buffer at -500 mV and processed with a low-pass filter of 10 kHz. (c) Distributions of the subpeak amplitude extracted from individual translocation events for Sn-K72 (n = 578), SfCherry-K72 (n = 389), eGFP-K72 (n = 765), and mIFP-K72 (n = 341). The mean amplitude of subpeaks shows an increasing trend as the size of proteins increases. Distribution is fitted by the Gumbel function. (d) Distributions of fractional subpeak position (i.e., relative location) suggest subpeaks located at either start or end of individual events, consistent with the protein-SUP structure. Protein Data Bank (PDB) codes: Sn, 3BOI; SfCherry, 4KF4; eGFP, 2Y0G; mIFP, 5VIQ. .....[223]

Figure 5.20 Dependence of subpeak amplitude on molecular weight. Subpeak amplitude of different proteins as a function of molecular weight. The red line represents a linear fitting through the blue markers. This experiment was repeated at least three times for each protein, showing a similar linear dependence for these globular proteins. .....[225]

Figure 5.21 Nanopore detection of V40K72. (a) Protein model and sequence of V40K72. (b) Typical events and current-time traces of 1 nM V40K72 translocation were recorded in 1 M KCl, 10 mM Tris-EDTA, pH 8.0 buffer at -500 mV. Data was sampled at 1 MHz and digitally filtered using a Bessel low-pass filter at 10 kHz. (c) Scatter plot of peak amplitude versus dwell time. (d) Distribution of the dwell time and peak amplitude for V40K72 translocation. .....[225]

Figure 5.22 Nanopore detection of eGFP-K72 at low ionic strengths. (a) Schematic of eGFP-K72 translocation at a low salt concentration (100 mM KCl, 10 mM10 mM Tris-EDTA, pH 8.0 buffer). In this case, the protein was added inside the nanopipette (*trans* chamber), and a negative voltage was applied to drive protein molecules translocating from *trans* to *cis* side. Cationic SUPs had stronger electrostatic interaction with the nanopore inner walls at low ionic strengths. (b) Typical events and current-time traces of 10 nM eGFP-K72 show a two-level current signature with a subpeak at the end. (c) Illustration of eGFP-K72 translocation and corresponding current blockade. (d) Scatter plots of peak amplitude versus dwell time for the

first level (SUP level) and second level (eGFP level). (e) Statistics for the subpeak position and subpeak amplitude. .....[226]

Figure 5.23 Subpeak analysis of rational design of protein-SUP constructs. (a) Schematic of the structure of K36-protein-K36, in which the net charge is equivalent to K72 carriers, but target protein is bound at the centre of the carrier. (b) An example translocation event for K36-protein-K36 shows the subpeak is shifted to the centre of the signal where the target protein is. (c) Structures of K36-SfCherry-K36 and K36-SfGFP-K36 used for single-molecule protein identification. (d) Representative translocation events (scale bar: 50 pA; 20 ms; filtered to 5 kHz) indicating nanopore signals were consistent with the protein structures with a folded protein at the centre. Nanopore experiments were performed in 1 M KCl, 10 mM Tris-EDTA pH 8.0 buffer at -500 mV with a low-pass filter of 10 kHz. (e) Distributions of the subpeak amplitude extracted from individual events for K36-SfCherry-K36 (n = 286) and K36-SfGFP-K36 (n = 307) were fitted with the Gaussian function. (f) Distributions of fractional subpeak position suggest that subpeaks are located at the centre of individual events as designed in the structure. ..
.....[227]

Figure 5.24 Nanopore detection of K36-SfCherry-K36 and K36-SfGFP-K36. Representative current-time traces of (a)1 nM K36-SfCherry-K36 and (b) 1 nM K36-SfGFP-K36 translocation recorded in 1 M KCl, 10 mM Tris-EDTA, pH 8.0 buffer at -500 mV. Data was sampled at 1 MHz and digitally filtered using a Bessel low-pass filter at 10 kHz. Distributions of the elapsed time between successive captured events for (c) 1 nM K36-SfCherry-K36 and (d) 1 nM K36-SfGFP-K36 with a single-exponential decay fitting. .....[228]

Figure 5.25 Nanopore sensing of single protein-protein interactions using cationic SUPs. A proof-of-concept demonstrated here is using eGFP-K72 as the antigen to detect anti-GFP antibody. Schematic representation of antibody-eGFP complexes and antibody-eGFP-K72 complexes. Representative ionic current traces for (i) antibody (10 nM)-eGFP (1 nM) interactions and (ii) antibody (10 nM)-eGFP-K72 (1 nM) interactions recorded in PBS + 1 M KCl, 10 mM Tris-EDTA pH 8.0 buffer (1: 9, v/v) at -500 mV. Typical individual events show an enhanced subpeak for antibody-eGFP-K72 complexes compared with eGFP-K72. Data was sampled at 1 MHz and re-filtered to 5 kHz for visualisation. .....[230]

Figure 5.26 Nanopore detection of anti-GFP antibody. (a) Protein model of anti-GFP antibody (IgG1). (b) Typical events and current-time traces of 10 nM anti-GFP antibody translocation recorded in 1 M KCl, 10 mM Tris-EDTA, pH 8.0 buffer at -500 mV. Data was sampled at 1 MHz and digitally filtered using a Bessel low-pass filter at 10 kHz. (c) Scatter plot of peak amplitude versus dwell time. (d) Distribution of the dwell time and peak amplitude for anti-GFP antibody translocation. .....[231]

Figure 5.27 Nanopore detection of eGFP with anti-GFP antibody. (a) Protein model of eGFP-anti-GFP antibody complex. (b) Typical events and current-time traces of 1 nM eGFP + 10 nM anti-GFP antibody translocation were recorded in 1 M KCl, 10 mM Tris-EDTA, pH 8.0 buffer at -500 mV. Data was sampled at 1 MHz and digitally filtered using a Bessel low-pass filter at 10 kHz. (c) Scatter plot of peak amplitude versus dwell time. (d) Distribution of the dwell time and peak amplitude for the translocation of eGFP with anti-GFP antibody (1: 10). .....[232]

Figure 5.28 Nanopore detection of K72 with anti-GFP antibody. (a) Protein model of K72 and anti-GFP antibody. (b) Typical events and current-time traces of 1 nM K72 + 10 nM anti-GFP antibody translocation were recorded in 1 M KCl, 10 mM Tris-EDTA, pH 8.0 buffer at -500 mV. Data was sampled at 1 MHz and digitally filtered using a Bessel low-pass filter at 10 kHz. (c) Scatter plot of peak amplitude versus dwell time. (d) Distribution of the dwell time and peak amplitude for the translocation of K72 with anti-GFP antibody (1: 10). .....[233]

Figure 5.29 Nanopore detection of eGFP-K72 with anti-GFP antibody. (a) Protein model of eGFP-K72-anti-GFP antibody complex. (b) Typical events and current-time traces of 1 nM eGFP-K72 + 10 nM anti-GFP antibody translocation were recorded in 1 M KCl, 10 mM Tris-EDTA, pH 8.0 buffer at -500 mV. Data was sampled at 1 MHz and further low-pass filtered at 10 kHz. (c) Scatter plot of peak amplitude versus dwell time. (d) Distribution of the dwell time and peak amplitude for the translocation of eGFP-K72 with anti-GFP antibody (1: 10). .....[234]

Figure 5.30 Identification of protein-protein interactions with SUP and without SUP. (a) Schematic illustration of antibody-eGFP binding and density scatter plots of peak amplitude versus dwell time for separate translocation experiments of 10 nM antibody (n = 1220), 750 nM eGFP (n = 845), and 10 nM antibody + 1 nM eGFP (n = 979). (b) Same antigen-antibody binding, but the antigen was replaced with eGFP-K72. Density scatter plots for separate

experiments of 10 nM antibody (n = 1220), 1 nM eGFP-K72 (n = 1865), and 10 nM antibody + 1 nM eGFP-K72 (n = 1378). .....[235]

Figure 5.31 Binding assays of eGFP-K72 with its antibody. (a) Subpeak analysis of eGFP-K72 (1 nM) interacting with antibody (10 nM). Distribution of subpeak amplitude and fractional position (n =425) showed the antibody bound with eGFP at the ends of SUP carriers resulting in a boost in subpeak amplitude. Threshold: subpeak amplitude > 50 pA; dwell time > 1 ms was selected to distinguish antibody-eGFP-K72 complexes from unbound states. (e) Binding assays of 1 nM eGFP-K72 in the presence of anti-GEP antibody ranging from 1 pM to 50 nM. The binding curve was fitted using the Hill-Langmuir equation and the dissociation constant (K_{d}) was determined to be ~ 7.85 nM under this condition. Error bars represent one standard deviation of at least three independent experimental repeats. .....[236]

Figure 6.1 Integration of a tunnelling detector into a nanopore sensor for protein analysis. (a) Schematic of a gold tunnelling detector embedded in a quad-barrel nanopipette. (b) Fabrication of the integrated device. i. Quad-barrel nanopipettes are fabricated using the laser-assisted pulling technique. ii. Two channels of the pipettes are filled with carbon to serve as conductive nanoelectrodes. iii. Tunnelling gold electrodes with a gap less than 2 nm are formed by a feedback-controlled electrodeposition. iv. Simultaneous reading of tunnelling currents and ionic currents by the integrated detector. (c) Expected current traces of tunnelling currents (T channel) and ionic currents (two N channels). .....[246]

Figure 6.2 Feedback controlled electrodeposition. (a) Carbon etching. Excess carbon outside the pipette was removed by a cyclic voltammetry (CV) process (0 – 2 V, 2 cycles). (b) Gold was first pre-deposited on the carbon surface using a bipotentiostatic method. (WE 1: -0.73 V, WE 2: -0.75 V, time: 50 s). (c) Feedback-controlled galvanostatic deposition was used for fabrication of gold nanogap (I_{set} = 1 nA). The jump of V-t curve suggests the formation of a tunnelling junction. .....[248]

Figure 6.3 Feedback controlled electromigration. (a) Flowchart of the algorithm governing the feedback-controlled electromigration process. (b) Electrical setup for electromigration of gold nanocontacts. (c) I-V curve for feedback controlled electromigration. .....[249]

Figure 6.4 Characterisation of tunnelling detector integrated quad-barrel nanopipettes. SEM images of quad-barrel nanopipettes before (a) and after being integrated with a tunnelling

detector (b). Flowchart of the algorithm governing the feedback-controlled electromigration process. (c) Typical I-V curves of fabricated tunnelling detectors. .....[251]

Figure 6.5 Measurements of single amino acids using a tunnelling detector. (a) Recognition tunnelling detector where the electrodes are functionalised with recognition molecules. (b) Single amino acid detection using a sub-nm nanogap. Panel (a) adapted from reference and panel (b) adapted from reference. .....[252]

List of Tables

Table 2.1 Parameters for the pulling protocol of nanopipette fabrication. ..... [92]

Table 2.2 Buffer solutions used in this thesis. .....[101]

Table 3.1 Solution conductivity for buffers with different concentrations of urea used in actin unfolding assays. .....[131]

Table 4.1 Sequences of the aptamer probes used in this chapter. .....[161]

Table 5.1 Information on SUP samples used in this work. .....[201]

Abbreviation

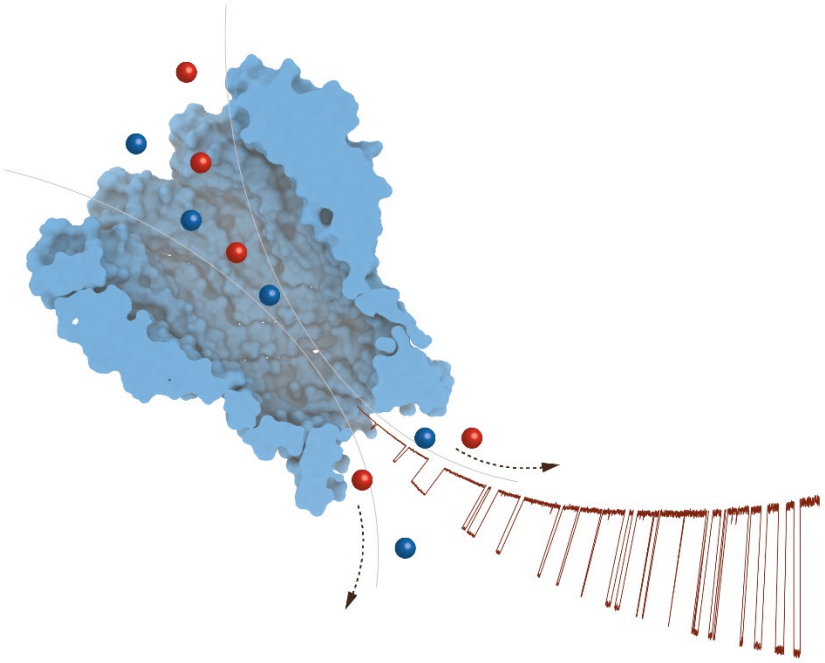
AA	Amino acid
AFM	Atomic force microscopy
ATP	Adenosine triphosphate
BU-MS	Bottom-up mass spectrometry
CBD	Controlled breakdown
CE	Capillary electrophoresis
Cherry	Red fluorescent protein
ClyA	Cytolysin A
c-Me treceptor	Hepatocyte growth factor receptor
cryo-EM	Cryo-electron microscopy
CSF	Cerebrospinal fluid
CUSUM	Cumulative sums
DEP	Dielectrophoretic
DI water	Deionised water
DNA	Deoxyribonucleic acid
dsDNA	Double-stranded DNA
eGFP	Enhanced green fluorescent protein
ELISA	Enzyme-linked immunosorbent assay
EO	Electroosmotic
EOF	Electroosmotic flow
EP	Electrophoretic
ESI-TOF MS	Electrospray ionisation time-of-flight mass spectrometry
F-actin	Filamentous actin
FET	Field-effect transistor
FraC	Fragaceatoxin C
FRET	Fluorescence resonance energy transfer
FWHM	Full-width at half maximum

G-actin	Globular actin
HGF	Hepatocyte growth factor
I.D.	Inner diameter
ICR	Ionic current rectification
IHL	Inner Helmholtz layer
K	Lysine
K_d	Dissociation constant
LC-MS	Liquid chromatography–mass spectrometry
LOD	Limit of detection
MALDI	Matrix-assisted laser desorption/ionization
MALDI-TOF MS	Matrix-assisted laser desorption/ionisation time-of-flight mass spectrometry
MB	Molecular beacon
mIFP	Monomeric near-infrared fluorescent protein
MS	Mass spectrometry
MspA	Mycobacterium smegmatis porin A
nexFET	Nanopore extended field-effect transistor
NTA	Nitrilotriacetic acid
O.D.	Outer diameter
OHL	Outer Helmholtz layer
OmpG	Outer membrane protein G
PCR	Polymerase chain reaction
PDGF	Platelet-derived growth factor
PEG	Polyethylene glycol
pI	Isoelectric point
PlyAB	Pleurotolysin AB
pM	Picomolar
POI	Proteins of interest
PPI	Protein-protein interaction
PSD	Power spectral density
pyrene	N-(1-pyrene)iodoacetamide

RDL	Recursive directional ligation
RNA	Ribonucleic acid
RTK	Receptor tyrosine kinase
SDS-PAGE	Sodium dodecyl sulphate polyacrylamide gel electrophoresis
SECM	Scanning electrochemical microscopy
SEM	Scanning electron microscope
SERS	Surface-enhanced Raman spectroscopy
SfCherry	Superfolder Cherry
SfGFP	Superfolder GFP
SICM	Scanning ion conductance microscopy
SICS	Scanning ion conductance spectroscopy
SiNx	Silicon nitride
Sn	Antifreeze protein
SNR	Signal-to-noise ratio
SPR	Surface Plasmon Resonance
ssDNA	Single-stranded DNA
STD	Standard deviation
STM	Scanning tunnelling microscopy
SUP	Supercharged unstructured polypeptide
TEM	Transmission electron microscopy
VEGF	Vascular endothelial growth factor
α-HL	Alpha-hemolysin
α-thrombin	Alpha thrombin
λ-DNA	Lambda phage DNA

CHAPTER 1

Introduction



Synopsis

In the introductory chapter of this thesis, I delve into the emerging field of single molecule sensing within the framework of nanopores. This chapter lays the foundational understanding by discussing the origins and underlying principles of nanopore sensors, along with a review of the most recent pertinent literature. The exploration extends to the applications of solid-state nanopores in the context of protein sensing and proteomics analysis, as well as an acknowledgment of the limitations associated with this technology. The aims and objectives of my entire PhD work are illuminated with an outline within this chapter.

1.1 Single-molecule science

The rapid advancements in measurement sciences have propelled our understanding of the biological world to unprecedented levels. Over the past century, pioneering measurement techniques have been harnessed to delve into the intricacies of biomolecules. Some of these methods, such as the polymerase chain reaction (PCR) [1] and the enzyme-linked immunosorbent assay (ELISA), [2] continue to be foundational in contemporary scientific research. However, the insatiable quest to probe ever-smaller biological systems persists. The trajectory of analytical techniques has followed a path of continuous reduction in sample size and improvement in resolution. Historically, these methods have converged towards examining single cells and molecules (**Figure 1.1a**). [3] While conventional measurement techniques are invaluable for studying the collective properties of biomolecules, they harbour limitations. These include their inability to furnish detailed insights into individual molecules, constraints posed by low analyte concentrations, the intricacy of sample preparations, and the time-consuming nature of procedures. The pursuit of a deeper comprehension of molecular behaviour and properties necessitates a shift from characterising molecules in large ensembles to scrutinising them at the level of individual entities. Enter the field of single-molecule science, a transformative approach that empowers scientists to explore the morphology, properties, and dynamics of single molecules. This approach stands in stark contrast to traditional methods, which yield averaged results from entire molecular populations.

As illustrated in **Figure 1.1b**, conventional sensing techniques only capture the ensemble properties of a sample, producing a single averaged signal devoid of information about individual molecules. Conversely, single-molecule sensors possess the remarkable capability to resolve individual molecules, generating multiple signals that unveil variations among these molecules. Over the past two decades, research in single-molecule methods has experienced a remarkable surge, garnering widespread recognition and finding practical applications. Fluorescence, a well-established technology with decades of research, has been adapted for single-molecule investigations. These adaptations encompass techniques based on dye localisation, [4] quenching effect, [5] fluorescence anisotropy, [6] and fluorescence resonance energy transfer (FRET). [7] Atomic force microscopy (AFM) represents another potent tool for

scrutinising single molecules, providing the means to visualise them in three dimensions. [8] Optical and magnetic tweezers have also made substantial contributions to the field of single-molecule science. [9] However, these techniques are not without their limitations. For instance, single-molecule fluorescence detection often mandates chemical modifications of target analytes with dyes, potentially altering the molecular structure. AFM necessitates the immobilisation of analytes on a flat surface and offers static rather than real-time information about the analytes. Optical and magnetic tweezers require customised engineering of the beam for specific analytes, demanding meticulous optimisation.

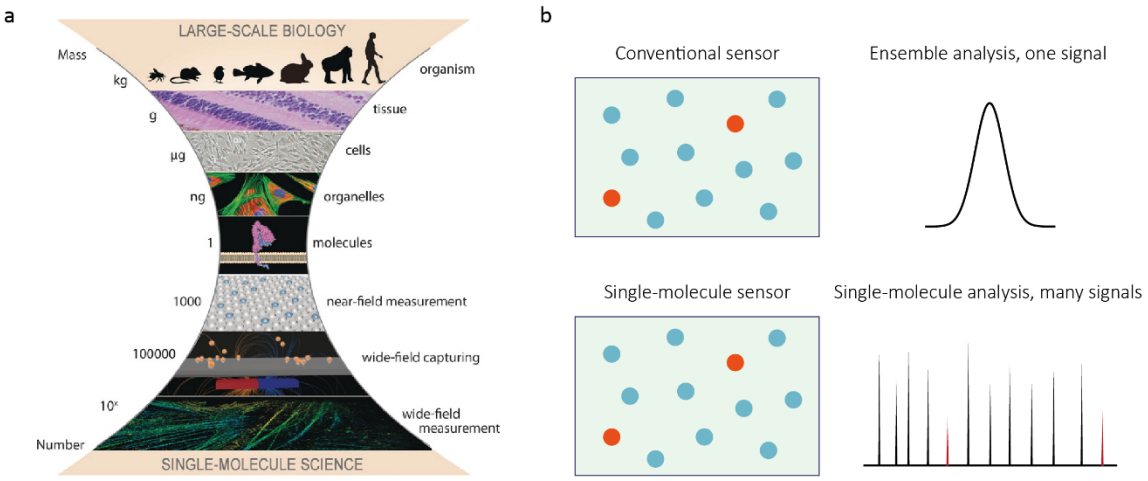


Figure 1.1 The development of measurement techniques from large-scale entities to single molecules. (a) The evolution of measurement techniques has traversed a remarkable trajectory, progressing from studying entire organisms down to individual cells and even single molecules. As our scientific capabilities have surged, the focus has shifted towards detecting ever-smaller entities, leading to a radical reduction in sample sizes. This shift has brought us to an exciting juncture where single-molecule measurements are transitioning into the quantitative science. (b) Conventional sensors analyse an ensemble sample, providing an averaged signal that represents the combined behaviour of all the molecules in the sample. In contrast, single-molecule sensors have the remarkable capability to measure and analyse individual molecules one by one. This provides insights into the intrinsic heterogeneity present in the sample. Every molecule is treated as a unique entity, enabling the detection of variations, interactions, and behaviours that would otherwise be masked in ensemble measurements. Panel (a) adapted from reference, [3] Wiley.

In contrast, nanopores, minuscule apertures with internal diameters at the nanometre scale, represent a relatively recent addition to the arsenal of single-molecule techniques. [10] The principle underpinning nanopore-based single-molecule sensing is elegantly simple: when subjected to an electric field, individual analyte molecules are driven through the nanopore, leading to detectable changes in current. This approach enables the real-time analysis of unlabelled molecules without the need for immobilising them on a surface. Consequently, nanopore technology has garnered significant attention for its versatility among different single-molecule techniques. Moreover, nanopore technology has demonstrated immense potential for DNA sequencing, offering higher speeds and lower costs compared to conventional methods such as capillary electrophoresis (CE). [11] A notable example is the biological nanopore-based DNA sequencing device developed and commercialised by Oxford Nanopore Technologies. [12]

1.2 Nanopore technology

The concept of using nanopores as single-molecule sensors emerged approximately three decades ago, drawing inspiration from the operating principle of the Coulter Counter introduced in the 1950s. [13] The Coulter Counter, initially designed for detecting blood cells and pathogens as they traversed a micrometre-scale channel between electrolyte-filled chambers, employed pressure or transmembrane potential bias to propel particles or cells through the pore. This passage induced alterations in the ionic conductance within the channel, giving rise to the 'resistive pulse sensing' mode. This technique enabled particle counting or volume characterisation based on the resistance changes in the pulses. [14] Building upon this foundation, Neher and Sakmann proposed the method of single-channel current recordings using the patch-clamp technique in the 1970s, a groundbreaking advance that earned them the Nobel Prize in Physiology or Medicine in 1991. [15]

A seminal milestone in this journey was the demonstration by Bezrukov et al. in 1994 of using resistive pulse sensing to detect a single molecule, specifically a polyethylene glycol (PEG)

polymer, via an alamethicin nanopore embedded in a lipid bilayer. [16] Shortly thereafter, in 1996, Kasianowicz et al. showcased the detection of single biomolecules, specifically polynucleotides, using an alpha-hemolysin (α-HL) nanopore. [17] This pioneering study not only introduced single-molecule signals of nucleic acids (DNA or RNA) but also established a correlation between the molecular length of biopolymers and the duration of resistive pulses. These groundbreaking endeavours laid the foundation for harnessing nanopores as label-free single-molecule methods and played a crucial role in the development of nanopore-based nucleic acid sequencing, considered a pinnacle achievement in the field. Over the past three decades, the field has evolved with the concurrent development of two main types of nanopores: biological and solid-state nanopores. These nanopores have been applied to a diverse array of target analytes, with a predominant focus on nucleic acids and proteins. [18, 19]

1.2.1 Biological nanopores

Biological nanopores, derived from natural protein channels responsible for regulating ion transport across cell membranes, represent a fundamental cornerstone in many nanopore applications. Their intrinsic properties make them well-suited for nanopore sensing due to their small size, alignment with crucial biomolecules, and precise atomic-level structural reproducibility. [20] Moreover, various techniques, such as site-directed mutagenesis or adaptor decoration, can be employed to customise protein nanopores for the detection of specific molecules. [21]

While the alamethicin protein nanopore marked the inception of single-molecule detection, [16] the α-hemolysin (α-HL) nanopore, initially introduced by Kasianowicz et al., [17] has emerged as the most extensively used protein-based nanopore over the past two decades. α-HL, resembling a mushroom structure, is produced by the bacterium Staphylococcus aureus. [22] It self-assembles from seven monomer units (32 kDa) within lipid bilayers, as depicted in **Figure 1.2a.** Consisting of two chambers, one with a 2.6 nm aperture facing the cis side and another with a 2 nm aperture facing the trans side, the α-HL structure harbours a 1.4 nm narrowest constriction and a 4.6 nm widest portion. Its overall length is approximately 10 nm, as shown

in Figure 1.2a. [20, 22, 23] This remarkably slender constriction (1.4 nm) makes α-HL an exceptionally effective tool for single-molecule sensing, particularly for single-stranded DNA (ssDNA), [24] RNA, [17] ions, [25] proteins, [26] as well as for distinguishing between DNA and RNA. [27]

Another frequently employed biological nanopore in the field of single-molecule sensing is mycobacterium smegmatis porin A (MspA), as depicted in Figure 1.2b. [28] MspA assumes a funnel-shaped octameric configuration, featuring a constriction with a diameter of 1.2 nm and a length of 1.0 nm. [29] This reduced constriction size makes it exceptionally well-suited for distinguishing between various nucleotide types along single-stranded DNA, a critical attribute for DNA sequencing. [30] Substantial progresses have been made in the identification of epigenetic and post-translational modifications using MspA. [31, 32] Aerolysin, another emerging nanopore sensor, is a β-barrel pore forming toxin implicated in pathogenic infections by Aeromonas. [33] Aerolysin heptamers exhibit a mushroom-like structure with a β-barrel stem inserted in the lipid membrane, as shown in Figure 1.2c. Unlike α-HL with a vestibule, aerolysin has an extracellular cap with a collar structure measuring 16 nm in size. The internal pore diameter is 1.8 nm. Aerolysin nanopores have been demonstrated resistance to harsh experimental conditions, including denaturing agent, [34] varying pH levels[35] and high temperatures, [36] making them robust and highly suitable for biosensing applications.

Several other protein nanopores, such as outer membrane protein G (OmpG), [37] fragaceatoxin C (FraC), [38] Cytolysin A (ClyA) [39] and pleurotolysin AB (PlyAB), [40] have also been extracted from nature and adopted as single-molecule sensing tools for a vast array of biomolecules. However, it is essential to acknowledge that the utilisation of biological nanopores for sensing purposes comes with certain limitations. For instance, the lipid bilayer that underlies protein-based nanopores is susceptible to external factors such as temperature, pH, and ionic strength, significantly constraining their practical use in various experimental settings. [41] Additionally, the size of these biological nanopores, typically less than 2 nm, is relatively small and unchangeable, posing challenges in detecting whole proteins with a wide range of molecular sizes.

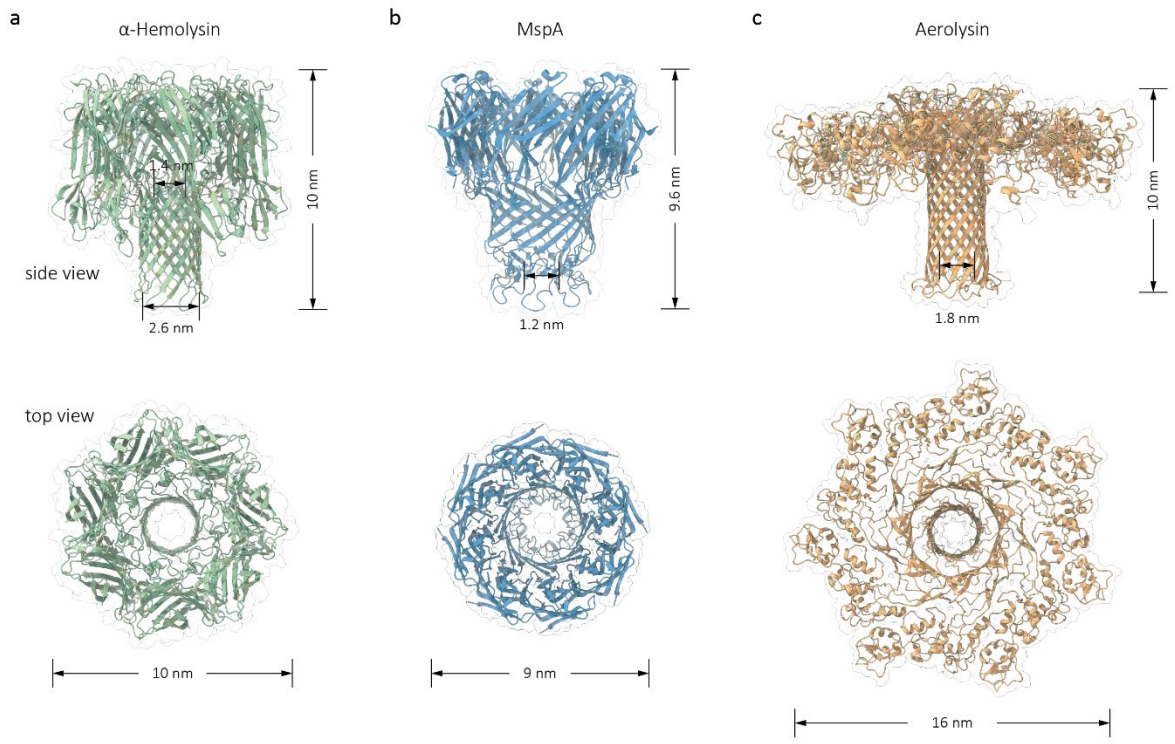


Figure 1.2 Biological nanopores. Side view and top view of (a) α-Hemolysin (PDB: 7AHL), (b) MspA (PDB: 1UUN) and (c) Aerolysin (PDB: 5JZT).

1.2.2 Solid-state nanopores

To address the challenges posed by biological nanopores, solid-state nanopores constructed from synthetic membrane materials have emerged as a viable alternative. [42] These solid-state nanopores offers several distinct advantages: 1) Advances in nano/micro fabrication techniques enable the precise adjustment of pore sizes and geometries to match the dimensions of analyte molecules. This flexibility significantly expands their potential applications. 2) Solid-state nanopores exhibit remarkable resilience against extreme external environmental conditions. This durability ensures their reliability in various operational settings. 3) Synthetic nanopores can be easily tailored through various covalent or non-covalent methods, allowing for customisation to specific experimental requirements. 4) The creation of nanopores in solid-state membranes opens up the possibility of constructing arrays of pores in parallel. This capability facilitates high-throughput detection of multiple targets simultaneously.

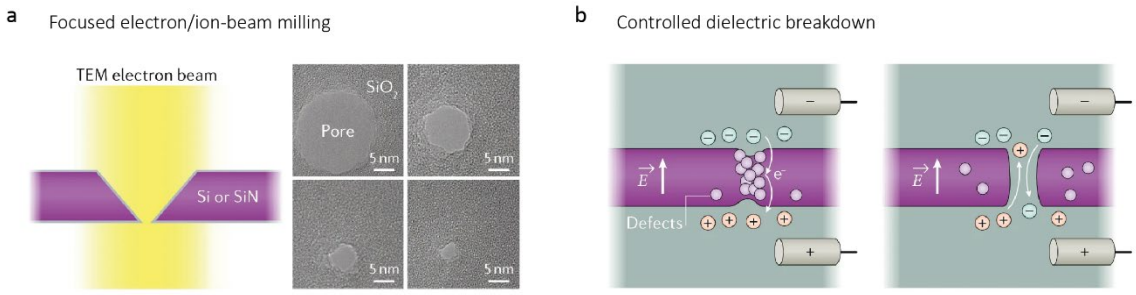


Figure 1.3 Fabrication of solid-state nanopores. (a) Fabrication of sub-10 nm nanopores on a membrane using focused electron or ion-beam milling, in which the pore size and shape and be monitored by TEM during the fabrication process. TEM images showing SiO_2 nanopore formation using an electron beam. (b) Pore formation using controlled dielectric breakdown. The membrane material, such as SiN, HfO_2 and SiO_2, is immersed in an electrolyte (such as KCl, NaCl or LiCl) and exposed to an electric field with intensity comparable to the dielectric strength of the membrane. This leads to the generation of structural via tunnelling leakage current, resulting in the dielectric breakdown of the membrane and in the formation of a nanopore. Panel (a) adapted from reference, [43] Springer Nature Limited. Panel (b) adapted from reference, [44] Springer Nature Limited.

Solid-state nanopores are commonly crafted by creating a nanoscale aperture in a self-supporting membrane, such as low-stress silicon nitride (SiN_x). SiN_x stands out as an excellent substrate for nanopores due to its robustness, exceptional insulation properties (1016 Ω cm^{-1}), [45] mechanical durability (10 MV/cm^{-1}), [45] and chemical stability. Alternative membrane materials include SiO_2, [43] SiC, [46] Al_2O_3, [47] as well as two-dimensional materials such as graphene[48] and MoS_2. [49] **Figure 1.3** provides a simplified overview of the process for fashioning nanopores in a solid-state membrane, employing established techniques to tailor pore sizes for specific applications. [42, 44, 50, 51, 52, 53]

For example, as shown in **Figure 1.3a**, Storm et al. introduced a fabrication technique that combines transmission electron microscopy (TEM) and silicon technology to create SiO_2 nanopores with precision at the single-nanometre level, offering direct visual feedback. [43] The process involves initially opening a 20 nm pore in a silicon membrane using electron-beam

lithography and anisotropic etching. After thermal oxidation, exposure to a high-energy electron beam reduces the pore to a single-nanometre size by fluidising the silicon oxide, causing the small pore to shrink due to surface tension. More importantly, beyond pore size, the thickness of the pore membrane significantly contributes to enhancing spatial resolution and achieving a higher signal-to-noise ratio (SNR). [54] In pursuit of this goal, certain research groups have employed two-dimensional materials such as graphene, [48, 55, 56] MoS_2, [49] and WS_2[57] as membrane materials for nanopore fabrication, resulting in exceptional SNRs and spatial resolution, particularly advantageous for distinguishing small biomolecules. [49]

However, the beam-based nanopore fabrication technique has encountered limitations due to its high cost, low yield, and unstable reproducibility. In contrast, a low-cost and scalable method pioneered by the Tabard-Cossa group, known as controlled breakdown (CBD), has rapidly gained popularity for solid-state nanopore fabrication. [44, 58] When an electric field with an intensity comparable to, but smaller than, the dielectric strength of the membrane material is applied across the membrane, it induces a tunnelling leakage current through the insulating membrane, causing defects to form. These defects serve as additional charge carriers, reinforcing the leakage current. Once a connected path of these defects spans the membrane, breakdown occurs, leading to the rapid removal of membrane material and the creation of a nanopore. These pores can be made as small as 1 nm in diameter, with an accuracy of 0.5 nm and angstrom-level precision. [59] The fabrication time depends strongly on the electrical field strength and the composition of the electrolyte used in the process. [60]

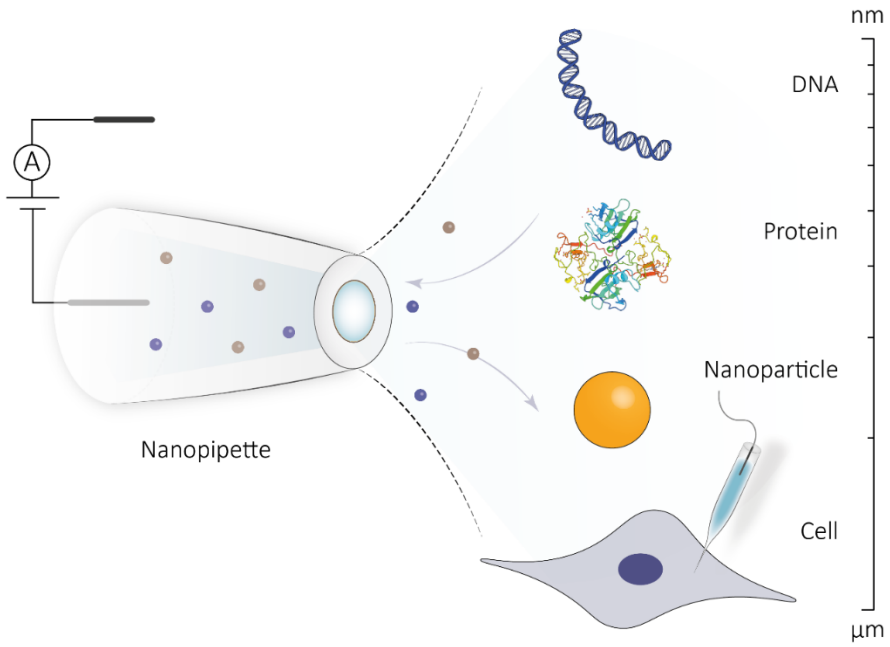


Figure 1.4 Nanopipette sensors. Nanopipettes offer a promising confined space that enables advances in electrochemical, optical, mass spectrometric measurements from microscale to nanoscale. The pipettes can be used for non-invasive detection within single cells. Also, they can also be used to sense single particles or single biomolecules such as protein or DNA to reveal the hidden population properties and dynamics.

While solid-state nanopores embedded in membranes currently dominate the field due to their precise control, cost remains a significant challenge. Moreover, the processes involved in membrane fabrication, chemical etching, and ion beam drilling are time-consuming and technically demanding. An emerging type of solid-state nanopore, known as nanopipettes, created by pulling quartz or borosilicate capillaries, has recently gained considerable attention. [61] These nanopipettes can be swiftly and inexpensively fabricated in a matter of seconds, eliminating the need for expensive equipment and cleanroom facilities. [62] Nanopipettes, as a subset of solid-state nanopores, offer several advantages, including low noise levels and robust mechanical stability, making them highly suitable for single-molecule detection (**Figure 1.4**). [63, 64, 65] With advancements in microfabrication, it is now possible to fabricate multi-channel nanopipettes using a top-down approach, expanding their utility in biosensing and beyond. Their needle-like geometry and mechanical resilience provide a unique capability for single-

molecule manipulation. [66, 67] This includes tasks such as the delivery or extraction of molecules from individual cells and the scanning of surface properties of cells or tissues. [68, 69] These applications are exemplified by techniques such as scanning electrochemical microscopy (SECM) [70] and scanning ion conductance microscopy (SICM). [71, 72, 73]

1.3 Working principle of nanopore sensing

1.3.1 Ionic current detection

Nanopores function as single-molecule sensors by detecting changes in the ionic current as molecules translocate through them. This sensing mechanism, referred to as resistive pulse sensing, is widely employed in the nanopore field due to its label-free manner for single-molecule detection. Figure 1.5a provides an illustration of the typical setup of nanopore experiments. where a nanopore is immersed in an electrolyte solution (e.g., KCl) on both sides. When a transmembrane potential bias is applied using a pair of electrodes (typically Ag/AgCl), a steady ionic current called the "open-pore current" is recorded (Figure 1.5b). [74]

Nanopores typically exhibit resistance in the mega-ohm or giga-ohm range, with the potential drop primarily occurring across the nanopore, having a negligible impact from the bulk solution. The conductance of a nanopore can be approximated using Equation 1.1, assuming a cylindrical pore shape and relatively high salt concentration (greater than 100 mM). [75] In this equation, the overall conductance consists of contributions from the bulk electrolyte, which depends on the pore geometry as shown in the first term, and from the surface charge of the nanopore, taking into account the counter ions that shield the nanopore as shown in the second term.

$$G_o = (\mu_{K^+} + \mu_{Cl^-}) c_{KCl} F \frac{\pi d^2}{4L} + \frac{\pi d}{L} \sigma \mu_{K^+} \quad (1.1)$$

Where:

μ_{K^+} and μ_{Cl^-} are the electrophoretic mobility of cations and anions.

c_{KCl} represents the electrolyte concentration inside the nanopore.

d and L are the diameter and length of the nanopore.

σ represents the surface charge density of the nanopore.

F is the Faraday constant.

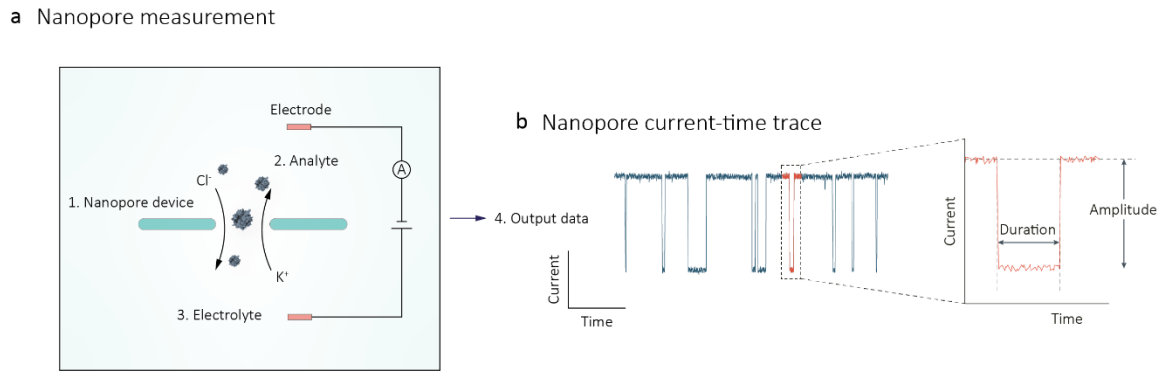


Figure 1.5 Working principle of nanopore sensing. (a) Two reservoirs filled with an electrolyte such as KCl, NaCl or LiCl are separated by a non-conductive membrane and connected via a single nanopore. Two electrodes, typically Ag/AgCl electrodes, are immersed in the two reservoirs and a constant bias is applied across the pore, resulting in a steady ionic current through the pore. Under the application of voltage, analytes such as DNA or proteins are captured by the local electric field and translocate through the nanopore. (b) Current-time trace showing the current blockade events of single-molecule translocation. By analysing the features of individual events such as the duration, amplitude, and noise level, the properties of the analytes such as size, shape and charge can be revealed.

When a molecule, such as DNA, is driven through the nanopore, it causes a transient change in the steady-state current, which can manifest as either a blockade or an enhancement. This change stems from the displacement of electrolyte within the nanopore caused by the charged molecule, as illustrated in **Figure 1.4b**. Notably, if the size of the molecule, indicated by its gyration radius, exceeds the pore size, a free energy barrier arises during translocation, hindering the motion of the molecule. [76] Nonetheless, this entropic barrier can be overcome

by applying a sufficiently high transmembrane potential. By analysing the resistive current blockade resulting from single-molecule translocation, various characteristics of the translocating molecule can be deduced. In **Figure 1.4b**, for instance, the dwell time, which corresponds to the duration of the current blockade, indicates how long the molecule resides within the nanopore. This temporal parameter is directly related to the dimension and electrical properties of the molecule as well as its interaction with the pore. In addition, the peak amplitude typically reflects the size, shape and secondary structure of the translocating molecule. The time intervals between events provide information about the rate at which individual molecules are captured, which can be correlated with analyte concentration or used in the study of molecular electrokinetics under electrophoretic or electroosmotic forces. [77] Moreover, the integrated area under the peaks yields insights into the equivalent charge of the molecules. [66]

It is crucial to recognise that during the translocation of a charged molecule through a nanopore, the expected current blockade does not always occur. Instead, an enhanced pulse may be observed. This distinctive ionic current pulse, indicative of molecule translocation, arises from the intricate interplay between the ionic strength of the electrolyte and the surface charge densities of the analyte molecule. [78] This phenomenon can be attributed to two opposing effects. On one hand, when a molecule occupies the pore, it can exclude electrolyte ions, leading to a reduction in conductance (G_{block}). Conversely, the counter ions present on the charged molecule's surface act as charge carriers, resulting in an overall increase in conductance (G_{charge}). Considering both these factors, the total change in nanopore conductance can be represented by **Equation 1.2**. Consequently, at low electrolyte concentrations, the charge density of a molecule might surpass that of the excluded charge carriers, resulting in an observable increase in the measured ionic current. Conversely, a decrease in current is measured when the effective charge density of the molecule is lower than that of the excluded electrolyte ions. Changes in nanopore conductance due to varying ionic strengths can be mathematically expressed using **Equation 1.3**, [75] where the first term encapsulates the excluded electrolyte volume, and the second term accounts for the surface charge density of analyte molecules.

$$\Delta G = -G_{\text{block}} + G_{\text{charge}} \quad (1.2)$$

$$\Delta G = -(\mu_{K^+} + \mu_{Cl^-})c_{KCl}F\frac{\pi d_{\text{analyte}}^2}{4L_{\text{pore}}} + \frac{\lambda_q}{L_{\text{pore}}}\mu_{K^+(Cl^-)} \quad (1.3)$$

Where:

μ_{K^+} and μ_{Cl^-} are the electrophoretic mobility of cations and anions.

c_{KCl} represents the electrolyte concentration inside the nanopore.

d_{analyte} is the diameter of the molecule, and L_{pore} is the length of the nanopore.

λ_q represents the effective charge per unit length of the counter ions screening the nanopore wall.

F is the Faraday constant.

1.3.2 The effect of surface charge

The primary driving force behind the motion of analytes through nanopores is the non-contact flows generated by the electric field. However, local electrostatic interactions around the pore also play a significant role, particularly when analytes approach the charged surface of the nanopore. [79] This phenomenon is particularly pronounced due to the charged properties of amino acids in protein pores and the insulated materials in solid-state pores when immersed in a polar solvent, typically water. In the case of solid-state nanopores, the inner wall's surface carries charges, a result of various factors such as the protonation of surface groups or the ionisation of functional groups on the surface. Consequently, the free ions present in the electrolyte, carrying charges opposite to those on the solid-state surface, become electrostatically attracted to and absorbed onto the charged surface. This interplay between charged solid surfaces and the surrounding electrolyte ions gives rise to the formation of an electrical double-layer system.

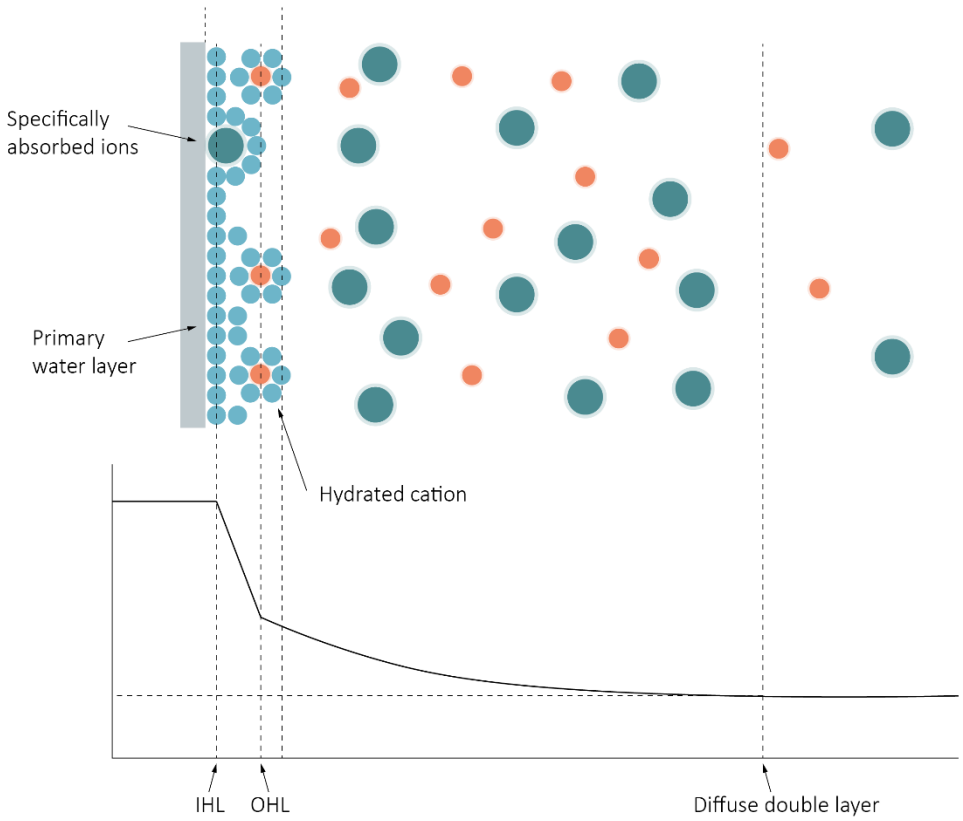


Figure 1.6 Schematic of the electrical double layer in aqueous solution at the interface with a charged surface. Ion distribution as well as local potential distribution is characterised by Gouy-Chapman-Stern model. The decay length is estimated to be the Debye length, λ_D.

At the interfaces between the surface and the electrolyte, an electrical double layer forms, and its behaviour can be elucidated using the Gouy-Chapman-Stern model. [74] This model amalgamates insights from two earlier models: the Helmholtz model, developed in 1853, [80] which explained the separation of charges at the surface/solution interface, and the Gouy-Chapman model introduced in 1913, [81] which introduced the concept of a diffuse layer in this system. The Gouy-Chapman-Stern model synthesises these concepts, merging the compact layer and the diffuse layer, as depicted in **Figure 1.6**. The innermost layer, often referred to as the inner Helmholtz layer (IHL) or Stern layer, consists of immobilised solvent molecules and ions that are specifically absorbed onto the solid-state surfaces. The outer layer, or the outer Helmholtz layer (OHL) or diffuse layer, comprises solvated ions that are mobile due to their non-specific adsorption and the long-range electrostatic interactions between ions and the

charged surface. Due to thermal motion in the electrolyte, these solvated ions tend to disperse into the region of the diffuse double-layer, the extent of which is roughly equivalent to the Debye length (λ_D). This Debye length can be calculated using **Equation 1.4**: [82, 83]

$$\lambda_D = \sqrt{\frac{\varepsilon_0 \varepsilon_r k_B T}{2en^2}} \quad (1.4)$$

Where:

ε_0 is the permittivity of free space and ε_r is the relative dielectric constant.

e is the electronic charge.

T is the temperature in Kelvin.

n is the electrolyte concentration.

k_B is the Boltzmann constant.

While the Gouy-Chapman-Stern model is valuable for illustrating ion and charge distributions at surface/solution interfaces, it has certain limitations. This model is particularly effective in low ionic strength environments but encounters constraints due to its simplified assumptions. Notably, these assumptions involve point ions, uniformly charged surfaces, and a continuous solvent. [84] In the case of solid-state nanopores such as conventional Si_3N_4 nanopores or quartz nanopipettes, when submerged in polar solutions such as KCl, NaCl, or LiCl, the predominant surface charges are negative. [85] This negative surface charge primarily results from the dissociation of terminal silanol groups present on silica and silicate surfaces. [86] The zeta potential of the inner pore surface can be assessed through streaming potential measurements. In this process, the nanopore is installed into a pressure chip which a differential static pressure can be applied. The streaming potential is determined by tuning the potential across the pore until the ionic current generated by the pressure driven flow vanishes. Furthermore, the electrostatic interactions between cations and the negatively charged inner walls of the nanopore play a significant role in shaping the electrical double layer. This dynamic diffuse layer is responsible for generating electroosmotic flow (EOF), a critical factor that either influences or opposes processes in molecular translocation, as I will elaborate on later in this chapter.

1.3.3 Ionic current rectification

Ionic current rectification (ICR) is a phenomenon often observed in nanoscale channels, characterised by a non-linear relationship between the ionic current (I) and the applied voltage (V), as illustrated in Figure 1.7. Numerous efforts have been dedicated to explaining ICR, and the prevailing explanation suggests that ions are differentially transported through an asymmetrically shaped nanochannel when the thickness of the diffused layer is comparable to the diameter of the pore opening. For instance, when a positive potential is applied within the nanopipette, certain cations become trapped on the negatively charged surface due to electrostatic absorption. Conversely, when a negative potential is applied, these cations can pass through without hindrance. This behaviour is described by the Ratchet model, [87, 88] resulting in the non-linear relationship between current and voltage, as observed in the I-V characteristics.

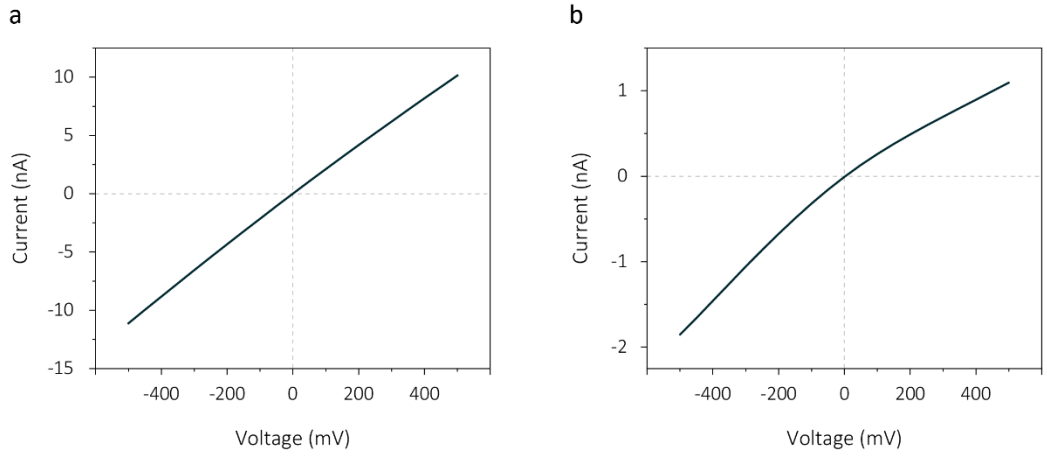


Figure 1.7 Ionic current rectification in nanopores. I-V curves of a nanopipette with a diameter of 15 nm at (a) 1 M KCl, 10 mM Tris-EDTA, pH 8.0 buffer, and (b) 0.1 M KCl, 10 mM Tris-EDTA, pH 8.0 buffer.

While the exact mechanism behind ICR remains uncertain, several factors have been identified to influence the degree of rectification. These factors include nanopore size, geometry, and surface charge, as well as pH and concentration of the electrolyte. ICR is observed only when the thickness of the electrical double layer matches the nanopore dimensions, making nanopore diameter the most influential parameter. Furthermore, the extent of ICR is strongly linked to the ionic strength due to the inverse relationship between the Debye length (representing the thickness of the diffused layer) and the concentration of ions. As a result, pronounced ICR is evident at low ionic strengths, while high-concentration ionic strengths show minimal to no ICR effect. [89] For example, in **Figure 1.7a**, a roughly 15 nm nanopore exhibits linear current-voltage (I-V) characteristics in a solution containing 1 M KCl, whereas **Figure 1.7b** illustrates negatively rectified current as the pore is measured in 100 mM KCl. An additional means of altering ICR, potentially even achieving full reversal, involves functionalising the nanopore surface. [90]

1.3.4 Electrophoretic and electroosmotic flow

During translocation experiments, various forces come into play, with the most prominent ones being electrophoresis, electroosmosis, and diffusion. [91] These forces work together to guide analytes through the nanopore. Charged analytes are inherently driven by the electrophoretic (EP) force toward the electrode with an opposing polarity. The strength of the EP force is intricately linked to the molecular charge, and the velocity ν_{EP} can be quantified through the Helmholtz-Smoluchowski **Equation 1.5**: [91]

$$\nu_{\mathrm{EP}} = \frac{\varepsilon_0 \varepsilon_{\mathrm{r}}}{\eta} \xi_{\mathrm{molecule}} E \quad (1.5)$$

Where:

ε_0 is the permittivity of free space and ε_{r} is the relative dielectric constant.

η is the viscosity of the electrolyte.

ξ_{molecule} is the zeta potential of the target molecule.

E represents the external electrical field.

However, as molecules approach the charged surface of the nanopore, the behaviour of the double electrical layer begins to impede the motion of analytes due to electroosmotic (EO) flow. This phenomenon emerges when the diffuse layer aligns with the electric field direction. [92, 93] The electroosmotic velocity v_{EO} can be mathematically captured by **Equation 1.6**: [94]

$$v_{\mathrm{EO}} = -\frac{\varepsilon_0 \varepsilon_{\mathrm{r}}}{\eta} \xi_{\mathrm{nanopore}} E \quad (1.6)$$

Here, ξ_{nanopore} represents the zeta potential of the nanopore inner wall.

Electroosmosis is a significant force capable of either enhancing, opposing, or even reversing the effects of electrophoresis, particularly in cases where the target molecule carries a moderate charge, as often seen with proteins. [95] By combining **Equation 1.5** and **Equation 1.6**, one can calculate the effective velocity of molecule transportation influenced by these two forces: [91]

$$v = v_{\mathrm{EP}} + v_{\mathrm{EO}} = \frac{\varepsilon_0 \varepsilon_{\mathrm{r}}}{\eta} (\xi_{\mathrm{molecule}} - \xi_{\mathrm{nanopore}}) E \quad (1.7)$$

Figure 1.8 provides an illustrative case of avidin translocating through a Si_3N_4 nanopore, with its surface charge modulated by varying pH levels. [91] At pH 2, despite being somewhat counteracted by electroosmosis, the electrophoretic flow still prevailed. At pH 4, where the ξ_{molecule} approximately equalled ξ_{nanopore}, electroosmosis balanced out the electrophoretic flow, making diffusion the primary driver of protein translocation in this context. pH 6 and 8 displayed heightened throughput due to electrophoresis accentuated by electroosmosis. At pH 10, the alkaline conditions led to amino group deprotonation on the protein, inverting the surface charge of avidin. This prompted electroosmosis to dominate and propelled the weakly charged protein through the nanopore. This pH-dependent behaviour demonstrates how changes in surface charge can significantly influence the translocation of molecules through a nanopore, with electrophoresis and electroosmosis playing crucial roles in different pH conditions.

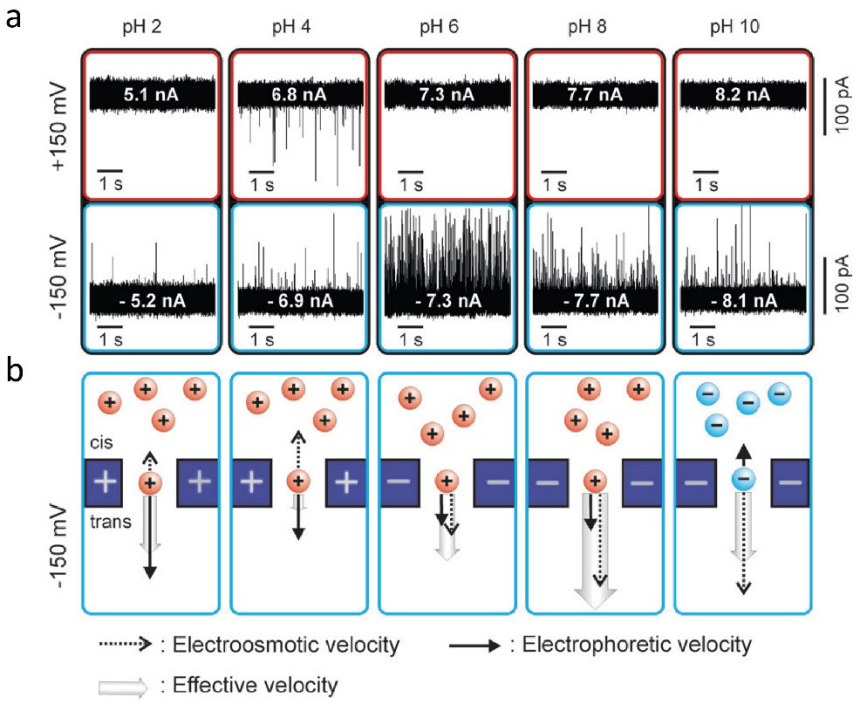


Figure 1.8 Electrophoretic and electroosmotic flow in nanopore sensing. (a) Current traces of avidin translocation under an application of positive and negative bias at varying pH values (pH 2-10). (b) Schematic of electrophoretic and electroosmotic velocities in protein translocation with varying protein and pore charges. Figures adapted from reference, [91] American Chemical Society.

1.3.5 Sensing of biomolecules using solid-state nanopores

So far, solid-state nanopores have demonstrated their high effectiveness in detecting a vast range of biomolecules, including nucleic acids, [54] proteins[96] and glycosaminoglycans. [97] Despite substantial progress in this field, a significant challenge remains in sensing and characterising smaller biomolecules, such as microRNA or small proteins (< 15 kDa). These molecules pose challenges due to their small size, rapid transport speed, and varying electrokinetic behaviour as they translocate through a nanopore. This complexity is further compounded when attempting to analyse target molecules within biological fluids, where substantial background interference is prevalent. Moreover, the spatiotemporal limitation of nanopore measurements in their ability to differentiate between closely related molecules has impeded their practical application in areas like molecular diagnostics. Addressing these challenges is crucial for adapting nanopores for effective biomedical applications.

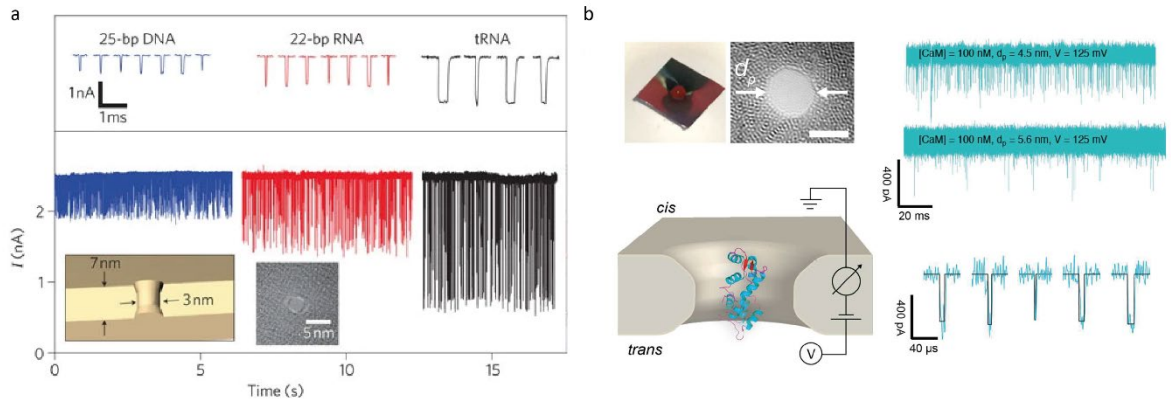


Figure 1.9 Nanopore sensing of single biomolecules. (a) Differentiation of small nucleic acids using a nanopore with 3 nm in diameter and 7 nm in thickness. Specifically, 25-bp DNA, 22-bp RNA and tRNA are distinguished based on their current amplitudes. (b) Protein detection using an ultra-thin solid-state nanopore based on a freestanding HfO_2 membrane. The current traces are recoded using a high-bandwidth and low-noise system. Calmodulin is shown as an example. Panel (a) adapted from reference, [54] Springer Nature Limited. Panel (b) adapted from reference, [96] American Chemical Society.

In the quest to directly detect small biomolecules using unmodified solid-state nanopores, researchers have made notable advancements. For instance, they have employed ultrathin and ultrasmall nanopores combined with high-bandwidth recording techniques to enhance spatiotemporal resolution of single-molecule detection. [54, 98] In a study by Wanunu et al., the membrane thickness was reduced to as little as 6 nm, and the pore diameter was scaled down to 3 nm, resulting in significantly improved signal-to-noise ratios. [54] This approach facilitated the effective detection and discrimination of small nucleic acids with similar molecular weights, such as 22-bp RNA and 25-bp DNA, as well as tRNA molecules, as shown in **Figure 1.9a**. Regarding protein detection, capturing small proteins (< 100 kDa) using conventional nanopore (> 10 nm) can be challenging based on the Smoluchowski rate equation, mainly due to the lack of sufficient temporal resolution. [99] To overcome this limitation, Waduge and coworkers employed high-bandwidth ionic current measurement in conjunction with an ultrathin HfO_2 nanopore to detect the transit of protein molecules. Through this high-resolution approach, the current blockade amplitude can be correlated to the radius of gyration and shape of proteins being analysed. Calmodulin, a canonical protein that undergoes a conformational

change in response to calcium binding, was successfully resolved into two states using this method. These advances in nanopore fabrication and instrumental measurements hold promise for sensing small biomolecules and rapidly advancing the detection of proteins and protein-protein interactions, which are critical steps toward realising practical applications of nanopores in the field of molecular diagnostics and beyond.

1.4 Single-molecule protein and proteome analysis

Proteins and their interactions are the linchpin of biological systems, performing diverse and vital roles in the intricate machinery of life. They function as the architects shaping cellular structures, conductors of intricate signalling pathways that enable communication between cells and tissues, and catalysts propelling the chemical reactions essential for metabolism. The form of a protein, intricately linked to its structure, governs its function. Even subtle alterations in a protein's structure can trigger dysfunction, underpinning a multitude of diseases. For instance, misfolded proteins are implicated in devastating neurodegenerative disorders such as Alzheimer's and Parkinson's disease. [100] However, the adaptability of proteins extends beyond causing disease; they also serve as potent tools for treatment and cure. Antibodies, a class of proteins produced by the immune system, play a pivotal role in our defence against viral and bacterial infections. They have been engineered and employed as therapeutics to combat a wide spectrum of diseases. [101] The dynamic and multifaceted roles of proteins in biology underscore their fundamental significance in comprehending, diagnosing, and treating various conditions. As such, they occupy a central position in ongoing research and innovation in fields spanning medicine, biotechnology, and beyond.

1.4.1 Current development of proteomic analysis

The complete sequencing of the human genome marked a significant milestone in our quest to unravel the mechanisms of life. [102] However, it is the proteins, the end products encoded in the genome, that have garnered increasing attention in the field of omics studies. [103] Unlike genomic and transcriptomic analyses, proteomics goes beyond merely sequencing proteins. It

encompasses the identification of post-translational modifications, exploration of complex structures, and examination of protein interactions. Additionally, proteomics quantifies protein concentrations within specific biological contexts. [104] While obtaining the primary structure, i.e., the sequence, of proteins is a fundamental step, protein sequencing techniques have lagged significantly behind the remarkable advances in DNA sequencing. Currently, the available methods for protein sequencing primarily revolve around Edman degradation, mass spectrometry, or their combined technologies. [105, 106, 107]

The current gold standard for protein sequencing is mass spectrometry (MS), [108, 109, 110, 111] particularly the bottom-up mass spectrometry (BU-MS) approach for protein-level analysis. [112] BU-MS entails enzymatic digestion of proteins, such as trypsin, ionisation of resulting peptides, separation of ions based on their mass/charge ratio (m/z), and subsequent ion detection. These "tryptic peptides" are analysed using techniques like electrospray ionisation or matrix-assisted laser desorption/ionization (MALDI), which ionise peptides in a gas phase, analyse their masses, and fragment ions to extract information about their sequence from the mass spectrometry data. [112] Alternatively, liquid chromatography–mass spectrometry (LC-MS) can be employed to separate compounds before ionisation and analysis.

However, the MS techniques has inherent limitations concerning its limit of detection (LOD) and dynamic range. [113] One of the significant challenges in proteomics is dealing with the vast dynamic range of protein concentrations in complex biological samples. For instance, human plasma contains proteins ranging from a few picograms per millilitre (e.g., interleukin 6) to a few milligrams per millilitre (e.g., albumin). [114] Achieving a comprehensive proteome analysis necessitates an extremely high dynamic range (around 10^9). Unfortunately, state-of-the-art mass spectrometers can only cover a dynamic range of around 10^4 to 10^5, falling far short of what is required. [115] Another issue is the detection limit, which poses challenges for biomarker discovery and often demands substantial sample volumes. To put this into perspective, if we consider a protein present in cells in low copy numbers (< 1,000 copies per cell), [116] millions of cells are needed to reach the instrumental limit of detection (typically 0.1 to 10 femtomole).

[117] Consequently, comprehensive single-cell proteome analysis remains a distant goal given the current capabilities of mass spectrometry.

1.4.2 Challenges of nanopore-based protein analyser

Building on the success of DNA nanopore sequencing, the nanopore community is now embarking on the challenging path of single-molecule protein sequencing. [118, 119, 120, 121, 122] This is a groundbreaking endeavour with unique advantages for single-cell studies compared to existing methods such as MS and emerging techniques such as fluorosequencing and affinity-based methods. [123] One of the central challenges in nanopore sequencing, especially for proteins, is controlling the translocation of the polymer through the pore. For DNA and RNA nanopore sequencing, this challenge has been largely addressed by employing nucleic acid-processive motors such as polymerases or helicases to regulate strand movement through the pore. [12] Computational approaches, often based on machine learning algorithms, are then employed to translate raw current signals into nucleotide sequences. However, when it comes to protein sequencing, numerous challenges remain.

Firstly, proteins consist of twenty different amino acids (AAs), each with varying charge, polarity, and hydrophobicity. This inherent diversity leads proteins to adopt complex three-dimensional structures in aqueous environments. Their complex folding patterns and the heterogeneous charge distribution on their surfaces make capturing and translocating proteins through nanopores challenging, mainly due to the presence of weak electrokinetic forces. [124] Distinguishing between twenty different types of amino acids is undoubtedly more complex than the four types encountered in DNA sequencing, even with sophisticated analytical algorithms. Secondly, while DNA samples can be amplified using techniques such as PCR, proteins lack a comparable amplification method. This becomes a challenge when considering the typically high concentration requirements for effective nanopore measurements. Detecting proteins with low copy numbers, as often found in cells, becomes especially difficult due to these concentration limitations. Lastly, unlike DNA sequencing, which uses motor proteins to control translocation, protein sequencing lacks an equivalent motor protein.

Protein translocation through nanopores can be extremely fast in solid-state nanopores, particularly for smaller proteins (less than 15 kDa), sometimes exceeding the temporal resolution of the detection system. [99] This high-speed translocation results in numerous events becoming undetectable and distorted, undermining the reliability of nanopore readouts. Despite advances in high-bandwidth instrumentation, optimising nanopore fabrication and enhancing SNRs remain persistent technical challenges to overcome. [96]

Currently, there are two popular strategies for protein nanopore sequencing. One involves borrowing the DNA sequencing platform to read the electrical signals of peptide or protein translocation with the assistance of DNA molecules. [119, 120, 125] The other strategy involves digesting the protein into peptide fragments and reading the electrical spectrum, similar to mass spectrometry. [126, 127, 128] Besides sequencing, proteomic analysis also involves direct measurements of whole proteins to unveil their native folded structures and potential interacting domains with other molecules. In this regard, solid-state nanopores offer several advantages, such as flexible pore geometry and size, ease of modification, robustness, stability, and the potential to advance proteomic analysis. [53]

1.4.3 Surface-functionalised nanopores

The surface properties of solid-state nanopores play a pivotal role in the translocation process and have a significant impact on various factors, including interactions between the pore and analyte surfaces, receptor binding, and electroosmotic flow. While some progress has been made using unmodified nanopores, there are critical limitations in the effective sensing of proteins, including rapid translocation speeds, [99] lack of selectivity, [129] and non-specific adsorption. [130] Distinguishing between molecules that share similar attributes, especially size and charge, poses substantial challenges. For instance, when proteins with closely matched sizes or charges translocate through the pore, the resulting resistive pulses can be remarkably similar. One promising approach to overcome these challenges is surface functionalisation of the nanopore, particularly through the introduction of recognition receptors on the surface. [131] By adding a specific binding site around the nanopore surface, selectivity can be

incorporated into the nanopore system. [129, 132] This not only improves the ability to transport specific molecules but also reduces irreversible adhesion. For example, Wei et al. functionalised a gold-coated silicon nitride (SiN_x) nanopore with a receptor to precisely detect proteins. [129] The process involved anchoring multivalent nitrilotriacetic acid (NTA) onto the metallised surface, followed by chelation of Ni^{2+} ions to the NTA, as depicted in **Figure 1.10a**. This setup allowed for the capture of His-tagged proteins onto the surface, resulting in a decelerated translocation pace and prolonged dwell times in the nanopore. This method exemplifies a targeted approach to differentiate molecules based on specific interactions. Furthermore, antibodies can be selectively identified by utilising His-tagged protein A chelation, effectively serving as a receptor.

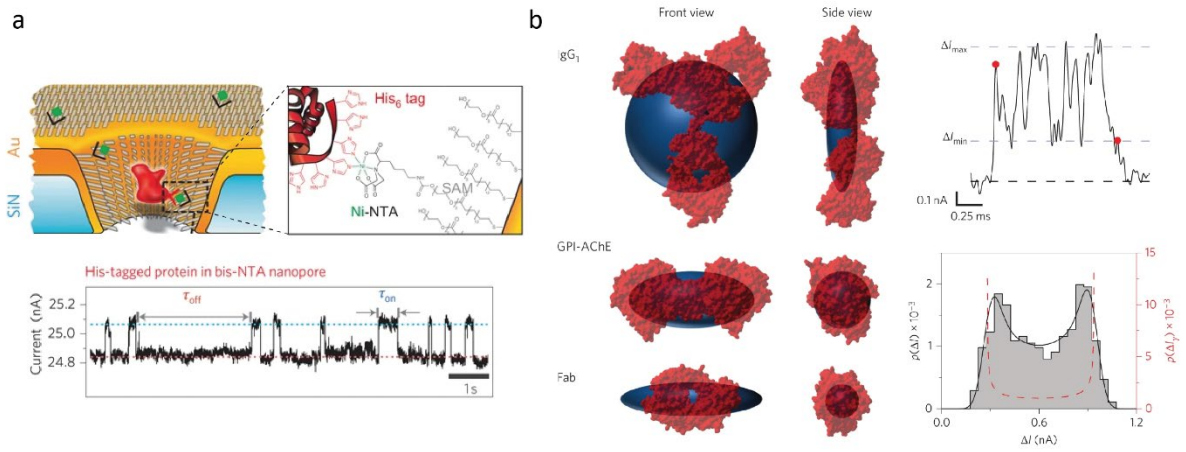


Figure 1.10 Functionalised nanopores. (a) Schematic of a His-tagged protein translocated through a bi-NTA (shown in green) functionalised gold-coated nanopore. A zoomed-in view shows the His6-tag chelated with the Ni-NTA during translocating. A typical current trace, as seen in the bottom panel, shows the prolonged translocation events upon the specific binding of target molecules. (b) Real-time shape approximation of single proteins using a lipid coated nanopore. Proteins with different sizes and shapes can be obtained from the current modulations within individual translocation events. Panel (a) adapted from reference, [129] Springer Nature Limited. Panel (b) adapted from reference, [133] Springer Nature Limited.

In a groundbreaking development, Yusko et al. used a nanopore to expand the concept of protein fingerprinting by unambiguously identifying whole proteins (Figure 1.10b). [133] They achieved this by measuring not only the volume but also the shape, charge, rotational diffusion coefficient, and dipole moment of proteins. They utilised a pore approximately 30 nm in diameter through a 275-nm-thick membrane coated with a lipid layer. This lipid layer effectively reduced the nonspecific adsorption of proteins to the nanopore wall. They analysed proteins tethered to the lipid layer by tracking how they modulated the blockade current as they translocated slowly across the membrane through the pore. In addition to obtaining volumetric information, this method successfully revealed shape information from the current blockade. The idea behind this approach is that the rotation of a single non-spherical object during nanopore translocation modulates the current blockade. The maximum blockade occurs when the spheroidal particle is in its extreme crosswise orientation, while a minimum develops in the extreme lengthwise configuration. Thus, the magnitude of the current blockade depends on molecular volume and charge, whereas the ratio between the minimal and maximal blockade current modulation depends on the shape. The bias in the distribution of maximum blockade currents is affected by the dipole moment, and the time dependence of the modulation measures the rotational diffusion coefficient. These milestones underscore the advantages of surface-functionalised solid-state nanopores for whole protein fingerprinting and selective recognition.

1.4.4 Molecular carriers

While significant progress has been made in the development of surface-functionalised pores, there remains a need for further advancements in protein analysis. These include precise control over the modification location on the pore surface, the ability to differentiate target proteins from complex biological backgrounds, and the capacity to detect rare proteins at extremely low concentrations. Molecular carriers emerge as promising solutions to address these challenges. A molecular carrier typically consists of a charged backbone, such as DNA, [134, 135] or charged peptides, [124] along with metallic nanoparticles. [136] These charged components facilitate the efficient transport of proteins through nanopores. Moreover, the carrier features a linking element that attaches to the analyte protein, which can either be covalent[120] or

noncovalent. [135] The translocation of a carrier bound to an analyte can be distinguished from that of the carrier alone by monitoring the ionic-current blockade. The presence of the analyte induces a distinct subpeak, which overlays the signal. [134, 135, 137, 138] Utilising molecular carriers offers several advantages. Firstly, it eliminates the need for functional modifications to the nanopore, maintaining a versatile platform design capable of detecting various targets. Additionally, carriers can slow down protein transport through the pore, thereby enhancing temporal resolution and increasing the likelihood of detecting smaller proteins. Lastly, carriers can be engineered with multiple recognition sites, potentially allowing for multiplexing. [135, 137, 139] However, this introduces another challenge: aligning the binding locations for individual events, particularly when the carrier does not translocate through the pore at a constant velocity. [140]

DNA carriers have garnered significant attention in recent years due to their rapid development. This can be attributed to their rigid and well-defined double-helix structure, customisable sequences, and the availability of origami scaffolds. [141] Among the various carrier options, DNA stands out for its versatility. Several strategies have emerged to enhance the selectivity and multiplexing capacity of DNA carriers. For instance, Bell et al. employed a molecular carrier based on 7.2 kbp M13mp18 DNA to detect multiple proteins. [134, 137] By strategically modifying the recognition sites along the carrier backbone, they were able to sequentially identify analyte proteins from the subpeaks observed during individual translocation events. One potential challenge arises as DNA carriers enter the pore in random directions, potentially complicating the correlation between subpeak locations and analyte types. Drawing inspiration from DNA origami technology, carriers have been further engineered with nanostructure barcodes to encode various carriers targeting different analytes. A 3-bit barcode, labelled with DNA dumbbell hairpins, could be assigned with an impressive 94% accuracy through subpeak analysis, enabling selective detection of multiple antibodies. [137] In another approach, Sze et al. reported multiplexed protein detection using aptamer-modified 48.5 kbp (λ-DNA) carriers, as illustrated in **Figure 1.11a**. [135] In comparison to unbound DNA carrier translocation, the binding of proteins induced distinct subpeaks on the primary DNA signals, enabling the simultaneous detection of multiple analytes within a single carrier translocation. This strategy relies on analysing the relative positions and sizes of the

subpeaks to differentiate between different targets. Notably, this approach demonstrated compatibility with selective protein sensing in unprocessed biological samples, such as human serum.

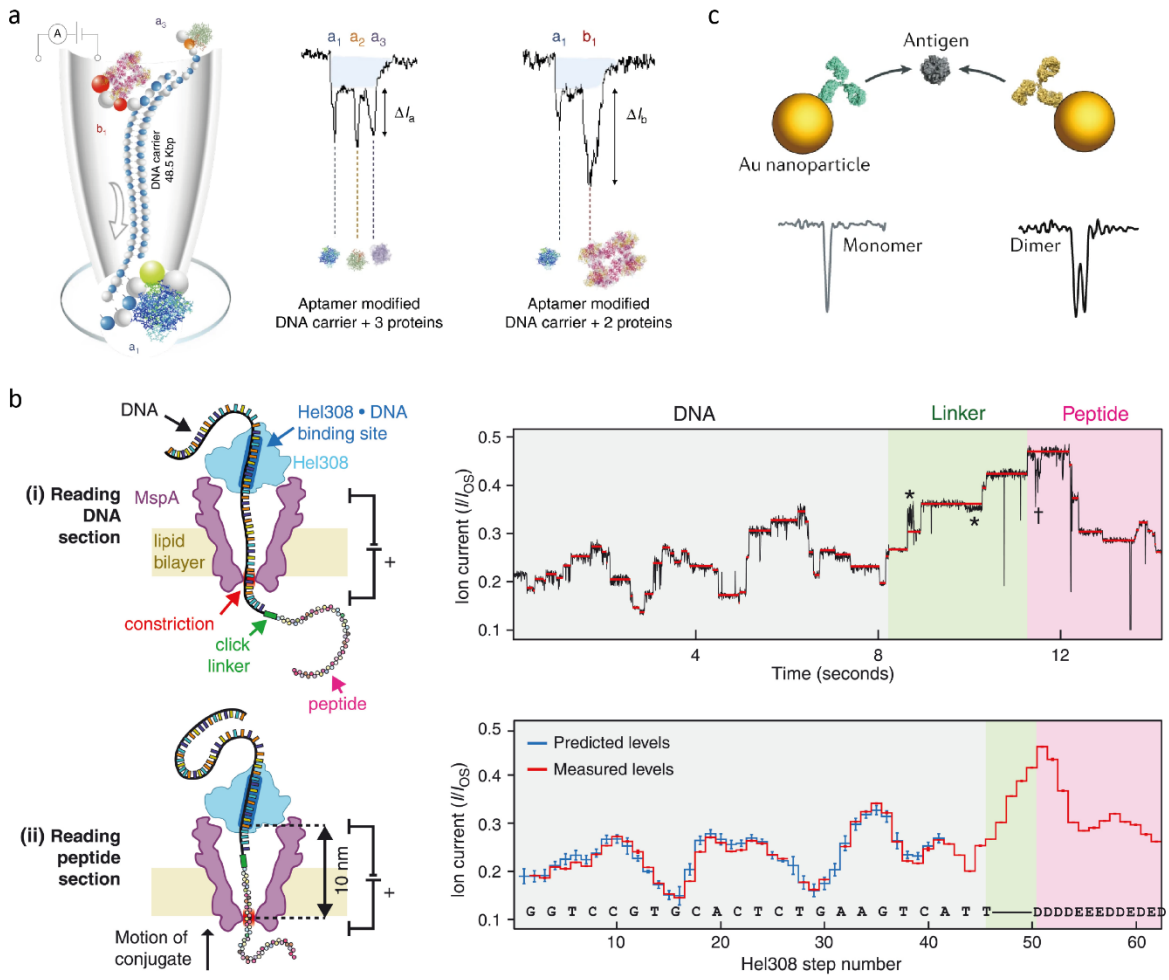


Figure 1.11 Molecular carriers used in protein nanopore sensing. (a) Multiplexed detection of proteins using aptamer-modified DNA carriers. The analyte protein is recognised by the subpeak positioned within individual events, where the subpeak amplitude indicates the protein size. (b) Peptide nanopore sequencing assisted by a carrier DNA. Based on the nanopore sequencing system, the carrier DNA is controlled by the motor protein under a precise speed, resulting in a high-resolution reading of the conjugated peptide. (c) Antigen detection based on the dimerisation of gold nanoparticle carriers. The doublet signals suggest the translocation of particle dimers, which further indicate the presence of analyte proteins. Panel (a) adapted from reference, [135] Springer Nature Limited. Panel (b) adapted from reference, [120] AAAS. Panel (c) adapted from reference, [136] Wiley.

Very recently, a significant breakthrough was made by Brinkerhoff and colleagues in the field of peptide sequencing and the identification of post-translational modifications. They accomplished this by integrating analyte peptides with carrier DNA molecules through covalent conjugation (as depicted in **Figure 1.11b**). [32, 120] This innovative approach draws inspiration from DNA nanopore sequencing and relies on the precise control of translocation, guided by the DNA carrier. In this method, the DNA carrier, meticulously propelled by a translocase, demonstrated the remarkable capability to pull peptides through the nanopore in single-amino-acid steps. This breakthrough allowed for the resolution of sequential differences among the analysed peptides. Notably, this achievement was performed using a biological nanopore, underscoring the potential of utilising DNA carriers in the future of proteomic analysis within the nanopore research community.

Another alternative carrier entity gaining traction is functional nanoparticles. [62, 136] Nanoparticles are a highly popular nanomaterial for biosensing due to their ease of synthesis and functionalisation with surface ligands. For instance, metallic nanoparticles can be easily functionalised using thiol[142] or amine[143] linked receptors, while oxide nanoparticles can also be functionalised using silanes. [144] Illustrated in **Figure 1.11c**, Ren et al. have utilised single-antibody-functionalised gold nanoparticles to recognise target antigens. [136] These nanoparticles form a sandwich structure involving an antibody-protein-antibody configuration. Dimeric nanoparticles, bound to the target protein, produce doublet translocation signals, which can be distinguished from the singlet translocation signals generated by bare monomeric nanoparticles. This innovative platform allows for binding assays to be conducted at nearly physiological salt concentrations, achieving an ultra-low limit of detection.

1.4.5 Integrated nanopore technology

Another significant advantage of solid-state nanopores is their seamless integration with various technology platforms. One approach involves attaching a protein channel to a solid-state pore, combining the sensitivity and reproducibility of biological nanopores with the robustness and non-diffusivity of solid-state nanopores. The first demonstration of hybrid

nanopore formation entailed electrophoretically inserting α-hemolysin (α-HL) conjugated to a DNA tether into a 3.6 nm SiN_x pore, as depicted in **Figure 1.12a**. [145] This hybrid nanopore could then be utilised to detect single-stranded DNA (ssDNA). Subsequently, other hybrid pores incorporating channels such as DNA origami[146] and viral portal proteins[147] were successfully demonstrated. However, it is important to note that in hybrid nanopore platforms, signal fluctuations are often observed due to factors such as leakage current caused by protein channel deformation and the entry or exit of the protein from the solid-state pore. To address this, ongoing research is focused on chemically binding the organic pore to the solid-state matrix, with or without chemical conjugation, resulting in a fixed channel inserted into the solid-state pore with a well-defined position and orientation. An example of this can be seen in Figure **1.12b**, where the G20C portal protein is inserted into a chemically functionalised SiN_x nanopore, forming covalent disulfide bridges between the cysteine residues of the G20C portal protein and the thiol groups on the pore surface to create a stable hybrid nanopore. [148]

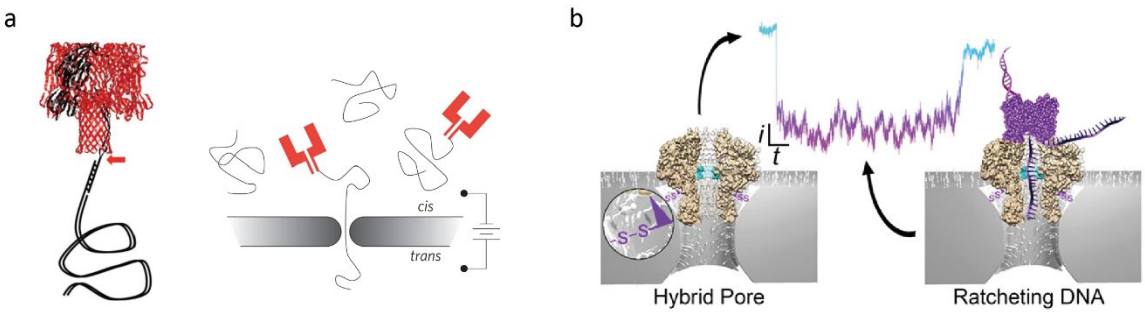


Figure 1.12 Hybrid nanopores. (a) Structure of α-Hemolysin conjugated with a carrier DNA. Under an applied voltage, the protein-dsDNA conjugate is electrophoretically driven through the solid-state nanopore, forming a stable hybrid pore. (b) Covalent linkage between the solid-state nanopore and the G20C portal protein. The solid-state nanopore is chemically functionalised thiol groups, which can form disulfide bridges with the cysteine residues of the G20C portal protein to ensure a stable hybrid nanopore. Panel (a) adapted from reference, [145] Springer Nature Limited. Panel (b) adapted from reference, [148] American Chemical Society.

Furthermore, nanopores offer the advantage of molecular confinement, which can enhance the information obtained beyond just ionic current measurements. Consequently, there has been a growing interest in integrating nanopore platforms with optical-sensing techniques, enabling various applications: 1) Fluorescence detection: One approach involves the detection of single molecules labelled with fluorescent dyes, either in combination with simultaneous electrical measurements (as depicted in **Figure 1.13a**) or without. 2) Label-Free fluorescent sensing: Label-free molecule sensing relies on fluorescent-ion indicators, as illustrated in **Figure 1.13b**. 3) Plasmonic nanopores: Plasmonic nanopores (**Figure 1.13c**) leverage the interaction between light and metallic nanostructures to enhance detection sensitivity. 4) Surface-enhanced Raman spectroscopy (SERS): SERS (**Figure 1.13d**) is employed for highly sensitive single-molecule analysis by the enhancement in Raman scattering as the molecules pass through the metallic pore. [149]

Recently, Cai and colleagues introduced an aptamer-based molecular beacon (MB) system for identifying single-nucleotide mismatches and target proteins directly in human serum and urine (**Figure 1.13e**). [150, 152] In this method, electrical signals from nanopores were observed in the absence of target proteins, indicating the translocation of MB-modified DNA carriers. However, the presence of target proteins opened the hairpin structure of the MB, leading to synchronised optical and electrical signals. It is worth noting that optical techniques may face challenges, such as background autofluorescence and electrical noise generated by laser illumination. Therefore, optimising nanopore-chip design is crucial for achieving high-bandwidth simultaneous optoelectrical measurements. [153] Furthermore, in **Figure 1.13f**, a bowtie nanoplasmonic structure was employed to control the translocation of DNA molecules through a solid-state nanopore. [154] Sequence information was read from the SERS signals generated. This approach uses high-intensity optical hot spots created by metallic nanostructures to regulate DNA translocation speed, presenting exciting prospects for single-molecule protein sequencing.

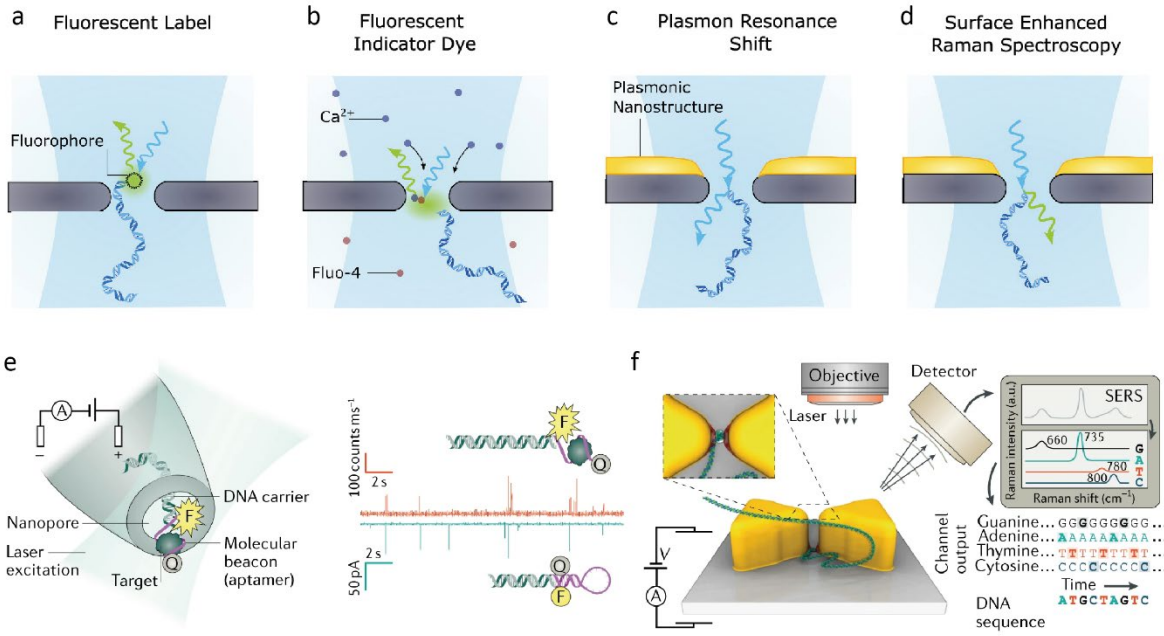


Figure 1.13 Optical nanopore sensing. (a) Detecting the translocation of a fluorophore-labelled analyte through the nanopore. (b) Detecting the nanopore translocation of an analyte labelled with an indicator dye. Analyte translocation changes the fluorescence signal by modifying the transport of Ca^{2+} ions through the pore. (c) Detecting an analyte translocating through a plasmonic nanostructure. Analytes in close proximity to the nanostructure change the local refractive index which changes the plasmon resonance frequency. (d) Detection by surface-enhanced Raman spectroscopy. (e) Protein detection using molecular-beacon-modified DNA carriers. The simultaneous detection of optical and electrical signals suggests the presence of target proteins. (f) A plasmonic bow-tie nanostructure is fabricated next to a nanopore, which is used for DNA sequencing. Panels (a)-(d) adapted from reference, [149] American Chemical Society. Panel (e) adapted from reference, [150] Springer Nature Limited. Panel (f) adapted from reference, [151] American Chemical Society.

Moreover, solid-state nanopores have found fruitful applications in coupling with scanning probe microscopy techniques, including scanning ion-conductance microscopy (SICM), [73, 156] scanning tunnelling microscopy (STM), [157] and atomic force microscopy (AFM). [155, 158] By incorporating feedback from these scanning microscopes, nanopore sensors can be precisely positioned at specific target areas, such as single cells or molecules, enabling highly accurate analysis. A significant milestone achieved by the Radenovic group involves the combination of

nanopipettes with SICM to enhance both spatial and temporal resolution in nanopore sensing (**Figure 1.14a**). [73] In contrast to conventional nanopore sensing where analytes traverse the pore, this approach involves moving the pore along single analyte molecules to extract structural information at a controlled speed. By reducing velocity and averaging thousands of consecutive readings of the same molecule, the signal-to-noise ratio is significantly enhanced, improving it by two orders of magnitude compared to free translocation. This versatile method has been extended to the detection of DNA-binding proteins, DNA rulers, and DNA gaps, achieving resolutions down to single-nucleotide gaps (**Figure 1.14b**).

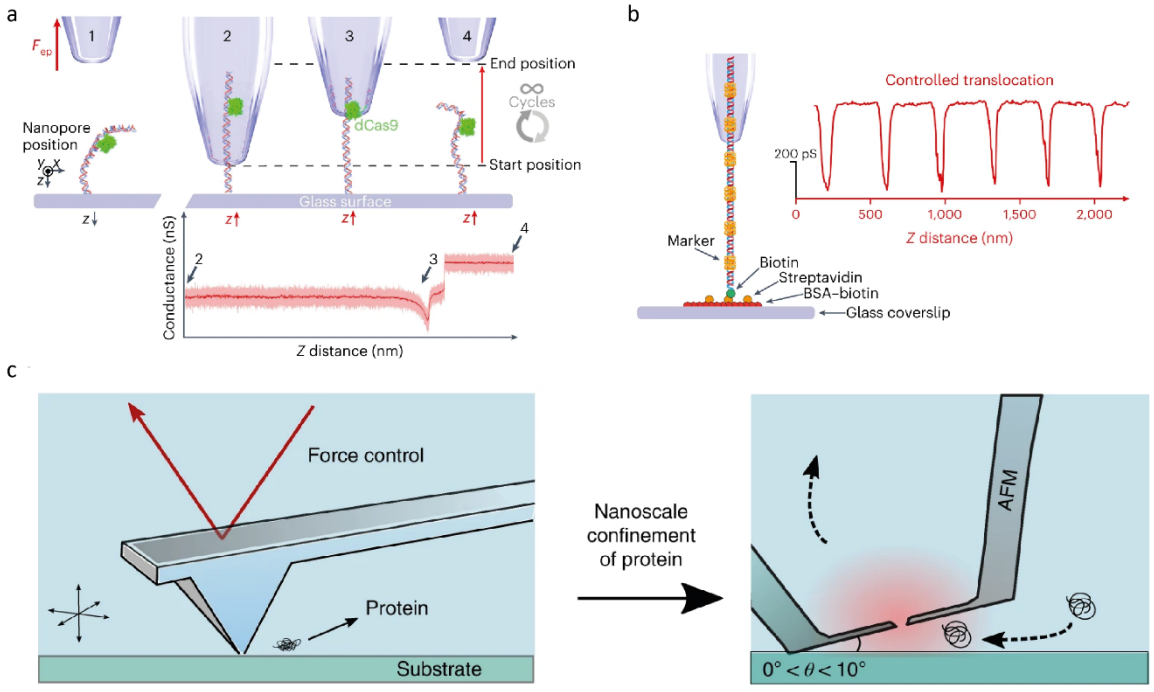


Figure 1.14 Nanopore sensing integrated with scanning microscopy. (a) Principle of scanning ion conductance spectroscopy (SICS). Molecule capture followed by controlled translocation and corresponding conductance-distance spectrum. (b) Controlled translocation of a DNA ruler using SICS, where DNA is grafted upon a glass surface by biotin-streptavidin interactions. The subpeaks shown in the SICS result correspond to the positions and sizes of the DNA markers on the DNA backbone. (c) Localised protein detection using a nanopore AFM. The tip of AFM approaching to the surface creates a nanoconfined area that produces an energy barrier for biomolecular translocation before entering to the nanopore. Panels (a) and (b) adapted from reference, [73] Springer Nature Limited. Panel (c) adapted from reference, [155] Springer Nature Limited.

In another notable breakthrough in 2019, Aramesh et al. demonstrated the integration of a solid-state nanopore with an AFM for stochastic sensing of secreted molecules and ion channel activity at arbitrary locations both inside and outside cells (**Figure 1.14c**). [155] This setup enables controlled mechanical confinement of ion and single biomolecule translocation through the nanopore, facilitating the scanning imaging of a nuclear membrane by high-resolution ion conductance measurements.

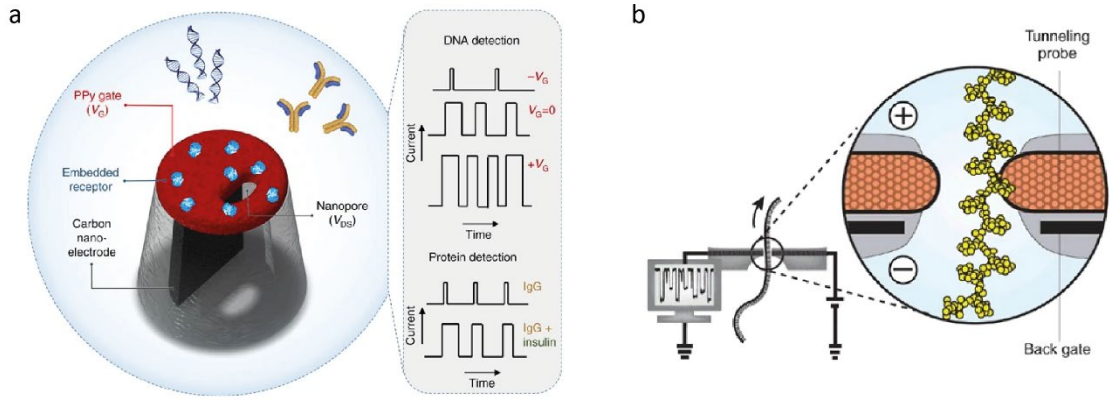


Figure 1.15 Nanopore field-effect transistors (FETs) and tunnelling junctions. (a) A nanopore sensor integrated with a FET component. Polypyrrole can serve as a gate to modulate molecule translocation through the nanopore. Recognition receptors can be dopped in the polymeric film to improve the selectivity of nanopore sensing. (b) Schematic of tunnelling sequencing embedded on a nanopore. The DNA molecule is led through a nanopore, which is modified with integrated emitter and collector tunnelling probes, alongside a back gate. As the DNA translocates through the pore, the changes in the tunnelling currents are expected to differentiate the nucleotide type. Panel (a) adapted from reference, [159] Springer Nature Limited. Panel (b) adapted from reference, [10] Springer Nature Limited.

Integrating nanopores with field-effect transistors (FETs) while confining charged analytes within nanoscale pores offers several advantages, notably the active transport of analytes to the FET. Various approaches have been employed to achieve this nanopore integration,

including the use of nanowires, [160] graphene nanoribbons, [161, 162] and aligned gold electrodes within the pore lumen. [163] Detection within both the FET and nanopore channel can be synchronised, as demonstrated in the context of DNA[160, 161, 162, 163] and nanoparticle detection. [164] This synchronization mechanism is based on either capacitive coupling, [165] resulting from a change in the local potential at the gate electrode during DNA translocation, or electrostatic gating driven by the charge of the translocating molecule. [160, 161] In terms of protein analysis, Ren and colleagues introduced a new nanopore extended field-effect transistor, referred to as nexFET, which was created through the electrodeposition of polypyrrole within a dual-barrel nanopipette (**Figure 1.15a**). [159] By doping insulin onto the polymeric film, this device selectively detected anti-insulin antibodies rather than other isotype IgG, relying on observations of the adhesion behaviours of antigen-antibody interactions. Additionally, an aptamer-doped nexFET device was demonstrated for the selective detection of thrombin. [90]

An intriguing strategy aimed at enhancing spatial resolution within nanopores is based on quantum tunnelling. In this configuration, two electrodes are positioned in close proximity to each other, typically spaced less than 5 nm apart, forming a junction through which electrons can tunnel. This detection approach holds the promise of significantly improving the spatial resolution for identifying translocating analytes. Depending on the fabrication process, these electrodes can be suspended over the nanopore, [166] embedded within a membrane, [167] or layered between 2D insulators to create a tunnelling junction within the nanopore itself. [168] The idea of combining nanopore detection and quantum tunnelling was, to some extent, inspired by the goal of achieving next-generation nucleic acid sequencing. [169, 170] This innovative approach brings together the advantages of nanopore-based single-molecule confinement and the high spatial resolution, approaching atomic levels, offered by tunnelling junctions. As depicted in **Figure 1.15b**, when a DNA molecule is electrophoretically driven through a nanopore modified with integrated tunnelling probes, changes in the tunnelling currents are expected to provide differentiation among nucleotide types. [10] While the initial work primarily focused on nucleic acids, substantial effort has been invested in proteomic analysis, as it holds the potential for advancing protein sequencing and conformational analysis. [171, 172, 173]

1.5 Objectives and thesis overview

This thesis focuses on the exploration of single-molecule protein analysis using nanopores, specifically quartz nanopipettes. The objectives of my research projects are to develop new approaches to improve the sensitivity and selectivity of protein nanopore sensing and to add multiplexing capabilities to current methods. The key approaches explored in this thesis are:

Chapter 2: This chapter serves as foundational guide to the experimental information and methodologies used throughout the thesis for nanopore measurements. It encompasses various aspects, including fabrication and characterisation of nanopores, nanopore measurements of single-molecule translocation, and procedures for data analysis.

Chapter 3: This chapter presents a comprehensive study on actin dynamics and drug binding using nanopores. Nanopore sensing provides insights into the molecular states of actin molecules without the need for labelling. The study distinguishes between globular monomeric, oligomeric, and filamentous actin. It also observes the unfolding process induced by urea and voltage, along with transient partial and full folding states. Real-time visualisation of actin polymerisation is demonstrated, suggesting potential applications in measuring protein aggregations. Additionally, the structural changes of actin in response to drug binding are resolved, highlighting the potential for drug screening and discovery.

Chapter 4: This chapter introduces a novel strategy for protein detection by combining nanopore sensing with DNA carriers. Unlike conventional methods, this approach uses two aptamer-modified DNA carriers to bind the same protein, forming a carrier-protein-carrier sandwich structure. By differentiating protein-bound DNA dimers from free monomers, target proteins can be quantified at low concentrations. The method relies on the equivalent charge of individual events for the classification of dimers from monomers. It effectively detects thrombin, dimeric proteins such as VEGF and PDGF, and performs ligand-induced receptor dimerisation, even in low ionic strength solutions and complex biofluids such as human serum.

Chapter 5: In this chapter, supercharged unstructured polypeptides (SUPs) are introduced as protein-based molecular carriers to control protein transport through the nanopore. Cationic SUPs are shown to improve protein capture rates and slow down protein translocation speed through electrostatic interactions with the nanopore surface. This method enables protein concentration measurements at picomolar (pM) levels and has been successfully used for the size identification of small proteins and protein-protein interactions at the single-molecule resolution.

Chapter 6: This chapter provides a summary of the conclusions drawn from the thesis and outlines potential future directions for protein nanopore analysis. It proposes the integration of nanopores with a tunnelling detector to enhance spatial resolution and sensitivity, combining the advantages of solid-state nanopores and molecular carriers.

Overall, this thesis explores innovative approaches to advance protein nanopore sensing, providing valuable insights into the field of single-molecule protein analysis and its potential applications in drug discovery and diagnostics.

1.6 References

1. Bartlett JMS, Stirling D. A Short History of the Polymerase Chain Reaction. In: *PCR Protocols* (eds Bartlett JMS, Stirling D). Humana Press (2003).
2. Weiland G. [The enzyme-linked immunosorbent assay (ELISA)--a new serodiagnostic method for the detection of parasitic infections (author's transl)]. *MMW Munch Med Wochenschr* **120**, 1457-1460 (1978).
3. Gooding JJ, Gaus K. Single-Molecule Sensors: Challenges and Opportunities for Quantitative Analysis. *Angewandte Chemie International Edition* **55**, 11354-11366 (2016).
4. Lelek M*, et al.* Single-molecule localization microscopy. *Nature Reviews Methods Primers* **1**, 39 (2021).

5. Zhuang X, Ha T, Kim HD, Centner T, Labeit S, Chu S. Fluorescence quenching: A tool for single-molecule protein-folding study. *Proceedings of the National Academy of Sciences* **97**, 14241-14244 (2000).

6. Ha T, Laurence TA, Chemla DS, Weiss S. Polarization Spectroscopy of Single Fluorescent Molecules. *The Journal of Physical Chemistry B* **103**, 6839-6850 (1999).

7. Roy R, Hohng S, Ha T. A practical guide to single-molecule FRET. *Nature Methods* **5**, 507-516 (2008).

8. Müller DJ*, et al.* Atomic Force Microscopy-Based Force Spectroscopy and Multiparametric Imaging of Biomolecular and Cellular Systems. *Chemical Reviews* **121**, 11701-11725 (2021).

9. Neuman KC, Nagy A. Single-molecule force spectroscopy: optical tweezers, magnetic tweezers and atomic force microscopy. *Nature Methods* **5**, 491-505 (2008).

10. Branton D*, et al.* The potential and challenges of nanopore sequencing. *Nature Biotechnology* **26**, 1146-1153 (2008).

11. Deamer D, Akeson M, Branton D. Three decades of nanopore sequencing. *Nature Biotechnology* **34**, 518-524 (2016).

12. Wang Y, Zhao Y, Bollas A, Wang Y, Au KF. Nanopore sequencing technology, bioinformatics and applications. *Nature Biotechnology* **39**, 1348-1365 (2021).

13. Coulter WH. Means for counting particles suspended in a fluid. United States (1953).

14. Henriquez RR, Ito T, Sun L, Crooks RM. The resurgence of Coulter counting for analyzing nanoscale objects. *Analyst* **129**, 478-482 (2004).

15. Neher E, Sakmann B. Single-channel currents recorded from membrane of denervated frog muscle fibres. *Nature* **260**, 799-802 (1976).

16. Bezrukov SM, Vodyanoy I, Parsegian VA. Counting polymers moving through a single ion channel. *Nature* **370**, 279-281 (1994).

17. Kasianowicz JJ, Brandin E, Branton D, Deamer DW. Characterization of individual polynucleotide molecules using a membranechannel. *Proceedings of the National Academy of Sciences* **93**, 13770-13773 (1996).

18. Venkatesan BM, Bashir R. Nanopore sensors for nucleic acid analysis. *Nature Nanotechnology* **6**, 615-624 (2011).

19. Oukhaled A, Bacri L, Pastoriza-Gallego M, Betton J-M, Pelta J. Sensing Proteins through Nanopores: Fundamental to Applications. *ACS Chemical Biology* **7**, 1935-1949 (2012).

20. Shi W, Friedman AK, Baker LA. Nanopore Sensing. *Analytical Chemistry* **89**, 157-188 (2017).

21. Bayley H. Designed membrane channels and pores. *Current Opinion in Biotechnology* **10**, 94-103 (1999).

22. Song L, Hobaugh MR, Shustak C, Cheley S, Bayley H, Gouaux JE. Structure of Staphylococcal α-Hemolysin, a Heptameric Transmembrane Pore. *Science* **274**, 1859-1865 (1996).

23. Gu L-Q, Shim JW. Single molecule sensing by nanopores and nanopore devices. *Analyst* **135**, 441-451 (2010).

24. Howorka S, Cheley S, Bayley H. Sequence-specific detection of individual DNA strands using engineered nanopores. *Nature Biotechnology* **19**, 636-639 (2001).

25. Braha O, Gu L-Q, Zhou L, Lu X, Cheley S, Bayley H. Simultaneous stochastic sensing of divalent metal ions. *Nature Biotechnology* **18**, 1005-1007 (2000).

26. Van Meervelt V, Soskine M, Maglia G. Detection of Two Isomeric Binding Configurations in a Protein–Aptamer Complex with a Biological Nanopore. *ACS Nano* **8**, 12826-12835 (2014).

27. Meller A, Nivon L, Brandin E, Golovchenko J, Branton D. Rapid nanopore discrimination between single polynucleotide molecules. *Proceedings of the National Academy of Sciences* **97**, 1079-1084 (2000).

28. Niederweis M. Mycobacterial porins – new channel proteins in unique outer membranes. *Molecular Microbiology* **49**, 1167-1177 (2003).

29. Manara RMA, Jayne Wallace E, Khalid S. DNA sequencing with MspA: Molecular Dynamics simulations reveal free-energy differences between sequencing and non-sequencing mutants. *Scientific Reports* **5**, 12783 (2015).

30. Derrington IM*, et al.* Nanopore DNA sequencing with MspA. *Proceedings of the National Academy of Sciences* **107**, 16060-16065 (2010).

31. Wang Y*, et al.* Identification of nucleoside monophosphates and their epigenetic modifications using an engineered nanopore. *Nature Nanotechnology* **17**, 976-983 (2022).

32. Nova IC, Ritmejeris J, Brinkerhoff H, Koenig TJR, Gundlach JH, Dekker C. Detection of phosphorylation post-translational modifications along single peptides with nanopores. *Nature Biotechnology*, (2023).

33. Cressiot B, Ouldali H, Pastoriza-Gallego M, Bacri L, Van der Goot FG, Pelta J. Aerolysin, a Powerful Protein Sensor for Fundamental Studies and Development of Upcoming Applications. *ACS Sensors* **4**, 530-548 (2019).

34. Pastoriza-Gallego M*, et al.* Dynamics of Unfolded Protein Transport through an Aerolysin Pore. *Journal of the American Chemical Society* **133**, 2923-2931 (2011).

35. Cao C, Ying Y-L, Hu Z-L, Liao D-F, Tian H, Long Y-T. Discrimination of oligonucleotides of different lengths with a wild-type aerolysin nanopore. *Nature Nanotechnology* **11**, 713-718 (2016).

36. Payet L*, et al.* Thermal Unfolding of Proteins Probed at the Single Molecule Level Using Nanopores. *Analytical Chemistry* **84**, 4071-4076 (2012).

37. Sanganna Gari RR, Seelheim P, Liang B, Tamm LK. Quiet Outer Membrane Protein G (OmpG) Nanopore for Biosensing. *ACS Sensors* **4**, 1230-1235 (2019).

38. Huang G, Voet A, Maglia G. FraC nanopores with adjustable diameter identify the mass of opposite-charge peptides with 44 dalton resolution. *Nature Communications* **10**, 835 (2019).

39. Soskine M, Biesemans A, Moeyaert B, Cheley S, Bayley H, Maglia G. An Engineered ClyA Nanopore Detects Folded Target Proteins by Selective External Association and Pore Entry. *Nano Letters* **12**, 4895-4900 (2012).

40. Huang G*, et al.* PlyAB Nanopores Detect Single Amino Acid Differences in Folded Haemoglobin from Blood**. *Angewandte Chemie International Edition* **61**, e202206227 (2022).

41. Kang X, Alibakhshi MA, Wanunu M. One-Pot Species Release and Nanopore Detection in a Voltage-Stable Lipid Bilayer Platform. *Nano Letters* **19**, 9145-9153 (2019).

42. Dekker C. Solid-state nanopores. *Nature Nanotechnology* **2**, 209-215 (2007).

43. Storm AJ, Chen JH, Ling XS, Zandbergen HW, Dekker C. Fabrication of solid-state nanopores with single-nanometre precision. *Nature Materials* **2**, 537-540 (2003).

44. Waugh M*, et al.* Solid-state nanopore fabrication by automated controlled breakdown. *Nature Protocols* **15**, 122-143 (2020).

45. Gad-el-Hak M. *MEMS: Design and Fabrication (1st ed.)*. CRC Press (2005).

46. Gierak J*, et al.* Sub-5nm FIB direct patterning of nanodevices. *Microelectronic Engineering* **84**, 779-783 (2007).

47. Venkatesan BM, Shah AB, Zuo J-M, Bashir R. DNA Sensing Using Nanocrystalline Surface-Enhanced Al2O3 Nanopore Sensors. *Advanced Functional Materials* **20**, 1266-1275 (2010).

48. Schneider GF*, et al.* DNA Translocation through Graphene Nanopores. *Nano Letters* **10**, 3163-3167 (2010).

49. Feng J*, et al.* Identification of single nucleotides in MoS2 nanopores. *Nature Nanotechnology* **10**, 1070-1076 (2015).

50. Miles BN, Ivanov AP, Wilson KA, Doğan F, Japrung D, Edel JB. Single molecule sensing with solid-state nanopores: novel materials, methods, and applications. *Chemical Society Reviews* **42**, 15-28 (2013).

51. Gibb T, Ayub M. Chapter 5 - Solid-State Nanopore Fabrication. In: *Engineered Nanopores for Bioanalytical Applications* (eds Edel JB, Albrecht T). William Andrew Publishing (2013).

52. Li J, Stein D, McMullan C, Branton D, Aziz MJ, Golovchenko JA. Ion-beam sculpting at nanometre length scales. *Nature* **412**, 166-169 (2001).

53. Xue L, Yamazaki H, Ren R, Wanunu M, Ivanov AP, Edel JB. Solid-state nanopore sensors. *Nature Reviews Materials* **5**, 931-951 (2020).

54. Wanunu M, Dadosh T, Ray V, Jin J, McReynolds L, Drndić M. Rapid electronic detection of probe-specific microRNAs using thin nanopore sensors. *Nature Nanotechnology* **5**, 807-814 (2010).

55. Nam S*, et al.* Graphene Nanopore with a Self-Integrated Optical Antenna. *Nano Letters* **14**, 5584-5589 (2014).

56. Russo CJ, Golovchenko JA. Atom-by-atom nucleation and growth of graphene nanopores. *Proceedings of the National Academy of Sciences* **109**, 5953-5957 (2012).

57. Danda G*, et al.* Monolayer WS2 Nanopores for DNA Translocation with Light-Adjustable Sizes. *ACS Nano* **11**, 1937-1945 (2017).

58. Kwok H, Briggs K, Tabard-Cossa V. Nanopore Fabrication by Controlled Dielectric Breakdown. *PLOS ONE* **9**, e92880 (2014).

59. Briggs K, Kwok H, Tabard-Cossa V. Automated Fabrication of 2-nm Solid-State Nanopores for Nucleic Acid Analysis. *Small* **10**, 2077-2086 (2014).

60. Briggs K*, et al.* Kinetics of nanopore fabrication during controlled breakdown of dielectric membranes in solution. *Nanotechnology* **26**, 084004 (2015).

61. Yu R-J, Ying Y-L, Gao R, Long Y-T. Confined Nanopipette Sensing: From Single Molecules, Single Nanoparticles, to Single Cells. *Angewandte Chemie International Edition* **58**, 3706-3714 (2019).

62. Lin X, Ivanov AP, Edel JB. Selective single molecule nanopore sensing of proteins using DNA aptamer-functionalised gold nanoparticles. *Chemical Science* **8**, 3905-3912 (2017).

63. Steinbock LJ, Otto O, Chimerel C, Gornall J, Keyser UF. Detecting DNA Folding with Nanocapillaries. *Nano Letters* **10**, 2493-2497 (2010).

64. Gong X*, et al.* Label-Free In-Flow Detection of Single DNA Molecules using Glass Nanopipettes. *Analytical Chemistry* **86**, 835-841 (2014).

65. Fraccari RL, Ciccarella P, Bahrami A, Carminati M, Ferrari G, Albrecht T. High-speed detection of DNA translocation in nanopipettes. *Nanoscale* **8**, 7604-7611 (2016).

66. Cadinu P*, et al.* Single Molecule Trapping and Sensing Using Dual Nanopores Separated by a Zeptoliter Nanobridge. *Nano Letters* **17**, 6376-6384 (2017).

67. Cadinu P*, et al.* Double Barrel Nanopores as a New Tool for Controlling Single-Molecule Transport. *Nano Letters* **18**, 2738-2745 (2018).

68. Nadappuram BP*, et al.* Nanoscale tweezers for single-cell biopsies. *Nature Nanotechnology* **14**, 80-88 (2019).

69. Ying Y-L*, et al.* Manipulating and visualizing the dynamic aggregation-induced emission within a confined quartz nanopore. *Nature Communications* **9**, 3657 (2018).

70. Ebejer N, Güell AG, Lai SCS, McKelvey K, Snowden ME, Unwin PR. Scanning Electrochemical Cell Microscopy: A Versatile Technique for Nanoscale Electrochemistry and Functional Imaging. *Annual Review of Analytical Chemistry* **6**, 329-351 (2013).

71. Gorelik J*, et al.* The use of scanning ion conductance microscopy to image A6 cells. *Molecular and Cellular Endocrinology* **217**, 101-108 (2004).

72. Korchev YE*, et al.* Cell Volume Measurement Using Scanning Ion Conductance Microscopy. *Biophysical Journal* **78**, 451-457 (2000).

73. Leitao SM*, et al.* Spatially multiplexed single-molecule translocations through a nanopore at controlled speeds. *Nature Nanotechnology*, (2023).

74. Albrecht T, Gibb T, Nuttall P. Chapter 1 - Ion Transport in Nanopores. In: *Engineered Nanopores for Bioanalytical Applications* (eds Edel JB, Albrecht T). William Andrew Publishing (2013).

75. Smeets RMM, Keyser UF, Krapf D, Wu M-Y, Dekker NH, Dekker C. Salt Dependence of Ion Transport and DNA Translocation through Solid-State Nanopores. *Nano Letters* **6**, 89-95 (2006).

76. Muthukumar M. Mechanism of DNA Transport Through Pores. *Annual Review of Biophysics and Biomolecular Structure* **36**, 435-450 (2007).

77. Ivanov AP, Actis P, Jönsson P, Klenerman D, Korchev Y, Edel JB. On-Demand Delivery of Single DNA Molecules Using Nanopipets. *ACS Nano* **9**, 3587-3595 (2015).

78. Otto O, Keyser UF. Chapter 2 - DNA Translocation. In: *Engineered Nanopores for Bioanalytical Applications* (eds Edel JB, Albrecht T). William Andrew Publishing (2013).

79. De Richemont P. *Electrochemistry: Volume 11: Nanosystems Electrochemistry*. The Royal Society of Chemistry (2012).

80. Helmholtz H. Ueber einige Gesetze der Vertheilung elektrischer Ströme in körperlichen Leitern mit Anwendung auf die thierisch-elektrischen Versuche. *Annalen der Physik* **165**, 211-233 (1853).

81. Allen J. Bard LRF, Henry S. White. *Electrochemical Methods: Fundamentals and Applications, 3rd Edition*. Wiley (2022).

82. Singh KP, Kumar M. Effect of Nanochannel Diameter and Debye Length on Ion Current Rectification in a Fluidic Bipolar Diode. *The Journal of Physical Chemistry C* **115**, 22917-22924 (2011).

83. Liu S*, et al.* Studies of Ionic Current Rectification Using Polyethyleneimines Coated Glass Nanopipettes. *Analytical Chemistry* **84**, 5565-5573 (2012).

84. Torrie GM, Valleau JP. Electrical double layers. 4. Limitations of the Gouy-Chapman theory. *The Journal of Physical Chemistry* **86**, 3251-3257 (1982).

85. Behrens SH, Grier DG. The charge of glass and silica surfaces. *The Journal of Chemical Physics* **115**, 6716-6721 (2001).

86. Lowe BM, Skylaris C-K, Green NG. Acid-base dissociation mechanisms and energetics at the silica–water interface: An activationless process. *Journal of Colloid and Interface Science* **451**, 231-244 (2015).

87. Siwy Z, Heins E, Harrell CC, Kohli P, Martin CR. Conical-Nanotube Ion-Current Rectifiers: The Role of Surface Charge. *Journal of the American Chemical Society* **126**, 10850-10851 (2004).

88. Siwy ZS. Ion-Current Rectification in Nanopores and Nanotubes with Broken Symmetry. *Advanced Functional Materials* **16**, 735-746 (2006).

89. Wei C, Bard AJ, Feldberg SW. Current Rectification at Quartz Nanopipet Electrodes. *Analytical Chemistry* **69**, 4627-4633 (1997).

90. Ren R*, et al.* Selective Sensing of Proteins Using Aptamer Functionalized Nanopore Extended Field-Effect Transistors. *Small Methods* **4**, 2000356 (2020).

91. Firnkes M, Pedone D, Knezevic J, Döblinger M, Rant U. Electrically Facilitated Translocations of Proteins through Silicon Nitride Nanopores: Conjoint and Competitive Action of Diffusion, Electrophoresis, and Electroosmosis. *Nano Letters* **10**, 2162-2167 (2010).

92. Schmid G. Electrochemistry of capillary systems with narrow pores. II. Electroosmosis1Zur Elektrochemie feinporiger Kapillarsysteme II, Elektroosmose, Ber. Bunsenges. Phys. Chem. (Z. Elektrochem.) 55 (1951) 229–237.1. *Journal of Membrane Science* **150**, 159-170 (1998).

93. Schoch RB, Han J, Renaud P. Transport phenomena in nanofluidics. *Reviews of Modern Physics* **80**, 839-883 (2008).

94. Experton J, Wu X, Martin CR. From Ion Current to Electroosmotic Flow Rectification in Asymmetric Nanopore Membranes. *Nanomaterials* **7**, 445 (2017).

95. Bandara YMNDY, Farajpour N, Freedman KJ. Nanopore Current Enhancements Lack Protein Charge Dependence and Elucidate Maximum Unfolding at Protein's Isoelectric Point. *Journal of the American Chemical Society* **144**, 3063-3073 (2022).

96. Waduge P*, et al.* Nanopore-Based Measurements of Protein Size, Fluctuations, and Conformational Changes. *ACS Nano* **11**, 5706-5716 (2017).

97. Im J, Lindsay S, Wang X, Zhang P. Single Molecule Identification and Quantification of Glycosaminoglycans Using Solid-State Nanopores. *ACS Nano* **13**, 6308-6318 (2019).

98. Larkin J, Henley RY, Muthukumar M, Jacob, Wanunu M. High-Bandwidth Protein Analysis Using Solid-State Nanopores. *Biophysical Journal* **106**, 696-704 (2014).

99. Plesa C, Kowalczyk SW, Zinsmeester R, Grosberg AY, Rabin Y, Dekker C. Fast Translocation of Proteins through Solid State Nanopores. *Nano Letters* **13**, 658-663 (2013).

100. Soto C. Unfolding the role of protein misfolding in neurodegenerative diseases. *Nature Reviews Neuroscience* **4**, 49-60 (2003).

101. Lu R-M*, et al.* Development of therapeutic antibodies for the treatment of diseases. *Journal of Biomedical Science* **27**, 1 (2020).

102. Nurk S*, et al.* The complete sequence of a human genome. *Science* **376**, 44-53 (2022).

103. Suhre K, McCarthy MI, Schwenk JM. Genetics meets proteomics: perspectives for large population-based studies. *Nature Reviews Genetics* **22**, 19-37 (2021).

104. Labib M, Kelley SO. Single-cell analysis targeting the proteome. *Nature Reviews Chemistry* **4**, 143-158 (2020).

105. Miyashita M*, et al.* Attomole level protein sequencing by Edman degradation coupled with accelerator mass spectrometry. *Proceedings of the National Academy of Sciences* **98**, 4403-4408 (2001).

106. Shimonishi Y, Hong Y-M, Kitagishi T, Matsuo T, Matsuda H, Katakuse I. Sequencing of Peptide Mixtures by Edman Degradation and Field-Desorption Mass Spectrometry. *European Journal of Biochemistry* **112**, 251-264 (1980).

107. Bradley CV, Williams DH, Hanley MR. Peptide sequencing using the combination of Edman degradation, carboxypeptidase digestion and Fast Atom Bombardment mass spectrometry. *Biochemical and Biophysical Research Communications* **104**, 1223-1230 (1982).

108. Steen H, Mann M. The abc's (and xyz's) of peptide sequencing. *Nature Reviews Molecular Cell Biology* **5**, 699-711 (2004).

109. Yates Iii JR. A century of mass spectrometry: from atoms to proteomes. *Nature Methods* **8**, 633-637 (2011).

110. Aebersold R, Mann M. Mass-spectrometric exploration of proteome structure and function. *Nature* **537**, 347-355 (2016).

111. Walther TC, Mann M. Mass spectrometry–based proteomics in cell biology. *Journal of Cell Biology* **190**, 491-500 (2010).

112. Chait BT. Mass Spectrometry: Bottom-Up or Top-Down? *Science* **314**, 65-66 (2006).

113. Domon B, Aebersold R. Options and considerations when selecting a quantitative proteomics strategy. *Nature Biotechnology* **28**, 710-721 (2010).

114. Anderson NL, Anderson NG. The Human Plasma Proteome: History, Character, and Diagnostic Prospects *. *Molecular & Cellular Proteomics* **1**, 845-867 (2002).

115. Zubarev RA. The challenge of the proteome dynamic range and its implications for in-depth proteomics. *PROTEOMICS* **13**, 723-726 (2013).

116. Huang B*, et al.* Counting Low-Copy Number Proteins in a Single Cell. *Science* **315**, 81-84 (2007).

117. Pagel O, Loroch S, Sickmann A, Zahedi RP. Current strategies and findings in clinically relevant post-translational modification-specific proteomics. *Expert Review of Proteomics* **12**, 235-253 (2015).

118. Hu Z-L, Huo M-Z, Ying Y-L, Long Y-T. Biological Nanopore Approach for Single-Molecule Protein Sequencing. *Angewandte Chemie International Edition* **60**, 14738-14749 (2021).

119. Nivala J, Marks DB, Akeson M. Unfoldase-mediated protein translocation through an α-hemolysin nanopore. *Nature Biotechnology* **31**, 247-250 (2013).

120. Brinkerhoff H, Kang ASW, Liu J, Aksimentiev A, Dekker C. Multiple rereads of single proteins at single–amino acid resolution using nanopores. *Science* **374**, 1509-1513 (2021).

121. Yu L*, et al.* Unidirectional single-file transport of full-length proteins through a nanopore. *Nature Biotechnology* **41**, 1130-1139 (2023).

122. Martin-Baniandres P*, et al.* Enzyme-less nanopore detection of post-translational modifications within long polypeptides. *Nature Nanotechnology*, (2023).

123. Alfaro JA*, et al.* The emerging landscape of single-molecule protein sequencing technologies. *Nature Methods* **18**, 604-617 (2021).

124. Wang X*, et al.* Nanopore Detection Using Supercharged Polypeptide Molecular Carriers. *Journal of the American Chemical Society* **145**, 6371-6382 (2023).

125. Yan S*, et al.* Single Molecule Ratcheting Motion of Peptides in a Mycobacterium smegmatis Porin A (MspA) Nanopore. *Nano Letters* **21**, 6703-6710 (2021).

126. Afshar Bakshloo M*, et al.* Nanopore-Based Protein Identification. *Journal of the American Chemical Society* **144**, 2716-2725 (2022).

127. Lucas FLR, Versloot RCA, Yakovlieva L, Walvoort MTC, Maglia G. Protein identification by nanopore peptide profiling. *Nature Communications* **12**, 5795 (2021).

128. Zhang S*, et al.* Bottom-up fabrication of a proteasome–nanopore that unravels and processes single proteins. *Nature Chemistry* **13**, 1192-1199 (2021).

129. Wei R, Gatterdam V, Wieneke R, Tampé R, Rant U. Stochastic sensing of proteins with receptor-modified solid-state nanopores. *Nature Nanotechnology* **7**, 257-263 (2012).

130. Frutiger A, Tanno A, Hwu S, Tiefenauer RF, Vörös J, Nakatsuka N. Nonspecific Binding—Fundamental Concepts and Consequences for Biosensing Applications. *Chemical Reviews* **121**, 8095-8160 (2021).

131. Eggenberger OM, Ying C, Mayer M. Surface coatings for solid-state nanopores. *Nanoscale* **11**, 19636-19657 (2019).

132. Rotem D, Jayasinghe L, Salichou M, Bayley H. Protein Detection by Nanopores Equipped with Aptamers. *Journal of the American Chemical Society* **134**, 2781-2787 (2012).

133. Yusko EC*, et al.* Real-time shape approximation and fingerprinting of single proteins using a nanopore. *Nature Nanotechnology* **12**, 360-367 (2017).

134. Bell NAW, Keyser UF. Specific Protein Detection Using Designed DNA Carriers and Nanopores. *Journal of the American Chemical Society* **137**, 2035-2041 (2015).

135. Sze JYY, Ivanov AP, Cass AEG, Edel JB. Single molecule multiplexed nanopore protein screening in human serum using aptamer modified DNA carriers. *Nature Communications* **8**, 1552 (2017).

136. Ren R*, et al.* Single-Molecule Binding Assay Using Nanopores and Dimeric NP Conjugates. *Advanced Materials* **33**, 2103067 (2021).

137. Bell NAW, Keyser UF. Digitally encoded DNA nanostructures for multiplexed, single-molecule protein sensing with nanopores. *Nature Nanotechnology* **11**, 645-651 (2016).

138. Yang W*, et al.* Detection of CRISPR-dCas9 on DNA with Solid-State Nanopores. *Nano Letters* **18**, 6469-6474 (2018).

139. Weckman NE*, et al.* Multiplexed DNA Identification Using Site Specific dCas9 Barcodes and Nanopore Sensing. *ACS Sensors* **4**, 2065-2072 (2019).

140. Chen K, Jou I, Ermann N, Muthukumar M, Keyser UF, Bell NAW. Dynamics of driven polymer transport through a nanopore. *Nature Physics* **17**, 1043-1049 (2021).

141. Seeman NC, Sleiman HF. DNA nanotechnology. *Nature Reviews Materials* **3**, 17068 (2017).

142. Li S*, et al.* Dual-Mode Ultrasensitive Quantification of MicroRNA in Living Cells by Chiroplasmonic Nanopyramids Self-Assembled from Gold and Upconversion Nanoparticles. *Journal of the American Chemical Society* **138**, 306-312 (2016).

143. Nath N, Chilkoti A. Label-Free Biosensing by Surface Plasmon Resonance of Nanoparticles on Glass: Optimization of Nanoparticle Size. *Analytical Chemistry* **76**, 5370-5378 (2004).

144. Jana NR, Earhart C, Ying JY. Synthesis of Water-Soluble and Functionalized Nanoparticles by Silica Coating. *Chemistry of Materials* **19**, 5074-5082 (2007).

145. Hall AR, Scott A, Rotem D, Mehta KK, Bayley H, Dekker C. Hybrid pore formation by directed insertion of α-haemolysin into solid-state nanopores. *Nature Nanotechnology* **5**, 874-877 (2010).

146. Engst CR, Ablay M, Divitini G, Ducati C, Liedl T, Keyser UF. DNA Origami Nanopores. *Nano Letters* **12**, 512-517 (2012).

147. Cressiot B, Greive SJ, Mojtabavi M, Antson AA, Wanunu M. Thermostable virus portal proteins as reprogrammable adapters for solid-state nanopore sensors. *Nature Communications* **9**, 4652 (2018).

148. Mojtabavi M, Greive SJ, Antson AA, Wanunu M. High-Voltage Biomolecular Sensing Using a Bacteriophage Portal Protein Covalently Immobilized within a Solid-State Nanopore. *Journal of the American Chemical Society* **144**, 22540-22548 (2022).

149. Fried JP, Wu Y, Tilley RD, Gooding JJ. Optical Nanopore Sensors for Quantitative Analysis. *Nano Letters* **22**, 869-880 (2022).

150. Cai S, Sze JYY, Ivanov AP, Edel JB. Small molecule electro-optical binding assay using nanopores. *Nature Communications* **10**, 1797 (2019).

151. Belkin M, Chao S-H, Jonsson MP, Dekker C, Aksimentiev A. Plasmonic Nanopores for Trapping, Controlling Displacement, and Sequencing of DNA. *ACS Nano* **9**, 10598-10611 (2015).

152. Cai S*, et al.* Single-molecule amplification-free multiplexed detection of circulating microRNA cancer biomarkers from serum. *Nature Communications* **12**, 3515 (2021).

153. Pitchford WH*, et al.* Synchronized Optical and Electronic Detection of Biomolecules Using a Low Noise Nanopore Platform. *ACS Nano* **9**, 1740-1748 (2015).

154. Zhou J, Lan Q, Li W, Ji L-N, Wang K, Xia X-H. Single Molecule Protein Segments Sequencing by a Plasmonic Nanopore. *Nano Letters* **23**, 2800-2807 (2023).

155. Aramesh M*, et al.* Localized detection of ions and biomolecules with a force-controlled scanning nanopore microscope. *Nature Nanotechnology* **14**, 791-798 (2019).

156. Yoshihara R, Nomi S, Shoji K. Nanopore Probes Using Hydrogel-Filled Nanopipettes as Sensors for Chemical Imaging. *ACS Applied Nano Materials* **5**, 15808-15816 (2022).

157. Yu L*, et al.* Long-Lived Gold Single-Atom Junctions Formed by a Flexible Probe for Scanning Tunneling Microscopy Applications. *ACS Applied Nano Materials* **3**, 3410-3416 (2020).

158. Schlotter T*, et al.* Force-Controlled Formation of Dynamic Nanopores for Single-Biomolecule Sensing and Single-Cell Secretomics. *ACS Nano* **14**, 12993-13003 (2020).

159. Ren R*, et al.* Nanopore extended field-effect transistor for selective single-molecule biosensing. *Nature Communications* **8**, 586 (2017).

160. Xie P, Xiong Q, Fang Y, Qing Q, Lieber CM. Local electrical potential detection of DNA by nanowire–nanopore sensors. *Nature Nanotechnology* **7**, 119-125 (2012).

161. Traversi F*, et al.* Detecting the translocation of DNA through a nanopore using graphene nanoribbons. *Nature Nanotechnology* **8**, 939-945 (2013).

162. Heerema SJ, Vicarelli L, Pud S, Schouten RN, Zandbergen HW, Dekker C. Probing DNA Translocations with Inplane Current Signals in a Graphene Nanoribbon with a Nanopore. *ACS Nano* **12**, 2623-2633 (2018).

163. Xue L*, et al.* Gated Single-Molecule Transport in Double-Barreled Nanopores. *ACS Applied Materials & Interfaces* **10**, 38621-38629 (2018).

164. Panday N, Qian G, Wang X, Chang S, Pandey P, He J. Simultaneous Ionic Current and Potential Detection of Nanoparticles by a Multifunctional Nanopipette. *ACS Nano* **10**, 11237-11248 (2016).

165. Puster M*, et al.* Cross-Talk Between Ionic and Nanoribbon Current Signals in Graphene Nanoribbon-Nanopore Sensors for Single-Molecule Detection. *Small* **11**, 6309-6316 (2015).

166. Ivanov AP, Freedman KJ, Kim MJ, Albrecht T, Edel JB. High Precision Fabrication and Positioning of Nanoelectrodes in a Nanopore. *ACS Nano* **8**, 1940-1948 (2014).

167. Ivanov AP*, et al.* DNA Tunneling Detector Embedded in a Nanopore. *Nano Letters* **11**, 279-285 (2011).

168. Pang P*, et al.* Fixed-Gap Tunnel Junction for Reading DNA Nucleotides. *ACS Nano* **8**, 11994-12003 (2014).

169. Lindsay S. The promises and challenges of solid-state sequencing. *Nature Nanotechnology* **11**, 109-111 (2016).

170. Di Ventra M, Taniguchi M. Decoding DNA, RNA and peptides with quantum tunnelling. *Nature Nanotechnology* **11**, 117-126 (2016).

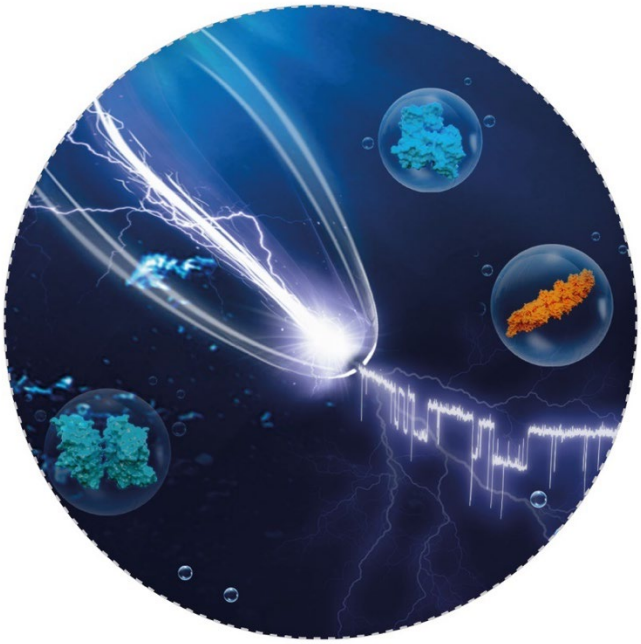
171. Zhao Y*, et al.* Single-molecule spectroscopy of amino acids and peptides by recognition tunnelling. *Nature Nanotechnology* **9**, 466-473 (2014).

172. Ohshiro T, Tsutsui M, Yokota K, Furuhashi M, Taniguchi M, Kawai T. Detection of post-translational modifications in single peptides using electron tunnelling currents. *Nature Nanotechnology* **9**, 835-840 (2014).

173. Tang L*, et al.* Measuring conductance switching in single proteins using quantum tunneling. *Science Advances* **8**, eabm8149.

CHAPTER 2

Methodology



Synopsis

This chapter provides an overview of the materials, instruments, methods, and data analysis techniques used in the experiments conducted for this thesis. It includes the fabrication process of the nanopipettes, along with their characterisation using microscopy and conductance measurements. The setup for ionic current measurements is also introduced, and the process of recording and analysing translocation events is explained. Overall, the chapter serves as a comprehensive guide to the experimental procedures employed in the thesis, laying the foundation for the results and findings in the subsequent chapters.

2.1 Nanopore fabrication and characterisation

2.1.1 Nanopore fabrication

The nanopipettes used in the experiments were fabricated from single-barrel quartz capillaries, specifically the GQF100-50-7.5 model from World Precision Instruments, UK. These capillaries have an outer diameter (O.D.) of 1.0 mm, an inner diameter (I.D.) of 0.5 mm, and a length of 75 mm. The capillaries contain filaments, which aid in the capillary effect, making it easier to fill the barrel with electrolytes. Before conducting nanopore measurements, all capillaries were subjected to a cleaning process using a plasma cleaner (Harrick Plasma). The plasma cleaner utilises ionised gas to remove most of the contaminants present on the surface of the quartz capillaries. This cleaning step is crucial to ensure the cleanliness and reliability of the nanopipettes for subsequent experiments.

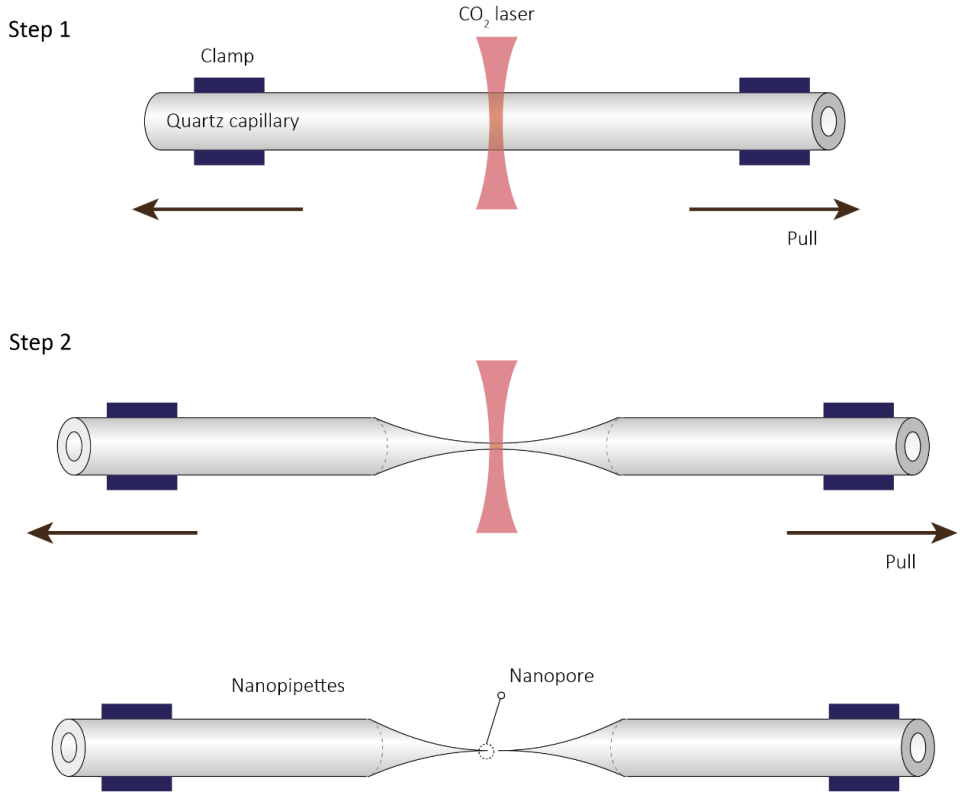


Figure 2.1 Fabrication of single-barrel nanopipettes. Single-barrel quartz nanopipettes are fabricated using a laser-assisted puller following a two-line protocol.

After plasma cleaning, the single-barrel capillaries were loaded into a laser-based pipette puller for the fabrication of the nanopipettes. The protocol employed for pulling the single-barrel capillaries involved a two-line process, referred to as Protocol 1 and Protocol 2, as outlined in Table 2.1. In the first step of the pulling process (Line 1), the capillary was gently heated and pulled, resulting in the formation of an hourglass shape. This initial pulling step prepared the capillary for further refinement in the second step. In the second step (Line 2), the narrowest part of the hourglass-shaped capillary was further heated using the laser, which resulted in the formation of two identical nanopores after a strong pulling. The laser-induced heating allowed precise control over the size and shape of the nanopores, ensuring consistency and reproducibility in the fabrication process. Figure 2.1 provides a visual representation of this step, showing the formation of two identical nanopores. By pulling a single-barrel quartz capillary using this two-line protocol, a pair of single-barrel nanopipettes could be generated. These nanopipettes were then ready for further characterisation and use in the subsequent experiments.

The choice of nanopore size and shape is a crucial consideration in nanopore-based experiments, as it directly influences sensitivity, spatial resolution, and overall experimental outcomes. Tailoring nanopore dimensions to specific research questions and analyte characteristics is essential for optimising experimental results. In Chapter 3 of the thesis, Protocol 1 was employed to create larger nanopores, which proved suitable for studying protein aggregation. Larger pores minimise clogging issues and enable real-time observation of protein growth during aggregation, accommodating the larger protein structures involved in this complex process. On the other hand, Chapters 4 and 5 utilised Protocol 2 to generate smaller nanopores. The smaller pore size was necessary for achieving higher spatial resolution in single-molecule studies, including the detailed analysis of individual molecular substructures. Smaller nanopores typically offer improved spatial resolution but require careful experimental optimisation to ensure reliable results.

Table 2.1 Parameters for the pulling protocol of nanopipette fabrication.

	Line	HEAT	FIL	VEL	DEL	PUL	Expected pore size	Pulling time
Protocol 1	Line 1	775	4	30	170	80	25 nm	6.0 s
	Line 2	825	3	20	145	180		
Protocol 2	Line 1	825	4	30	130	80	12 nm	5.5 s
	Line 2	850	3	20	127	185		

It should be noted that these parameters are instrument and environment specific.

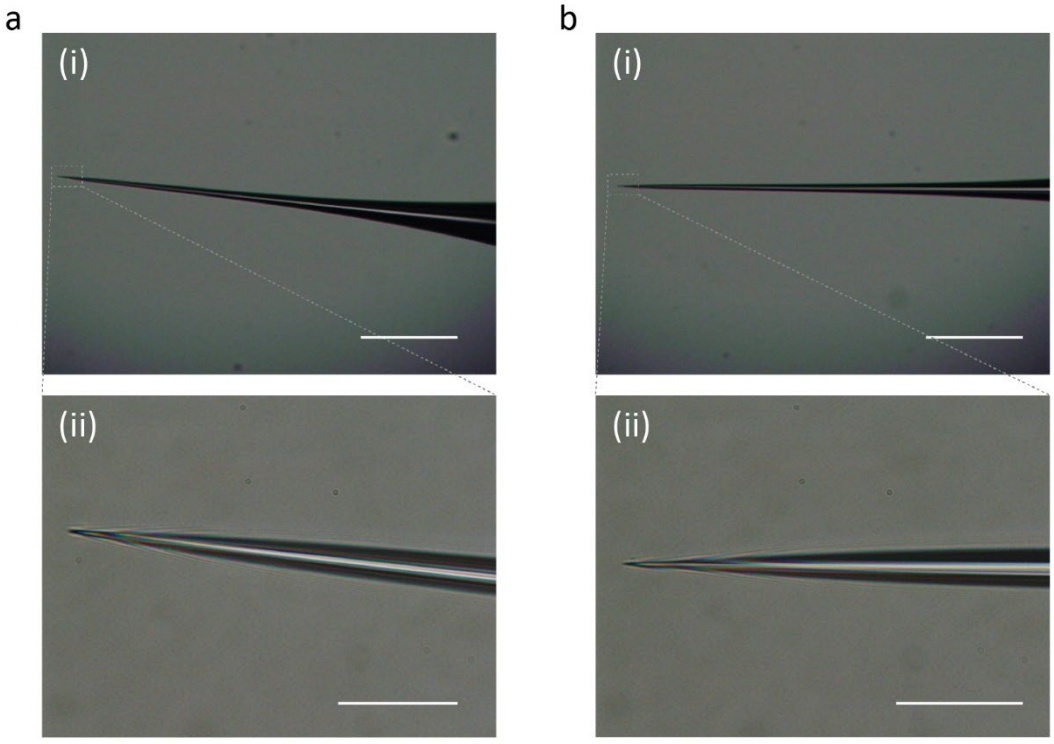


Figure 2.2 Optical imaging of single-barrel nanopipettes. Single-barrel quartz nanopipettes fabricated after a two-line laser pulling with (a) Protocol 1 and (b) Protocol 2. Scale bar: (i) 200 µm; (ii) 20 µm.

2.1.2 Nanopore characterisation by microscopes

Following the fabrication process, the nanopipettes were promptly examined using an optical microscope (Olympus BX51, Japan) to verify their quality. To facilitate this inspection, a custom-made holder was used to place the nanopipettes horizontally on the glass slide. It was crucial to ensure that none of the objective lenses came into contact with the tip area during this examination. The images of the nanopipettes were obtained from the microscope software (Stream Smart), aiding in the assessment of their structure for subsequent experiments (Figure 2.2). Proper microscope examination was an essential step in confirming the quality and suitability of nanopipettes for use in the experiments.

The exact geometry and size of the fabricated nanopipettes were characterised using a high-resolution scanning electron microscope (SEM) (Zeiss Gemini Sigma300, Germany). To enhance their conductivity, a 5 nm gold layer was applied to the nanopipettes using a sputtering coater (Quorum Technologies Ltd). During the SEM imaging, the nanopipettes were securely held in place on the sample stage using conductive carbon tape. An example of the SEM image of the nanopipette fabricated using Protocol 2 is depicted in Figure 2.3, providing a visual representation of the structure and dimensions of the nanopipette. This characterisation step ensured the accuracy and reproducibility of the nanopipette fabrication, allowing us to confidently proceed with subsequent experiments knowing the precise properties of the nanopipettes.

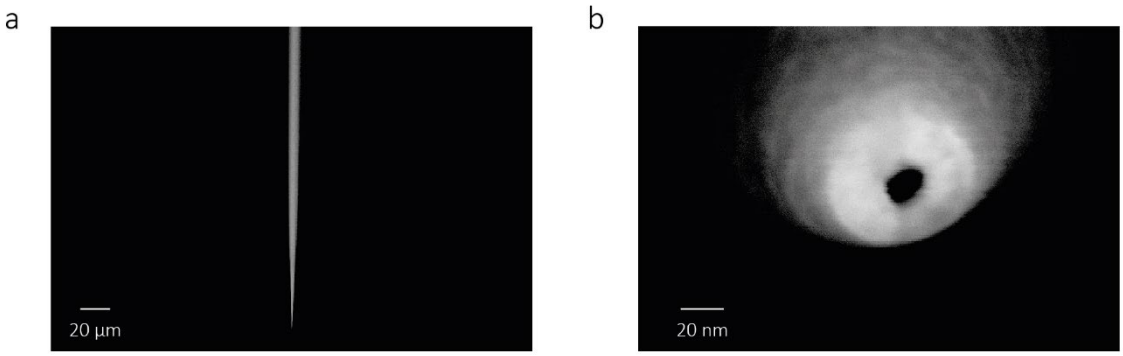


Figure 2.3 SEM imaging of single-barrel nanopipettes. A single-barrel quartz nanopipette fabricated using Protocol 2 was shown with a side view (a) (scale bar: 20 µm) and a top view (b) (scale bar: 20 nm).

2.1.3 Nanopore characterisation by conductance

After the fabrication of the nanopipettes, a fast and straightforward method to characterise the nanopore is by measuring its conductance, which is closely related to the geometry and size of the pore, as discussed earlier. The conductance of the nanopore can be easily determined by plotting the current-voltage (I-V) curve, as described by **Equation 2.1**:

$$G = \frac{1}{R} = \frac{I}{V} \quad (2.1)$$

Where:

G represents the conductance.

R is the resistance of the nanopore.

V denotes the applied voltage, and I corresponds to the ionic current.

This conductance measurement serves as a valuable quality control step to ensure that the fabricated nanopipettes meet the desired specifications for subsequent experiments.

The I-V characterisation of the nanopipettes was performed using an AxoPatch 200B patch-clamp amplifier (Molecular Devices, US) and a 1440A digitizer (Molecular Devices, US). To

measure the ionic current under each applied voltage, a specific protocol, as shown in **Figure 2.4a**, was followed. By selecting the stable current point at each bias voltage, I-V curves were generated as depicted in **Figure 2.4b**.

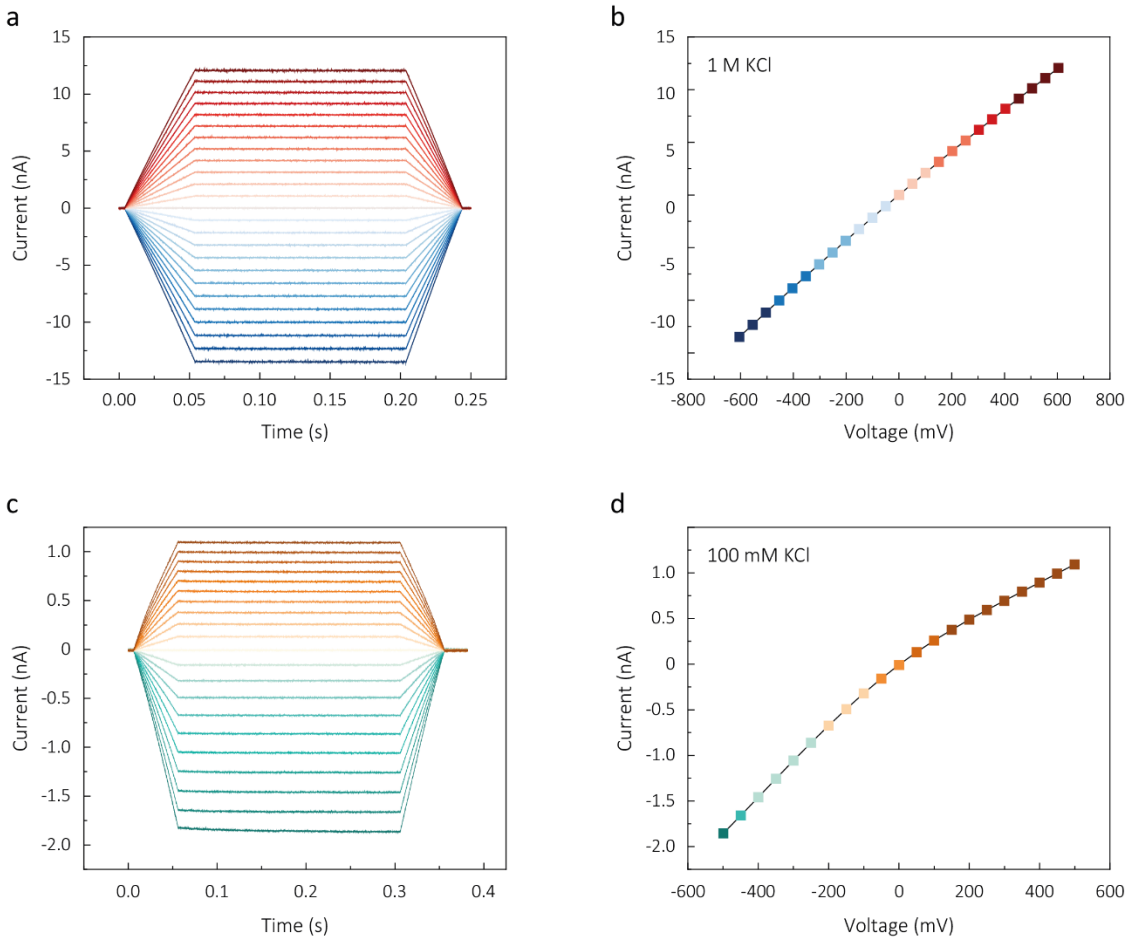


Figure 2.4 I-V characterisation of a nanopipette. I-t measurement of a typical nanopipette under the bias from -600 mV to 600 mV in (a) 1 M KCl Tris-EDTA buffer and (b) 100 mM KCl Tris-EDTA buffer. The I-V curve was obtained from the steady current at each voltage. (c) and (d) I-V curves of the nanopipette corresponding to (a) and (b), respectively, which can be used to calculate the conductance and the ionic current rectification of the nanopore.

2.1.4 Calculation of the diameter of nanopores

In this thesis, the resistive properties of the nanopipettes were approximated by considering them as truncated hollow cones. The resistance (R) of the nanopipette can be determined based on its inner cone angle (θ) and aperture radius (r) using the following **Equation 2.2**:[1]

$$R = \frac{1}{\kappa\pi r \tan\theta} + R_{\text{access}} \approx \frac{1}{\kappa\pi r \tan\theta} + \frac{1}{4\kappa r} \quad (2.2)$$

Where:

κ is the solution conductivity.

R_{access} represents the access resistance.

To experimentally determine the nanopipette resistance, I-V characterisation was performed, for example, as shown in **Figure 2.4b**. Additionally, the semi-angle of the nanopipettes (θ) was directly measured from SEM images of their first 100 nm geometry, as depicted in **Figure 2.5**.

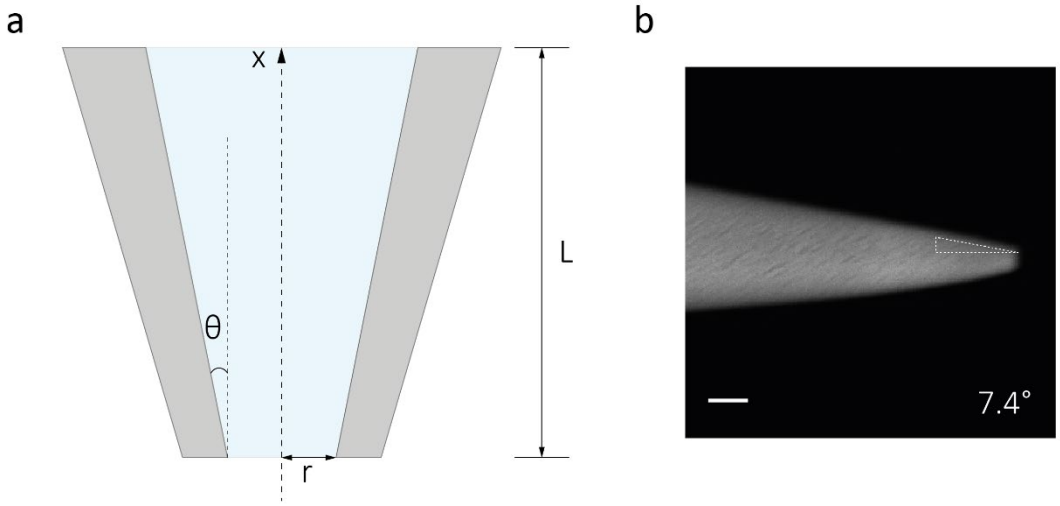


Figure 2.5 Schematic representation of a nanopipette geometry. (a) The geometric model was used for the calculation of the diameter and effective length of nanopipettes. (b) SEM images of the nanopipettes show the taper and geometry (scale bar: 100 nm). The outer half cone angle was directly measured from these side-view images. The inner semi-angle was assumed is equal to the outer semi-angle when calculating the nanopore size.

2.1.5 Calculation of the effective length of nanopores

Figure 2.5a shows the conical model for the calculation of the effective length H_{eff} of nanopipettes. Here, r represents the radius at the pipette opening, θ is the inner nanopipette half cone angle, L is the distance between the pipette opening and the reference electrode inserted into the pipette ($L \gg r$), and κ is the solution conductivity.

The total resistance (R_{int}) of the inner solution can be evaluated for the total length L using Equation 2.3:

$$R_{\text{int}} = \int_0^L \frac{1}{\kappa} \frac{\mathrm{d}x}{\pi(r+x\tan\theta)^2} = \frac{L}{\pi\kappa r(r+L\tan\theta)} \approx \frac{1}{\pi\kappa r\tan\theta} \quad (2.3)$$

The solution resistance within the length l from the orifice can also be evaluated using Equation 2.4 as:

$$R_{\text{l}} = \frac{l}{\pi\kappa r(r+l\tan\theta)} \quad (2.4)$$

or in the dimensionless form (Equation 2.5): [2]

$$\frac{R_{\text{l}}}{R_{\text{int}}} = \frac{\frac{l}{r}\tan\theta}{1+\frac{l}{r}\tan\theta} \quad (2.5)$$

A typical plot of $R_{\text{l}}/R_{\text{int}}$ versus normalised length (l/r) is shown in Figure 2.6. The effective length H_{eff} of a nanopipette can be defined as the length of its tapered shaft adjacent to the tip that contributes most (e.g., 90%) of the resistance. [3]

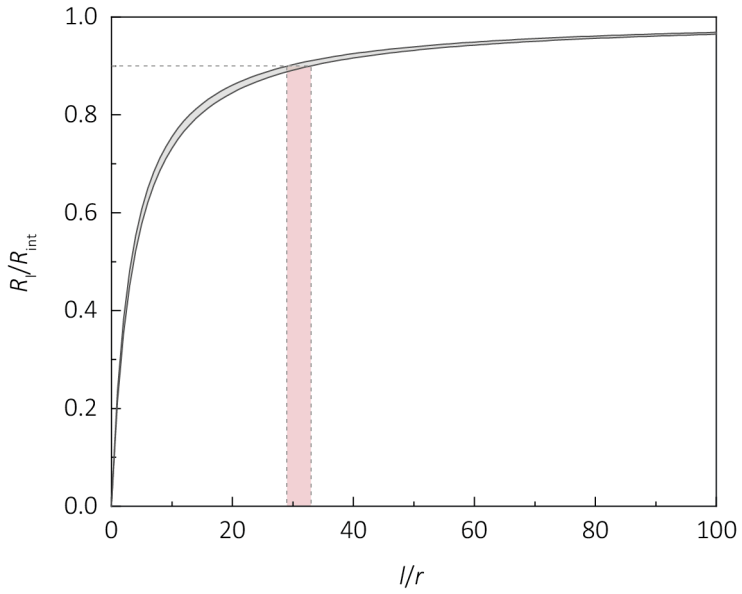


Figure 2.6 Calculation of the effective length of nanopipettes. Plots of R_l/R_{int} versus normalised length (l/r) showing the increase of resistance contribution with the distance for 20 different conical nanopipettes. The effective length was calculated at the region of 90% as marked in the plot.

2.2 Nanopore translocation of single molecules

2.2.1 Setup of nanopore experiments

Figure 2.7 shows a typical instrumental setup a nanopore experiment. In addition to ensuring the reproducible fabrication of nanopores, several key factors contribute to the success of a nanopore measurement experiment. These crucial steps include preparation of Ag/AgCl electrodes, preparation of sample and electrolyte solutions as well as shielding of electrical noise and stable circuit connection.

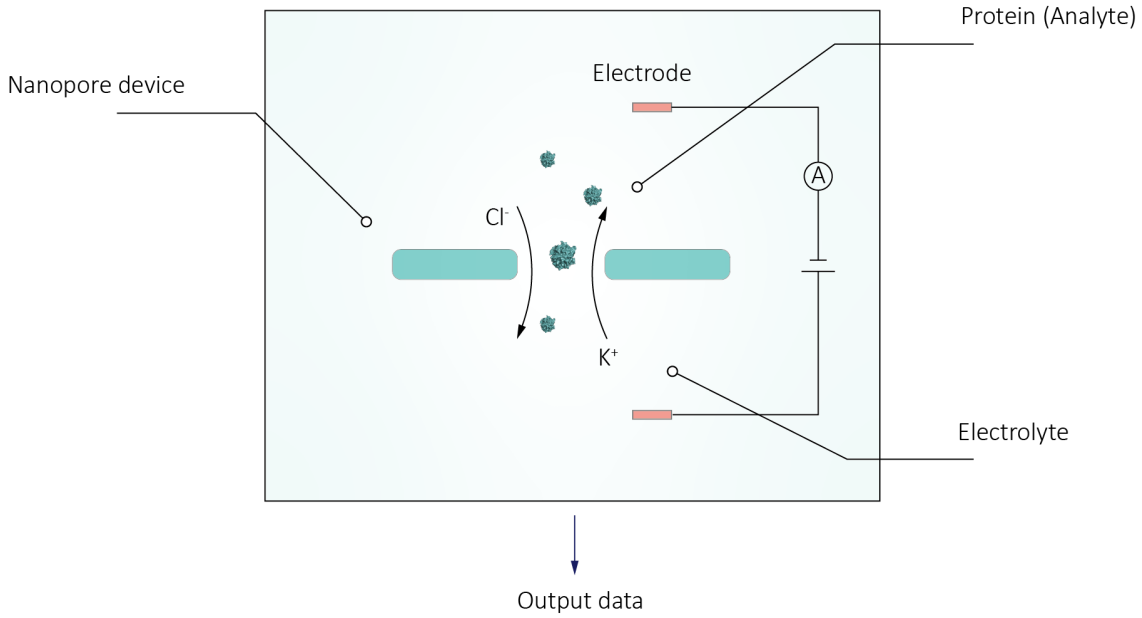


Figure 2.7 Experimental setup for nanopore measurements. In a typical nanopore experiment, the nanopore separates the electrolyte solution into two chambers. Two Ag/AgCl electrodes are used to connect the circuit. Analytes are introduced into one of the chambers and translocate through the pore under the application of voltage.

2.2.2 Preparation of Ag/AgCl electrodes

All the nanopore measurements in this thesis used Ag/AgCl electrodes to connect the circuit. These electrodes were selected due to their non-polarisable nature, characterised with negligible capacitive current at the electrode/electrolyte interface.[4] The fabrication process involved electrodeposition of silver in a concentrated KCl solution to form silver chloride on the surface of electrodes,[5] which is illustrated in **Figure 2.8.**

To be compatible with the nanopipette setup, 0.125 mm silver wires (Goodfellow Cambridge, UK) were used for preparation of Ag/AgCl electrodes and further nanopore experiments. Approximately 2 cm of Ag wires were immersed into a 1 M KCl solution, as depicted in **Figure 2.8a**. A 2 V bias was applied using a CHI 760C potentiostat (CH Instruments) to facilitate the

electrode preparation process. The quality of the electrodes was monitored through current-time curves (**Figure 2.8b**). The entire electrode preparation process typically lasted around 2 minutes. During the process, the formation of AgCl was evident through observable changes. The Ag wire lost its shine, and bubble formation occurred at the cathode. The reactions at both the anode and cathode can be explained using the following **Equation 2.6** and **Equation 2.7**:

$$\text{Anode: } \mathrm{Ag} + \mathrm{Cl}^- \rightarrow \mathrm{AgCl} + e^- \quad (2.6)$$

$$\text{Cathode: } 2\mathrm{H}^+ + 2e^- \rightarrow \mathrm{H}_2 \quad (2.7)$$

After the electrodeposition process, the generated Ag/AgCl electrodes were thoroughly flushed with deionised (DI) water to remove any residual salt and impurities. This step ensures that the electrodes are free from contaminants, providing a clean surface for subsequent measurements. In all the nanopore experiments, the Ag/AgCl electrodes were prepared freshly before ionic current recordings.

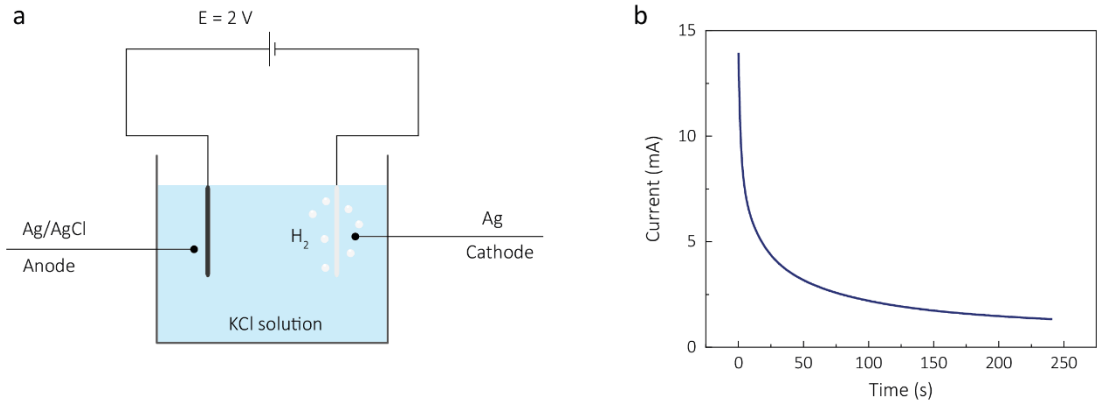


Figure 2.8 Fabrication of Ag/AgCl electrodes. (a) Experimental setup for preparation of Ag/AgCl electrodes. A potentiostatic technique was used for the electrodeposition. Concretely, a potential of +2 V was applied at the working electrode where AgCl grew on the surface of the Ag wire. The same Ag wire was used as the reference electrode where hydrogen bubbles were generated accordingly. (b) I-t curve showing an electrodeposition of AgCl in a 1 M KCl solution under a bias of 2 V.

2.2.3 Preparation of buffer solutions

In the experiments conducted in the thesis, most buffer solutions were composed of 10 mM Tris-HCl, 1 mM EDTA (Sigma-Aldrich), and KCl (Sigma-Aldrich) electrolyte. However, the pH and salt concentrations of these buffer solutions varied depending on the specific experiment, as detailed in **Table 2.2**. To ensure the highest quality of the buffer solutions, all buffers were freshly prepared using DI water. Subsequently, they were further purified using a 0.2-µm syringe filter (Life Sciences, UK) before being used in the translocation experiments. This additional purification step helps eliminate any potential particulate matter or contaminants that might interfere with the experiments, ensuring clean and consistent buffer solutions for further measurements. The pH and conductivity of the buffer solutions were then measured using a conductivity/pH meter (Mettler-Toledo, UK).

Table 2.2 Buffer solutions used in this thesis.

	Electrolyte	Buffer type	pH	Other compounds	Chapter	Experiment
1	1 M KCl	20 mM Tris-HCl	8.0	0.4 mM ADP, 0.1 mM $CaCl_2$, 0.01% DMSO, 10% glycerol	3	Nanopore translocation of actin proteins
2	1 M KCl	20 mM Tris-HCl	8.0	0.4 mM ADP, 0.1 mM $CaCl_2$, 0.01% DMSO 0.4 mM ATP, 10 mM EGTA, 10 mM $MgCl_2$, 10% glycerol	3	Real-time observation of actin polymerisation
3	100 mM KCl	10 mM Tris-HCl	8.0	1 mM EDTA	4	DNA translocation
4	1 M KCl	10 mM Tris-HCl	8.0	1 mM EDTA	5	Protein translocation
5	1 M KCl	10 mM Tris-HCl	8.0	1 mM EDTA, 10% PBS	5	Antibody binding assays

2.2.4 Ionic current measurements

Before performing nanopore translocation experiments, the electrolyte buffer solution was added into the nanopipette using a Microfil needle (MF34G, World Precision Instruments, UK). It is important to ensure that no air bubbles are present are the tip area. If bubbles exist, they can be removed by rubbing the pipette gently using a tweezer or by applying a negative air pressure using a syringe. One Ag/AgCl electrode was inserted into the nanopipette as the working electrode (*trans* chamber) and the other electrode was placed in the external bath as the reference electrode (*cis* chamber). The analytes were introduced into the *cis* chamber in **Chapter 3** and **Chapter 5**, whereas added into the *trans* chamber in **Chapter 4**. A high-bandwidth amplifier Chimera VC100 (Chimera Instruments, US) was used to record the ionic current with a sampling rate of 4.17 MHz (0.24 μs) by a MATLAB-based GUI (Chimera Instruments, US). The overall experimental configuration is shown in **Figure 2.9**.

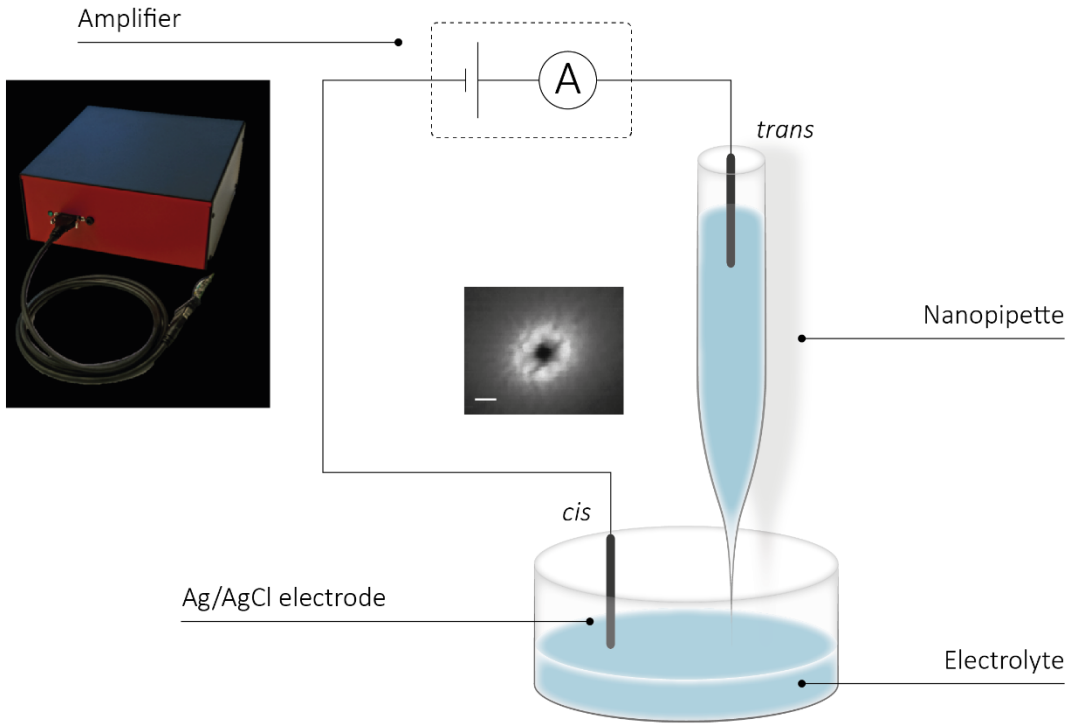


Figure 2.9 Schematic of nanopipette-based ionic current measurements. Two Ag/AgCl electrodes were filled into the nanopipette (*trans* chamber) and the external bath (*cis* chamber), respectively. Voltage was applied across these two electrodes to drive molecule translocating through the nanopore. Inset is the SEM image of a nanopore (scale bar: 20 nm). Ionic current was recorded using a high-bandwidth amplifier (Chimera VC100) as shown aside.

2.3 Data analysis

2.3.1 Single-molecule data processing

Single-molecule data analysis is distinct differs conventional data analysis methods. While conventional analysis focuses on ensembles of data points to identify trends and patterns, single-molecule data analysis aims to extract useful information from individual events. This approach allows us to gain a deeper understanding of molecular behaviours and better comprehend biological processes at the molecular level. In this thesis, the nanopore translocation data was processed using a custom-written MATLAB App (The Nanopore App), developed by Professor Joshua B. Edel from Imperial College London, UK. The typical workflow for data processing is illustrated in **Figure 2.10**. The example data used in this section involved the nanopore translocation of 100 pM lambda DNA (New England Biolab, UK) in 1 M KCl Tris-EDTA pH 8.0 buffer under a voltage of 500 mV. During the experiment, DNA samples were loaded into the external bath (*cis* chamber).



Figure 2.10 Workflow of single-molecule data processing. A diagram showing a typically procedure to analyse nanopore translocation data using The Nanopore App.

2.3.2 Extraction of individual events

This part involves 1) importing data, 2) resampling and applying a low-pass filter, 3) tracking the baseline, 4) applying a threshold to determine translocation events and 5) extracting individual events and features.

1) **Import data**

The Nanopore App supports several file formats for importing data, including .abf file format (Axon Digidata, Molecular Devices), .wcp file format (NI-DAQ, National Instruments), .log file format (Chimera VC100, Chimera Instruments) and .dat file format (eONE, Elements), etc. In **Figure 2.11**, raw data of lamdba DNA translocation recorded from Chimera VC100 (.log file format) was loaded in the Nanopore APP without being resampled and filtered.

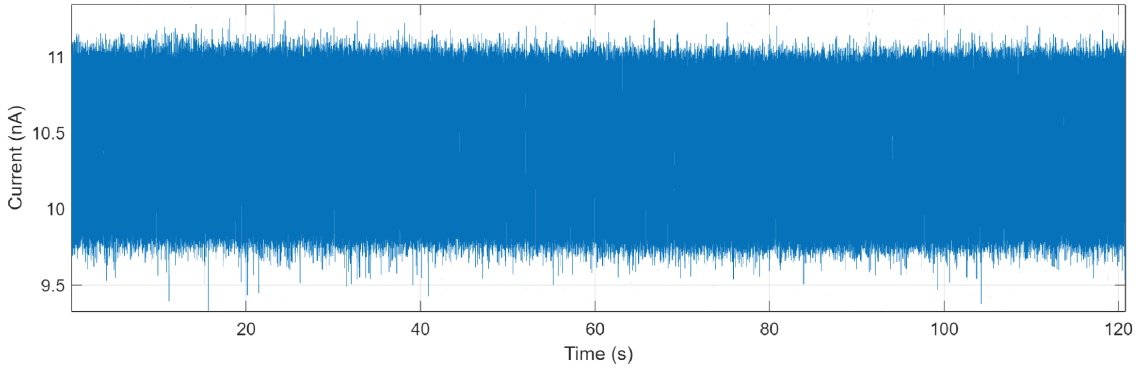


Figure 2.11 Data import. Raw data of lambda DNA translocation (100 pM in 1 M KCl Tris-EDTA pH 8.0 buffer) recorded by Chimera VC100 under a bias of +500 mV was imported into The Nanopore App.

2) **Resample and filter**

To ensure sufficient temporal resolution in the nanopore readouts, the data files were saved with their original sampling rate (e.g., 0.24 µs for Chimera VC100). However, for better signal-to-noise ratio (SNR) and further event extraction, the current-time traces can be resampled and low-pass filtered using The Nanopore App. The resampling process involves adjusting the time intervals between data points without altering the fundamental information. Furthermore, a low-pass filter (Bessel filter) is applied to the data, removing high-frequency noise components from the signal. The selection of the filter frequency is critical and depends on factors such as the translocation speed and SNR in the data. The objective is to achieve an

acceptable SNR in the event peaks without distorting the signal. In the example shown in **Figure 2.12**, a resampling time of 1 µs and a low-pass filter of 50 kHz were used.

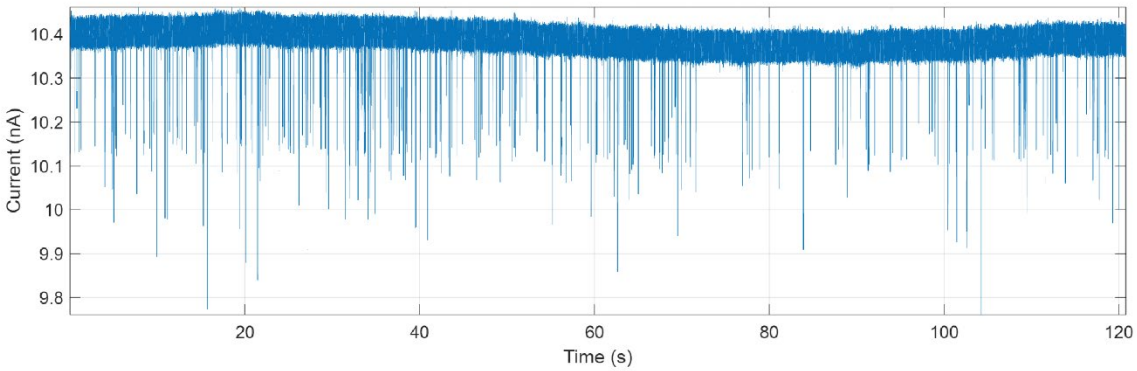


Figure 2.12 Data resampling and filtering. Imported data of lambda DNA translocation (100 pM in 1 M KCl Tris-EDTA pH 8.0 buffer) recorded by Chimera VC100 was resampled to 1 µs and low-pass filtered to 50 kHz in The Nanopore App.

3) Track baseline

Tracking the baseline is a key step in compensating for signal fluctuations, enabling an improved classification of translocation events. Prior to track the baseline, it is essential to ensure that the event peaks are upward. If the event peaks are initially downward, the data needs to be flipped to ensure correct baseline tracking and further analysis as shown in **Figure 2.13a**.

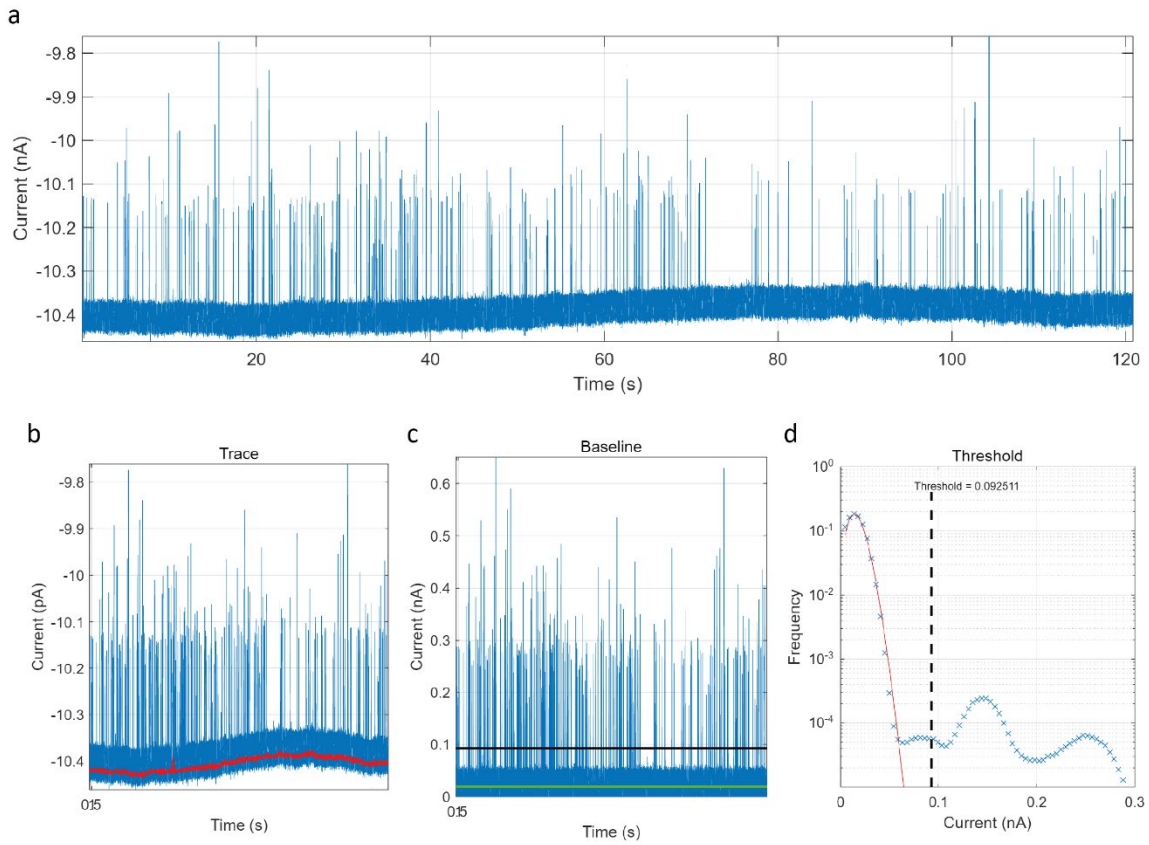


Figure 2.13 Baseline tracking and data thresholding. (a) Current-time trace after being flipped to ensure the events are upward. (b) The baseline was tracked using a polynomial fitting with a step of 200 data points. (c) A threshold of 9 standard deviations of the baseline distribution was applied to determine the translocation events. (d) Poisson probability distribution of current points, where the baseline level was fitted with red line and the threshold was shown with black dashed line.

The polynomial fitting was used to track the baseline by optimising three parameters: Step, Poly-1 and Poly-2. The Step parameter determines the number of data points used in each step of the polynomial fitting process. A larger Step value can result in smoother baseline tracking, but it may also lead to oversimplification of the data. On the other hand, a smaller Step value may capture more fluctuations but could also lead to excessive noise in the baseline tracking. Poly-1 and Poly-2 represent the degrees of the polynomial function used for fitting the data points. The choice of these degrees affects the flexibility of the polynomial curve in approximating the baseline. A higher degree polynomial allows for a more complex fit to the

data, but it may also be more susceptible to overfitting, capturing noise as part of the baseline. Figure 2.13b shows an example baseline tracking using Step: 200; Poly-1: 1e+7; Poly-2: 1e-2.

4) Apply threshold

In the thresholding process shown in Figure 2.13c, an upper threshold (black line) and a lower threshold (green line) were applied to distinguish event peaks from the baseline noise. The upper threshold acts as the SNR limit. Events that surpass this upper threshold are considered as translocation events of single molecules. The starting and ending points of these events are determined by the lower threshold. To determine the upper threshold, the baseline standard deviation (STD, σ) was calculated by fitting it with the Poisson probability distribution (red line in Figure 2.13d). A threshold set too high may result in the exclusion of events with low SNR, while a threshold set too low may lead to the inclusion of events that are merely noise-induced. By choosing an appropriate number of standard deviations, the true single-molecule events can be extracted for further analysis. For example, 9 standard deviations were used for determining the translocation events of lambda DNA in Figure 2.13d.

5) Find events

After applying the threshold, the next step involves determining the event boundaries. In Figure 2.14a and Figure 2.14b, if the full-width at half maximum (FWHM) option is selected, the event boundaries will be set to the half-maximum points of the peak. On the other hand, if FWHM is not selected, the event boundaries will be determined by the lower threshold from the previous step. To further refine the found events, a variety of thresholds, such as dwell time, peak current and charge, can be applied. These thresholds help to filter out noisy or irrelevant events, ensuring that only meaningful events are included in the analysis.

Each event was analysed using the CUSUM+ algorithm, [6, 7] an adaptation of the cumulative sums algorithm specifically designed for nanopore data, especially for long events with internal substructure, and this analysis resulted in a fitted event curve (indicated by the red dashed line in Figure 2.14c). The algorithm was employed to extract various features from the event,

including translocation time, peak amplitude, peak area, the number of subpeaks, and their fractional positions. These features are crucial because different molecules, such as DNA, proteins, and peptides, produce distinct disruptions in the current. These disruptions manifest as "steps" in the signal, corresponding to the size and charge of the specific molecules. The CUSUM+ algorithm is instrumental in identifying these distinctive "steps" in the signal. Once these significant changes or steps are detected, the continuous signal can be divided into discrete "events," with each event representing a particular molecule, whether it is DNA, protein, or a DNA/protein complex. The CUSUM+ algorithm is an abrupt change detection method that not only identifies these different levels or steps but also provides accurate fitting of the current blockages. This enables rapid identification of the various levels and subpeaks within each event. Consequently, event features such as translocation time, peak amplitude, peak area, and subpeak details can be extracted from the signal.

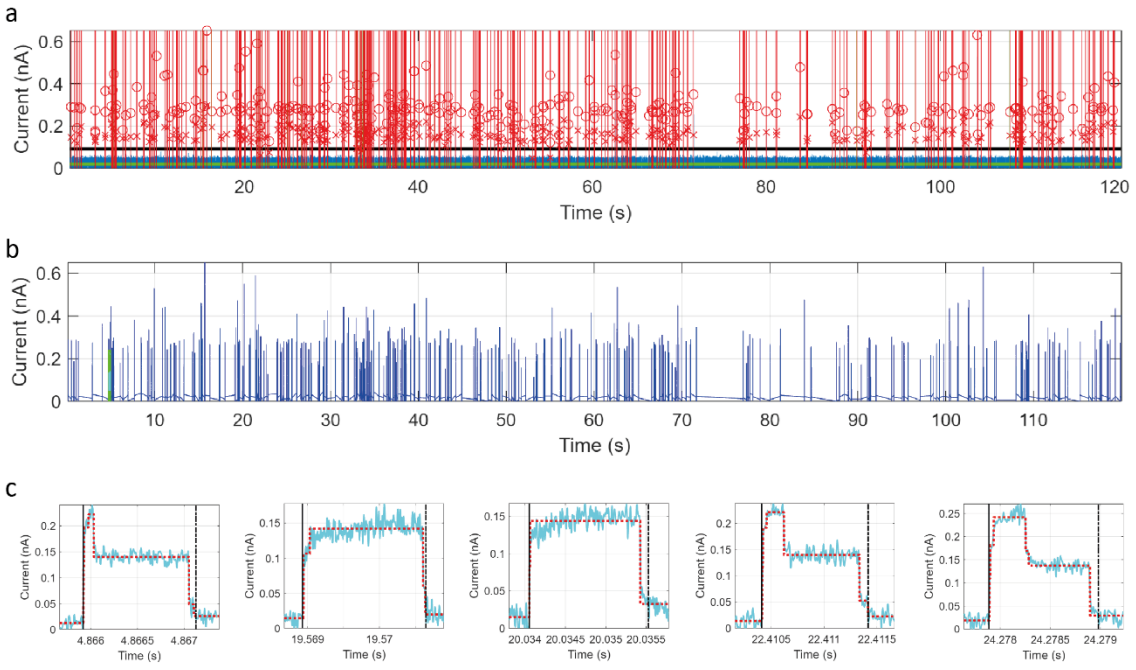


Figure 2.14 Single-molecule translocation event extraction. (a) Individual events were extracted after applying the lower and upper thresholds from the previous step. (b) Individual events were separated after removing the inter-event baseline. (c) Each event was fitted using the CUSUM+ algorithm to characterise its features.

2.3.3 Subpeak analysis

The subpeak analysis is a crucial step in nanopore data processing as it can reveal sub-molecular information of the detected analytes. For instance, in the case of double-stranded DNA (dsDNA), partial folding can result in a subpeak within the translocation event, as illustrated in Figure 2.15. More importantly, in nanopore sensing using molecular carriers, the presence and characteristics of subpeaks can be indicative of the successful binding of target proteins to the carriers. The Nanopore App automates the subpeak analysis of individual events based on the CUSUM+ fitting results from the previous step. It extracts subpeak dwell time, subpeak amplitude, and subpeak location as part of the output. To enhance the accuracy of subpeak analysis and eliminate false positives, appropriate thresholding can be applied to isolate expected events, as shown in Figure 2.15.

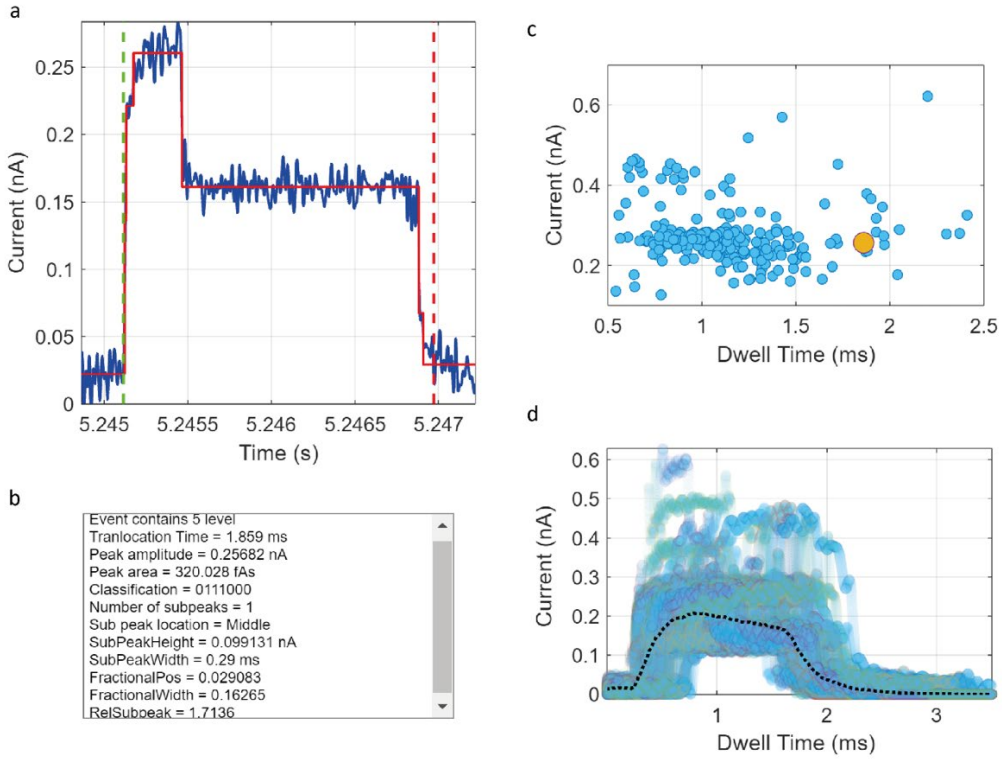


Figure 2.15 Subpeak analysis of translocation events. (a) Events with at least one subpeak were isolated in this section. (b) The Nanopore App can automate the subpeak features from the CUMSUM+ fitting. (c) Scatter plots of current vs. dwell time for the isolated events. (d) Aligned events with the normalised event width. Dashed line shows the average event shape.

2.3.4 Statistical analysis

In The Nanopore App, the features extracted from individual events, including subpeak information, can be easily exported directly from the app. Additionally, the app provides the functionality to plot the distribution (Gaussian) of dwell time, charge, and peak current, as demonstrated in **Figure 2.16a**. Alternatively, the app can also use a 1D drift-diffusion model[8, 9, 10, 11, 12] (Ling distribution, **Equation 2.8**) to fit the histogram of dwell time as follows:

$$P(t) = \frac{H_{\text{eff}}}{\sqrt{4\pi D t^3}} e^{-(H_{\text{eff}} - vt)^2/4Dt} \quad (2.8)$$

Where:

H_{eff} is the effective length of the nanopore.

D is the in-pore diffusion coefficient of the molecules.

v is the molecule drift velocity inside the pore.

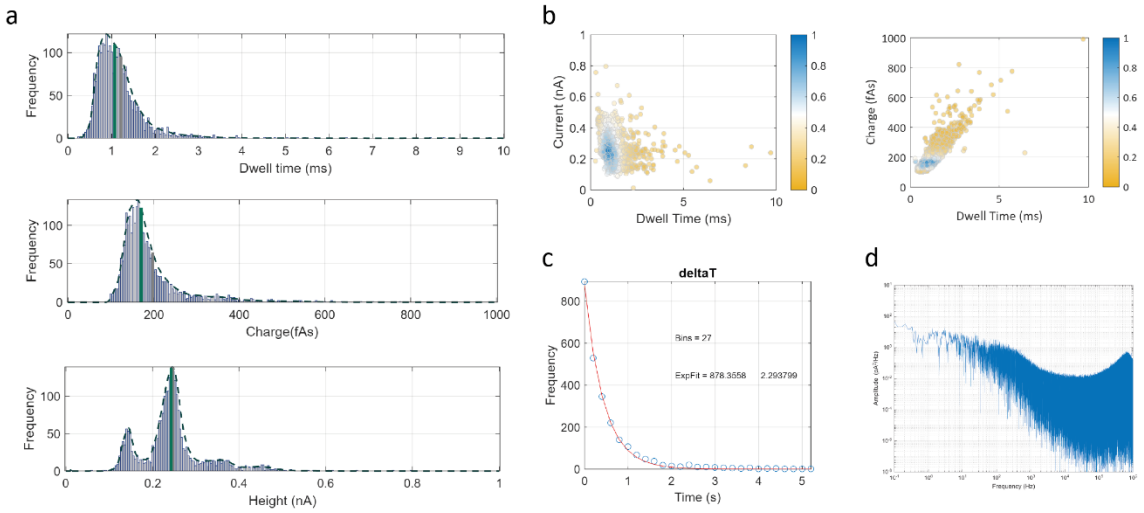


Figure 2.16 Statistical analysis of translocation events. (a) Histograms of dwell time, charge and peak current showing the molecular behaviours of lambda DNA during nanopore translocation. It should be noted that the histograms can be fitted using Gaussian distribution, while the distribution of dwell time can also be fitted by Ling distribution if needed. (b) Density scatter plots of peak current vs. dwell time and charge vs. dwell time. (c) The distribution of inter-event times fitted with an exponential decay curve. (d) The power spectral density (PSD) of the ionic current recordings.

Figure 2.16b shows density scatter plots that are useful for revealing various populations in the single-molecule statistical data. These plots help identify different groups or clusters of events with distinct characteristics or behaviours, indicative of the heterogeneity of the analytes.

The capture rate, which represents the frequency of translocation events, is an essential feature that describes the electrokinetic behaviour of molecules as they approach and translocate through the nanopore. At low analyte concentrations, the molecular capture of a nanopore follows an exponentially distributed random nature. [13] This means that the probability distribution of the inter-event times (Δt) between consecutive translocation events follows an exponential decay. A histogram of the inter-event times can be simply built and fitted to a single-parameter exponential decay (Figure 2.16c). The capture rate can be extracted from Equation 2.9: [14]

$$P_1(t) = re^{-rt} \quad (2.9)$$

Where:

$P_1(t)$ is the probability of finding one event in a given time interval t.

r represents the capture rate.

Alternatively, the capture rate can be simply extracted by counting the number of events that occur in a given time interval and dividing it by the length of the interval. However, this method assumes that the nanopore behaves consistently without encountering issues such as clogging or other disruptions. Therefore, the simplicity of this approach might be suitable only when the nanopore operates smoothly without complications.

Furthermore, assessing the noise level in nanopore experiments is essential for data reproducibility. The electrical noise can originate from various sources, including the nanopore itself and the circuit connected to the amplifier. Different types of noise contribute to the overall noise, which include 1) low-frequency ($\leq$ 100 Hz) $1/f$ noise and protonation noise; 2) shot noise and thermal current noise (~0.1–2 kHz); 3) high-frequency dielectric (~1–10 kHz);

4) capacitive (>10 kHz) noise. [15, 16] These noises have different frequencies where a power spectrum density (PSD) can be used to assess each of them, as shown in Figure 2.16d.

3.5 References

1. Perry D, Momotenko D, Lazenby RA, Kang M, Unwin PR. Characterization of Nanopipettes. *Analytical Chemistry* **88**, 5523-5530 (2016).
2. Wang Y, Kececi K, Mirkin MV, Mani V, Sardesai N, Rusling JF. Resistive-pulse measurements with nanopipettes: detection of Au nanoparticles and nanoparticle-bound anti-peanut IgY. *Chemical Science* **4**, 655-663 (2013).
3. Ren R*, et al.* Single-Molecule Binding Assay Using Nanopores and Dimeric NP Conjugates. *Advanced Materials* **33**, 2103067 (2021).
4. Wanunu M. Nanopores: A journey towards DNA sequencing. *Physics of Life Reviews* **9**, 125-158 (2012).
5. East GA, del Valle MA. Easy-to-Make Ag/AgCl Reference Electrode. *Journal of Chemical Education* **77**, 97 (2000).
6. Raillon C, Granjon P, Graf M, Steinbock LJ, Radenovic A. Fast and automatic processing of multi-level events in nanopore translocation experiments. *Nanoscale* **4**, 4916-4924 (2012).
7. Forstater JH*, et al.* MOSAIC: A Modular Single-Molecule Analysis Interface for Decoding Multistate Nanopore Data. *Analytical Chemistry* **88**, 11900-11907 (2016).
8. Talaga DS, Li J. Single-Molecule Protein Unfolding in Solid State Nanopores. *Journal of the American Chemical Society* **131**, 9287-9297 (2009).
9. Li J, Talaga DS. The distribution of DNA translocation times in solid-state nanopores. *Journal of Physics: Condensed Matter* **22**, 454129 (2010).
10. Ling DY, Ling XS. On the distribution of DNA translocation times in solid-state nanopores: an analysis using Schrödinger's first-passage-time theory. *Journal of Physics: Condensed Matter* **25**, 375102 (2013).
11. Larkin J, Henley RY, Muthukumar M, Jacob, Wanunu M. High-Bandwidth Protein Analysis Using Solid-State Nanopores. *Biophysical Journal* **106**, 696-704 (2014).

12. Waduge P*, et al.* Nanopore-Based Measurements of Protein Size, Fluctuations, and Conformational Changes. *ACS Nano* **11**, 5706-5716 (2017).

13. Charron M, Briggs K, King S, Waugh M, Tabard-Cossa V. Precise DNA Concentration Measurements with Nanopores by Controlled Counting. *Analytical Chemistry* **91**, 12228-12237 (2019).

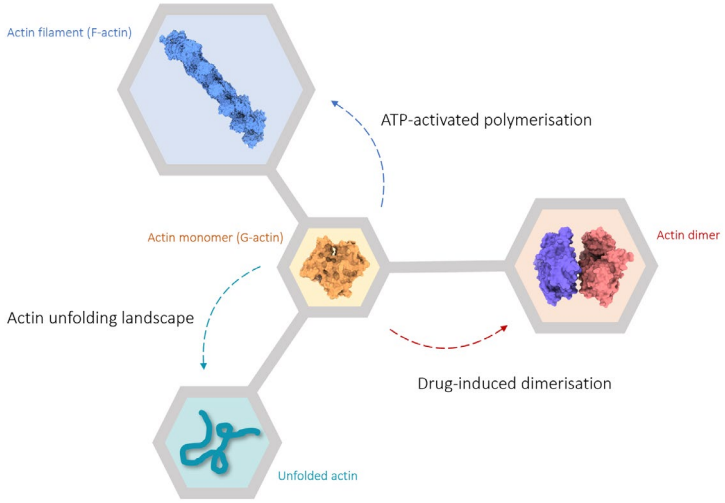
14. Meller A, Branton D. Single molecule measurements of DNA transport through a nanopore. *ELECTROPHORESIS* **23**, 2583-2591 (2002).

15. Smeets RMM, Keyser UF, Dekker NH, Dekker C. Noise in solid-state nanopores. *Proceedings of the National Academy of Sciences* **105**, 417-421 (2008).

16. Fragasso A, Schmid S, Dekker C. Comparing Current Noise in Biological and Solid-State Nanopores. *ACS Nano* **14**, 1338-1349 (2020).

CHAPTER 3

Single-molecule nanopore sensing of actin dynamics and drug binding



Synopsis

This chapter showcases label-free nanopore sensing of actin, a crucial protein in eukaryotic cells. Nanopores offer insights into the molecular state of actin without compromising its stability. Macromolecular forms including globular and filamentous states, as well as monomeric and dimeric states while bound to drugs were determined. Dynamic states, influenced by urea and voltage, revealed unfolding processes and transient actin oligomers. Real-time detection of filament growth and drug binding at the single-molecule level highlights the potential of nanopore sensing for understanding protein folding and drug discovery. Overcoming limitations, it becomes a powerful tool for studying actin and advancing drug development.

Part of this chapter was published as **Wang, X.**; Wilkinson, M. D.; Lin, X.; Ren, R.; Willison, K. R.; Ivanov, A. P.; Baum, J.; Edel, J. B. Single-Molecule Nanopore Sensing of Actin Dynamics and Drug Binding. ***Chem. Sci.*** 2020, 11, 970. In this work, the actin samples were obtained from Mark Wilkinson, Department of Life Sciences, Imperial College London, UK.

3.1 Introduction

Actin is an essential protein present in all eukaryotes, exhibiting high conservation and functioning as an ATPase. It plays a crucial role in numerous cellular processes, including the formation of eukaryotic cytoskeletal structures, cell division, and cell movement. [1] The significance of actin extends to human diseases, where rare point mutations in the actin molecule can lead to abnormal aggregation and conditions such as actin-accumulation myopathy. [2] There is a growing interest in exploring actin as a potential target for therapeutic intervention to combat various diseases. This includes targeting divergent pathogens that rely on their own actin dynamics for infectivity, such as the malaria parasite, [3] as well as pathogens that exploit host cell actin for infection, such as bacteria. [4] Within human cells, actin interacts with hundreds of binding partners, facilitating dynamic interplay between its monomeric G-actin and filamentous F-actin forms. [1] G-actin exists as a stable, globular monomer with intrinsic flexibility and ATPase activity. [5, 6, 7] Above a critical concentration, G-actin spontaneously assembles into filamentous F-actin. Understanding the dynamics of actin, its folding process, and its interactions with co-factors, including drugs, is of great interest. Advancements in technologies that can explore these actin dynamics hold significant potential for the discovery of therapeutics that target host cellular processes or pathogen infections.

To date, studying the protein dynamics and drug binding of native actin has presented a complex and challenging problem. While most proteins fold based on their amino acid sequence, with hydrophobic residues being buried to prevent aggregation and hydrophilic residues being exposed to the cellular cytoplasm, actin deviates from this canonical folding pathway. Instead, it relies on the species-specific chaperonin known as TCP-1 (CCT) complex. The CCT complex plays a crucial role in facilitating the folding of actin into its native, polymerisation-competent form by aiding in the addition of co-factors ATP and divalent metal ions. [8] Without proper folding, actin remains only partially functional. [9] Various methods, such as atomic force microscopy (AFM), [10] cryo-electron microscopy (cryo-EM), [7] crystallography, [11] and tomography, [12] have enhanced the understanding of actin in its G- and F- states. However, these non-temporal-resolved techniques offer only static information and have yet to reveal the intricate protein folding pathway and intermediate states of actin folding. Although

fluorescently labelled actin can provide valuable insights, achieved through the addition of fluorophores like N-(1-pyrene)iodoacetamide (pyrene) to the C-terminus, such chemical modifications alter the thermostability of actin monomers. [13] Consequently, studying polymerisation kinetics and free energy values in correlation with a native, unlabelled molecule becomes challenging due to the altered monomer thermostability. Limitations also persist in studying drug binding and its mechanisms. [14] For instance, pyrenylation of actin is a common method for investigating drug binding, but this fluorophore only labels a minority of actin molecules, providing a readout at the population level and masking potential changes in sub-population polymerisation kinetics. Moreover, this method provides limited information regarding how compounds specifically interact with different actin species. Traditional approaches to understanding drug inhibition or stimulation and their mechanisms have relied heavily on structural characterisation, [15, 16] which is time-consuming and, similar to other techniques, offers only a static image of a protein in a non-aqueous environment.

One promising approach to overcome the limitations mentioned above is the utilisation of single-molecule nanopore sensing. In recent years, nanopores have proven to be effective tools for label-free biosensing of fundamental biological components, such as nucleic acids[17] and proteins. [18, 19] This technique offers several advantages in studying actin and its dynamics. In a typical experiment, analytes are propelled through a nanopore *via* electrophoresis or electroosmosis, driven by an externally applied electric field. As the analyte translocates through the nanopore, it induces characteristic changes in the measured ionic current passing through the pore. These alterations in the ionic current provide useful insights into various molecular properties of the analyte, including size, charge, conformational states, and interactions with other biomolecules. [20] Both biological and solid-state nanopores have been successfully employed to investigate protein folding at the single-molecule level. These studies have revealed conformational changes and dynamics during protein unfolding, [21, 22, 23, 24] as well as macromolecular changes of proteins. [25, 26] Quartz nanopipettes, which fall under the category of solid-state nanopores, offer an additional advantage as they are relatively low-cost and straightforward to fabricate. This circumvents the technical challenges associated with using conventional and expensive solid-state nanopores or biological nanopores.

In this chapter, quartz nanopipettes are used as a platform to investigate the real-time dynamics of actin molecules in both their monomeric and polymerised states, as well as their interactions with actin-binding drugs. This approach allows us to distinguish between the two macromolecular forms of actin, G-actin and F-actin. Through this system, the unfolding dynamics of native actin can be observed using urea denaturation, by tracking thousands of single-molecule events. Furthermore, I demonstrate the capability to monitor the real-time growth of F-actin. Last, an essential aspect of this study is the ability to differentiate the binding mechanisms of two drugs, Latrunculin B and Swinholide A, both of which hinder filament formation but through different modes of action. The quartz nanopipette-based nanopores enable us to discern between these drug interactions. Meanwhile, I showcase the potential of this platform in drug discovery by measuring real-time drug binding at the single-molecule level. By calculating the observed rate constant and saturation concentration of Swinholide A dimer formation, understanding into its mechanism can be deduced. Based on my measurements, a positively cooperative actin-binding model is proposed for Swinholide A. The ability to conduct such studies in a label-free manner with single-molecule resolution underscores the potential of quartz nanopipettes for protein analysis. These findings not only shed light on the unfolding dynamics of complex biomolecules but also highlight the potential applications of this technology in molecular diagnostics and drug discovery.

3.2 Methods and materials

3.2.1 Fabrication of nanopipettes

Quartz capillaries (GQF100-50-7.5, World Precision Instruments, UK) with an outer diameter of 1.0 mm and an inner diameter of 0.5 mm with an inner filament were cleaned using the plasma cleaner and then pulled by a laser-based pipette puller (Sutter Instrument, P-2000). The nanopipettes used in all nanopore experiments were fabricated through a two-line protocol: (1) HEAT = 775, FIL = 4, VEL = 30, DEL = 170, PUL = 80; (2) HEAT = 825, FIL = 3, VEL = 20, DEL = 145, PUL = 180. It should be noted that these parameters are instrument specific and were optimised to yield nanopore openings of 25 ± 4 nm, as described in the reference. [27]

3.2.2 Preparation of actin samples

I specially acknowledge Mark Wilkinson for the preparation and purification of actin proteins. Chicken gizzard actin was purified from acetone powder using established methods. Acetone powder was suspended in 20 ml Calcium buffer G (CaBG: 2 mM Tris pH 8, 0.2 mM ATP, 0.5 mM DTT, 0.1 mM $CaCl_2$, 1 mM NaAzide) per gram of powder and stirred for 30 mins at 4°C. The suspension was centrifuged at 16 000 RPM for 30 mins at 4°C in a JA25.5 rotor. The supernatant was collected, and the pellet was resuspended in the initial volume of CaBG and stirred for another 30 mins at 4°C followed by centrifugation as before. The supernatants were combined and adjusted to 50 mM KCl and 2 mM $MgCl_2$ and stirred at 4°C for 1 hour to polymerise the actin. The solution was subsequently adjusted to 0.8 M KCl and stirred for a further 30 mins at 4°C before being centrifuged at 38000 RPM in an MLA 80 rotor (Beckman) for 2 hrs at 4°C to pellet the filaments. The supernatant was discarded, and the pellet was resuspended in 3-5 ml CaBG and homogenised using a 1 ml Tight Dounce Tissue Grinder (Wheaton) and dialysed into fresh CaBG overnight at 4°C. The suspension was removed from dialysis and passaged through a 26-gauge syringe 20-30 times to break down the filaments and returned to dialysis for a maximum of 3 days. The solution was centrifuged at 38000 RPM in an MLA 80 rotor (Beckman) for 2 hrs at 4°C to pellet contaminating filaments and aggregates, leaving monomeric actin in the supernatant. The supernatant was loaded onto an S200 16/600 (GE Healthcare) equilibrated with CaBG and fractions containing pure monomeric actin were analysed by SDS-PAGE, pooled and stored at 4°C for a maximum for 3 months. The sample was dialysed into fresh CaBG and centrifuged at 38000 RPM in an MLA 80 rotor (Beckman) for 2 hrs at 4°C to pellet any contaminating filaments immediately before conducting experiments.

Purified chicken actin was dialysed and diluted to 300 – 1000 nM into the nanopipette buffer (20 mM Tris pH 8, 1 M KCl, 0.4 mM ADP, 0.1 mM $CaCl_2$, 0.01% DMSO and 10 % glycerol). Actin for the urea unfolding experiments was dialysed into the nanopipette buffer supplemented with 1 – 6 M Urea. For comparison to the filament, F-actin was prepared as described.[28] Briefly, 2.5 µM G-actin was incubated 10X Mg-EGTA exchange buffer (ME) to make Mg-ATP-Actin, which was followed by the addition of the polymerisation buffer 10X KMEI (0.5 M KCl, 0.1 M imidazole, 0.01 M EGTA pH 8.0, 10 mM $MgCl_2$) before being incubated for 2 hrs at room

temperature. This was then added to the nanopipette tip using wide orifice pipette tips. For observing actin polymerisation, actin was dialysed into nanopipette buffer containing 0.4 mM ATP. The polymerisation was induced by adding 10 X KME buffer (0.5 M KCl, 10 mM EGTA pH 8.0, 10 mM $MgCl_2$). The preparation of the actin-LatB or actin-SwinA complex required incubation and equilibration with 10 µM LatB or 10 µM Swinholide A (dissolved in DMSO) for 30 mins before voltage application.

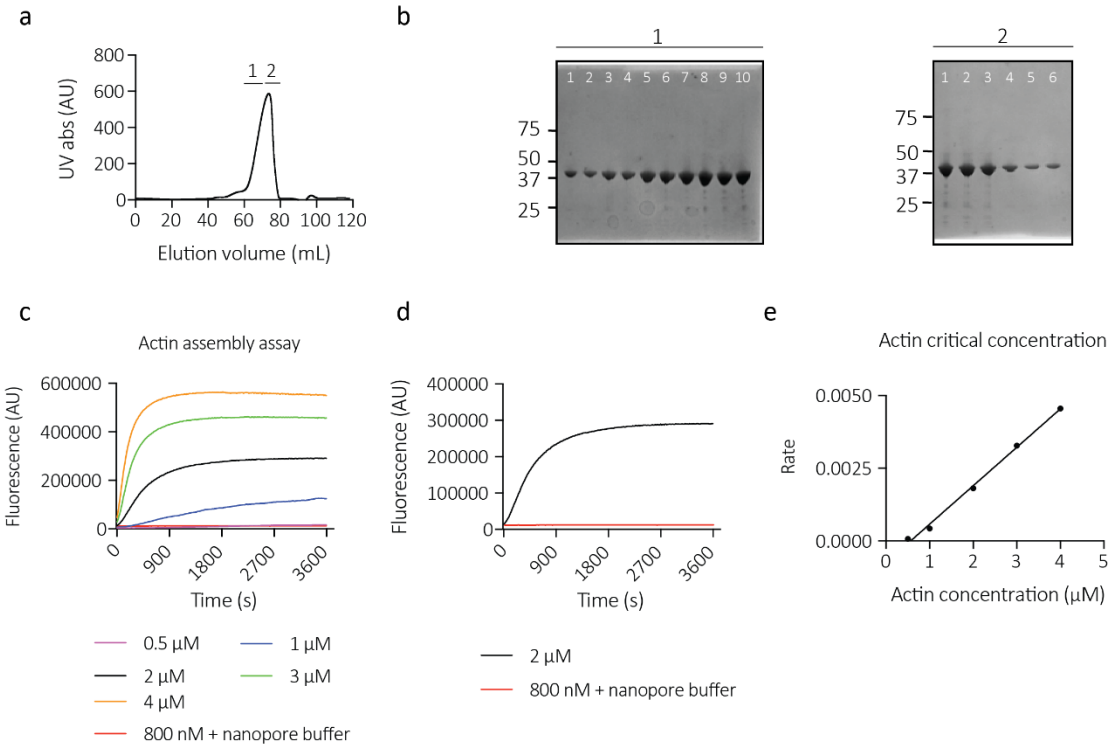


Figure 3.1 Purification and characterisation of actin and its activity. (a) A size exclusion chromatography profile of the purified actin. Monomeric actin eluted between elution fractions 60 mL and 80 mL. (b) SDS-PAGE analysis of the monomeric elution fractions. Gel 1 and 2 correspond to the elution fractions show in panel a, in which different columns represent different loading amounts. (c) A sample of the actin was labelled with pyrene and checked for activity using a pyrene fluorescence filamentation assay. Actin polymerised as normal under the presence of polymerisation enhancing factors (c and d) with a critical concentration of 0.6 µM. (e) actin did not form filaments in the nanopore buffer at the concentrations used in the nanopore experiments.

3.2.3 Nanopore measurements and data processing

Before performing translocation experiments, 1 M KCl buffer was added into the nanopipette using a Microfil needle (MF34G, World Precision Instruments, UK). Electrodes (Ag/AgCl) were inserted into the nanopipette (working electrode) and the external bath (reference/ground electrode), respectively. Voltages from 150 mV to 350 mV were applied, and the ionic current was recorded as a function of time by Chimera amplifier VC100 (Chimera Instruments, US) with a sampling rate of 4.17 MHz and a low-pass kHz digital Bessel filter of 50 kHz and analysed using custom-written MATLAB code by Joshua B. Edel unless otherwise stated. Power spectral density (PSD) plots for this low-noise configuration were analysed before each nanopore measurement. Protein fluxes (J_C) were extracted from a single-exponential decay fitting of the distribution of interval time between two successive translocation events (δt) as previously reported. [29] All data collected at different voltages was obtained from the same nanopipette and error bars represent one standard deviation of at least three independent experiments with different nanopipettes unless stated otherwise. Traces shown were collected at 1 MHz and low-pass filtered to 50 kHz.

3.2.4 Calculation of the actin unfolding free energy

First, the free energy at each urea concentration was determined using **Equation 3.1** shown below:

$$\Delta G = -RTln\frac{[\mathrm{U}]}{[\mathrm{N}]} = -RTln\frac{F_{\mathrm{U}}}{F_{\mathrm{N}}} \quad (3.1)$$

Where:

F_{U} and F_{N} is the fraction of unfolded and native actin.

T is given as 298 K.

Then by plotting the free energy as a function of urea concentration, the free energy of unfolding at 0 M urea can be obtained from the intercept in **Equation 3.2**.

$$\Delta G = \Delta G_{\mathrm{U}} - m_{\mathrm{U}}[\mathrm{urea}] \quad (3.2)$$

3.2.5 Estimation of the zeta potential for folded and unfolded actin

The effective velocity of protein transport can be described by Equation 3.3: [30]

$$v_{\mathrm{eff}} = \frac{\varepsilon E}{\eta}\left(\zeta_{\mathrm{m}} - \zeta_{\mathrm{p}}\right) \quad (3.3)$$

Where:

ε represents the permittivity of the medium ($\varepsilon = \varepsilon_0 \varepsilon_r$).

η is the solution viscosity.

E denotes the strength of the electric field.

ζ_{m} and ζ_{p} correspond to the zeta potential of the protein and the walls of the nanopore, respectively.

From protein translocation events, particularly the dwell time, the zeta potential of analytes can be estimated using the Equation 3.4 shown below:

$$\zeta = \frac{\eta H_{\mathrm{eff}}^2}{\varepsilon} \frac{\partial\left(\frac{1}{t_{\mathrm{d}}}\right)}{\partial \psi} = \frac{\eta H_{\mathrm{eff}}}{\varepsilon} \frac{\partial (v_{\mathrm{eff}})}{\partial \psi} \quad (3.4)$$

Where:

η is the solution viscosity.

H_{eff} is the effective length of the nanopore.

$\varepsilon = \varepsilon_0\ \varepsilon_{\mathrm{r}}$ is the solution dielectric constant.

t_{d} is dwell time of protein translocation.

ψ is the applied voltage.

v_{eff} is the average effective velocity.

Prior to performing calculation, the physical constants of solutions were calibrated mainly based on the concentration of KCl and urea at 25°C. The viscosity is 0.874 Pa s for 1 M KCl actin monomeric buffer and 1.228 Pa s for the same buffer with 6 M urea. The corresponding dielectric constant (ε_{r}) is 78.57 and 94.43, respectively.

$\partial(v_{\mathrm{eff}})/\ \partial\psi$ was extracted from the slope in the linear fitting of v_{eff} vs. voltages.

3.2.6 Theoretical model of protein flux in nanopore translocations

The normalised capture rates (J_C/C_0) for protein translocation in nanopore can be generally expressed as **Equation 3.5**:

$$J_C/C_0 = \frac{D_m}{H_{eff}}\left[\frac{\eta\left(e^{\tilde{F}}-1\right)}{\tilde{F}} + \frac{(1-\eta)}{(\tilde{F}+|\tilde{z}\psi|)}\left(e^{\tilde{F}} - e^{-|\tilde{z}\psi|}\right)\right]^{-1} \quad (3.5)$$

Where:

C_0 is the protein concentration.

D_m is the diffusion coefficient of proteins.

H_{eff} is the effective length of nanopores.

η is the solution viscosity.

$\tilde{F}$ is the total energy barrier.

$\tilde{z} = \mu/D_m$ is a corrected factor of electrophoretic mobility.

ψ is the applied voltages.

3.2.7 Estimation of the protein size and shape

Nanopore readouts are able to directly provide volumetric information of analytes. It is related to the current blockade transients (ΔI_b), which depend on the excluded ionic volume (Λ) occupied by individual molecules as they translocate through the nanopore. This relationship can be described by **Equation 3.6**: [23]

$$\Delta I_b = -\frac{\sigma\psi}{H_{eff}^2}\Lambda\left[1 + f\left(\frac{d_m}{D_p}, \frac{l_m}{H_{eff}}\right)\right] \quad (3.6)$$

Where:

σ represents the solution conductivity.

ψ is the applied voltage.

D_p is the nanopore diameter.

H_{eff} is the effective length of the nanopore.

d_m refers to the diameter and l_m refers to the length of a protein molecule.

The correction factor $f(d_{\mathrm{m}}/D_{\mathrm{p}}\,, l_{\mathrm{m}}/H_{\mathrm{eff}}\,)$ accounts for various parameters, including the relative dimensions between the molecules and the nanopore.

To estimate the excluded volume for small spherical proteins or particles, the approximate **Equation 3.7** $\Lambda \approx \Delta I_{\mathrm{b}} \cdot H_{\mathrm{eff}}^{2}/(\sigma\psi)$ (3.7) based on **Equation 3.6** can be used. For long linear molecules such as double-strand DNA (dsDNA) or polymeric/filamentous proteins where l_{m} is much larger than H_{eff}, **Equation 3.6** can be simplified to $\Delta I_b \approx \sigma\psi \cdot A_m/H_{eff}$ (3.8), where A_{m} represents the mean atomic volume per unit length of the molecule. The effective length (H_{eff}) of the nanopipette can be achieved to be 45 nm based on the previous measurements. [27]

Protein hydrodynamic radii (R_{H}), assuming they maintain their globular structures during transport through the nanopore, can be estimated from fractional current amplitude data based on **Equation 3.9**[31]

$$R_{\mathrm{H}} \cong \frac{1}{2}\left[\langle \Delta I/I_{\mathrm{o}} \rangle \left(H_{\mathrm{eff}} + 0.8D_{\mathrm{p}}\right) D_{\mathrm{p}}^{2}\right]^{1/3} \quad (3.9)$$

Where:

ΔI is the blockade current.

I_{o} is the open current.

D_{p} is the diameter and H_{eff} is the effective length of a nanopipette.

The theoretical value of ρ is 0.775 for a hard-sphere with uniform density, whereas for an oblate ellipsoid, values of ρ range from 0.875 to 0.987, and for a prolate ellipsoid, values range from 1.36 to 2.24.

3.2.8 Kinetics measurements of actin binding with Swinholide A

In a typical kinetic experiment of actin monomer with Swinholide A, the actin monomers in the external bath were induced to translocate through a nanopipette under the application of voltages. This procedure lasted at least 1 hr to make sure the protein flux is stable. Without stopping the recording, the Swinholide A was then added to the bath as the time zero point. The dimer number was counted per two minutes with threshold of 75 pA and the population fraction was calculated to plot a time-dependent curve. The curves were fitted by a three-component model with positive cooperativity:

$$[\mathrm{D}]_{\mathrm{t}} = [\mathrm{D}]_{\mathrm{max}}(1 - e^{-k_{\mathrm{obs}}t}) \quad (3.10)$$

Where:

$[\mathrm{D}]_{\mathrm{max}}$ is the maximum percentage of the final product.

k_{obs} is the observed constant.

3.3 Results and Discussion

3.3.1 Experimental configuration and sensing principle

The nanopipettes utilised in this study were fabricated using laser-assisted pulling, following a previously reported method. [32] These pulled nanopipettes featured a single nanopore with an average diameter of 25 ± 4 nm, as confirmed by Scanning Electron Microscopy (SEM) analysis (**Figure 3.2**). In the monomeric actin buffer, linear current-voltage (I-V) curves were obtained, and the nanopore conductance was determined to be 37.0 ± 3.9 nS (**Figure 3.3**).

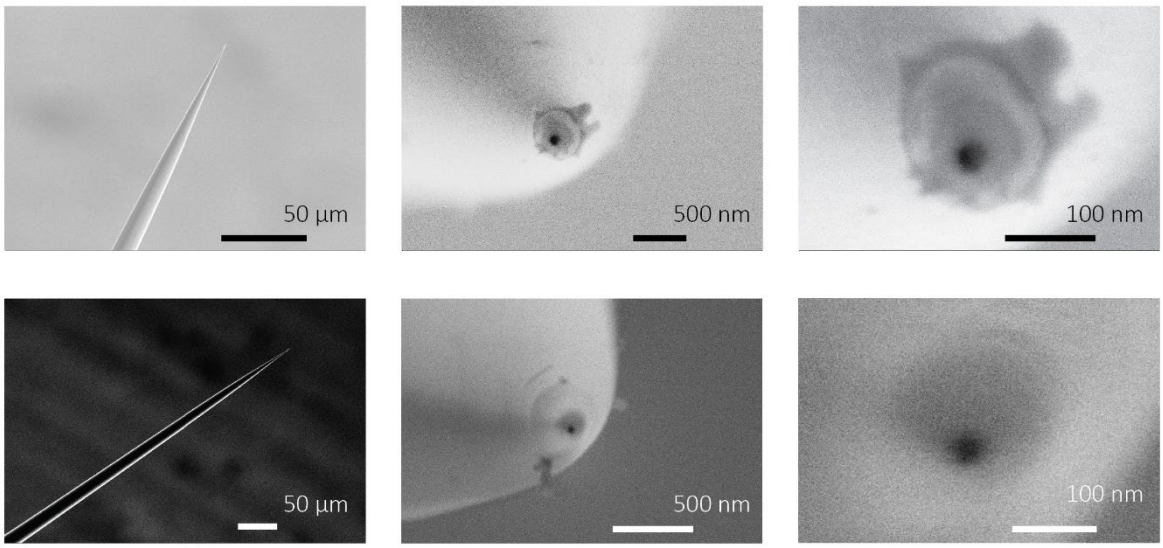


Figure 3.2 SEM images of nanopipettes fabricated by a laser-assisted pulling protocol of quartz capillaries. Left: SEM images showing a conical shape at the tapered tip of nanocapillaries. Middle: deeper landscape of the tip of nanopipettes with a nanoscale pore in the centre. Right: close-up SEM images of the nanopore with a diameter of 25 ± 4 nm formed in the pipettes.

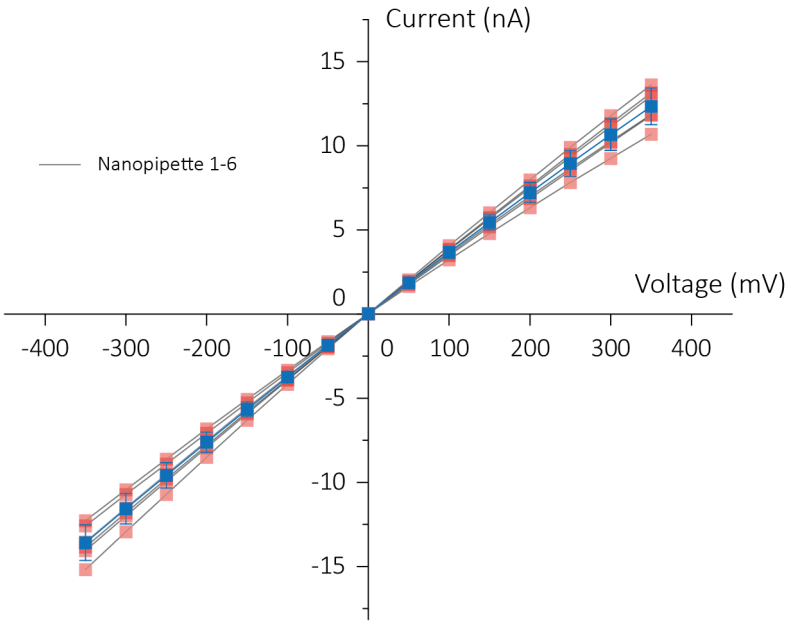


Figure 3.3 Current-voltage curves of nanopipettes used in nanopore measurements. I-V curves obtained in 1 M KCl actin monomeric buffer (containing 20 mM Tris pH 8, 0.4 mM ADP, 0.1 mM $CaCl_2$, 0.01% DMSO and 10% glycerol). The nanopore conductance was estimated to be 37.0 ± 3.9 nS by linear fitting.

In all experiments, the analyte was introduced into the external reservoir (*cis*) along with a reference/ground Ag/AgCl electrode. The nanopipette was filled solely with buffer solution, and a patch/working Ag/AgCl electrode was inserted (**Figure 3.4**). The translocation of proteins through the nanopore, driven by the applied external electric field, arises from cooperative and competitive contributions of diffusion, electrophoretic (EP), and electroosmotic (EO) flows.[30] At pH 8.0, both the nanopipette surface and actin (with an isoelectric point around 5.3) carry negative charges. Consequently, no translocation events were observed under negative voltage conditions (**Figure 3.5**). To suppress the electroosmotic flow and maximise the signal-to-noise ratio of the nanopore, a relatively high concentration of potassium chloride (1 M) was employer. Under such conditions, electrophoretic transport dominates, causing negatively charged actin molecules to translocate from the bath into the interior of the nanopipette under positive bias.

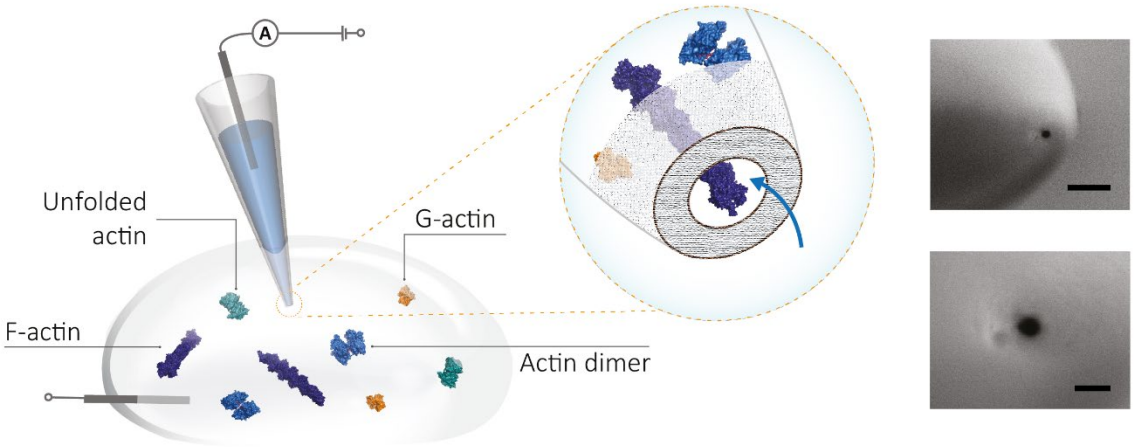


Figure 3.4 Schematic of experimental set-up of protein detection using nanopipette-based nanopore. The nanopipette and external bath were filled with a monomeric ADP-actin calcium buffer. One Ag/AgCl working electrode was inserted into the pipette, and the other one Ag/AgCl reference/ground electrode was fixed in the bath where the protein was introduced. Under external electric field, actin molecules in different states were translocated from the bath to the inside of the pipette through a conical nanopore at the pipette tip. Right insert: a typical SEM image showing that the nanopipette tapers down at the tip to form a nanopore with the diameter of 25 nm (scale bar 200 nm, top; 50 nm, bottom).

3.3.2 Discrimination of different actin species

To demonstrate the spatial and temporal resolution of the nanopipettes, a comparison of translocation characteristics among three different actin species: monomeric (G)-actin, drug-induced dimers, and filamentous (F)-actin was conducted. Throughout the experiments, a voltage of 250 mV was applied. By plotting two-dimensional scatterplots of dwell time (t_d) versus peak current and complementing them with box plots (**Figure 3.6** and **Figure 3.7**), a cluster of events along with outliers outside the 95% confidence interval were observed for all three species. These outliers are likely attributed to transient adsorption of proteins on the nanopore surface or transient oligomer formation during translocation. [33] It is worth noting that the distribution of dwell times, rather than the mean values alone, provides crucial information about various features such as the electrophoretic and electroosmotic properties of the molecule and its interactions with the nanopore itself. Importantly, this distribution-

based information, particularly related to filament length, is often masked in ensemble averaging methods commonly used for filament formation, such as the pyrene fluorescence assay (**Figure 3.1**). Furthermore, a discernible increase was observed in the mean dwell time of actin dimers compared to monomers, indicating a likely change in their electrophoretic mobilities. This finding highlights the ability of the nanopipette-based approach to capture differences in translocation dynamics between distinct actin species.

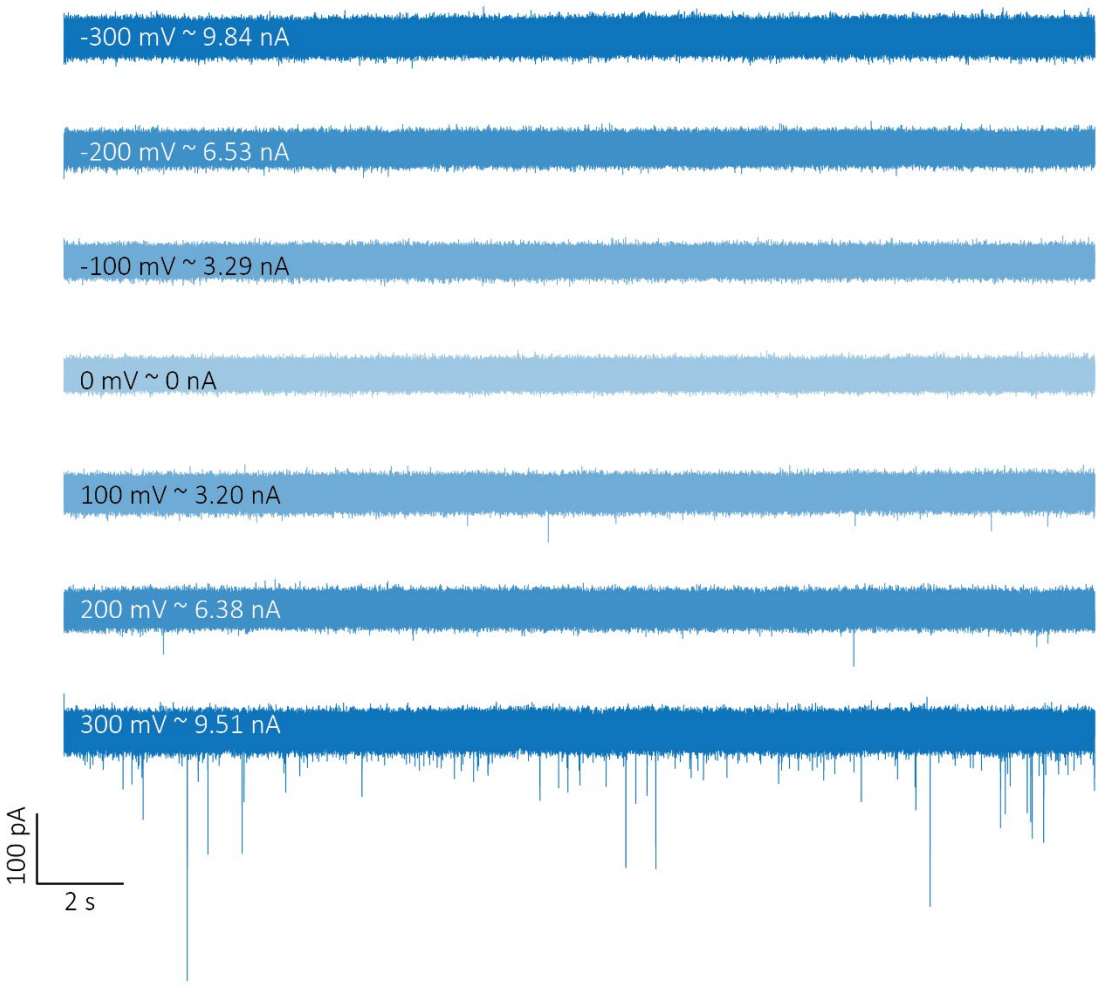


Figure 3.5 Ionic current-time traces of 800 nM actin monomers. The nanopore experiments were conducted in 1 M KCl buffer containing 20 mM Tris pH 8, 0.4 mM ADP, 0.1 mM $CaCl_2$, 0.01% DMSO and 10% glycerol, recorded at 4.17 MHz, filtered to 50 kHz, and collected at different voltages. These traces show translocation spikes at positive voltages with a voltage dependence but no translocation events at negative voltages, demonstrating that EP driving forces dominate the actin transport.

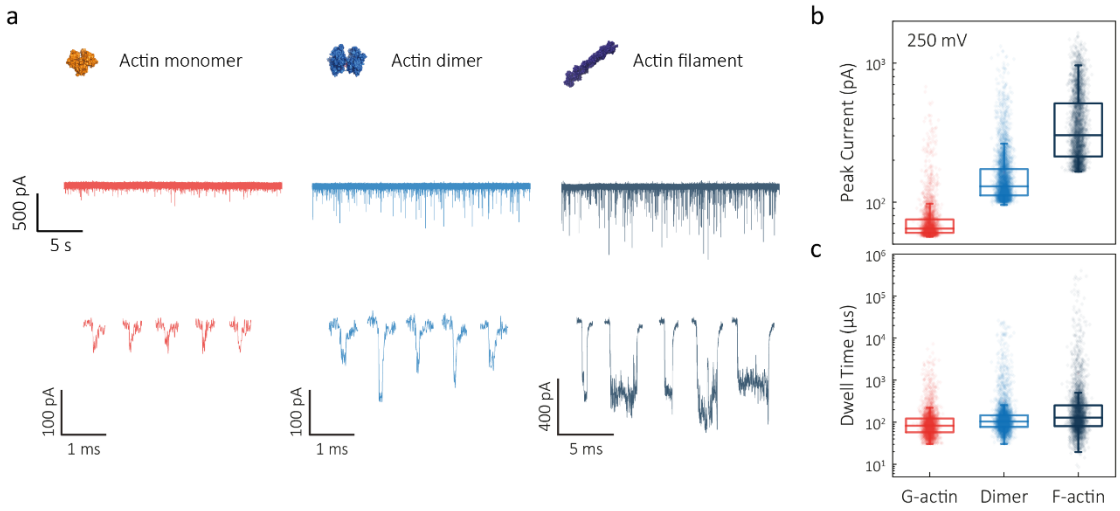


Figure 3.6 Nanopore detection of actin macromolecular states. (a) Top: protein structures (from left to right): G-actin monomer (42 kDa, PDB: 1NWK, 800 nM), drug-induced actin dimer (PDB: 1YXQ, 500 nM) and F-actin (up to 200 actin subunits, PDB: 3G37, 800 nM). Middle: representative current-time traces. Bottom: typical translocation events. Box and whisker plots showing the distribution of peak current (b) and dwell time (c) (median line and interquartile range, G-actin, n = 3268; Dimer, n = 4532; F-actin, n = 3859). All data in this figure was recorded at 250 mV, sampled at 1 MHz and low-pass filtered at 50 kHz.

The peak current serves as a crucial parameter for estimating the spatial resolution of the nanopipettes. In this analysis, **Equation 3.7** was employed to study the actin dimers. The mean peak current for actin dimers was determined to be 113.7 ± 15.8 pA, which is nearly double that of actin monomers (64.8 ± 6.7 pA). This increase in current aligns with the difference in volume between the two actin states. For F-actin, a larger mean peak current and a broader distribution were observed. This outcome was expected since F-actin is composed of monomeric actin subunits. During the actin polymerisation process, ATP-bound monomers assemble into filaments with a 37 nm helical repeat and a diameter ranging from 5 to 9 nm. [34] The polymerisation of actin resulted in an approximately ten-fold increase in the mean current blockade, measuring 298.5 ± 105.8 pA, compared to actin monomers. The long-tail distribution and variety of blockade currents observed are likely attributed to the range of potential actin filament lengths, which can vary from several subunits to micron-scale structures. These results demonstrate the effectiveness of combining spatial and temporal analysis to accurately

define the protein states, from monomers to dimers and filaments, in protein-protein assemblies. Moreover, this approach enables high-resolution characterisation of the kinetics associated with these protein states.

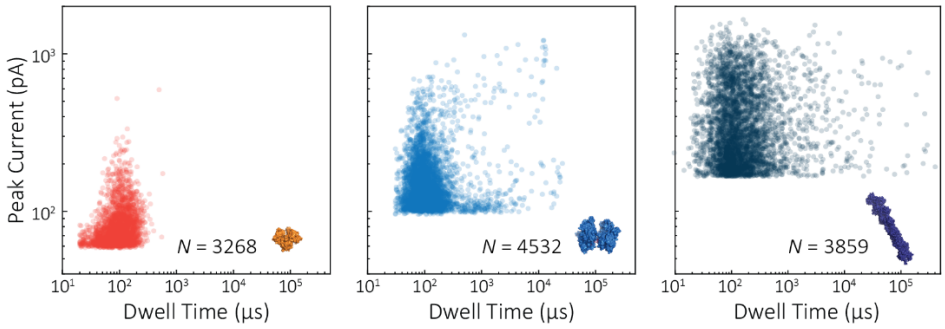


Figure 3.7 Statistical analysis of actin macromolecular states. Scatterplots of current blockades vs. dwell times for different actin species (from left to right: G-actin monomer, drug-induced actin dimer, and F-actin) with the voltage application of 250 mV.

3.3.3 Actin folding and unfolding landscape

Having established a system for studying the dynamics of actin monomers in solution, the next objective was to investigate protein folding at the single-molecule level. The folding process of actin is intricate and not yet well-understood, primarily due to the multitude of potential folding intermediates that may arise during the folding pathways of any given polypeptide. In addition, the intrinsic flexibility of the actin protein contributes to the complexity of its folding landscape. [35] To examine how the nanopore signal is influenced by the protein folding state, a nanopore analysis was conducted for actin monomers exposed to varying concentrations of urea, ranging from 0 M to 6 M, while maintaining a bias of 250 mV. Prior to the measurements, the nanopipettes were ensured to be compatible with the chemical denaturant urea, as demonstrated in **Figure 3.8**. Additionally, the solution conductivity for each buffer used was measured, as outlined in **Table 3.1**. These preliminary steps allowed us to proceed with the nanopore analysis of actin folding dynamics under denaturing conditions.

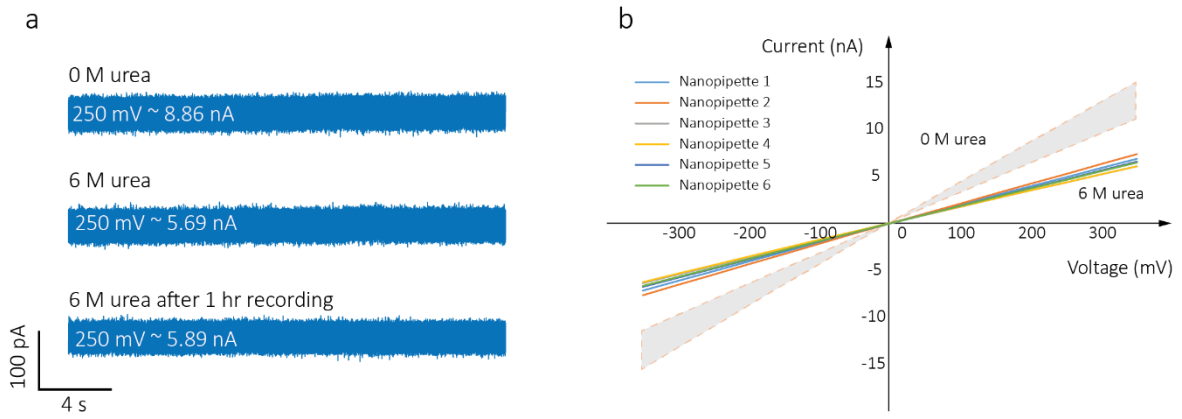


Figure 3.8 Nanopore compatibility with actin unfolding conditions. (a) Current-time traces of 1 M KCl actin monomeric buffer containing 0 M and 6 M urea respectively at 250 mV. The trace for 6 M urea shows a decrease of ionic current due to the decrease of solution conductivity and remains stable after a long-time recording, indicative of a good compatibility of quartz nanopipettes with urea. (b) I-V curves of nanopipettes obtained in 1 M KCl actin monomeric buffer with 6 M urea. The grey shadow is the I-V curves tested in the buffer without urea.

Table 3.1 Solution conductivity for buffers with different concentrations of urea used in actin unfolding assays.

	Conductivity (mS/cm)
Buffer*	103.5 ± 1.1
Buffer + 1 M urea	101.9 ± 1.0
Buffer + 2 M urea	96.4 ± 0.9
Buffer + 3 M urea	85.1 ± 0.8
Buffer + 4 M urea	74.9 ± 0.7
Buffer + 5 M urea	68.8 ± 0.7
Buffer + 6 M urea	65.8 ± 0.6

Buffer* contains 1 M KCl, 20 mM Tris pH 8, 0.4 mM ADP, 0.1 mM CaCl2, 0.01% DMSO and 10% glycerol.

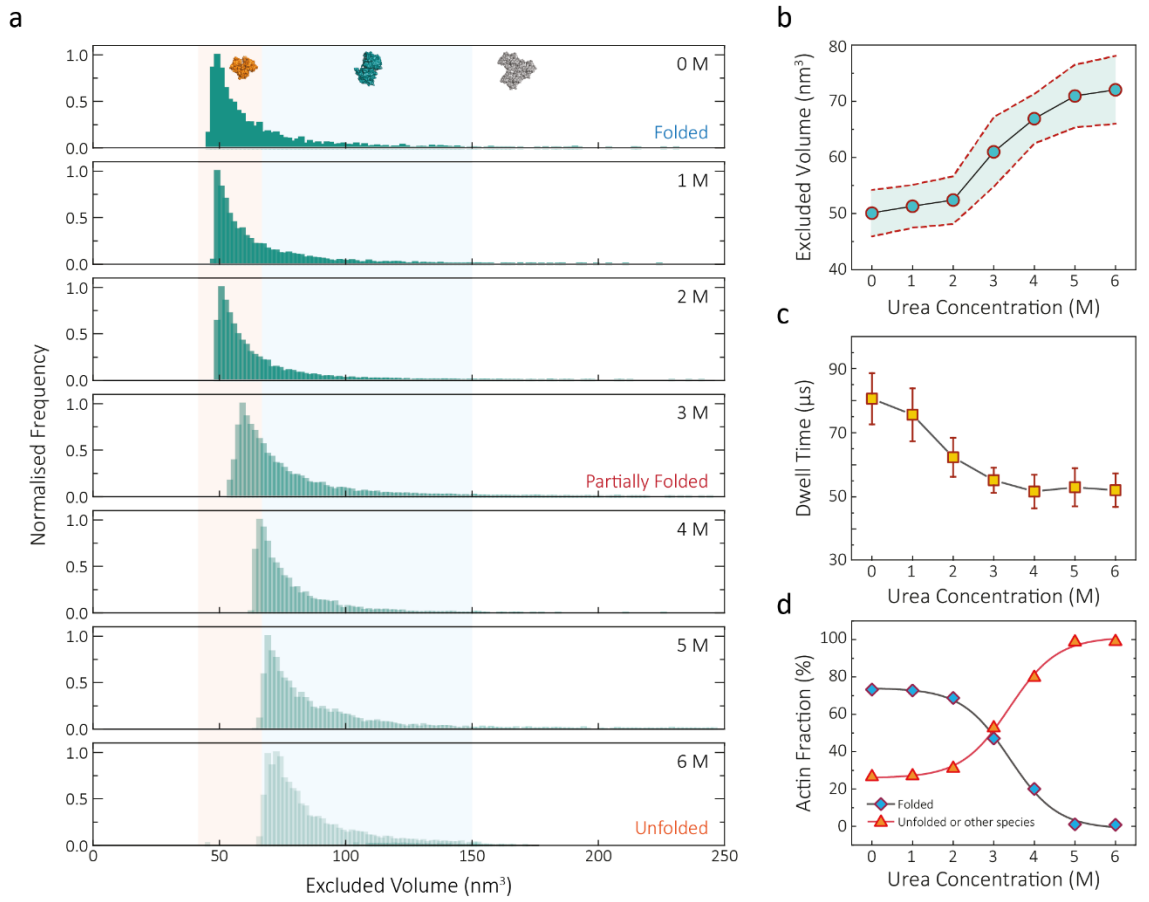


Figure 3.9 Discrimination of actin unfolding in a urea gradient using nanopipettes. (a) Normalised statistic of excluded volumes (calculated from $\Lambda \approx \Delta I_b \cdot H_{eff}^2/(\sigma\psi)$) from native actin to denatured actin in increasing urea concentration. The orange boundary represents the fully folded actin state, and blue boundary determines the unfolded actin or other transient aggregates at low urea concentrations. The population shifts from a mostly native, folded state to a higher excluded volume, consistent with an unfolded state with larger hydrodynamic radius, as the urea concentration increases. Protein models for each state based on the crystal structures of G-actin (PDB: 1NWK) are shown in the inset. (b) The mean excluded volume plot exhibits a sigmoid increase when urea concentration increases, indicative of actin unfolding with an increase of hydrodynamic radius. (c) Mean dwell time decreases as the urea concentration increases. (d) Proportion of actin in different states (monomeric folded, unfolded or transient aggregated) plotted against urea concentrations shows a sigmoid curve, suggesting a two-state transition between folded (including a small fraction of aggregates) and unfolded actin.

As the urea concentration increased, a corresponding increase in the excluded volume was observable, as shown in Figure 3.9a. It is important to note that the distribution of the excluded volume is not a standard Gaussian distribution due to the low translocation signals being cut off by the low-pass filter, as evident in the normalised current blockade ($\Delta I/I_o$) depicted in Figure 3.10. This trend can be attributed to the increased exposure of the protein surface to the solvent during unfolding. The interaction between the protein and the solvent becomes more significant, leading to an effective increase in the protein apparent size and consequently resulting in a larger amplitude of the current blockade. This effect has been previously observed and reported in literature. [21] The plot depicting the mean excluded volume as a function of urea concentrations exhibits a sigmoidal shape, demonstrating a transition from folded to unfolded actin. The mean excluded volume increases from 50.7 ± 4.2 nm^3 to 73.6 ± 6.2 nm^3, indicative of a two-state transition (Figure 3.9b). Conversely, an opposite trend for the translocation time was observed, with the dwell time decreasing from 80.6 ± 6.4 µs to 58.1 ± 3.7 µs with increasing urea concentration (Figure 3.9c). This decrease in dwell time suggests that unfolded, linear actin molecules translocate at a faster rate compared to the folded, globular ones. I attribute this increase in translocation speed of unfolded actin to the changes in charge distribution resulting from the conformational changes during unfolding. These changes in charge distribution, in turn, affect the electrophoretic mobilities during nanopore translocation.

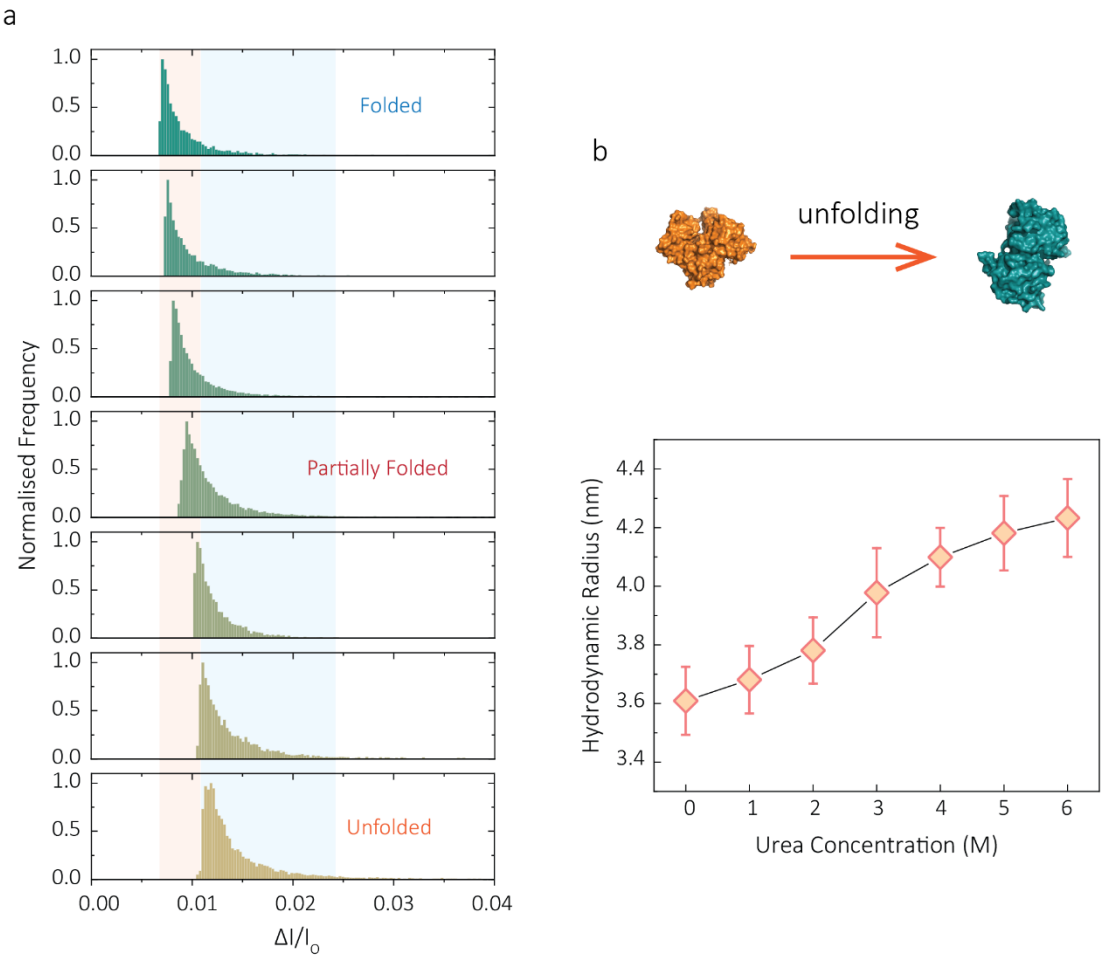


Figure 3.10 Changes of hydrodynamic radii (R_H) of actin monomers during unfolding process. (a) Normalised distribution of fractional current blockade ($\Delta I/I_o$) in different urea concentrations. The orange boundary represents the fully folded actin state, and blue boundary determines the unfolded actin or other transient aggregates at low urea concentrations. The population shifts from a mostly native, folded state to a higher excluded volume, consistent with an unfolded state with larger hydrodynamic radii, as the urea concentration increases. (b) Top: schematic of conformational changes during actin unfolding. Bottom: plot of R_H vs. urea concentrations showing a two-state trend.

To define the transition between folded and unfolded actin, a threshold value of 67 nm^3 was set for the excluded volume at 6 M urea. This threshold is based on the assumption that actin is fully unfolded at this concentration. This value is consistent with the reported value at 0 M urea without an applied voltage, as there is a slight decrease in the excluded volume upon the addition of voltage. At 0 M urea, around 26.8% of the translocation events exhibited a larger

amplitude than the folded monomer, which can be attributed to transient oligomers. The majority of the population (73.2%) represented natively folded monomers. From 0 M to 2 M urea, folded actin monomers and transient oligomers were predominant. However, at 3 M and higher urea concentrations, there was a sharp increase in the excluded volume, indicating a change in actin behaviour resulting from unfolding.

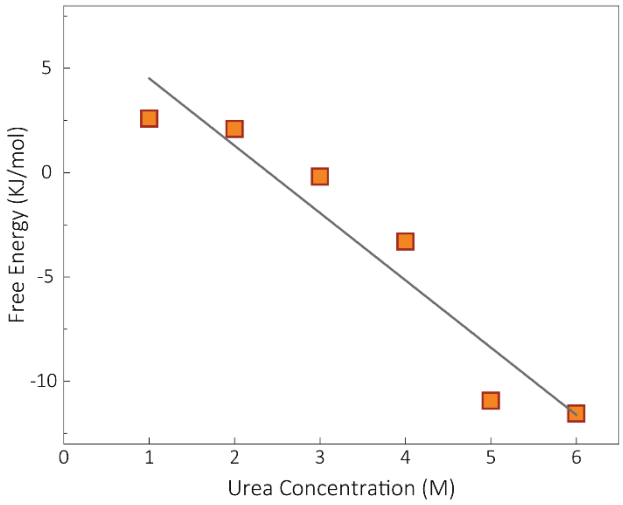


Figure 3.11 Plots of free energy as a function of urea concentration along with a linear fitting.

The data shown in **Figure 3.9d** suggests that actin unfolding follows a two-state pathway, with equilibrium reached at approximately 5 M urea. At this point, it can be assumed that the majority of the population is unfolded, which aligns with previous studies utilising fluorescence assays. [36] Traditional analysis of protein unfolding using denaturants typically shows a linear plot of unfolding free energy (ΔG) versus denaturant concentration in the transition zone. [37] Through linear extrapolation, the free energy of actin unfolding can be determined to be 7.74 kJ mol^{-1} at 25°C in the absence of denaturants (**Figure 3.11**). However, it is important to note that this value is specific to the buffer and environment used, serving as an estimate of the unfolding free energy using the nanopore platform. Despite the buffer- and environment-specific nature of the unfolding free energy estimate, these findings demonstrate that the

single-molecule statistical approach employed in this study effectively captures dynamic changes in protein conformations through translocation events. This approach complements traditional methods such as fluorescence and provides supplemental insights into actin folding dynamics.

3.3.4 Voltage dependence on actin confirmation

The applied voltage has a significant impact on protein translocation by influencing protein mobility and conformation. [21, 38] In the context of nanopore analysis, protein transport through the nanopore is governed by bulk diffusion, electrophoretic (EP) flow, and electroosmotic (EO) flow. The strong electric field generated at the tip of the nanopipette can considerably alter the velocity, direction, and even the conformation of the protein. To minimise the electroosmotic component, a high potassium chloride concentration was used, which was confirmed by recording translocation events only at positive bias. By recording at positive bias, only the negatively charged actin molecules were transported from the external bath into the interior of the nanopipette, regardless of the buffer components (Figure 3.12a).

In the voltage range of 150-350 mV, unfolded actin exhibited faster translocation compared to the folded monomer, regardless of the solution viscosity (Fig. 3.12b). By plotting effective velocities ($v_{\mathrm{eff}} = H_{\mathrm{eff}}/t_{\mathrm{d}}$) against applied voltages, the slope ($\partial v_{\mathrm{eff}}/\,\partial\psi$) can be extracted and the zeta potential of actin was then determined using an appropriate model. [39] The zeta potential was found to be -6.0 mV for folded actin and -12.1 mV for unfolded actin. This suggests that the unfolding process leads to an increase in net surface charge, resulting in a higher zeta potential, which is consistent with the altered behaviour observed in native gel electrophoresis of actin. [40]

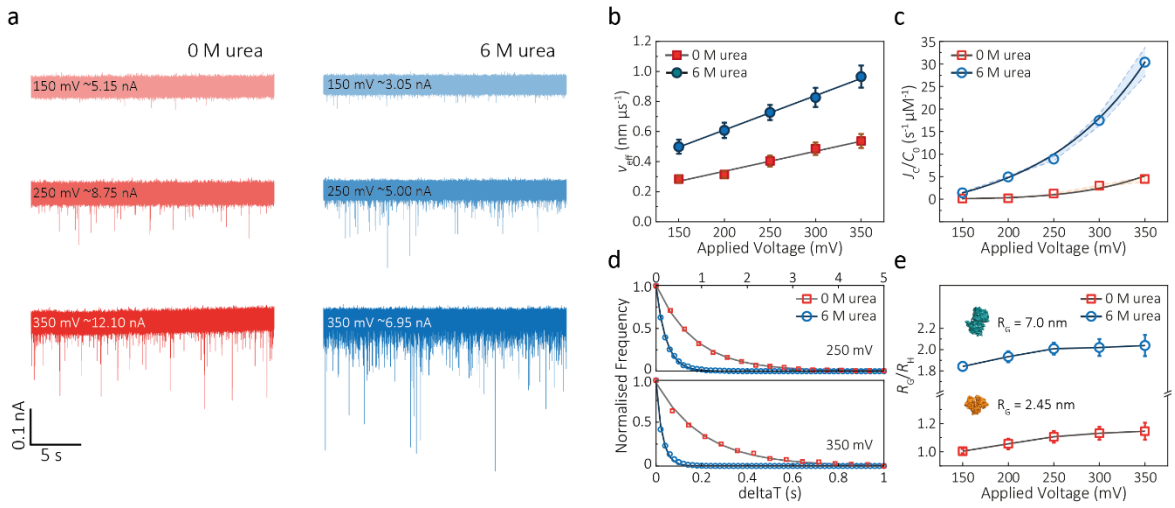


Figure 3.12 Voltage dependence upon actin translocation through nanopipettes. (a) Voltage-dependent ionic current traces show the translocation spikes of 800 nM folded actin in 0 M urea and unfolded actin in 6 M urea. Open currents (I_o) for each voltage were marked upon each baseline. (b) Effective velocity ($H_{\mathrm{eff}}/t_{\mathrm{d}}$) for both folded and unfolded actin shows a linearly voltage-dependent increase when increasing the applied voltage. (c) Normalised capture rates (J_{C}/C_0) shows an exponential function of applied voltages for both folded and unfolded actin. This nonlinear increase suggests a two-stage regime in which the entropic barriers restrict successful translocations at low voltages and electrophoretic forces dominate capture behaviours at higher voltages. (d) Normalised distributions of elapsed time between successive captured events (δt) for actin transport in 0 M and 6 M urea buffers at 250 mV and 350 mV. Solid lines represent a single-exponential decay fit, from which the protein flux (J_{C}) is extracted for (c). (e) Plots of the ratio of the radius of gyration to hydrodynamic radius ($R_{\mathrm{G}}/R_{\mathrm{H}}$) illustrate that the actin shape is an oblate ellipsoid in 0 M urea buffer, but a prolate ellipsoid in 6 M urea buffer during nanopore translocation. With the voltage increases, the value of $R_{\mathrm{G}}/R_{\mathrm{H}}$ increases both for folded and unfolded actin. This is unchanged at high voltages, indicating the protein was stretched under a high-strength localised electric field across the pipette tip.

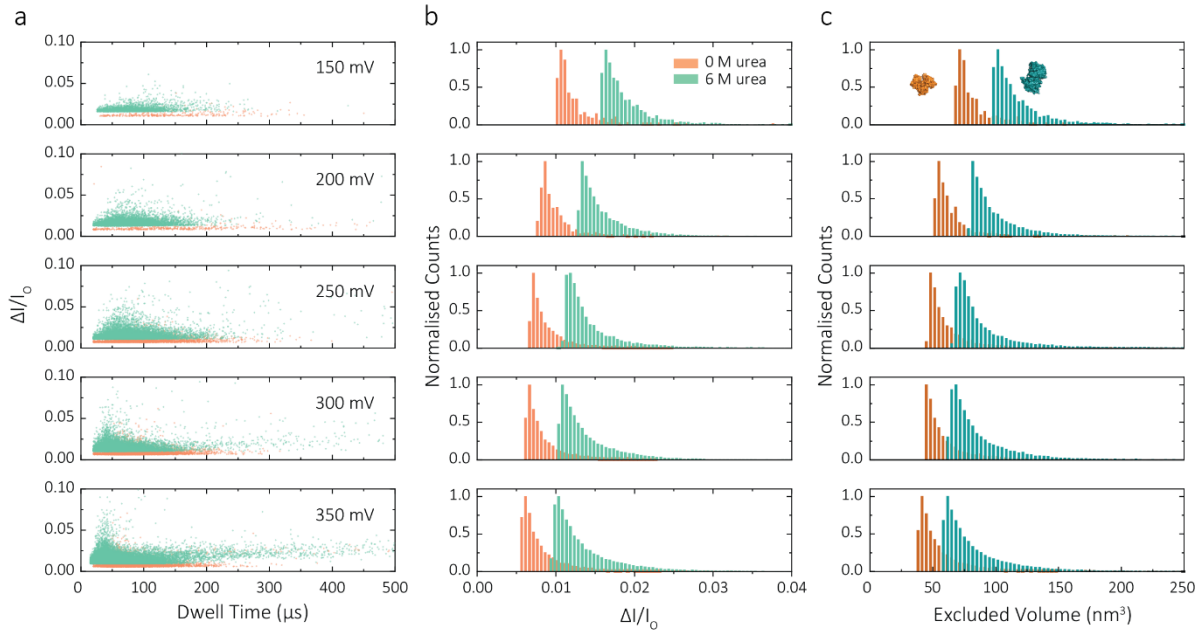


Figure 3.13 Discriminating folded and unfolded actin using nanopipettes performed in 1 M KCl with 0 M or 6 M urea. (a) Scatterplots of fractional current blockades vs dwell times for folded and unfolded actin at different voltages. (b) Distributions of fractional current blockades for both folded and unfolded actin at various voltages. (c) Statistic histograms of the excluded volume calculated from eq. 1 for folded and unfolded actin at different voltages from 150 mV to 350 mV.

The capture rate, or protein flux (J_C), is another informative parameter that aids in understanding protein conformation dynamics. The behaviour of J_C can be described by two regimes: the entropic barrier regime and the drift regime. In the entropic barrier regime, the capture rate is limited by the height of the energy barrier, resulting in an exponential response to applied voltages. Conversely, in the drift regime, the flux is dominated by the electric field and is independent of molecular diffusion and energy barriers. The crossover point between these two regimes is determined by the barrier height and molecular length.[41] In this study, a two-stage regime was observed: an entropic barrier regime at low voltages and a drift regime at higher voltages. In the drift-dominated regime, the steady-state flux can be expressed as $J_C/C_0 = (\mu\psi)/H_{\text{eff}}$, where μ represents the electrophoretic mobility of the proteins, and H_{eff} is the effective length of the nanopore. In this regime, the capture rate is directly proportional to the applied voltage. At lower voltages, the flux is primarily governed by the height of the

energy barrier and exhibits an exponential dependence. Figure 3.12c shows the normalised flux for folded and unfolded actin as a function of applied voltages. Both curves exhibit an exponential increase, highlighting the importance of the entropic barrier in actin translocation, particularly for folded actin monomers. Furthermore, the normalised flux for unfolded actin is higher than that of folded actin, which is consistent with folded actin having a lower negative charge and therefore a lower zeta potential. As a result, the capture rate increases for unfolded actin, as illustrated at two different voltages (250 mV and 350 mV, Figure 3.12d). This behaviour aligns with the distinct charge properties of folded and unfolded actin and their influence on the translocation kinetics.

To investigate how applied voltage influences protein conformation, the relationship between current blockade and the hydrodynamic radius (R_{H}) as well as radius of gyration (R_{G}) of the protein was examined. In this analysis, the protein was assumed to behave as a hard sphere during nanopore translocation.[31] Figure 3.13 presents the distributions of $\Delta I/I_{\mathrm{o}}$ for folded and unfolded actin at different voltages, revealing a decrease in $\Delta I/I_{\mathrm{o}}$ as the voltage increases. These distributions can be used to calculate the mean R_{H} and excluded volume as a function of applied voltages (Figure 3.14). An important parameter to evaluate the structural changes and degree of asymmetry and anisotropy in the protein is the ratio $\rho = R_{\mathrm{G}}/R_{\mathrm{H}}$.[31] Based on the crystal structure of G-actin, the R_{G} value for the folded monomer can be estimated to be approximately 2.45 nm.[42] For the unfolded protein, a model for denatured proteins was employed, resulting in an estimate of around 7.0 nm.[43] With these values, the ratio ρ for a globular protein with uniform density can be calculated, which yields a value of 0.775. An increase in ρ indicates a transition towards an ellipsoidal shape. Even under harsh denaturing conditions, unfolded proteins can exhibit native-like organised structures rather than a completely disordered linear conformation.[44]

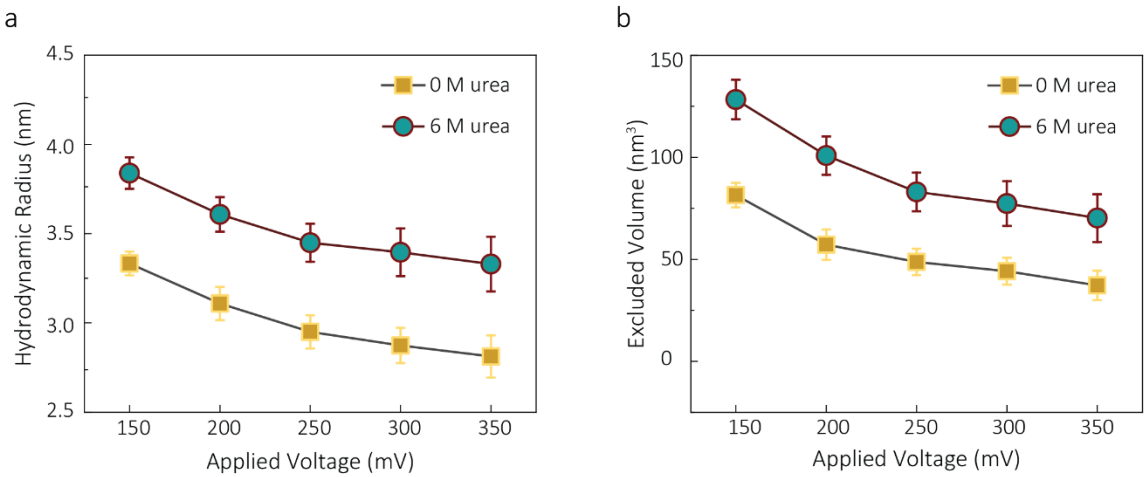


Figure 3.14 Plots of hydrodynamic radius (a) and excluded volume (b) vs. voltages for folded and unfolded actin.

The calculated ρ values for folded actin range from 0.999 ± 0.019 at 150 mV to 1.178 ± 0.071 at 350 mV (**Figure 3.12e**). This suggests that the protein is approximately defined as an oblate ellipsoid, in agreement with the stretching of proteins with a dipole moment under an electric field. [23] For unfolded actin, ρ also exhibits a similar trend, increasing from 1.825 ± 0.050 to 2.072 ± 0.121. These values are more consistent with a prolate ellipsoid. Based on these observations, it is evident that the localised electric field generated at the tip of the nanopipettes can alter the shape or conformation of translocating proteins due to their heterogeneous charge distribution. Therefore, it is recommended to apply low voltages during nanopore experiments to better understand protein-protein or protein-drug interactions. However, the altered behaviour at higher voltages can be advantageous for studying electrostatic properties such as dipole moment, net charges, and molecular conductivity. Alternatively, high electric fields can be employed as a method to unfold proteins without the presence of denaturants, serving as a complement to chemically-induced unfolding. [45]

3.3.5 Real-time sensing of actin polymerisation

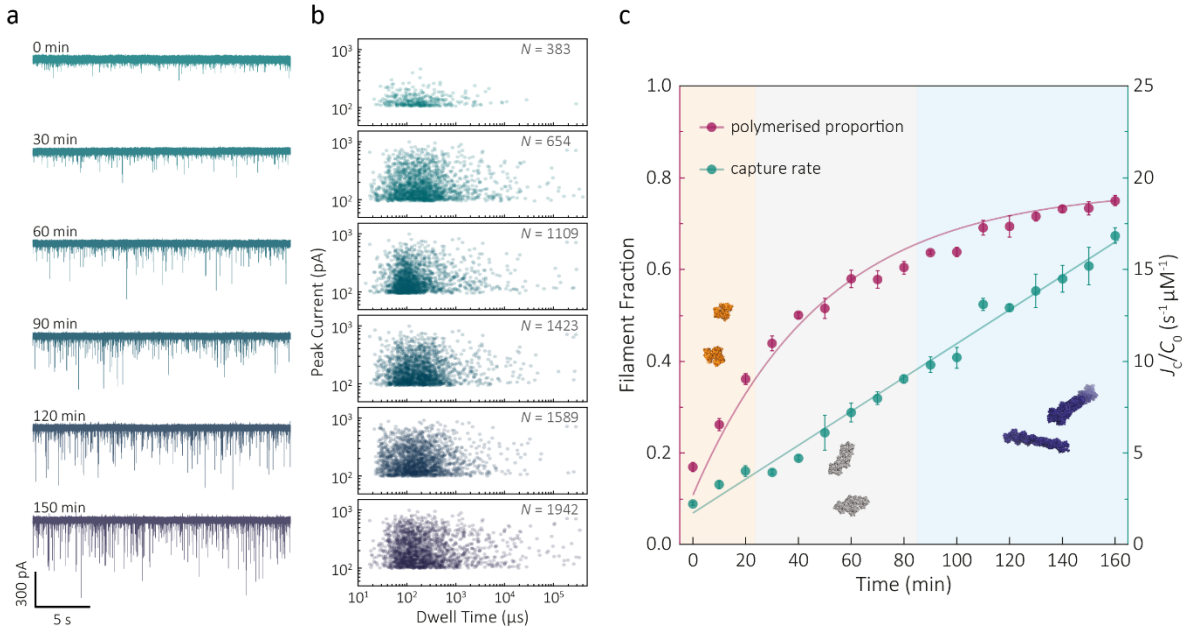


Figure 3.15 F-actin formation in real-time. (a) Time-dependent ionic current traces of actin filamentation. 1 µM actin was induced in the bath to form filaments and aggregation data was recorded in real-time. (b) Scatterplots of current blockades vs dwell times for F-actin formation at different time points corresponding to the I-t traces show in panel a. (c) Time-dependence of actin filament fraction (purple line) and normalised capture rate (green line) for 1 µM monomeric actin concentration. Each point was calculated every 10 min and averaged over a continuous 2 min trace. The threshold for the formation of actin oligomers and filaments was 150 pA (the mean of the second distribution in **Figure 3.16**). Three shadow areas and protein models (from left to right) represent actin monomers, oligomers and filaments, respectively.

Despite the existence of numerous well-studied actin structures, the understanding of the structural flexibility of actin and its polymerisation has been slow to progress. [1, 46] However, through the use of nanopore sensing, significant advancements have been made in this area. In this study, actin polymerisation can be recorded in real-time using nanopore sensing (**Figure**

3.15a). By monitoring the ionic current of ATP-activated actin monomers over time, translocation events with increasing peak amplitudes and capture rates could be observed. This significant increase in peak amplitudes (Figure 3.15b) is highly sensitive to molecular volumes and conformations, providing evidence of filament formation. Thus, the polymerisation process can be revealed from the single-molecule events and the distribution of dynamic interactions without averaging across the entire population.

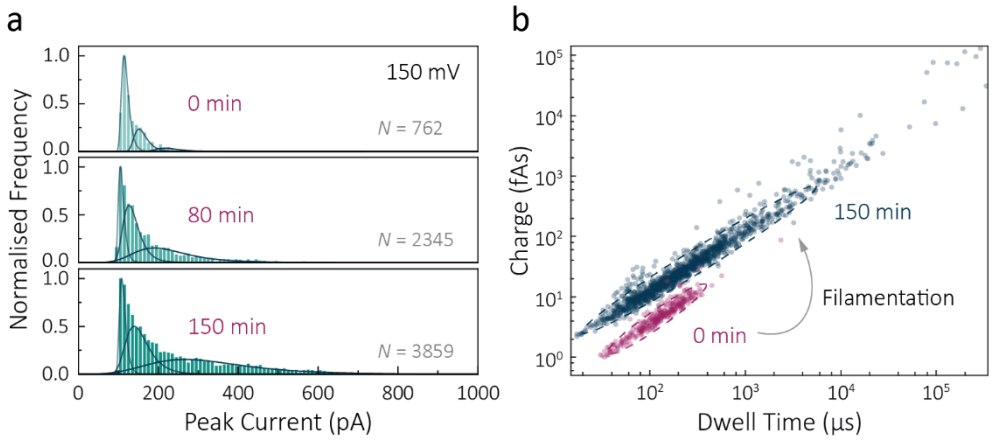


Figure 3.16 Statistical analysis of actin polymerisation. (a) Histograms of the peak current for actin filament formation at 0, 80 and 150 min at 150 mV, showing a distribution of multiple populations and an extension in higher peak currents. (b) Scatterplots of charge vs. dwell time for actin polymerisation at 0 and 150 min.

The distribution of peak current shown in Figure 3.16 demonstrates time-dependent multiple populations, indicating a concurrent increase in both the proportion and extent of ATP-actin polymerisation. Furthermore, the persistence of the lowest population (105.6 ± 16.8 pA) likely represents monomeric actin, which provides evidence for the treadmilling behaviour of actin filaments. To confirm that these changes are not caused by the interaction between the analytes and the nanopore itself, I-V curves were measured before and after the nanopore experiments (Figure 3.17). These results indicate that the observed changes are directly related

to filament formation and not influenced by the nanopore-analyte interaction. Through the real-time nanopore measurements, actin polymerisation dynamics at the single-molecule level can be gained, allowing us to study the distribution of interactions and observe the formation of filaments without the need for population averaging. This represents a significant step forward in the understanding of the structural flexibility of actin and its polymerisation process.

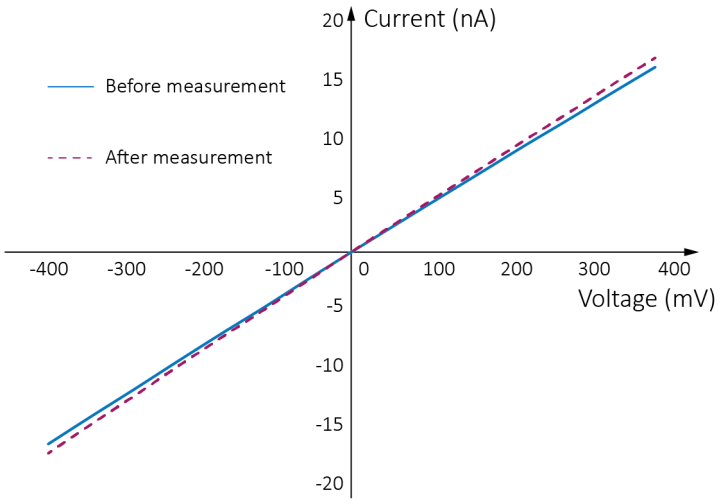


Figure 3.17 *I-V* curves before and after measurement of actin filament formation (1 µM monomer concentration in ATP buffer). The slight increase of conductivity is indicative of water evaporation over time and no significant interactions between proteins and the nanopore surface.

Nanopore sensing offers a visually rich and time-resolved method to obtain valuable information about the electro-behaviour of molecules during transient translocation. This approach enables quantitative readout of the real-time properties of analytes and their interactions. In the case of actin polymerisation, nanopore sensing allows us to monitor the degree of polymerisation by examining both the filamentous fraction and the event frequency (Figure 3.15c). Initially, the filamentous fraction is around 17% due to early actin nucleation

events triggered by high salt and ATP activation. However, as polymerisation is induced, the proportion of filaments increases over time, reaching a maximum of approximately 75%. This suggests that around 25% of actin monomers are undergoing nucleotide exchange as treadmilling occurs within the filament. This observation elucidates the dynamics of actin polymerisation at the single-molecule level.

Furthermore, the capture rate exhibits a linear increase, which is directly related to the size, mobility, and conformation of the analytes. Actin filaments, with their higher net charge and mobility, contribute to the increasing number of capture events in the drift regime. Thus, the capture rate can serve as a readout for actin polymerisation. This capability enables us to visualise the polymerisation of native actin at the single-molecule level, which is crucial for studying its complex physiological and pathological dynamics, including protein aggregation and filamentation.

3.3.6 Recognition of actin drug binding

Building upon the capability to resolve unfolding actin monomers, I proceeded to characterise two actin-binding drugs with well-defined modes of interaction with actin, as determined by X-ray crystallography. The first drug is Swinholide A, a marine toxin that binds to actin by interacting with two actin monomers in a manner that hinders the necessary interactions for filament formation. [47] The second drug is Latrunculin, a family of plant toxins that bind to the nucleotide-binding pocket of actin, thereby obstructing filament formation by blocking nucleotide exchange. [15, 48] By employing the nanopore sensing approach, the binding behaviour of these drugs can be further investigated in real-time at the single-molecule level. This allows us to gain insights into the kinetics and mechanisms of their interactions with actin. Specifically, this approach enables us to monitor the effects of these drugs on actin polymerisation dynamics, elucidate their binding affinities, and assess their impact on the conformational changes and functional properties of actin. The section aims to further understanding how actin-binding drugs modulate actin dynamics and providing insights for the development of therapeutics targeting actin-related processes and diseases.

During the experiments, the translocation events were recorded in the presence of either Swinholide A or Latrunculin B and were compared with the translocation events of actin monomers (Figure 3.18 and Figure 3.19a). A significant difference was found in the scatter plots of actin bound with Latrunculin B and Swinholide A, particularly in terms of the height of current blockades and the length of dwell times when binding to Swinholide A (Figure 3.19b). Upon the addition of excess Latrunculin B, the peak current of translocation events became more uniform compared to drug-free actin monomers (measured as 59.1 ± 5.4 pA compared to 64.8 ± 6.7 pA for native monomers at 250 mV, Figure 3.16). This indicates that incubation with excess Latrunculin B limits transient oligomeric interactions and effectively stabilises actin in a monomeric state. In contrast, incubation with Swinholide A resulted in a nearly twofold increase in the mean peak current, from 59.1 ± 5.4 pA to 113.7 ± 15.8 pA (at 250 mV, Figure 3.20), accompanied by an increase in the capture frequency from 1.58 ± 0.08 s^{-1} to 5.07 ± 0.16 s^{-1}. Conversely, no obvious difference was observed in the capture frequencies of monomeric actin with or without Latrunculin B. The twofold increase in current blockade observed with Swinholide A suggests an increase in excluded volume, indicating the formation of actin dimers induced by Swinholide A. This observation confirms the specific mode of action of Swinholide A, which prevents filament formation by binding to actin monomers and promoting their dimerisation.

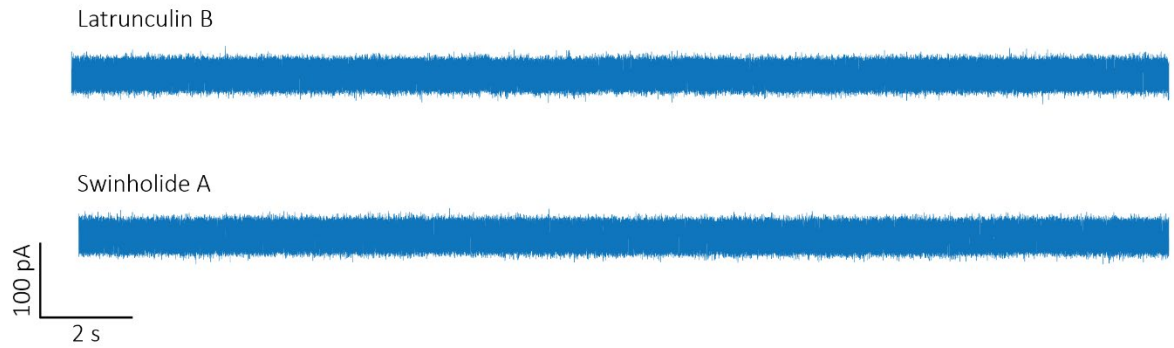


Figure 3.18 Latrunculin B and Swinholide A do not interact with the nanopipette surface. Current-time trances show no observable current changes for both drugs at 250 mV.

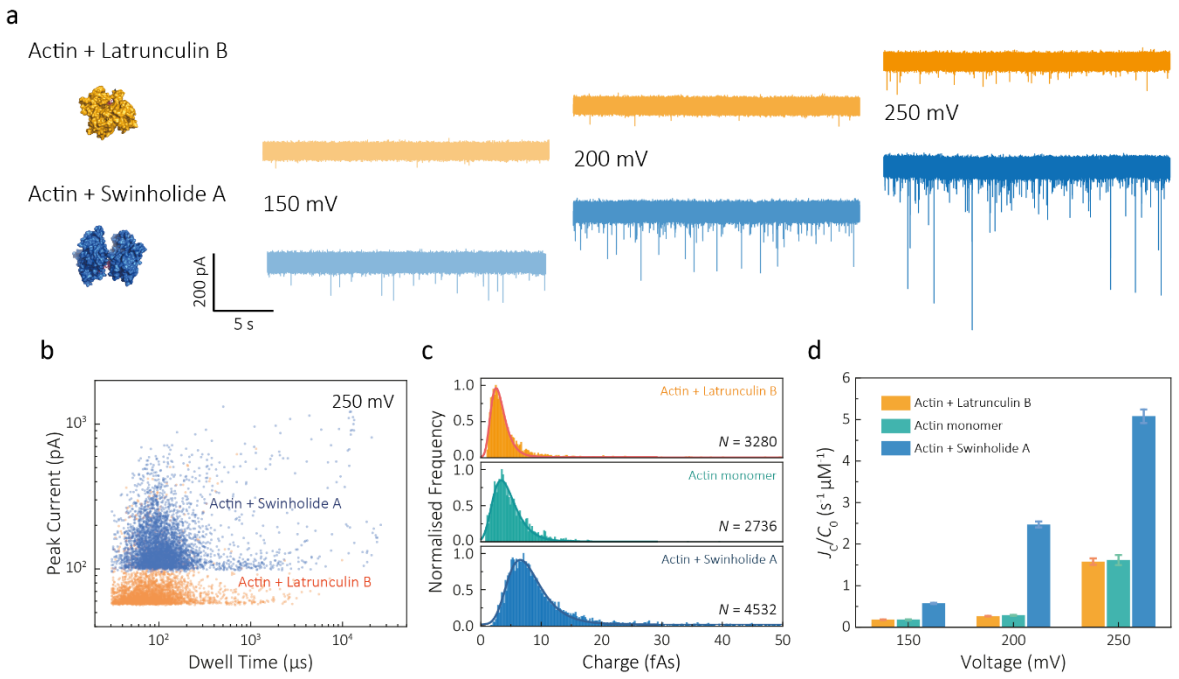


Figure 3.19 Actin drug binding assays. (a) Left: protein models based on the X-ray crystallographic structures (actin with Latrunculin B bound, PDB: 1IJJ and actin with Swinholide A bound, PDB: 1YXQ). Right: typical current traces for actin bound to different filament inhibitors at 150, 200 and 250 mV. Ionic currents were recorded in monomeric buffer, 1 µM actin monomer and 10 µM filament inhibitor. (b) Scatterplots of current blockades vs. dwell times for both actin monomers and dimers in the same scale at 250 mV. (c) Normalised statistic of charge drops along with a Gaussian distribution fitting for actin and actin bound with two drugs. The charge drop is equivalent to the integral area of individual translocation events. (d) Voltage dependence upon normalised capture rates of actin monomers and actin bound with two drugs.

The charge distributions were further compared for actin alone and actin in the presence of either Latrunculin B or Swinholide A (**Figure 3.19c**). The equivalent charge, calculated by integrating individual events, provides a comprehensive parameter that takes into account both dwell time and peak current. An increase in this charge profile suggests an increase in the effective charge of the molecules, which can be attributed to the spatial excluded volume in a high ionic-strength environment and molecular electrokinetics. The analysis revealed a charge profile of 2.5 ± 1.2 fAs for actin with Latrunculin B, 3.6 ± 2.0 fAs for monomeric actin, and 6.9 ± 2.9 fAs for actin with Swinholide A. The shift and wider distribution towards actin dimers, along with the increase in capture frequency, indicate the well-defined dimerisation observed in the measurements. These findings align with the crystal structure, which illustrates a limited burial of side-chain residues and a significant increase in overall surface exposure to surrounding solvent molecules upon binding with Swinholide A.

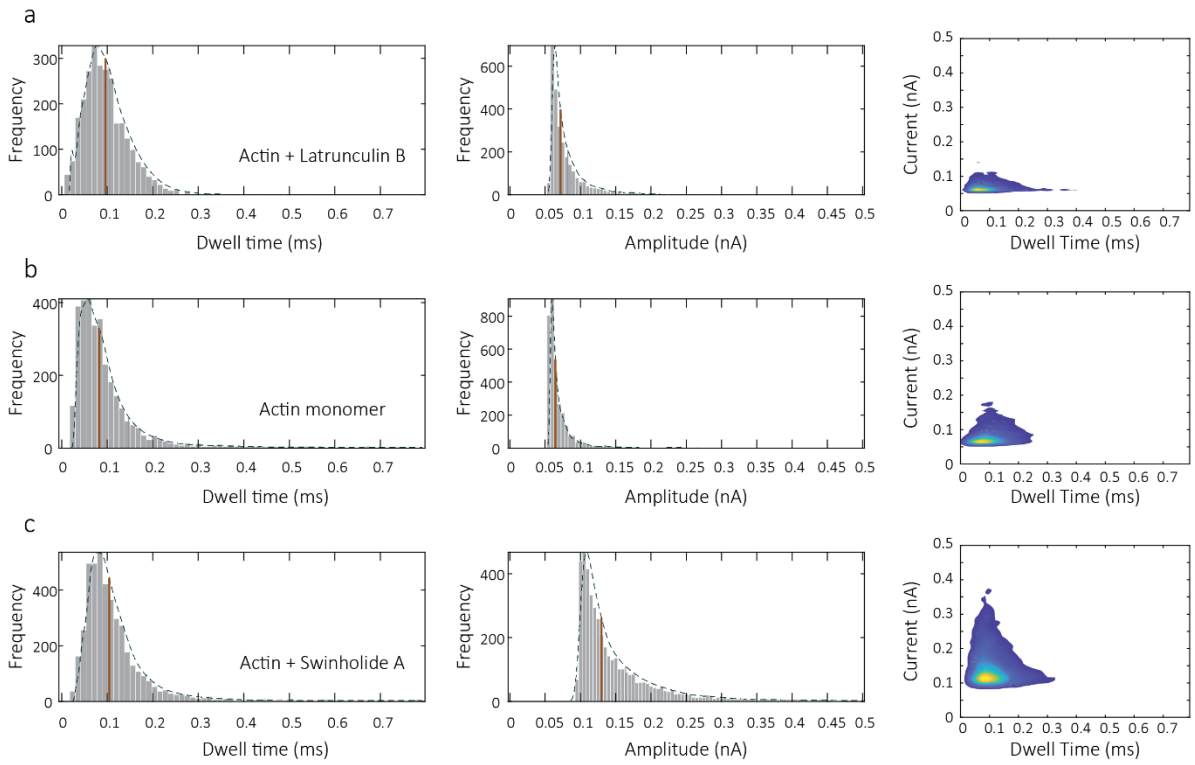


Figure 3.20 Statistic information for (a) Actin bound with Latrunculin B, (b) Actin monomers and (c) Actin bound with Swinholide A. Left: distributions of dwell time. Middle: distributions of peak current. Right: 2-D Kernel plots of peak current vs. dwell time. All data were collected in 1 µM actin and 10 µM drug at 250 mV.

The electrokinetic properties of actin monomers and dimers, including capture rate and dwell time, are shown in **Figure 3.19d and Figure 3.20**. These properties further support the conclusion that binding with Swinholide A leads to the formation of a dimeric state characterised by consistently higher net charge and electrophoretic mobility. By analysing the charge distributions and electrokinetic properties of actin with different drugs, biophysical information can be achieved into their modes of interaction and their impact on actin conformation and charge distribution. These findings contribute to the understanding of the specific mechanisms by which Latrunculin B and Swinholide A influence actin behaviour and provide a basis for further investigations into their functional implications.

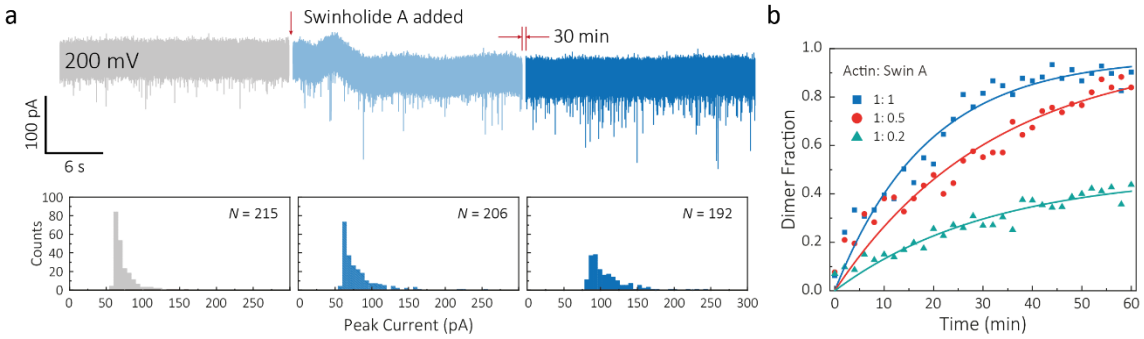


Figure 3.21 Kinetics measurements of actin drug binding. (a) Top: typical current traces for drug binding kinetics collected at 200 mV. The first extract is the stable 1 µM actin monomer translocation trace. The second is the initial trace when 1 µM Swinholide A added, and the recording after 30 min is shown in the third trace. Bottom: histograms represent the current blockade distributions corresponding to each trace above. (b) Time-dependent curves for 1 µM actin dimerisation with 1, 0.5, and 0.2 µM Swinholide A. The dimer fraction of each point was calculated from the statistical data in 2 min, with a threshold of 75 pA. The curves were fitted by a model of three-component interactions with positive cooperativity.

The efficiency of Swinholide A binding to actin was quantified by measuring the dimer fraction as a function of time (**Figure 3.21**). The measurement was conducted at 200 mV to minimise the potential effects of changes in protein conformation caused by the electric field. Prior to the addition of Swinholide A, the measurement was run for at least one hour to ensure the

stability of protein flux. Upon the addition of two equivalents of Swinholide A, an increase in the peak current distribution was observed, indicating the formation of actin dimers upon drug binding. The dimer fraction reached a plateau of around 90% after 30 minutes, as shown in the time-dependent binding curves (Figure 3.21b). Different drug concentrations (with molar ratios of 1: 1, 1: 0.5, 1: 0.2, Actin: Swinholide A) were fitted using a positive, cooperative model. [49] In this model, Swinholide A has a positive effect on actin dimerisation, resulting in an exponential accumulation curve of the dimer fraction. The plateau represents the saturated concentration of actin dimers, and its corresponding rate constant can be extracted using the provided equation.

It should be noted that the detection of dimers has a lag behind their in-situ formation due to free diffusion and drift caused by electric fields. Therefore, the results reflect the apparent kinetics of protein association. At a low drug binding ratio (e.g., 1: 0.2), the calculated saturated concentration of dimers (48%) is larger than the actual stoichiometric ratio (33%) because actin dimers have a higher flux than monomers at the same concentration (Figure 3.19d). This study represents the first visualisation of real-time drug binding of native actin molecules at a single-molecule level, highlighting the potential of quartz nanopipettes for targeted drug discovery. By providing insights into the kinetics and efficiency of drug binding, this approach offers a powerful tool for understanding the molecular interactions between drugs and their protein targets, paving the way for future advancements in drug discovery and development.

3.4 Conclusions

This chapter highlights the advantages of nanopore sensing for single-molecule analysis of actin and its interactions with drugs. Unlike other techniques that require protein modifications or labelling, nanopore sensing allows for the study of native actin without interfering with its structure or function. The high throughput and fast data acquisition rate of nanopore sensing provide unique insights into protein folding landscapes and drug binding with enhanced statistical power. The study also sheds light on the mechanism of urea-induced protein unfolding. The observed changes in excluded volumes and the disappearance of

subpopulations support the model of cooperative unfolding, where urea directly interacts with the protein rather than indirectly affecting water molecules. The ability to distinguish between actin-binding drugs, Latrunculin B and Swinholide A, and the detection of minor changes in charge highlight the potential of nanopore sensing in drug discovery. The real-time observation of drug-induced changes and the proposal of a positive cooperativity model demonstrate the power of this technique in understanding drug-protein interactions. The combination of experimental data with computational analysis and classification may enable high-throughput single-molecule drug screening and prediction of the mode of interaction. [24]

Looking ahead, the sensitivity of quartz nanopipettes to macromolecular and protein unfolding changes holds promise for studying diverse molecules and dynamic processes such as filament formation and protein aggregation. [50] This label-free method has potential applications in understanding diseases such as Parkinson's and Alzheimer's diseases by visualising amyloid protein aggregation in real-time. [51] Furthermore, the high sensitivity and single-molecule resolution of nanopore sensing make it a suitable platform for precise definition of reaction kinetics at the molecular level. [52] Overall, this study demonstrates the potential of nanopore sensing as a powerful tool in the study of protein dynamics, drug discovery, and molecular diagnostics. Its ability to provide real-time, label-free, and high-resolution analysis opens up new possibilities for understanding complex biological processes and developing targeted therapies.

3.5 References

1. Dominguez R, Holmes KC. Actin Structure and Function. *Annual Review of Biophysics* **40**, 169-186 (2011).

2. Agrawal PB*, et al.* Heterogeneity of nemaline myopathy cases with skeletal muscle α-actin gene mutations. *Annals of Neurology* **56**, 86-96 (2004).

3. Johnson S*, et al.* Truncated Latrunculins as Actin Inhibitors Targeting Plasmodium falciparum Motility and Host Cell Invasion. *Journal of Medicinal Chemistry* **59**, 10994-11005 (2016).

4. Cossart P, Sansonetti PJ. Bacterial Invasion: The Paradigms of Enteroinvasive Pathogens. *Science* **304**, 242-248 (2004).

5. Galkin VE, Orlova A, Lukoyanova N, Wriggers W, Egelman EH. Actin Depolymerizing Factor Stabilizes an Existing State of F-Actin and Can Change the Tilt of F-Actin Subunits. *Journal of Cell Biology* **153**, 75-86 (2001).

6. Galkin VE, VanLoock MS, Orlova A, Egelman EH. A New Internal Mode in F-Actin Helps Explain the Remarkable Evolutionary Conservation of Actin's Sequence and Structure. *Current Biology* **12**, 570-575 (2002).

7. Schmid MF, Sherman MB, Matsudaira P, Chiu W. Structure of the acrosomal bundle. *Nature* **431**, 104-107 (2004).

8. Stuart SF, Leatherbarrow RJ, Willison KR. A Two-step Mechanism for the Folding of Actin by the Yeast Cytosolic Chaperonin. *Journal of Biological Chemistry* **286**, 178-184 (2011).

9. Willison KR. The structure and evolution of eukaryotic chaperonin-containing TCP-1 and its mechanism that folds actin into a protein spring. *Biochemical Journal* **475**, 3009-3034 (2018).

10. Matusovsky OS, Mansson A, Persson M, Cheng Y-S, Rassier DE. High-speed AFM reveals subsecond dynamics of cardiac thin filaments upon Ca2+ activation and heavy meromyosin binding. *Proceedings of the National Academy of Sciences* **116**, 16384-16393 (2019).

11. Kabsch W, Mannherz HG, Suck D, Pai EF, Holmes KC. Atomic structure of the actin: DNase I complex. *Nature* **347**, 37-44 (1990).

12. Urban E, Jacob S, Nemethova M, Resch GP, Small JV. Electron tomography reveals unbranched networks of actin filaments in lamellipodia. *Nature Cell Biology* **12**, 429-435 (2010).

13. Ooi A, Yano F, Okagaki T. Thermal stability of carp G-actin monitored by loss of polymerization activity using an extrinsic fluorescent probe. *Fisheries Science* **74**, 193-199 (2008).

14. Unzue A*, et al.* Iriomoteolides: novel chemical tools to study actin dynamics. *Chemical Science* **9**, 3793-3802 (2018).

15. Morton WM, Ayscough KR, McLaughlin PJ. Latrunculin alters the actin-monomer subunit interface to prevent polymerization. *Nature Cell Biology* **2**, 376-378 (2000).

16. Bubb MR, Spector I, Bershadsky AD, Korn ED. Swinholide A Is a Microfilament Disrupting Marine Toxin That Stabilizes Actin Dimers and Severs Actin Filaments (∗). *Journal of Biological Chemistry* **270**, 3463-3466 (1995).

17. Ivanov AP, Actis P, Jönsson P, Klenerman D, Korchev Y, Edel JB. On-Demand Delivery of Single DNA Molecules Using Nanopipets. *ACS Nano* **9**, 3587-3595 (2015).

18. Houghtaling J*, et al.* Estimation of Shape, Volume, and Dipole Moment of Individual Proteins Freely Transiting a Synthetic Nanopore. *ACS Nano* **13**, 5231-5242 (2019).

19. Ren R*, et al.* Nanopore extended field-effect transistor for selective single-molecule biosensing. *Nature Communications* **8**, 586 (2017).

20. Miles BN, Ivanov AP, Wilson KA, Doğan F, Japrung D, Edel JB. Single molecule sensing with solid-state nanopores: novel materials, methods, and applications. *Chemical Society Reviews* **42**, 15-28 (2013).

21. Freedman KJ, Haq SR, Edel JB, Jemth P, Kim MJ. Single molecule unfolding and stretching of protein domains inside a solid-state nanopore by electric field. *Scientific Reports* **3**, 1638 (2013).

22. Oukhaled A*, et al.* Dynamics of Completely Unfolded and Native Proteins through Solid-State Nanopores as a Function of Electric Driving Force. *ACS Nano* **5**, 3628-3638 (2011).

23. Talaga DS, Li J. Single-Molecule Protein Unfolding in Solid State Nanopores. *Journal of the American Chemical Society* **131**, 9287-9297 (2009).

24. Si W, Aksimentiev A. Nanopore Sensing of Protein Folding. *ACS Nano* **11**, 7091-7100 (2017).

25. Yusko EC, Prangkio P, Sept D, Rollings RC, Li J, Mayer M. Single-Particle Characterization of Aβ Oligomers in Solution. *ACS Nano* **6**, 5909-5919 (2012).

26. Yu R-J*, et al.* Single molecule sensing of amyloid-β aggregation by confined glass nanopores. *Chemical Science* **10**, 10728-10732 (2019).

27. Sze JYY, Ivanov AP, Cass AEG, Edel JB. Single molecule multiplexed nanopore protein screening in human serum using aptamer modified DNA carriers. *Nature Communications* **8**, 1552 (2017).

28. Olshina MA*, et al.* Plasmodium falciparum coronin organizes arrays of parallel actin filaments potentially guiding directional motility in invasive malaria parasites. *Malaria Journal* **14**, 280 (2015).

29. Meller A, Branton D. Single molecule measurements of DNA transport through a nanopore. *ELECTROPHORESIS* **23**, 2583-2591 (2002).

30. Firnkes M, Pedone D, Knezevic J, Döblinger M, Rant U. Electrically Facilitated Translocations of Proteins through Silicon Nitride Nanopores: Conjoint and Competitive Action of Diffusion, Electrophoresis, and Electroosmosis. *Nano Letters* **10**, 2162-2167 (2010).

31. Waduge P*, et al.* Nanopore-Based Measurements of Protein Size, Fluctuations, and Conformational Changes. *ACS Nano* **11**, 5706-5716 (2017).

32. Cai S, Sze JYY, Ivanov AP, Edel JB. Small molecule electro-optical binding assay using nanopores. *Nature Communications* **10**, 1797 (2019).

33. Li W*, et al.* Single Protein Molecule Detection by Glass Nanopores. *ACS Nano* **7**, 4129-4134 (2013).

34. Egelman EH. A tale of two polymers: new insights into helical filaments. *Nature Reviews Molecular Cell Biology* **4**, 621-631 (2003).

35. Kuznetsova IM, Povarova OI, Uversky VN, Turoverov KK. Native globular actin has a thermodynamically unstable quasi-stationary structure with elements of intrinsic disorder. *The FEBS Journal* **283**, 438-445 (2016).

36. Levitsky DI, Pivovarova AV, Mikhailova VV, Nikolaeva OP. Thermal unfolding and aggregation of actin. *The FEBS Journal* **275**, 4280-4295 (2008).

37. Santoro MM, Bolen DW. A test of the linear extrapolation of unfolding free energy changes over an extended denaturant concentration range. *Biochemistry* **31**, 4901-4907 (1992).

38. Freedman KJ*, et al.* Chemical, Thermal, and Electric Field Induced Unfolding of Single Protein Molecules Studied Using Nanopores. *Analytical Chemistry* **83**, 5137-5144 (2011).

39. Arjmandi N, Van Roy W, Lagae L, Borghs G. Measuring the Electric Charge and Zeta Potential of Nanometer-Sized Objects Using Pyramidal-Shaped Nanopores. *Analytical Chemistry* **84**, 8490-8496 (2012).

40. Pappenberger G, McCormack EA, Willison KR. Quantitative Actin Folding Reactions using Yeast CCT Purified via an Internal Tag in the CCT3/γ Subunit. *Journal of Molecular Biology* **360**, 484-496 (2006).

41. Muthukumar M. Theory of capture rate in polymer translocation. *The Journal of Chemical Physics* **132**, 195101 (2010).

42. Matsudaira P, Bordas J, Koch MH. Synchrotron x-ray diffraction studies of actin structure during polymerization. *Proceedings of the National Academy of Sciences* **84**, 3151-3155 (1987).

43. Fitzkee NC, Rose GD. Reassessing random-coil statistics in unfolded proteins. *Proceedings of the National Academy of Sciences* **101**, 12497-12502 (2004).

44. Shortle D, Ackerman MS. Persistence of Native-Like Topology in a Denatured Protein in 8 M Urea. *Science* **293**, 487-489 (2001).

45. Tripathi P*, et al.* Electrical unfolding of cytochrome c during translocation through a nanopore constriction. *Proceedings of the National Academy of Sciences* **118**, e2016262118 (2021).

46. Chou SZ, Pollard TD. Mechanism of actin polymerization revealed by cryo-EM structures of actin filaments with three different bound nucleotides. *Proceedings of the National Academy of Sciences* **116**, 4265-4274 (2019).

47. Kudryashov DS*, et al.* The crystal structure of a cross-linked actin dimer suggests a detailed molecular interface in F-actin. *Proceedings of the National Academy of Sciences* **102**, 13105-13110 (2005).

48. Spector I, Shochet NR, Kashman Y, Groweiss A. Latrunculins: Novel Marine Toxins That Disrupt Microfilament Organization in Cultured Cells. *Science* **219**, 493-495 (1983).

49. Saito S-y*, et al.* Actin-Depolymerizing Effect of Dimeric Macrolides, Bistheonellide A and Swinholide A1. *The Journal of Biochemistry* **123**, 571-578 (1998).

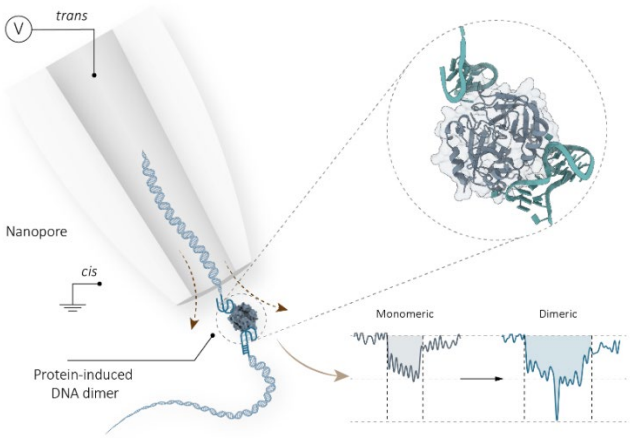
50. Jakova E, Lee JS. Behavior of α-synuclein–drug complexes during nanopore analysis with a superimposed AC field. *ELECTROPHORESIS* **38**, 350-360 (2017).

51. Bryan T, Luo X, Forsgren L, Morozova-Roche LA, Davis JJ. The robust electrochemical detection of a Parkinson's disease marker in whole blood sera. *Chemical Science* **3**, 3468-3473 (2012).

52. Chen X*, et al.* Label-Free Detection of DNA Mutations by Nanopore Analysis. *ACS Applied Materials & Interfaces* **10**, 11519-11528 (2018).

CHAPTER 4

Single-molecule protein profiling using nanopores and dimeric aptamer-modified DNA carriers



Synopsis

This chapter introduces a novel approach to single-molecule protein detection, centred on the use of aptamer-modified DNA carriers. Contrasting conventional nanopore sensing, this method harnesses protein-binding-induced DNA dimerisation, forsaking subpeaks, to achieve the identification of target proteins. The hallmark of this technique lies in its simplicity of charge classification, which facilitates a clear differentiation between DNA monomers and dimers. The approach efficiently detects dimeric proteins (e.g., VEGF, PDGF) using homogenous DNA carriers. It holds potential for detecting any protein with dual aptamer-binding domains, as seen with thrombin and HD1/HD22 aptamers. This method impressively visualises c-Met receptor dimerisation prompted by its ligand in complex human serum. These findings advance protein analysis, offering a promising routine towards early-stage diagnostics and prognostics.

Part of this chapter is in preparation as **Wang, X.**; Liu, Y.; Ren, R.; Ivanov, A. P.; Edel, J. B. Single-molecule protein profiling using nanopores and dimeric aptamer-modified DNA carriers.

4.1 Introduction

Early detection of disease biomarkers, particularly in cases such as cancer and neurodegenerative disorders, holds immense potential to enhance treatment outcomes and patient survival rates. [1] However, biomarkers in their early stages often exhibit low abundance and distinct characteristics compared to advanced stages. [2] Consequently, the demands on detection technologies are heightened. Conventional detection methods often struggle with providing the requisite sensitivity and specificity to multiplex diverse biomarkers, especially proteins. [3] Furthermore, clinical diagnosis and prognosis necessitate compatibility with small-volume biofluids, driving the need for robust and highly sensitive detection systems. [4] In contrast, nanopore-based analysers offer a distinctive set of advantages in protein analysis and even protein sequencing. [5] By applying an electric field, these analysers can detect unlabelled single molecules through the alteration of ionic current as these molecules translocate through the nanopore. Through the analysis of individual events generated, it becomes possible to comprehensively characterise biomolecules such as nucleic acids and proteins, thereby obtaining insights into their structural and functional attributes. [6] Building on the substantial advancements achieved in the development of nanopore-based DNA sequencers, the field is now rapidly progressing towards enabling proteomics analyses encompassing protein sequencing and fingerprinting. [7]

The success of nanopores for DNA sequencing has marked a significant achievement, yet the application of the same technology to protein analysis presents distinct challenges. [8] Firstly, proteins are composed of twenty different amino acids, each varying in charge, polarity, and hydrophobicity. This inherent variability prompts proteins to adopt intricate and adaptable three-dimensional structures within aqueous environments. Compounded by a heterogeneous charge distribution on their surfaces, in contrast to the uniformly negatively charged backbone of DNA, the complex folding patterns of proteins make them challenging to capture and translocate through nanopores due to the presence of weak electrokinetic forces. [9] Secondly, while DNA samples can be amplified through techniques such as PCR, proteins lack a comparable amplification method. This poses a predicament when considering the typical high concentration requirements for effective nanopore measurements. Thus, detecting proteins

with low copy numbers, such as those present in cells (< 1000 copies per cell), becomes hindered due to these concentration limitations. Lastly, the fast translocation of proteins through nanopores, particularly smaller proteins (< 15 kDa), often occurs at speeds that outpace the temporal resolution of the detection system. [10] This high-speed translocation results in numerous events becoming undetectable and distorted, consequently obscuring the reliability of nanopore readouts. Despite advancements in high-bandwidth instrumentation, the optimisation of nanopore fabrication and the enhancement of signal-to-noise ratios (SNRs) remain persistent technical challenges that need to be overcome. [11]

To date, the use of molecular carriers has emerged as a versatile and effective strategy used in protein nanopore sensing. [6] These molecular carriers typically feature a suitably charged backbone, which could be composed of DNA, [12, 13] charged peptides, [9] or metallic nanoparticles. [14] The charged carriers facilitate the transport of proteins through the nanopores, enhancing the overall efficiency of the detection process. Among the range of carriers available, DNA carriers have garnered notable attention due to their swift development. This is attributed to their rigid double-helix structure, customisable sequence, and the availability of origami scaffolds. Recently, a breakthrough was achieved in reading peptide sequences and identifying post-translational modifications through the integration of analyte peptides with carrier DNA molecules. [15, 16] The success of this method hinges upon the precisely controlled translocation guided by the DNA carrier, drawing inspiration from DNA sequencing systems. In the context of protein detection, the target protein is typically tethered to the DNA carrier, forming a bond either covalently or non-covalently. The presence of the target protein triggers a discernible subpeak within the DNA translocation signal, effectively acting as a distinct signature indicating the successful binding. [13] However, it is important to note that such detection methods often operate under high ionic strength conditions, reaching up to 4 M LiCl concentration. [12] While effective in the detection process, this elevated salt concentration substantially deviates from physiological levels, potentially disrupting the native conformation of proteins and interfering with their successful interaction with the DNA carrier. [17]

To address these key challenges, this chapter introduces a new nanopore-based protein profiling strategy based on the construction of an aptamer-protein-aptamer sandwich structure, further amplified by the incorporation of a DNA carrier, as illustrated in Figure 4.1. The DNA carrier is enzymatically engineered from lambda phage DNA (λ-DNA), boasting a length of 4361 base pairs. This carrier is subsequently subjected to hybridisation and ligation with an aptamer probe, positioned on its 12-base sticky overhang. Crucially, this detection methodology can be operated within low salt concentrations (100 mM KCl), showcasing enhanced conductive events during the translocation of individual molecules. A particularly noteworthy advancement lies in the proposition of a streamlined classification methodology. This approach employs a singular parameter, equivalent charge (peak area), to discern protein-binding-induced DNA dimers, effectively bypassing the necessity for subpeak identification. Theoretically, this strategy can be universally applied to detect proteins with dual aptamer-binding sites, enhancing its versatility. This methodology is exemplified by the detection of thrombin through carriers modified with HD1 and HD22 aptamers. Intriguingly, the HD1-thrombin-HD22 sandwich structure introduces an unexpected subpeak within the heterodimeric DNA events, resembling observations at higher salt concentrations. Additionally, this approach finds optimal utility in detecting protein dimers. Employing vascular endothelial growth factor (VEGF) and platelet-derived growth factor (PDGF) as model proteins, two identical aptamer-modified carriers orchestrate the formation of a sandwich structure, culminating in a remarkably low limit of detection. Furthermore, this strategy extends its utility to the observation of hepatocyte growth factor (HGF)-induced c-Met receptor dimerisation and the subsequent inhibitory impact of anti-HGF antibodies. It is worth highlighting that the subpeak height correlates consistently with the protein size, underlining its potential for precise identification of diverse proteins. Encouragingly, the compatibility of this method with real clinical samples, such as human serum, further accentuates its applicability. Ultimately, this approach unveils a universally applicable framework for the identification and quantification of minute proteins and their interactions in conditions mirroring physiological settings. As a result, this innovation holds promise for early-stage diagnosis and prognosis, elevating the potential for proactive disease management.

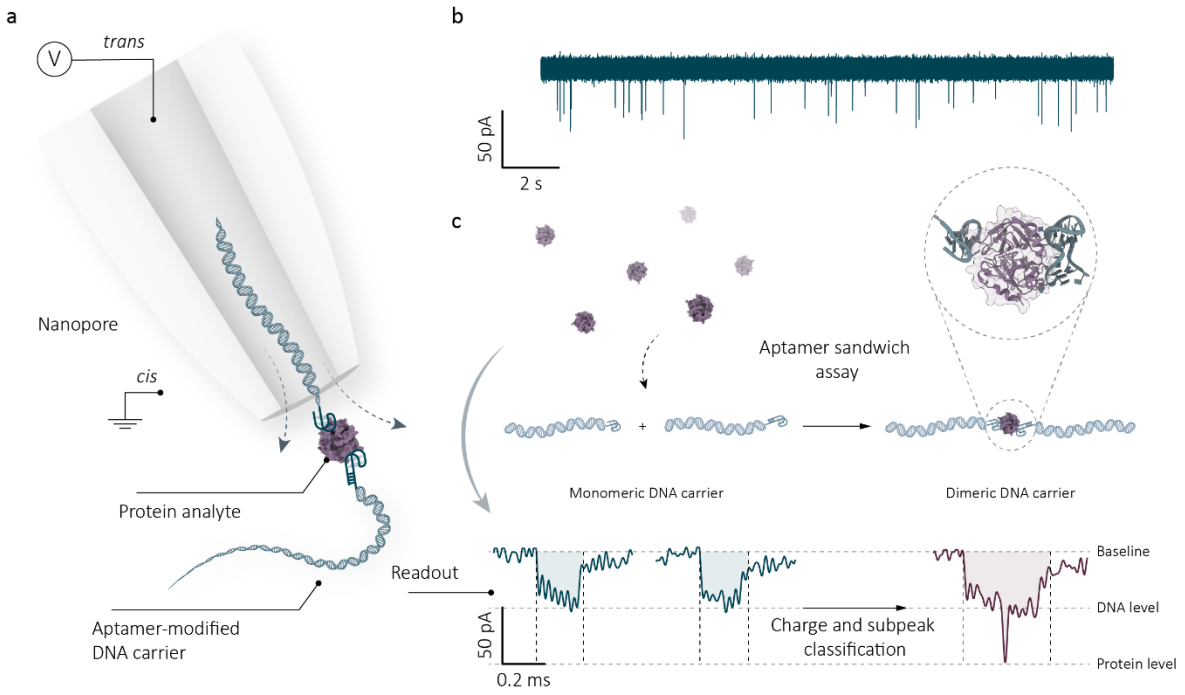


Figure 4.1 Nanopore-based protein detection using aptamer-protein-aptamer sandwich structures. (a) Schematic of the experimental setup of single-molecule detection process using nanopipettes. The protein analyte binds to two aptamer-modified DNA carriers, generating a dimeric complex that signifies the presence of the target protein. The protein analytes, along with the DNA carriers, is positioned within the interior of the nanopipette (*trans* side), where a working Ag/AgCl electrode is situated. The external bath (*cis* side) is filled with the measuring buffer (100 mM KCl, 10 mM Tris-EDTA pH 8.0), accompanied by the reference Ag/AgCl electrode. (b) A typical current trace highlighting the occurrence of conductive current events under the application of a bias of -300 mV. (c) Proteins possessing two aptamer-binding sites, exemplified by thrombin (PDB: 5EW2), have the capability to establish a sandwich structure in conjunction with the specially engineered DNA carriers. Upon the successful formation of such structures, translocation events exhibit distinctive characteristics including double dwell time and charge, as well as the emergence of a discernible subpeak at the midpoint of the event.

4.2 Methods and materials

4.2.1 Preparation of aptamer-modified DNA carriers

The 4.3 kbp aptamer-modified DNA carriers were prepared by digestion of lambda phage DNA (λ-DNA, 48.5 kbp) using a restriction enzyme, HindIII, followed by integrating the aptamer probe into the sticky overhangs of the 4.3 kbp fragments, separating and purifying using agarose gel. In brief, 12.5 µl of commercial λ-DNA (15.8 nM, New England Biolabs, UK) was mixed with 2.5 µl HindIII-HF (New England Biolabs, UK), 5 µl of 10× rCutSmart buffer (New England Biolabs, UK) and 30 µl of nuclease-free water (Thermo Scientific, US) and incubated at 37 °C for 60 min, followed by thermal inactivating at 80 °C for 20 min. After the digestion, excess phosphorylated DNA aptamer (1 µl of 100 µM aptamer solution) (Integrated DNA Technologies IDT, US) was added into the digested mixture. A hybridisation procedure was run using a PCR annealing device (TC-3000, TECHNE) with a customised protocol: the mixture was first heated to 75 °C for 5 min, then cooled down gradually to 15 °C at a rate of 1 °C/min, and finally held at 4 °C. The sequences of aptamers can be found in Table 4.1. The resulting product was then ligated by adding 2.5 µl of T4 DNA ligase (400 units/µl, New England Biolabs, UK) and 6 µl of 10× T4 DNA ligase reaction buffer (New England Biolabs, UK). The ligation was performed at 22 °C for 2 hours, followed by inactivation at 65 °C for 15 min. To purify the final product, the ligated DNA carriers were separated by a preparative gel and then extracted using Monarch DNA Gel Extraction Kit (New England Biolabs, UK). The final concentration of the carrier was determined by measuring the absorption at 260 nm using NanoDrop 2000 (Thermo Scientific, US).

4.2.2 Fabrication of nanopipettes

In the fabrication process of single-barrel nanopipettes, quartz capillaries (GQF100-50-7.5, World Precision Instruments, UK) were first subjected to plasma cleaning (Harrick Plasma, US) for at least 30 min. This cleaning step ensures the removal of any contaminants and improves the surface properties of the capillaries. The cleaned capillaries were then pulled by a laser-based pipette puller (Sutter Instrument, P-2000, USA following a two-line protocol: (1) HEAT =

825, FIL = 4, VEL = 30, DEL = 130, PUL = 80; (2) HEAT = 850, FIL = 3, VEL = 20, DEL = 127, PUL = 185. It is important to note that these pulling parameters are instrument-specific and were fine-tuned to achieve nanopore openings with a diameter of 15 ± 4 nm.

Table 4.1 Sequences of the aptamer probes used in this chapter.

Name	Sequences
Thrombin probe 1	5'-GGGCGGCGACCT TTTTTT GGTTGGTGTGGTTGG
Thrombin probe 2	5'-GGGCGGCGACCT TTTTTT AGTCCGTGGTAGGGCAGGTTGGGGTGACT
VEGF probe	5'-GGGCGGCGACCT TTTTTT TGTGGGGGTGGACGGGCCGGGTAGA
PDGF probe	5'-GGGCGGCGACCT TTTTTT CACAGGCTACGGCACGTAGAGCATCACCATGATCCTGTG
c-Met probe	5'-GGGCGGCGACCT TTTTTT TGGATGGTAGCTCGGTCGGGGTGGGTGGGTTGGCAAGTCT

The blue coloured sequence is the complementary bases to the 12-base sticky end of the carrier DNA, and the red coloured sequence is the aptamer probe targeting different proteins.

4.2.3 Nanopore measurements and data processing

Nanopore experiments were performed in a measuring buffer containing 100 mM KCl and 10 mM Tris-EDTA (pH = 8) unless noted otherwise. For the binding assays, 200 pM aptamer-modified DNA carriers were incubated with the analyte protein with a gradient of concentrations at 37 °C for at least 2 h prior to nanopore measurements. Analyte proteins tested in this work include Recombinant Human VEGF 165 Protein (R&D Systems, US), Recombinant Human PDGF-BB Protein (R&D Systems, US), Human alpha-Thrombin (Prolytix,

US), Recombinant Human HGFR/c-MET Fc Chimera His-tag Protein (R&D Systems, US), Recombinant Human HGF Protein (R&D Systems, US) and Human HGF Antibody (R&D Systems, US). Human serum was from Sigma-Aldrich, US.

To perform nanopore measurements, approximately 10 µL of the buffer solution containing the DNA carriers and proteins was filled inside the nanopipette (*trans* chamber) via a MicroFil needle (MF34G, World Precision Instruments, UK). Freshly made Ag/AgCl electrodes were then inserted into the nanopipette (*trans* chamber) and the bath (*cis* chamber), respectively. All ionic current recordings were performed using a high-bandwidth amplifier VC100 (Chimera Instruments, US). The recorded data were resampled to 1 MHz and low-pass filtered at 30 kHz. Analysis of all translocation events was performed using a MATLAB-based code, The Nanopore App, written by Professor Joshua B. Edel. A workflow of the analysis procedure is shown in Chapter 2.

4.3 Results and discussion

4.3.1 Experimental setup and sensing principle

Nanopore experiments were conducted using single-barrel quartz nanopipettes that were fabricated through a laser-assisted pulling process, following established protocols. [9] The size of the nanopores was thoroughly characterised using both scanning electron microscopy (SEM) and conductance measurements, as depicted in Figure 4.2. In the electrical experiments, a measuring buffer was employed, composed of 100 mM KCl and 10 mM Tris-EDTA, with a pH of 8.0, unless explicitly mentioned otherwise. The I-V curves displayed the characteristic ionic current rectification behaviour, consistent with the nanopipette feature reported previously. [18] Within the experimental setup, DNA carriers and protein analytes were introduced into the interior of the nanopipette (*trans* chamber), where a working Ag/AgCl electrode was situated. In the external bath (*cis* chamber), a reference Ag/AgCl electrode was immersed in the buffer solution. The ionic current traces were recorded using a high-bandwidth amplifier (Chimera Instruments, VC100) operating at a sampling rate of 1 MHz. Subsequently, these recorded

signals were subjected to further low-pass filtration, limiting their frequency range to 30 kHz, unless specific parameters dictated otherwise. The power spectral density (PSD) plot was employed to validate that the obtained signals maintained low noise levels, an anticipated attribute of such a measuring system, as displayed in Figure 4.3.

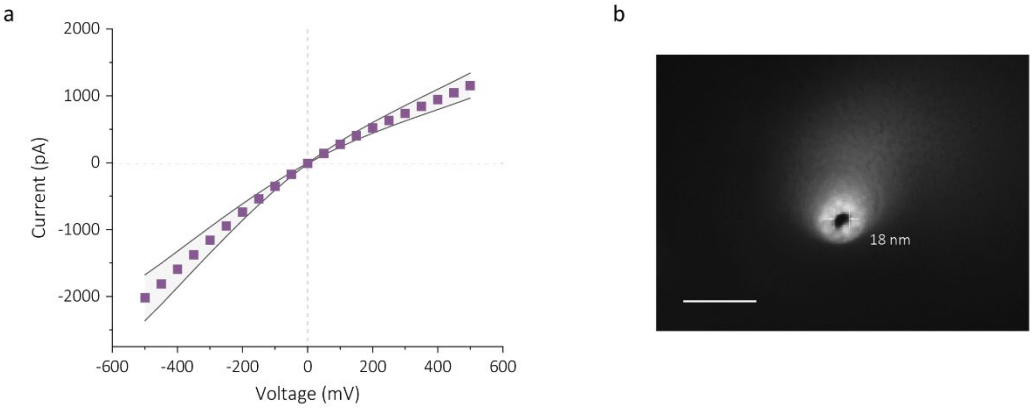


Figure 4.2 SEM and conductance characterisation of nanopipettes. The nanopipettes used in this work were fabricated from quartz capillaries (ID: 0.5 mm, OD: 1.0 mm) by a laser-assisted puller. (a) I-V curves were measured from 20 different pipettes in 100 mM KCl, 10 mM Tris-EDTA, pH 8.0 buffer, showing a current rectification feature. (b) Top-view SEM images of a typical nanopore (scale bar: 100 nm).

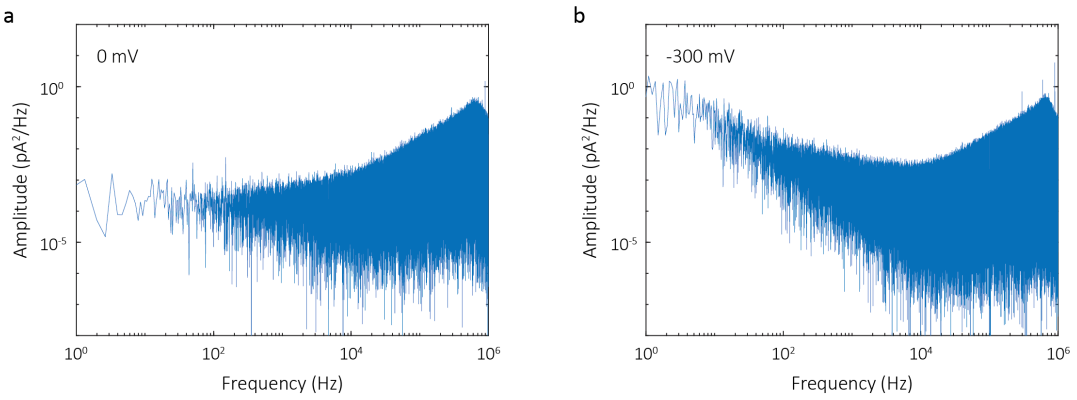


Figure 4.3 Noise evaluation for nanopore measurements. The power spectral density (PSD) plots for the nanopipette system under a bias of (a) 0 mV and (b) -300 mV.

In the experimental conditions, DNA translocation from the *trans* chamber to the *cis* chamber exhibited a conductive current enhancement when subjected to a negative bias. However, in the opposite direction, no translocation events were detected as shown in **Figure 4.4**, which closely aligns with the results reported in similar nanopore systems. [13] The absence of DNA translocation from *cis* to *trans* chamber has been attributed to the robust electroosmotic (EO) flow, which counters the electrophoretic (EP) motion of DNA molecules. This opposition is particularly prominent due to factors such as the decreasing salt concentration leading to an increase in EO flow. Additionally, the asymmetric geometry of the nanopipette also contributes significantly to this one-way DNA translocation phenomenon. Furthermore, unlike the conventional nanopore measurements typically performed at high salt concentrations that exhibit current blockade events, the conductive current enhancement observed during DNA translocation is attributed to the introduction of supplementary counterions, specifically K^+ ions, by the charged DNA molecules confined within the nanopore. This results in a denser ion population within the nanopore confinement compared to that of open-pore current flows. This effect provides a theoretical foundation for conducting further charge classification analyses.

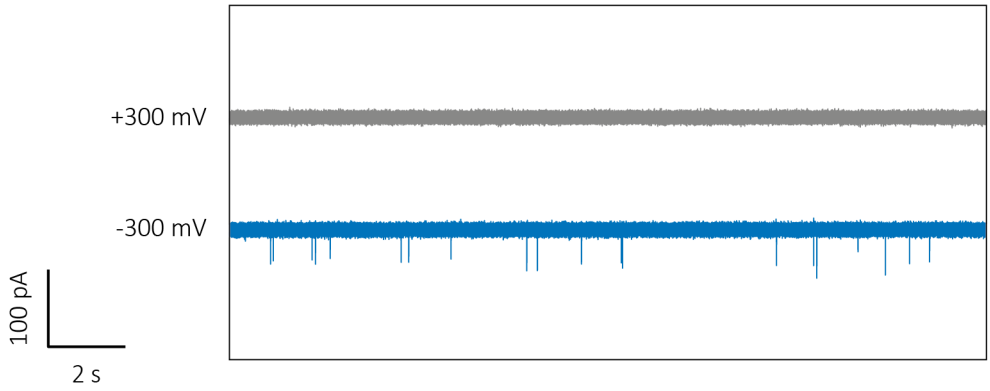


Figure 4.4 DNA translocation direction in the nanopore sensing. DNA molecules translocated from the inside to the outside of the nanopipette under a negative bias showing conductive enhancement events, whereas no translocation events were observed at positive voltages. The traces were collected from 200 pM 4.3 kbp DNA in 100 mM KCl, 10 mM Tris-EDTA pH 8.0 buffer with a voltage of ±300 mV.

4.3.2 Design and characterisation of aptamer-modified DNA carriers

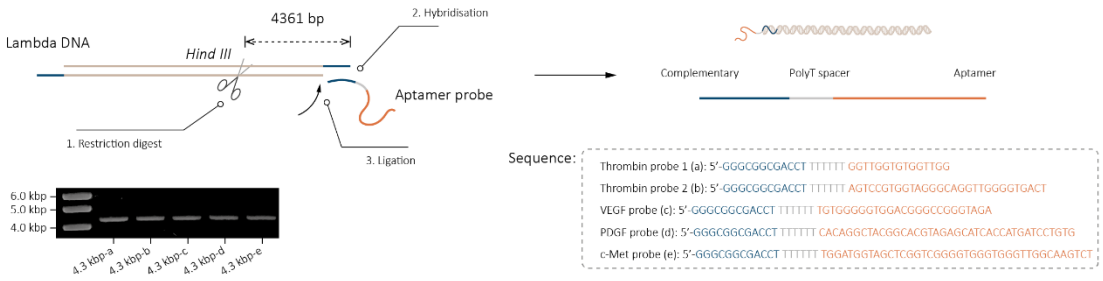


Figure 4.5 Preparation of 4.3 kbp aptamer-modified DNA carriers. 4.3 kbp DNA carriers were cleaved from λ-DNA using a restriction enzyme, Hind III, followed by hybridisation and ligation the aptamer probe to the carrier. The aptamer probe includes a sequence complementary to the 12-base sticky overhand of the 4.3 kbp carrier, a polyT spacer, and a protein aptamer sequence. Detailed sequence information is shown in the table. The final products were characterised by gel electrophoresis in the inset.

Double-stranded DNA (dsDNA) has emerged as an exceptionally well-suited molecular carrier for leading protein nanopore transport. Its rigid double-helix structure, brimming with negative charges, offers facile manipulation for the incorporation of functional recognition sites, consequently enhancing both the selectivity and efficiency of protein capture and detection. In this work specifically, phage lambda DNA (λ-DNA) was selected as the carrier source due to its extensively documented sequence information and the presence of 12-base sticky overhangs at both the 5' and 3' termini, a feature conducive to the hybridisation of a functional oligonucleotide. As depicted in Figure 4.5, the λ-DNA underwent enzymatic cleavage using the restriction endonuclease Hind III, resulting in a 4.3 kbp DNA fragment featuring a 12-base overhang at one end. Following the enzymatic digestion, an aptamer probe was hybridised and ligated to the exposed end of the 4.3 kbp DNA fragment, succeeded by a purification step involving gel extraction. The aptamer probe comprises three distinct components: a 12-base sequence complementary to the sticky end of the 4.3 kbp DNA, a spacer sequence consisting of polyT, and the aptamer sequence responsible for protein recognition. Detailed sequence information is presented in Table 4.1. The resultant aptamer-modified 4.3 kbp DNA carriers were subject to characterisation *via* gel electrophoresis and absorption spectrum, with the results presented in Figure 4.6.

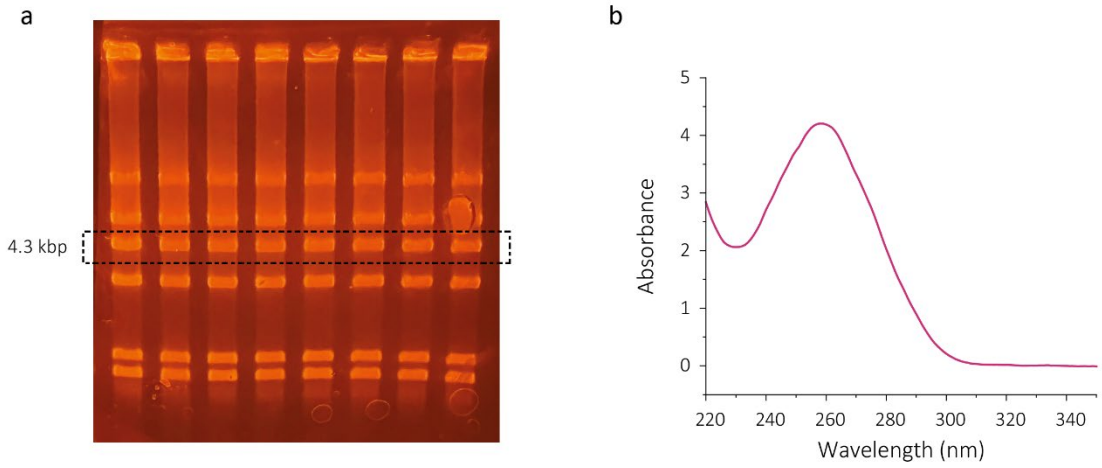


Figure 4.6 Characterisation of 4.3 kbp aptamer-modified DNA carriers. (a) Gel electrophoresis showing the fragments digested from λ-DNA using Hind III. The marked bands are the expected 4.3 kbp DNA fragments. (b) A typical absorption spectrum of the purified 4.3 kbp aptamer-modified DNA carriers showing its concentration and purity with a high 260/280 ratio.

Control experiments of the purified DNA carriers were performed under varying applied voltages, ranging from -200 to -400 mV, as shown in **Figure 4.7**. The capture rate, derived from the distribution of interval times (Δt) between consecutive translocation events, was observed to exhibit a linear voltage-dependent trend (**Figure 4.8a**). This linear relationship points toward a diffusion-limited regime governing the capture of DNA carrier molecules, particularly applicable to long molecules such as double-stranded DNA (dsDNA) under the influence of high electric fields. [19] Furthermore, the dwell time as a function of voltage was characterised through an exponential delay analysis, as depicted in **Figure 4.8b**. The resultant mean dwell time spanned from 256 ± 10 to 119 ± 2 µs, signifying the appropriateness of the applied low-pass filter of 30 kHz for signal analysis without inducing distortion. [20] As anticipated, the mean peak amplitude demonstrated a linear increment, ranging from 30.0 ± 2.3 to 77.8 ± 4.5 pA, in response to voltage variation, **Figure 4.8c**. In a delicate balance between capture efficiency and signal-to-noise ratio (SNR), an applied voltage of -300 mV was deemed optimal for subsequent nanopore measurements. Moreover, the integrated area encompassing individual events, referred to as the "equivalent charge," exhibited minimal variation amidst changes in voltage (**Figure 4.8d**). This equivalent charge is fundamentally linked to the quantity of counterions

associated with the DNA molecule.[21] This attribute holds potential for the classification of DNA lengths and even DNA conformations, thus adding to the analytical capabilities of the methodology.

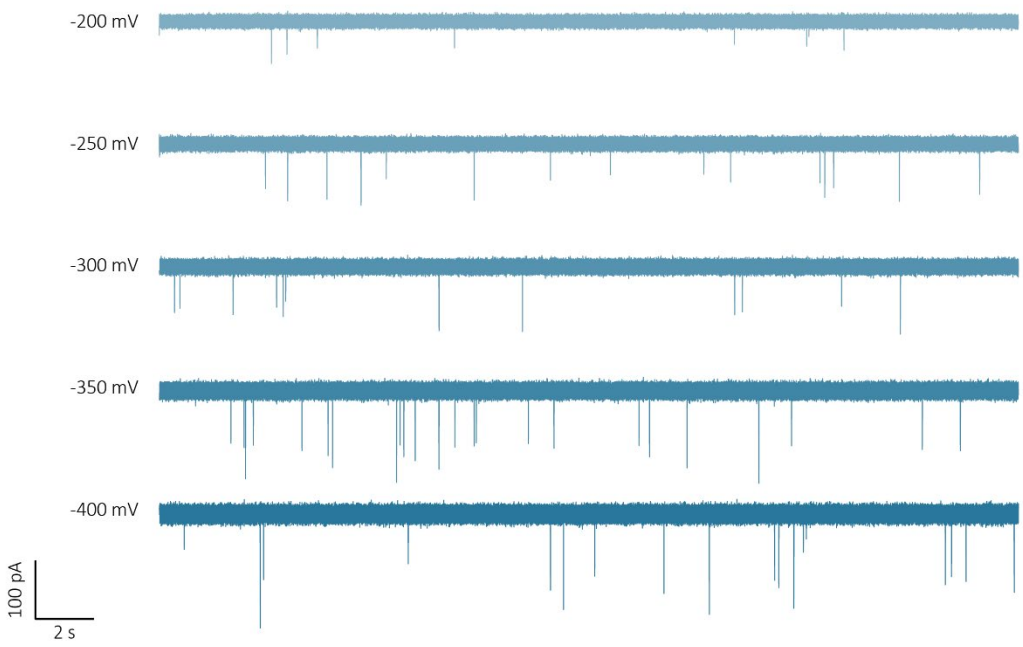


Figure 4.7 DNA translocation at varying applied voltages. Representative current traces at a gradient voltage showing the translocation of 4.3 kbp aptamer-modified DNA carrier in 100 KCl, 10 mM Tris-EDTA pH 8.0 measuring buffer.

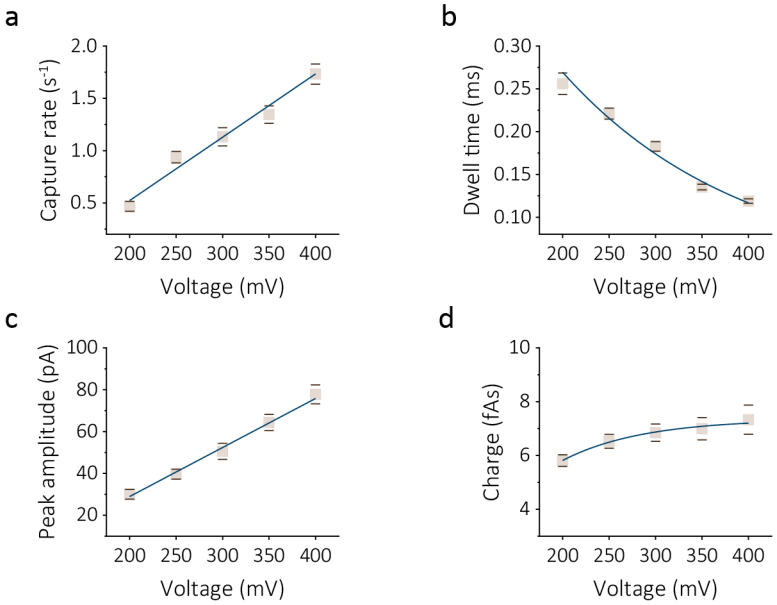


Figure 4.8 Voltage dependence of nanopore translocation for 4.3 kbp aptamer-modified DNA carriers. Plots of (a) capture rate, (b) dwell time, (c) peak amplitude and (d) equivalent charge are shown along with the fitting curve.

4.3.3 DNA length recognition by charge classification

The utilisation of aptamer-modified DNA carriers enables the targeted capture and binding of specific proteins to these carrier molecules. Conventionally, the presence of a bound protein induces a distinct subpeak in the signal, acting as the primary criterion for confirming successful protein binding. [12, 13] However, this method faces challenges in detecting smaller proteins (< 15 kDa) due to their limited SNR, making their resolution problematic. Additionally, partial folding of DNA carriers can generate similar subpeaks, leading to potential false positive events and complicating data interpretation. In this context, I have adopted a novel approach by exploiting protein-induced carrier dimerisation to indicate the presence of target proteins. This dimerisation triggers alterations in the length of DNA carriers, a characteristic that can be identified through parameters such as dwell time or peak amplitude. However, the potential for DNA folding introduces complexities in accurately distinguishing monomeric and dimeric DNA based solely on dwell time and peak amplitude. To address this challenge, I propose a

more straightforward yet informative parameter: the equivalent charge. This parameter encompasses the integration area from individual events ($Q = \int_0^t I\mathrm{d}t$, 4.1), incorporating insights from dwell time, peak amplitude, and even current fluctuations. [22]

To illustrate this concept, I employed commercially available 5 kbp and 10 kbp DNA samples to represent monomeric and dimeric DNA carriers, respectively. Recognising the sensitivity of peak area to event boundaries, I introduced the use of CUSUM+, a variant of the cumulative sum statistical algorithm, to ensure precise event detection, as demonstrated in **Figure 4.9**. [23] This strategy enhances the accuracy of event classification and serves as a pivotal step in the protein detection methodology.

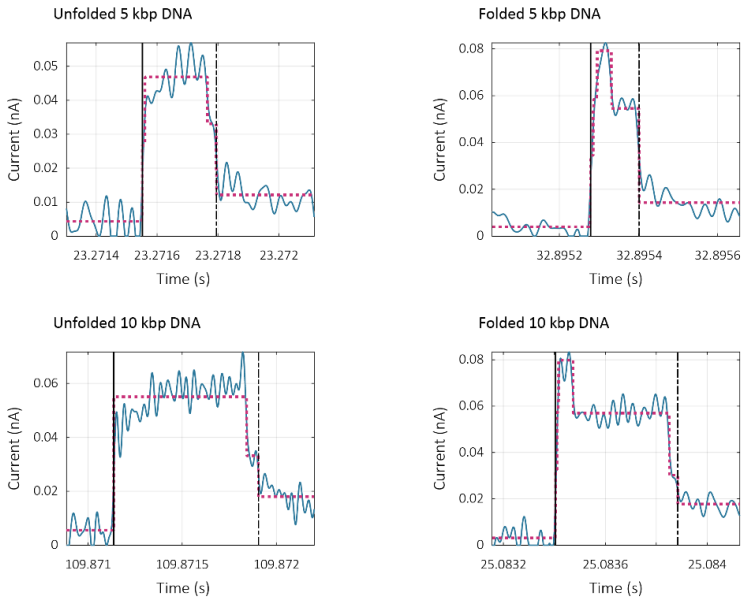


Figure 4.9 Event definition using CUSUM+ algorithm. Typical events for 5 kbp and 10 kbp DNA in both folded and unfolded states are shown in blue lines. The boundaries for event definition are established through the fitting of the CUSUM+ analysis. The equivalent charge is subsequently calculated based on the peak area within the boundaries determined by the CUSUM+ algorithm.

To validate the effectiveness of the proposed charge classification method for discriminating DNA lengths and conformations, I conducted nanopore translocation experiments using a mixture containing 200 pM 5 kbp and 200 pM 10 kbp DNA under a negative bias of -300 mV, employing the same experimental conditions. The results, as depicted in **Figure 4.10a**, revealed that the 5 kbp DNA translocates faster than the 10 kbp DNA, in line with expectations. However, due to the potential partial or full folding of DNA chains, the distribution of dwell time did not exhibit two distinct populations; instead, four overlapping populations were observed in **Figure 4.11a**. These corresponded to folded 5 kbp DNA, unfolded 5 kbp DNA, folded 10 kbp DNA, and unfolded 10 kbp DNA, in that sequence. A similar complexity was observed in the distribution of peak amplitude, **Figure 4.11b**, where the change resulting from various folding states masked the trend associated with DNA length.

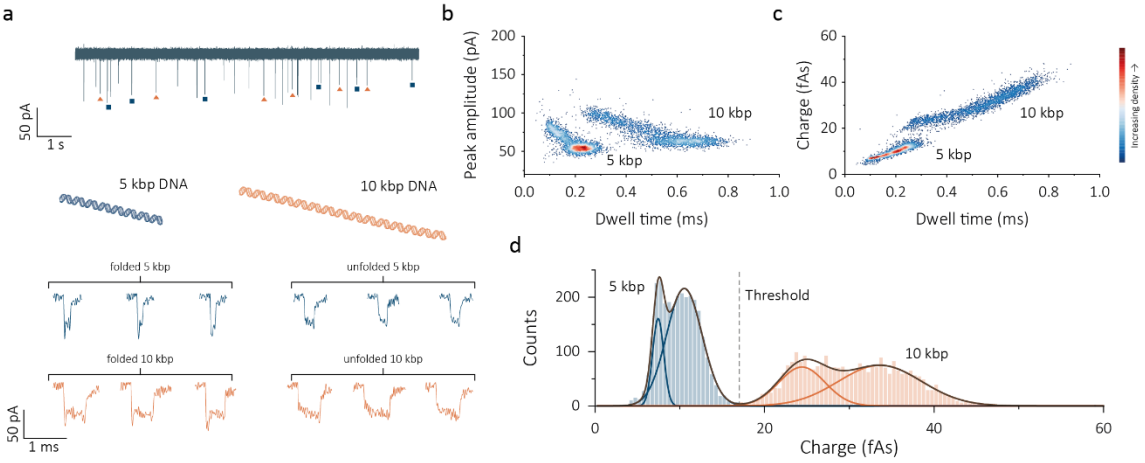


Figure 4.10 Charge classification for 5 kbp and 10 kbp DNA. (a) A representative current trace of nanopore translocation for a mixture of 200 pM 5 kbp and 200 pM 10 kbp DNA. Typical events are shown corresponding to 5 kbp and 10 kbp DNA at folded and unfolded conformations. Density scatter plots of (b) peak amplitude against dwell time, and (c) charge against dwell time for the mixture of 5 kbp and 10 kbp DNA. (d) Distribution of the charge showing that 5 kbp and 10 kbp DNA are easy to discriminate by setting a threshold of charge.

I addressed this challenge by presenting a 2D density scatter plot of peak amplitude against dwell time, showcased in **Figure 4.10b**. This plot highlighted four distinct populations corresponding to the different folded and unfolded states of 5 kbp and 10 kbp DNA. Although visually distinguishable, the precise classification of these populations required the development of a classification algorithm. [24] In contrast, the scatter plot of charge versus dwell time (**Figure 4.10c**) presented two clearly differentiated populations. Here, a singular charge threshold sufficed to separate and distinguish between the two main populations. Further solidifying the approach, the charge distribution histogram (**Figure 4.10d**) featured two well-defined primary populations, each with two sub-populations. The application of a straightforward threshold enabled the clear differentiation of 5 kbp and 10 kbp DNA. It is noteworthy that folded DNA exhibited lower charge values than unfolded DNA of the same length, primarily because the act of folding reduces the surface area of DNA molecules, subsequently decreasing the number of K+ ions bound to it. This experiment underscores the efficacy of charge classification in distinguishing DNA lengths and conformations, particularly in differentiating DNA dimers from monomers, as proposed in this study. This methodology demonstrates its potential in refining nanopore-based analysis techniques for complex DNA samples.

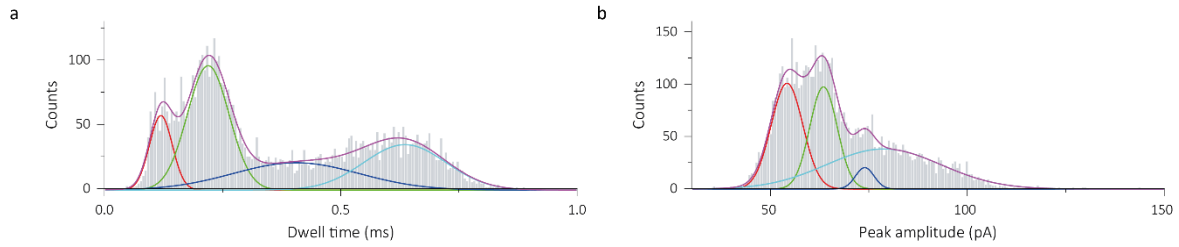


Figure 4.11 Charge classification for 5 kbp and 10 kbp DNA. Histograms of (a) dwell time and (b) peak amplitude for the mixture of 5 kbp and 10 kbp DNA, along with the multiple Gaussian fittings.

4.3.4 Thrombin detection by heterogenous dimerisation of DNA carriers

Having established the capability of this approach to distinguish between monomeric and dimeric DNA, I proceeded to investigate protein analytes with two distinct aptamer-binding sites. The initial model protein for this study was human alpha thrombin (α-thrombin), a protein with a molecular weight of 36.7 kDa and an isoelectric point (pI) ranging from 6.35 to 7.6. α-thrombin is a significant protein biomarker associated with various diseases, as it plays crucial roles in cardiovascular diseases, tumour growth regulation, and coagulation cascade reactions. [25] Additionally, it serves as a potent neurotoxin produced by injured brain endothelial cells, making it a critical biomarker for tracking Alzheimer's disease progression. [26] Detecting diseases related to thrombin at early stages necessitates a method with exceptional selectivity and sensitivity, capable of identifying trace levels of thrombin in complex biological fluids such as blood and cerebrospinal fluid (CSF). Previous research has extensively studied aptamer-based sandwich biosensors for thrombin detection, utilizing two G-quadruplex aptamers that target distinct exosites of the thrombin protein. [27] These aptamers include a 15-mer thrombin-binding aptamer (TBA), also known as HD1, with an affinity constant (K_d) of approximately 20.2 nM, and a 29-mer aptamer named HD22, with a K_d of around 3.5 nM. Furthermore, an avidity effect has been observed, resulting in a tenfold enhancement in the binding affinity against thrombin when HD1 and HD22 are dimerised. [28] This unique dimerisation of aptamers has contributed to improved sensitivity and selectivity in detecting thrombin and offers a promising avenue for the early diagnosis and monitoring of diseases linked to thrombin dysregulation.

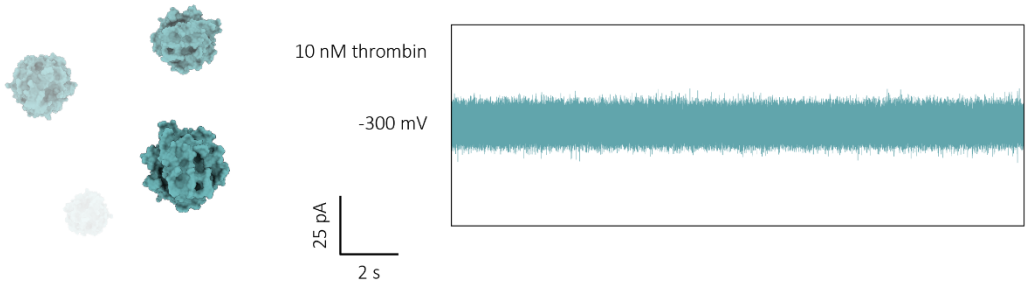


Figure 4.12 Nanopore measurements of pure thrombin. Nanopore experiments were performed using 10 nM thrombin in 100 mM KCl measuring buffer under a bias of -300 mV, without translocation events detectable under this condition.

Control experiments involving pure thrombin were conducted under the measuring conditions. The results displayed no discernible translocation events, as illustrated in **Figure 4.12**. Given thrombin's relatively small size and its near-neutral charge characteristics at physiological pH, directly detecting thrombin poses a considerable challenge when utilising an unmodified nanopore. To surmount these challenges, the study introduced a methodology involving 4.3 kbp DNA carriers that were separately modified with HD1 and HD22 aptamers. These carriers, each present at a concentration of 100 pM, were subjected to an incubation process with 100 pM thrombin within the measuring buffer. This incubation took place at 37°C for a duration of 2 hours prior to conducting nanopore measurements. Upon the introduction of thrombin, the nanopore measurements revealed a distinctive transformation in the event dynamics. Specifically, dimeric events emerged, characterised by extended dwell times and amplified peak areas, as illustrated in **Figure 4.13**. These dimeric 8.7 kbp DNA events were observable in contrast to the typical events representing the folded and unfolded states of the 4.3 kbp DNA monomers.

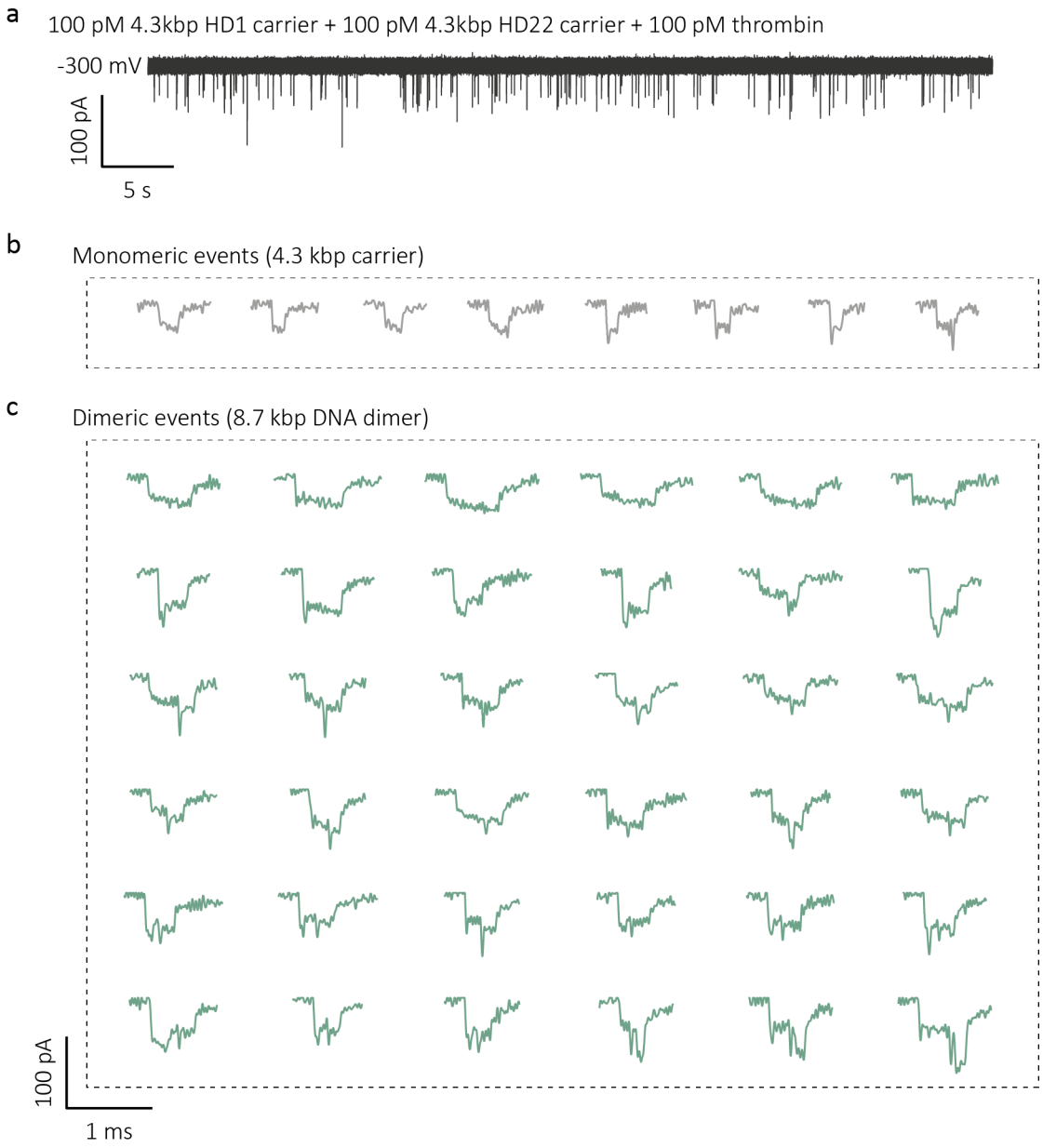


Figure 4.13 Representative current traces and events of thrombin detection. (a) A typical trace recorded using 100 pM thrombin and 100 pM DNA carrier in 100 mM KCl measuring buffer under a bias of -300 mV. (b) Monomeric events and (c) dimeric events with sandwich structure formed.

An intriguing observation within this context is the occurrence of a subset of dimeric events that feature a prominent and sharp subpeak situated within the central region of each event waveform, as depicted in **Figure 4.13** and **Figure 4.14**. The rationale behind this subpeak can be attributed to the unique structure of aptamer-protein complexes. Despite the conventional

limitation of proteins to generate conductive current enhancements at low salt concentrations, [29] the appearance of this subpeak is ascribed to the formation of the G-quadruplex structure within the aptamers themselves. [30] This approach leverages the HD1-thrombin-HD22 sandwich structure to augment the local charge density. This augmentation, in turn, enhances the ionic strength within the pore sensing region, giving rise to the appearance of these conductive subpeaks at the anticipated position. The presence of these subpeaks corroborates not only the successful formation of protein-induced DNA dimers but also underscores the feasibility and effectiveness of this method in protein detection even under challenging conditions.

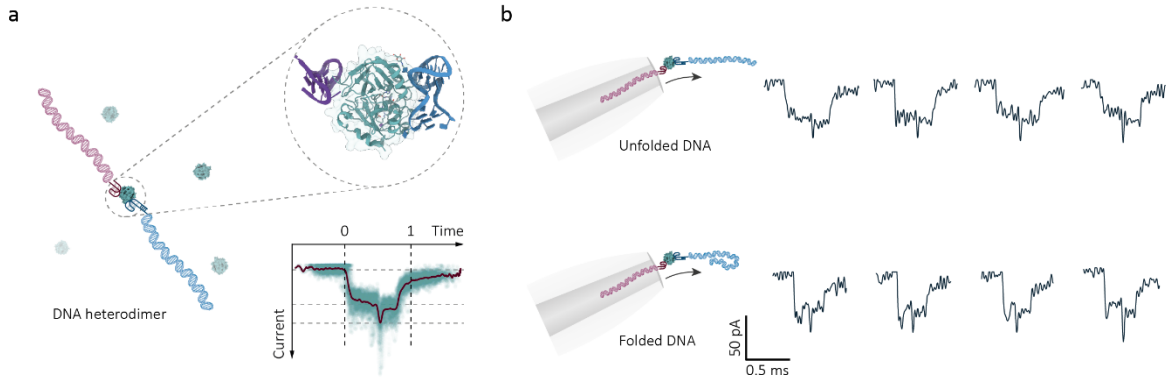


Figure 4.14 Nanopore detection of thrombin using dimerisation of aptamer-modified DNA carriers. (a) Schematic of the structure of thrombin sandwiched by HD1 and HD22 modified DNA carriers (PDB: 5EW2). Inset: overlay of 100 dimeric events formed by the HD1-thrombin-HD22 sandwich structure. (b) Diagrams of nanopore translocation for unfolded and partially folded dimeric events. Nanopore experiments were performed using 100 pM thrombin with 100 pM of each carrier in 100 mM KCl measuring buffer under a bias of -300 mV.

To quantify the amount of thrombin present, a threshold of 18.0 fAs was implemented on the distribution of charge, as depicted in **Figure 4.15** and **Figure 4.16a**. This threshold was employed to effectively discriminate between monomeric events (with a mean charge of 7.7 ± 0.4 fAs) and dimeric events (with a mean charge of 23.3 ± 1.7 fAs). Similar to the behaviour

observed with 5 kbp (mean charge: 9.9 ± 0.6 fAs) versus 10 kbp DNA (mean charge: 30.3 ± 2.3 fAs), the charge of dimeric DNA does not exactly equate to twice that of monomeric DNA. This is due to the fact that the charge reflects the difference between the ions bound to the DNA molecules and the ions diffusing in the solution, rather than a straightforward linear scaling.

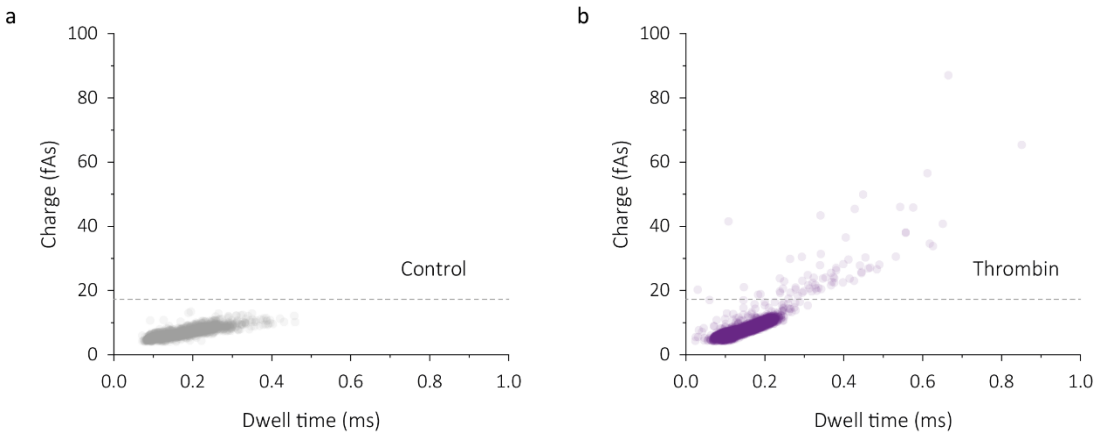


Figure 4.15 Statistics of carrier translocation with and without thrombin. Scatter plots of charge versus dwell time for (a) 100 pM HD1-modified carrier and 100 pM HD22-modified carrier; (b) 100 pM thrombin incubated with 100 pM HD1-modified carrier and 100 pM HD22-modified carrier. Nanopore experiments were performed in 100 mM KCl measuring buffer under a bias of -300 mV.

The subsequent analysis focused on examining the subpeaks within the extracted dimeric events, as displayed in **Figure 4.16b**. The dwell time associated with these subpeaks exhibited a remarkably rapid mean value of 32 µs. This swiftness is in stark contrast to the dwell time of DNA levels, which possessed a mean value of 432 µs. This disparity aligns with the small proportion of the aptamer-protein-aptamer sandwich complex within the entire carrier structure. Furthermore, the amplitude of the subpeaks was measured, yielding a mean value of 23.1 pA. This value was slightly lower than the amplitude exhibited by unfolded DNA levels (34.8 pA). To mitigate the impact of stochastic variations, individual events were standardised to begin at 0 and conclude at 1, as indicated in **Figure 4.14a**. A scatter plot was generated,

contrasting the fractional width (defined as the ratio of subpeak width to the width of DNA level) against the fractional position at which the subpeak maxima was situated along the event waveform, as shown in **Figure 4.16c**. Notably, the subpeaks were observed to preferentially occur around the 0.55 position, rather than being located precisely at the midpoint. This phenomenon is attributed to the tendency of DNA translocation to initially decelerate as time progresses, before subsequently accelerating close to the end of the event, which is consistent with known translocation dynamics observed in previous studies. [31]

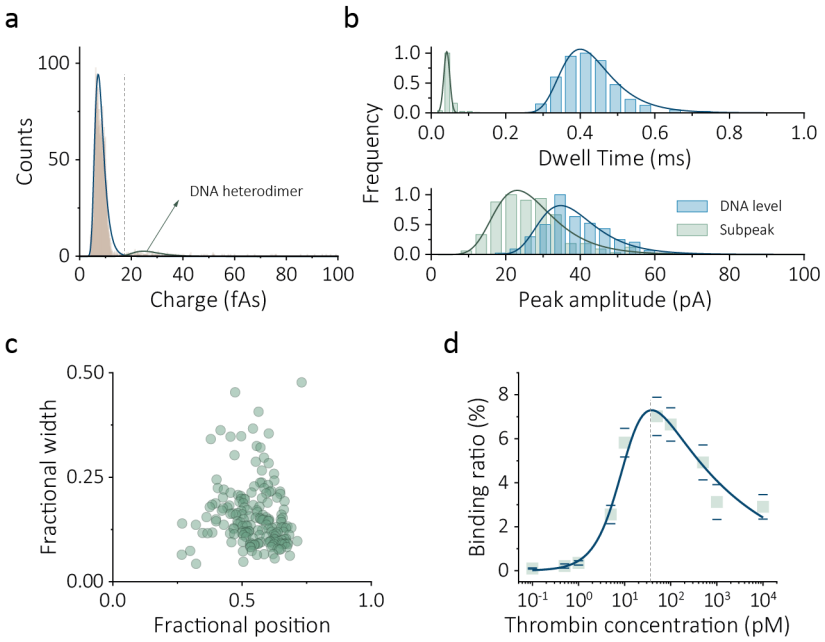


Figure 4.16 Statistical analysis of thrombin detection using dimeric carriers. (a) Histogram of charge showing two populations which correspond to monomeric DNA carriers and dimeric DNA carriers, respectively. (b) Distributions of extracted dwell time and peak amplitude for subpeaks and DNA levels. (c) Scattering points of fractional width (defined as the ratio of subpeak width to the width of DNA level) against the fractional position where the subpeak maxima was located along the event for extracted dimeric events. (d) Binding assays of 100 pM of each carrier in the presence of thrombin ranging from 100 fM to 10 nM. The binding curve was fitted with a biphasic Hill model and the K_d value was determined to be about 12.2 pM.

A binding assay encompassing thrombin concentrations ranging from 100 fM to 10 nM was carried out following the same process. For each concentration point, the binding ratio was calculated by dividing the number of dimeric events by the total number of events. This binding ratio effectively quantifies the quantity of thrombin detected. The obtained data were then used to construct a binding curve, revealing a distinctive two-step sigmoidal shape, as illustrated in Figure 4.16d. The binding curve was fitted using the biphasic Hill equation:

$$y = \frac{P_{\mathrm{m}}}{\left[1+\left(\frac{K_{\mathrm{a}}}{x}\right)^{H_{\mathrm{a}}}\right]\left[1+\left(\frac{x}{K_{\mathrm{i}}}\right)^{H_{\mathrm{i}}}\right]} \quad (4.2)$$

P_{m} = maximum, K_{a} = half-maximal activating, K_{i} = half-maximal inhibitory, H_{a} = activation Hill coefficient, H_{i} = inhibitory Hill coefficient.

From a chemical standpoint, it was observed that at low thrombin concentrations (0.1 – 50 pM), thrombin tends to form an aptamer-protein-aptamer sandwich structure by binding with two DNA carriers. However, as the concentration of thrombin escalates, thrombin appears to favour binding with only one DNA carrier, consequently hindering the formation of heterogeneous DNA dimers. From a detection perspective, the focus is primarily on the first half of the activating curve, which is closely linked to the total concentration of monomeric DNA carriers employed. When the carrier concentration was set at 200 pM, the dissociation constant (K_{d}) was determined to be 12.2 pM. Remarkably, this value was notably lower than the dissociation constant derived from bulk Surface Plasmon Resonance (SPR) measurements, as reported in previous studies.[28] The limit of detection (LOD), conventionally defined as three standard deviations (3σ) above the background noise, was found to be 0.21 pM. This determination was achieved by analysing the linear region within the low concentration range. Importantly, the sensitivity of this detection method could be further enhanced by reducing the concentration of the carrier DNA, a strategy that holds the potential to improve the limit of detection even further.

4.3.5 Detection of dimeric proteins by homogenous dimerisation of DNA carriers

An immediate and practical application of the detection strategy involves the utilisation of two DNA carriers to recognise dimeric proteins. Protein dimerisation is a crucial form of protein-protein interaction, where proteins come together with either identical monomers or other proteins to form functional homodimers or heterodimers. This interaction plays a pivotal role in regulating many physiological and disease-related processes, including enzymatic activation, recruitment of transcriptional cofactors, signal transduction, and even pathogenic pathways. [32] To exemplify the feasibility of this approach, I selected two homodimeric proteins: vascular endothelial growth factor (VEGF; 42 kDa; pI of 7.45) [33] and platelet-derived growth factor (PDGF; 30 kDa; pI of 9.8), [34] as proof of concept. Both VEGF and PDGF are critical signalling proteins involved in the development and growth of blood vessels. Additionally, they serve as biomarkers for certain diseases. For instance, VEGF is of paramount importance in the pathophysiology of neuronal tumours and other types of tumours. It functions as a potent inducer of angiogenesis, which is crucial for the growth and metastasis of cancerous cells. Cancers that express VEGF are empowered to flourish and spread within the body. [35] On the other hand, PDGF is deeply connected to the physiological progression of human cancers, vascular disorders, and fibrotic diseases. [36] The understanding of these proteins and their dimerisation processes is of immense significance in the context of disease development and therapeutic interventions.

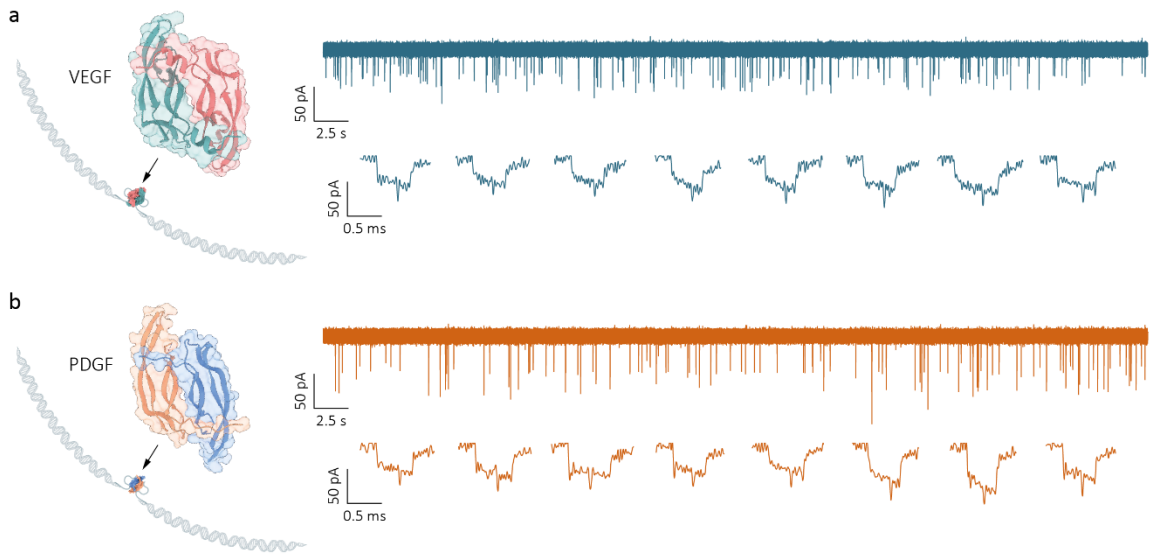


Figure 4.17 Nanopore detection of dimeric proteins using aptamer-modified DNA carrier. Schematic of the dimeric protein bound to two identical aptamer-modified DNA carriers for (a) VEGF and (b) PDGF. Representative current traces and typical dimeric events were collected with 100 pM protein concentration and 200 pM carrier concentration in 100 mM KCl measuring buffer under a bias of -300 mV.

As illustrated in **Figure 4.17a** and **Figure 4.17b**, this method involves the use of two identical aptamer-modified DNA carriers to detect protein dimers through the formation of an aptamer-protein-aptamer sandwich structure. Specifically, the VEGF aptamer (V7t1) with an affinity of approximately 1.4 nM was employed to capture VEGF-165 (38.4 kDa), [37] while a previously reported 39-mer PDGF aptamer (affinity ~ 0.1 nM) was chosen for detecting PDGF-BB (24.6 kDa), a variant of the PDGF family. [38] These DNA carriers, along with the protein analytes, were incubated at 37 °C for 2 hours before conducting the nanopore measurements. Control experiments involving pure VEGF and PDGF samples under the same experimental conditions showed no discernible translocation events, as depicted in **Figure 4.18**. Similar to the thrombin detection process, upon the addition of the respective protein analytes, dimeric events with double dwell times and charges were observed for both VEGF and PDGF as shown in **Figure 4.17**. Importantly, these events exhibited centrally located subpeaks, further confirming the successful formation of aptamer-protein-aptamer sandwich structures.

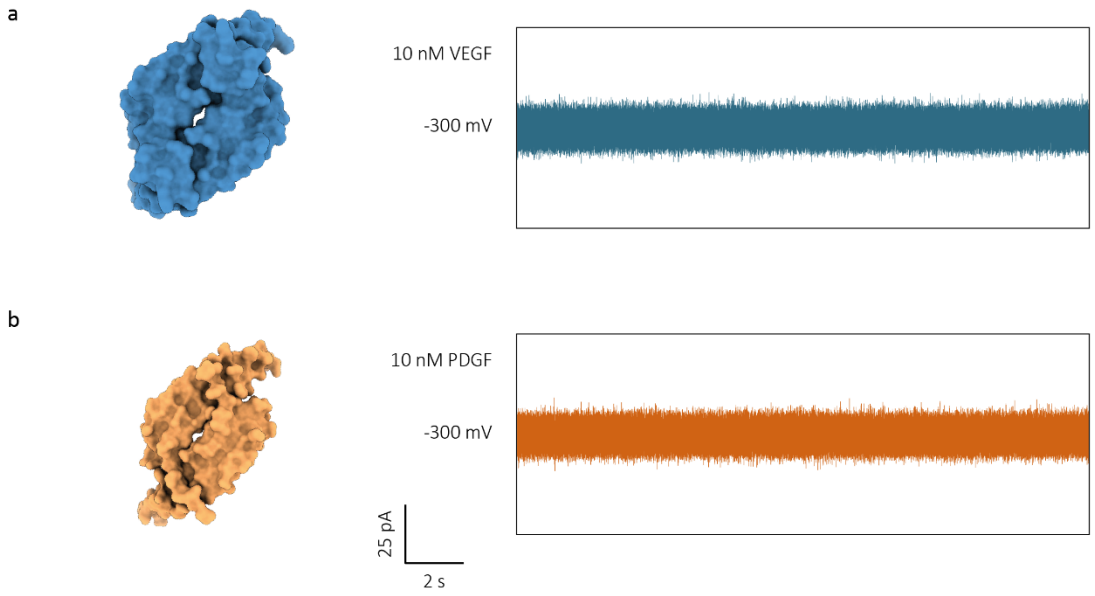


Figure 4.18 Nanopore measurements of pure VEGF and PDGF. Nanopore experiments were performed using 10 nM VEGF/PDGF in 100 mM KCl measuring buffer under a bias of -300 mV, without translocation events detectable under this condition.

Charge versus dwell time scatter plots for VEGF and PDGF are displayed in **Figure 4.19a**, where dimeric events are highlighted. Further subpeak analysis of the extracted dimeric events is depicted in **Figure 4.19b**. The mean fractional position for VEGF and PDGF was determined to be 0.59 and 0.57, respectively. This position slightly lags behind the midpoint of the event due to the acceleration of DNA translocation as the event progresses. The normalised subpeak amplitude, defined as the subpeak amplitude divided by the DNA amplitude, provides a standardised subpeak measurement that eliminates variations introduced by the measuring devices. The mean normalised amplitude for VEGF (0.879) was higher than that for PDGF (0.817), which correlates with the size of the respective proteins. Larger proteins bound with aptamers on their surfaces will form larger complexes, resulting in higher ion densities within the nanopore sensing region during translocation.

The binding assays conducted for both VEGF and PDGF exhibited characteristic two-phase transitions, with K_d values determined to be 1.0 pM and 5.9 pM, respectively. These results underline the potential and versatility of the approach in detecting protein dimers, a crucial type of protein-protein interaction in various biological processes.

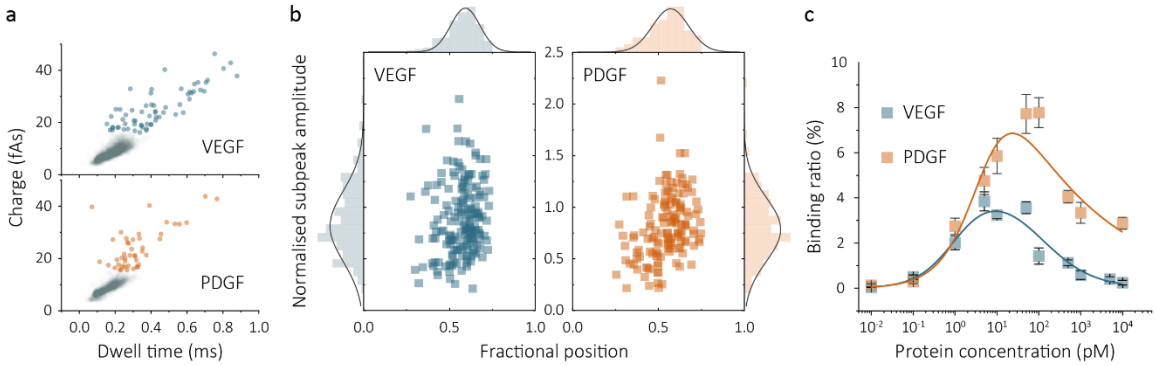


Figure 4.19 Statistical analysis of VEGF and PDGF detection using dimeric carriers. (a) Scatter plots of charge against dwell time for VEGF and PDGF, where the dimeric events over the charge threshold were highlighted with blue and orange colour, respectively. (b) Scattering points of normalised subpeak amplitude (defined as the ratio of subpeak amplitude to the height of DNA level) against the fractional position for extracted dimeric events, along with the statistical histograms. (c) Binding assays of 200 pM DNA carriers in the presence of VEGF and PDGF ranging from 10 fM to 10 nM. The binding curves were fitted with a biphasic Hill model and the K_d value was determined to be about 1.0 pM and 5.9 pM for VEGF and PDGF, respectively.

4.3.6 Direct observation of the activation and inhibition of c-Met dimerisation

This method was further explored for its capability to monitor dynamic protein dimerisation, specifically focusing on receptor protein dimerisation induced by binding with its ligand. Receptor protein dimerisation plays a fundamental role in initiating intracellular signal

transduction, which is critical for normal biological processes as well as the development of conditions such as cancer. [39] Receptor tyrosine kinases (RTKs) are a class of transmembrane proteins expressed widely. They serve as receptors for various extracellular signalling molecules, such as growth factors and neurotrophic factors, regulating essential cellular activities. [40] The canonical model for RTK activation suggests that ligand binding shifts the balance from monomeric inactive receptors to active receptor dimers. [41] This dimerisation of RTKs, coupled with intracellular domain phosphorylation, is pivotal for initiating a sequence of intracellular signalling cascades. [42] Therefore, understanding the expression levels and oligomerisation states of RTKs is crucial for comprehending the intricacies of signal transduction networks. To illustrate this concept, I chose the c-Met receptor (130 kDa) as a model, which acts as the cognate receptor for hepatocyte growth factor (HGF, 80 kDa). [43] HGF activates the c-Met receptor by promoting receptor dimerisation upon binding. [44] For this proof-of-principle demonstration, a 40-mer DNA aptamer specific to c-Met with an affinity of approximately 0.09 nM was employed to target the c-Met receptor. [45]

Prior to using DNA carriers, experiments with pure proteins were conducted, including the c-Met receptor alone, the c-Met receptor with HGF, and the c-Met receptor with HGF and an anti-HGF antibody. Under low salt concentration conditions, as depicted in Figure 4.20, no observable translocation events were detected for these pure protein samples. To validate the specificity and sensitivity of the approach, I performed control experiments using aptamer-modified DNA carriers with monomeric c-Met receptors. These experiments confirmed that self-dimerisation of c-Met receptors was not activated under the given measuring conditions. However, upon the addition of the ligand HGF, c-Met receptors were induced to form homodimers. The subsequent translocation events of dimerised DNA, as shown in Figure 4.21a, suggested that the c-Met receptors bound to the DNA carriers were engaged in dimerisation prompted by HGF binding. Furthermore, this approach was sensitive enough to detect changes in dimerisation status when the c-Met receptors were treated with an anti-HGF antibody, which inhibited the activity of HGF. Figure 4.21b displayed scatter plots of charge versus dwell time for non-activated, activated, and inhibited c-Met receptors, providing a direct visualisation of the varying proportions of dimerised signals.

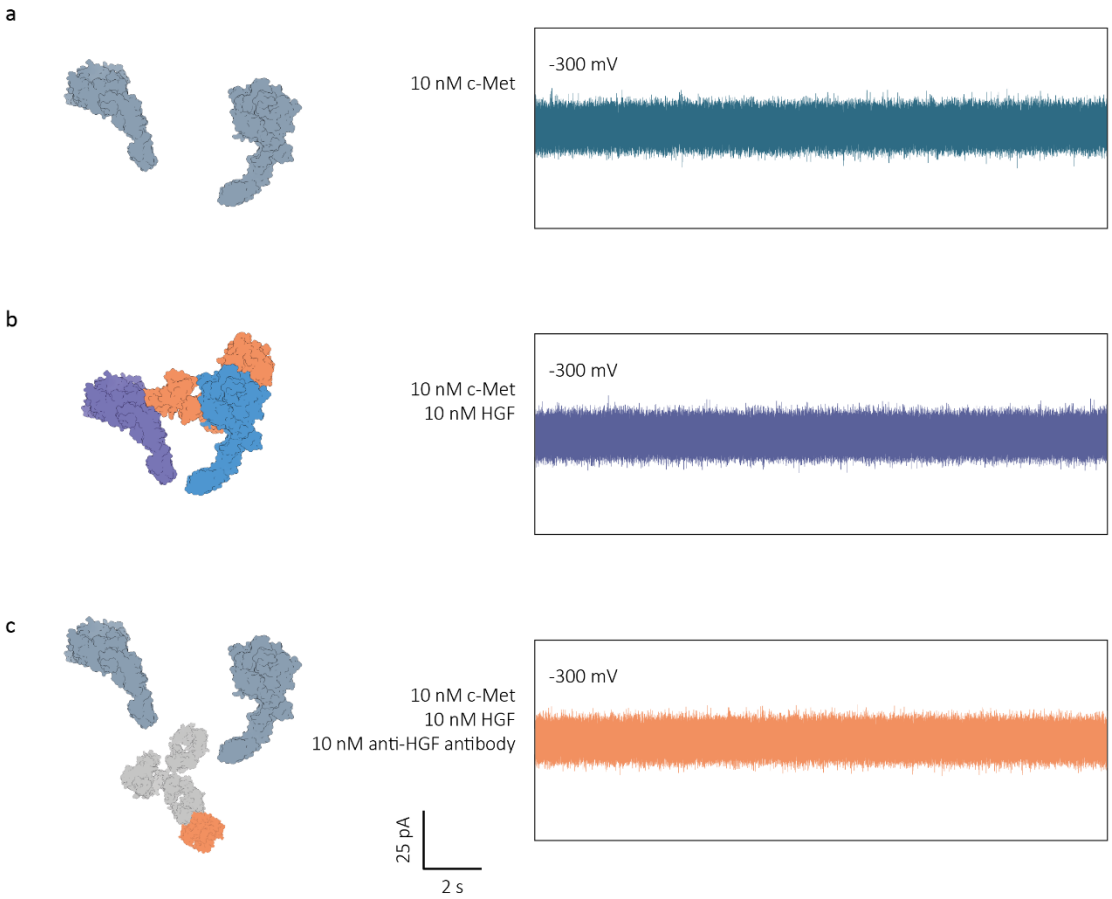


Figure 4.20 Nanopore measurements of pure c-Met. Nanopore experiments were performed using (a) 10 nM c-Met, (b) 10 nM c-Met + 10 nM HGF, and (c) 10 nM c-Met + 10 nM HGF + 10 nM anti-HGF antibody in 100 mM KCl measuring buffer under a bias of -300 mV, without translocation events detectable under this condition.

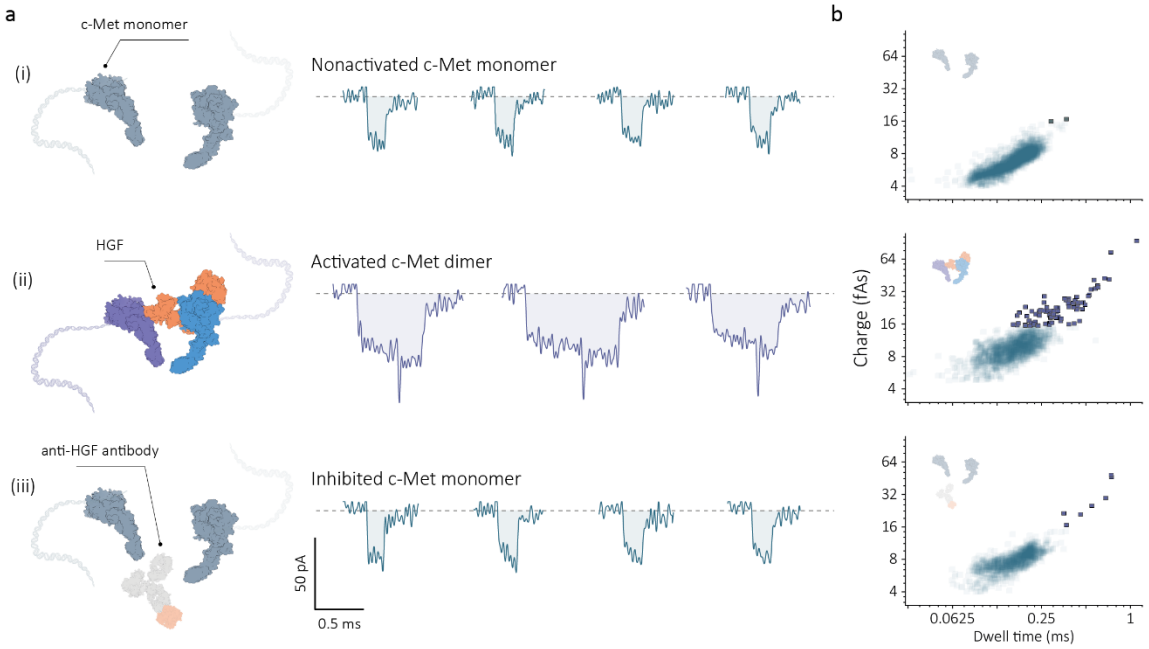


Figure 4.21 Nanopore detection of HGF-induced c-Met dimerisation using aptamer-modified DNA carrier. (a) Schematic and typical events for (i) monomeric c-Met receptors bound to the DNA carriers, (ii) HGF-induced c-Met dimers bound to two DNA carriers, and (iii) c-Met receptors and HGF under the inhibition of anti-HGF antibody. (b) Scatter plots of charge against dwell time for nonactivated c-Met monomers, activated c-Met dimers and inhibited c-Met monomers, where the dimeric events over the charge threshold were highlighted with purple colour, respectively. Representative events were collected with 200 pM protein concentration and 200 pM carrier concentration in 100 mM KCl measuring buffer under a bias of -300 mV.

The distribution of fractional position, as demonstrated in **Figure 4.22a**, underscored the capacity of the DNA carrier to transport bound proteins regardless of their size and molecular weight. DNA carriers carrying large protein complexes, such as HGF-induced c-Met dimers (340 kDa), exhibited a translocation behaviour similar to that of previous DNA-protein complexes, manifesting a subpeak at around 0.58 fractional position. Conversely, the normalised subpeak amplitude demonstrated a direct correlation with the protein size, as evidenced in **Figure 4.22b**. The amplitude for c-Met dimers was significantly higher than that of the three smaller proteins. Although protein translocation under low salt conditions has been less extensively studied compared to high salt conditions, the presence of the bound DNA aptamer in this approach

induced current enhancement, unveiling protein characteristics such as size, shape, and surface charge. The observation of a linear correlation between normalised subpeak amplitude and protein size, as depicted in **Figure 4.22c**, mirrors the principles established by conventional theories used in high salt conditions. [29, 46] These findings collectively highlight the robustness and adaptability of the approach in revealing protein-protein interactions and their dynamics.

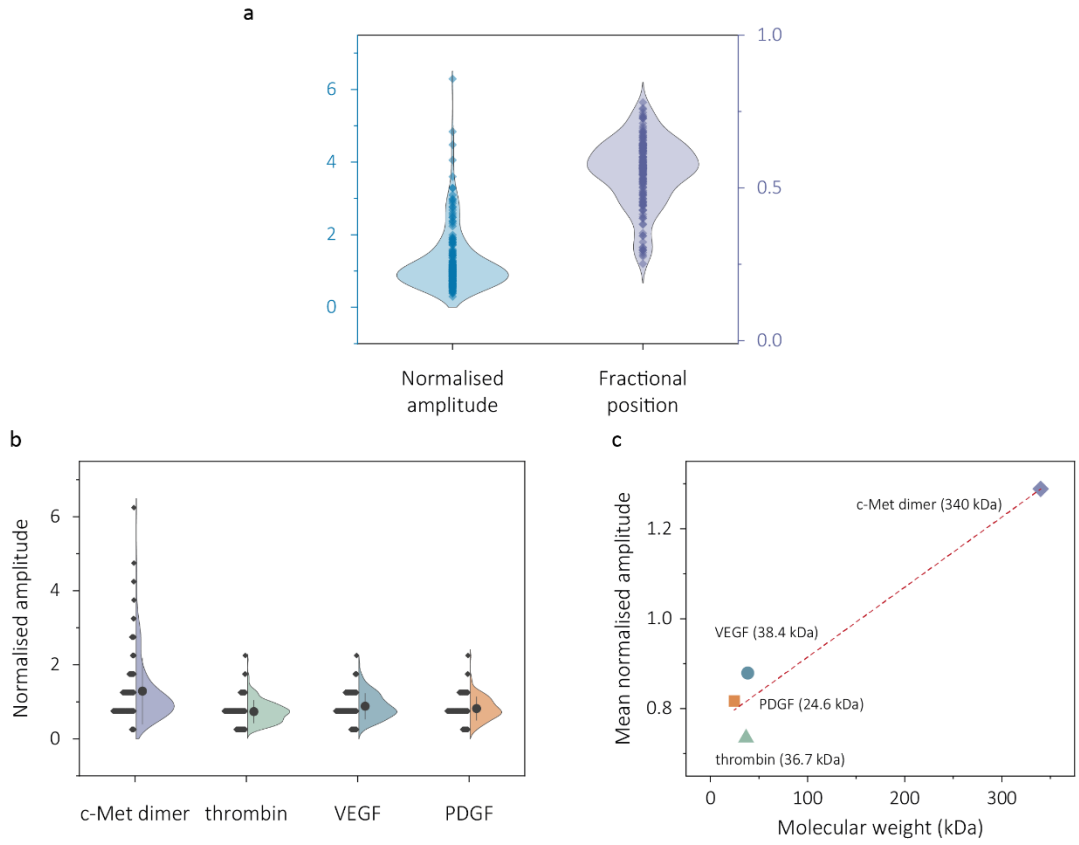


Figure 4.22 Subpeak analysis for translocation events of HGF-induced c-Met dimerisation. (a) The distribution of normalised subpeak amplitude and fractional position for dimeric events extracted from the translocation of HGF-induced c-Met dimers bound to DNA carriers. (b) Comparison of the distribution of normalised subpeak amplitude for the c-Met dimer, thrombin, VEGF and PDGF. (c) A linear correlation was shown on mean normalised subpeak amplitude against the molecular weight.

I also investigated the impact of varying HGF concentrations on the formation of c-Met dimers, as illustrated in Figure 4.23a. With increasing HGF concentrations ranging from 2 pM to 200 pM, a higher ratio of dimeric c-Met events was observed. Simultaneously, the inhibitory effect of an excess of anti-HGF antibody became more pronounced with the escalating HGF concentrations. This trend aligns with observations made using fluorescence methods, as reported in previous studies. [47] In the context of practical applications for clinical diagnostics and therapeutics, it is crucial for the nanopore biosensing approach to be compatible with unprocessed biological samples. [48] Human serum is a commonly utilised biofluid in clinical detection. However, serum contains a myriad of diverse proteins, which could potentially introduce background interference for nanopore detection. Under the specific measuring conditions with low salt concentrations, most proteins exhibit no translocation signals even if they possess a significant size. To ensure a stable current baseline for protein detection, I carried out a serial dilution of human serum using the measuring buffer (Figure 4.23b). The optimal dilution ratio was determined to be 1: 20 (serum: buffer, v/v), which yielded a noise level comparable to that of the measuring buffer alone. Subsequently, I performed the same c-Met activation and inhibition experiments within the diluted serum solution, as depicted in Figure 4.23c. Remarkably, I observed a similar trend to the one conducted in the measuring buffer. This finding underscores the adaptability of the detection platform in selectively sensing proteins within complex biological environments, such as human serum.

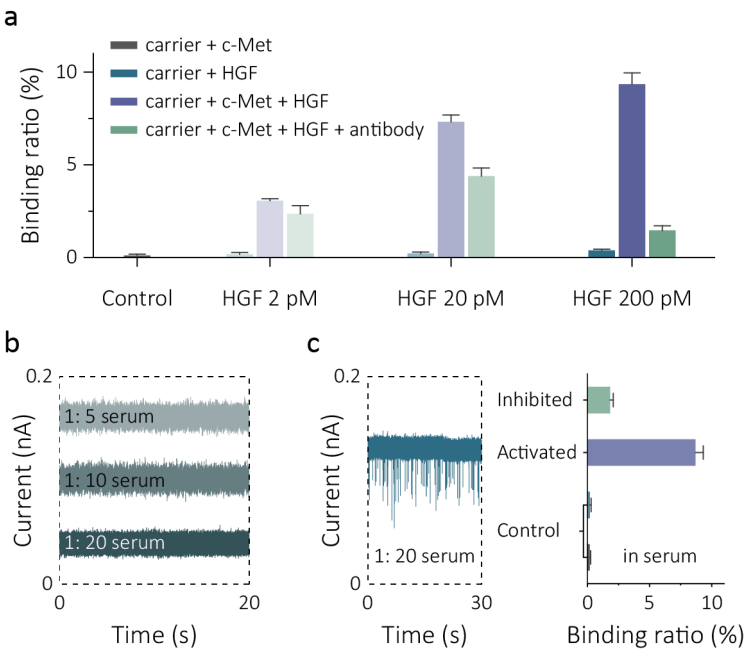


Figure 4.23 Nanopore detection of c-Met dimerisation in human serum. (a) Dimerisation ratio of c-Met in the presence of varying HGF concentrations (0, 2, 20, 200 pM). DNA carriers and c-Met concentration were fixed to be 200 pM and an excess concentration of 5 nM anti-HGF antibody were used to monitor the inhibitory effect. (b) Current baseline for the dilution of human serum to the measuring buffer (1: 5, 1: 10 and 1: 20). (c) Typical trace of DNA translocation in 1: 20 serum solution. Binding ratio of c-Met dimers to DNA carrier in 1: 20 serum solution.

4.4 Conclusions

Chapter 4 presents a versatile and innovative nanopore-based platform for the identification and quantification of proteins and protein-protein interactions using aptamer-modified DNA carriers. Unlike conventional methods that directly analyse subpeak information, this approach relies on the indirect detection of target proteins through the dimerisation of DNA carriers. Dimeric DNA carriers are easily differentiated through the classification of equivalent charge, providing a unique signature. This strategy is theoretically applicable to any protein that possesses two distinct aptamer-binding sites. I successfully demonstrated the ultrasensitive detection of thrombin by utilising HD1 and HD22 modified DNA carriers. The presence of a characteristic double dwell time, charge pattern, and a subpeak in the middle confirmed the

formation of the aptamer-protein sandwich structure. The approach was further extended to the detection of small dimeric proteins, such as VEGF and PDGF, by utilising two identical carriers. Moreover, I showcased the monitoring of ligand-induced receptor dimerisation, specifically HGF-induced c-Met receptor dimerisation, highlighting the adaptability of the detection platform for studying dynamic protein interactions. Even when operating at nearly physiological salt concentrations, the appearance of a subpeak due to the aptamer-protein complex provided information related to the protein size and shape. The entire system demonstrated compatibility with complex biological fluids, such as human serum, implying its potential application for clinical diagnosis using unprocessed samples.

Moving forward, there are exciting possibilities to enhance the practical clinical applicability of this strategy. Multiplexing capacity can be improved by incorporating different barcode labels or utilising carriers of varying lengths. [48, 49] To meet the demands of minimal sample volume requirements for clinical applications, local electric field modulation techniques, such as field-effect transistors (FETs) [50] and dielectrophoretic (DEP) traps, [51] can be integrated into solid-state nanopores, such as nanopipettes used in this work. Furthermore, the versatility of the approach extends beyond DNA/RNA aptamers. Protein-based recognition elements, including antibodies, nanobodies, and peptide aptamers, can be covalently attached to the DNA carrier, broadening the scope and specificity of this platform. [52] In summary, this study opens up a new avenue for protein profiling, particularly for the analysis of rare proteins. The potential for practical early-stage diagnosis and prognosis is a promising direction for further exploration.

4.5 References

1. Crosby D*, et al.* Early detection of cancer. *Science* **375**, eaay9040.

2. Saman S*, et al.* Exosome-associated Tau Is Secreted in Tauopathy Models and Is Selectively Phosphorylated in Cerebrospinal Fluid in Early Alzheimer Disease *. *Journal of Biological Chemistry* **287**, 3842-3849 (2012).

3. Chandramouli K, Qian PY. Proteomics: challenges, techniques and possibilities to overcome biological sample complexity. *Hum Genomics Proteomics* **2009**, (2009).

4. Liu Y, Zhan L, Qin Z, Sackrison J, Bischof JC. Ultrasensitive and Highly Specific Lateral Flow Assays for Point-of-Care Diagnosis. *ACS Nano* **15**, 3593-3611 (2021).

5. Ying Y-L*, et al.* Nanopore-based technologies beyond DNA sequencing. *Nature Nanotechnology* **17**, 1136-1146 (2022).

6. Xue L, Yamazaki H, Ren R, Wanunu M, Ivanov AP, Edel JB. Solid-state nanopore sensors. *Nature Reviews Materials* **5**, 931-951 (2020).

7. Alfaro JA*, et al.* The emerging landscape of single-molecule protein sequencing technologies. *Nature Methods* **18**, 604-617 (2021).

8. Wang Y, Zhao Y, Bollas A, Wang Y, Au KF. Nanopore sequencing technology, bioinformatics and applications. *Nature Biotechnology* **39**, 1348-1365 (2021).

9. Wang X*, et al.* Nanopore Detection Using Supercharged Polypeptide Molecular Carriers. *Journal of the American Chemical Society* **145**, 6371-6382 (2023).

10. Plesa C, Kowalczyk SW, Zinsmeester R, Grosberg AY, Rabin Y, Dekker C. Fast Translocation of Proteins through Solid State Nanopores. *Nano Letters* **13**, 658-663 (2013).

11. Waduge P*, et al.* Nanopore-Based Measurements of Protein Size, Fluctuations, and Conformational Changes. *ACS Nano* **11**, 5706-5716 (2017).

12. Bell NAW, Keyser UF. Specific Protein Detection Using Designed DNA Carriers and Nanopores. *Journal of the American Chemical Society* **137**, 2035-2041 (2015).

13. Sze JYY, Ivanov AP, Cass AEG, Edel JB. Single molecule multiplexed nanopore protein screening in human serum using aptamer modified DNA carriers. *Nature Communications* **8**, 1552 (2017).

14. Ren R*, et al.* Single-Molecule Binding Assay Using Nanopores and Dimeric NP Conjugates. *Advanced Materials* **33**, 2103067 (2021).

15. Brinkerhoff H, Kang ASW, Liu J, Aksimentiev A, Dekker C. Multiple rereads of single proteins at single–amino acid resolution using nanopores. *Science* **374**, 1509-1513 (2021).

16. Nova IC, Ritmejeris J, Brinkerhoff H, Koenig TJR, Gundlach JH, Dekker C. Detection of phosphorylation post-translational modifications along single peptides with nanopores. *Nature Biotechnology*, (2023).

17. Blanco MA, Perevozchikova T, Martorana V, Manno M, Roberts CJ. Protein–Protein Interactions in Dilute to Concentrated Solutions: α-Chymotrypsinogen in Acidic Conditions. *The Journal of Physical Chemistry B* **118**, 5817-5831 (2014).

18. Wei C, Bard AJ, Feldberg SW. Current Rectification at Quartz Nanopipet Electrodes. *Analytical Chemistry* **69**, 4627-4633 (1997).

19. Charron M, Briggs K, King S, Waugh M, Tabard-Cossa V. Precise DNA Concentration Measurements with Nanopores by Controlled Counting. *Analytical Chemistry* **91**, 12228-12237 (2019).

20. Wen C, Dematties D, Zhang S-L. A Guide to Signal Processing Algorithms for Nanopore Sensors. *ACS Sensors* **6**, 3536-3555 (2021).

21. Chang H, Kosari F, Andreadakis G, Alam MA, Vasmatzis G, Bashir R. DNA-Mediated Fluctuations in Ionic Current through Silicon Oxide Nanopore Channels. *Nano Letters* **4**, 1551-1556 (2004).

22. Cadinu P*, et al.* Single Molecule Trapping and Sensing Using Dual Nanopores Separated by a Zeptoliter Nanobridge. *Nano Letters* **17**, 6376-6384 (2017).

23. Forstater JH*, et al.* MOSAIC: A Modular Single-Molecule Analysis Interface for Decoding Multistate Nanopore Data. *Analytical Chemistry* **88**, 11900-11907 (2016).

24. Taniguchi M*, et al.* Combining machine learning and nanopore construction creates an artificial intelligence nanopore for coronavirus detection. *Nature Communications* **12**, 3726 (2021).

25. Posma JJN, Posthuma JJ, Spronk HMH. Coagulation and non‐coagulation effects of thrombin. *Journal of Thrombosis and Haemostasis* **14**, 1908-1916 (2016).

26. Iannucci J, Renehan W, Grammas P. Thrombin, a Mediator of Coagulation, Inflammation, and Neurotoxicity at the Neurovascular Interface: Implications for Alzheimer's Disease. *Frontiers in Neuroscience* **14**, (2020).

27. Tennico YH, Hutanu D, Koesdjojo MT, Bartel CM, Remcho VT. On-Chip Aptamer-Based Sandwich Assay for Thrombin Detection Employing Magnetic Beads and Quantum Dots. *Analytical Chemistry* **82**, 5591-5597 (2010).

28. Hasegawa H, Taira KI, Sode K, Ikebukuro K. Improvement of Aptamer Affinity by Dimerization. *Sensors (Basel)* **8**, 1090-1098 (2008).

29. Bandara YMNDY, Farajpour N, Freedman KJ. Nanopore Current Enhancements Lack Protein Charge Dependence and Elucidate Maximum Unfolding at Protein's Isoelectric Point. *Journal of the American Chemical Society* **144**, 3063-3073 (2022).

30. Bošković F, Zhu J, Chen K, Keyser UF. Monitoring G-Quadruplex Formation with DNA Carriers and Solid-State Nanopores. *Nano Letters* **19**, 7996-8001 (2019).

31. Chen K, Jou I, Ermann N, Muthukumar M, Keyser UF, Bell NAW. Dynamics of driven polymer transport through a nanopore. *Nature Physics* **17**, 1043-1049 (2021).

32. Dang DT. Molecular Approaches to Protein Dimerization: Opportunities for Supramolecular Chemistry. *Frontiers in Chemistry* **10**, (2022).

33. Varongchayakul N, Huttner D, Grinstaff MW, Meller A. Sensing Native Protein Solution Structures Using a Solid-state Nanopore: Unraveling the States of VEGF. *Scientific Reports* **8**, 1017 (2018).

34. Antoniades HN, Scher CD, Stiles CD. Purification of human platelet-derived growth factor. *Proceedings of the National Academy of Sciences* **76**, 1809-1813 (1979).

35. Carmeliet P. VEGF as a Key Mediator of Angiogenesis in Cancer. *Oncology* **69**, 4-10 (2005).

36. Raica M, Cimpean AM. Platelet-Derived Growth Factor (PDGF)/PDGF Receptors (PDGFR) Axis as Target for Antitumor and Antiangiogenic Therapy. *Pharmaceuticals* **3**, 572-599 (2010).

37. Nonaka Y, Sode K, Ikebukuro K. Screening and Improvement of an Anti-VEGF DNA Aptamer (2010).

38. Green LS, Jellinek D, Jenison R, Östman A, Heldin C-H, Janjic N. Inhibitory DNA Ligands to Platelet-Derived Growth Factor B-Chain. *Biochemistry* **35**, 14413-14424 (1996).

39. Heldin CH. Dimerization of cell surface receptors in signal transduction. *Cell* **80**, 213-223 (1995).

40. Lemmon MA, Schlessinger J. Cell Signaling by Receptor Tyrosine Kinases. *Cell* **141**, 1117-1134 (2010).

41. Maruyama IN. Mechanisms of Activation of Receptor Tyrosine Kinases: Monomers or Dimers (2014).

42. Trusolino L, Bertotti A, Comoglio PM. MET signalling: principles and functions in development, organ regeneration and cancer. *Nature Reviews Molecular Cell Biology* **11**, 834-848 (2010).

43. Gherardi E, Birchmeier W, Birchmeier C, Woude GV. Targeting MET in cancer: rationale and progress. *Nature Reviews Cancer* **12**, 89-103 (2012).

44. Ueki R, Ueki A, Kanda N, Sando S. Oligonucleotide-Based Mimetics of Hepatocyte Growth Factor. *Angewandte Chemie International Edition* **55**, 579-582 (2016).

45. Boltz A, Piater B, Toleikis L, Guenther R, Kolmar H, Hock B. Bi-specific Aptamers Mediating Tumor Cell Lysis. *Journal of Biological Chemistry* **286**, 21896-21905 (2011).

46. Varongchayakul N, Song J, Meller A, Grinstaff MW. Single-molecule protein sensing in a nanopore: a tutorial. *Chemical Society Reviews* **47**, 8512-8524 (2018).

47. Liang H*, et al.* Nongenetic Approach for Imaging Protein Dimerization by Aptamer Recognition and Proximity-Induced DNA Assembly. *Journal of the American Chemical Society* **140**, 4186-4190 (2018).

48. Cai S*, et al.* Single-molecule amplification-free multiplexed detection of circulating microRNA cancer biomarkers from serum. *Nature Communications* **12**, 3515 (2021).

49. Bell NAW, Keyser UF. Digitally encoded DNA nanostructures for multiplexed, single-molecule protein sensing with nanopores. *Nature Nanotechnology* **11**, 645-651 (2016).

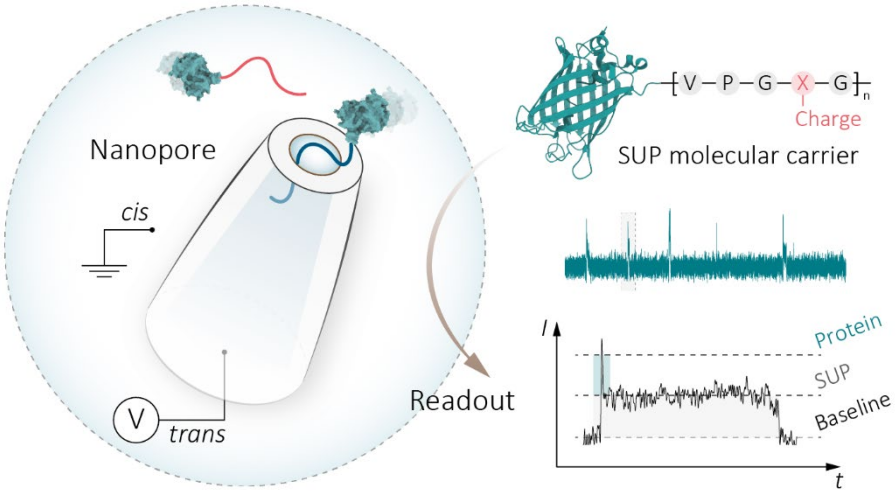
50. Ren R*, et al.* Nanopore extended field-effect transistor for selective single-molecule biosensing. *Nature Communications* **8**, 586 (2017).

51. Freedman KJ, Otto LM, Ivanov AP, Barik A, Oh S-H, Edel JB. Nanopore sensing at ultra-low concentrations using single-molecule dielectrophoretic trapping. *Nature Communications* **7**, 10217 (2016).

52. Gong H*, et al.* Simple Method To Prepare Oligonucleotide-Conjugated Antibodies and Its Application in Multiplex Protein Detection in Single Cells. *Bioconjugate Chemistry* **27**, 217-225 (2016).

CHAPTER 5

Nanopore detection using supercharged polypeptide molecular carriers



Synopsis

In this chapter, supercharged unstructured polypeptides (SUPs) are used as a new molecular carrier to control protein transport through a nanopore. It is shown that cationic SUPs can both improve protein capture and detection dramatically and slow down the protein translocation due to the electrostatic attraction with the pore. By using this SUP molecular carrier, the protein concentrations required for nanopore measurements are lowered to pM levels which can facilitate the characterisation of low-copy-number proteins within the cells. This approach has been successfully used for size identification of small proteins and precise recognition of protein-protein interactions at the single-molecule level.

Part of this chapter was published as Wang, X.; Thomas, T. M.; Ren, R.; Zhou, Y.; Zhang, P.; Li, J.; Cai, S.; Liu, K.; Ivanov, A. P.; Herrmann, A.; Edel, J. B. Nanopore detection using supercharged polypeptide molecular carriers. *J. Am. Chem. Soc.* 2023, 145, 11, 6371. In this work, the peptide and protein samples were obtained from Tina-Marie Thomas and Andreas Herrmann, DWI – Leibniz Institute for Interactive Materials, Germany.

5.1 Introduction

Proteomics analysis plays a crucial role in understanding the intricate processes that influence human biology. [1] By comprehensively mapping the spatial and temporal distribution of proteins, proteomics studies offer valuable insights into disease pathways, potential drug targets, and diagnostic biomarkers. [2] However, the conventional method of protein analysis using mass spectrometry (MS) has limitations when it comes to low-copy-number proteins. [3] In contrast, nanopore-based analysers present an alternative approach that offers several advantages. [4, 5, 6] These analysers provide a cost-effective and high-throughput platform for real-time analysis of individual biomolecules without the need for labelling. In this technique, biomolecules, including proteins, are driven through a nanopore by an electric field, leading to partial blockade of ionic current across the pore. By analysing the resulting current blockade (ΔI_{b}), which is caused by ion exclusion, it becomes possible to characterise biopolymers such as nucleic acids and proteins in a label-free manner. Over the past two decades, substantial progress has been made in the development of nanopore biosensors for single-molecule biosensing, including the direct sequencing of DNA. [7] This breakthrough has opened up new possibilities for the analysis of proteins and other biomolecules based on nanopore technology.

Achieving precise control over the transport of protein molecules through a nanopore is a critical factor in the success of nanopore-based protein analysis. [8] While significant progress has been made in nanopore-based DNA sequencing, the transport of proteins presents unique challenges. [9, 10] Protein molecules possess three-dimensional structures and heterogeneous surface charges, making their translocation signals complex and difficult to interpret. Second, proteins exhibit conformational flexibility, adding another layer of complexity to the measurement and analysis process. [11, 12] Moreover, proteins tend to translocate at faster timescales than can be reliably detected, resulting in a low capture rate, especially for smaller proteins. [13] Although this temporal limitation can be partially addressed using high-bandwidth amplifiers, [14] it requires extensive optimisation of nanopore noise and geometry, which can be highly challenging. Addressing these challenges and achieving high spatiotemporal resolution in controlling protein transport is essential for the development of efficient nanopore-based protein analysers. Such analysers have the potential to enable single-molecule protein

sequencing, thereby advancing the understanding of proteomes and facilitating novel applications in protein analysis. [15, 16]

Several strategies have been developed for nanopore-based protein sequencing, including the use of molecular carriers. [17, 18, 19, 20, 21] These carriers consist of charged entities such as DNA, [21, 22, 23] charged peptides, [17, 24] or nanoparticles[25, 26] that can facilitate the transport of proteins through a nanopore and act as a recognition site for protein binding. By employing carriers, specific targets can be selectively captured from complex solutions. The binding of a protein to a carrier can be detected by observing the difference in signals between the protein-carrier complex and the carrier alone. Typically, the presence of the protein induces a distinct subpeak in the signal, serving as a signature of protein binding. [21] This strategy also offers the advantage of controlling and slowing down protein translocation by utilising carriers, as their transport through the nanopore occurs on a longer timescale. Inspired by DNA nanopore sequencing, Yan et al. [19] and Brinkerhoff et al. [20] have reported initial attempts at protein nanopore sequencing using carrier DNA molecules conjugated to target peptides. These DNA carriers, precisely propelled by a translocase, were capable of pulling the peptides through the nanopore in single-amino-acid steps, enabling the resolution of sequential differences among the analysed peptides. However, this approach still relies on complex DNA-peptide linkages and is limited to very short linear peptides. Further advancements are necessary to overcome these limitations and expand the scope of protein nanopore sequencing. Future research efforts may focus on developing alternative carrier systems, improving the control and resolution of protein translocation, and expanding the applicability to longer peptides and natively folded proteins.

In this chapter, I present a novel approach for controlling the transport of whole proteins through nanopores by using supercharged unstructured polypeptides (SUPs) as molecular carriers. These SUPs are derived from tropoelastin and have a repetitive sequence of $(VPGXG)_n$, where X represents a variable amino acid (**Figure 5.1**). [27] By introducing different charged amino acids at the X position, the SUPs can be tailored to have a high net positive or negative charge. [28] The programmable nature of SUPs allows them to be genetically fused with target

proteins without affecting proteins' native structures and functions. [29] Moreover, SUPs enhance the stability of proteins in solution, making them suitable for nanopore measurements performed at high salt concentrations. [30] Similar to DNA carriers, the high-density charge on fused SUPs increases the electrokinetic driving force on the target protein during translocation through the nanopore, significantly improving the efficiency and resolution of the measurement system. Folded target proteins can be distinguished from linear unfolded SUPs based on the extent of nanopore current blockade.

Specifically, I demonstrate the utility of cationic SUPs in accurately identifying proteins based on their size and shape, starting with enhanced green fluorescent protein (eGFP) variants as a model system. The translocation of the eGFP variants fused with a positively charged SUP exhibits a substantial slowdown effect compared to the native and anionic variants. This slowdown effect is likely attributed to the electrostatic interactions between the cationic SUPs and the nanopore. [31] Furthermore, this approach enables the study of protein-protein interactions at the single-molecule level with high spatiotemporal resolution. This opens up possibilities for single-molecule proteomics and interomics using SUPs as precise controllers of protein transport through nanopores. Overall, the use of SUPs as molecular carriers offers a promising avenue for achieving precise control over protein transport through nanopores, paving the way for advancements in protein fingerprinting and single-molecule proteomics.

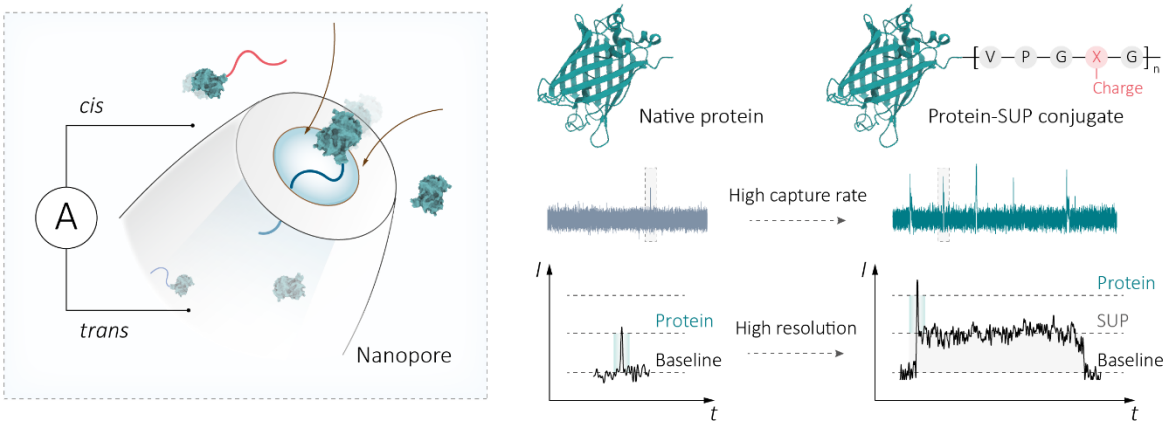


Figure 5.1 Schematic of nanopore detection using supercharged polypeptide carriers. Nanopore measurements of native proteins show fast translocation beyond the limits of traditional instruments, resulting in lower-than-expected capture rates and biased characteristic signals. With the assistance of SUP carriers, the protein capture rate is dramatically improved due to the introduction of a high net charge. In addition, translocation of such protein conjugates is substantially slowed down by the electrostatic attraction with the pore. Here, protein signals can be well distinguished from the SUP signals based on the difference in their excluded volume.

5.2 Methods and materials

5.2.1 Molecular cloning of protein-SUP conjugates

I would specially acknowledge Tina-Marie Thomas from DWI – Leibniz Institute for Interactive Materials for performing this section. The gene monomers of SUPs were ordered from Integrated DNA Technologies (Iowa, USA). One monomer corresponds to one building block of 9 charges. Sequences of genes and amino acid sequences are shown in **Table 5.1**. The gene fragments were ligated to pJET1.2/blunt vector using T4 DNA ligase (Thermo Fisher Scientific) according to the Blunt-end ligation protocol; the DNA fragment was used in a 3:1 molar ratio with pJET1.2/blunt vector, and the ligation mixture was transformed after 1h at 22°C incubation. A *Van91I* restriction site at the beginning and a *BglI* restriction site at the end of the sequence were used for recursive directed ligation as described by Chilkoti et al. [32] The

recognition sites of the restriction enzymes *Van91I* and *BglI* were preserved by incorporating one valine instead of a charged amino acid residue per ten pentapeptide repeats. The restriction was performed as described in the User Guide: Fast Digestion of DNA (Thermo Fisher Scientific). One monomer plasmid was opened with *Van91I* and alkaline phosphatase (FastAP; Thermo Fisher Scientific). A monomer of a second plasmid was cut out with *Van91I* and *BglI*. The resulting fragments were separated using a 1% agarose gel. The gel bands were cut out and purified using GFX™ PCR DNA and Gel Band Purification Kit (Cytiva). The restricted monomer fragment was ligated with T4 Ligase (Thermo Fisher Scientific) into the plasmid to form a dimer as described in User Guide: Self-circularization of Linear DNA. The plasmid was transformed into *E. coli* DH5α chemical competent cells, grown on LB agar plates with 100 µg/mL carbenicillin. Colonies were picked and grown in LB Lennox media overnight. Plasmid was extracted and isolated by using GeneJET Plasmid Miniprep kit. The DNA sequences were checked by sequencing (Microsynth Sequencing AG). The process was repeated, up to an oligomerisation of 8 building blocks. Thereby are 72 charges located in the respective SUP. To clone the fusion proteins of eGFP and circular permuted GFP with SUPs, the genes with the recognition sites of *Van91I* and *BglI* were ordered (IDT) and ligated to pJET1.2/blunt vector as described before. The eGFP gene was cut with *Van91I* and *BglI* and cloned in a pJET SUP vector, which was opened with *BglI*. By using the *NdeI* and *EcoRI* restriction site, the gene eGFP-SUP was cloned in the expression vector pET 25b (+). In case of pJET-CpGFP, the present *BglI* site on the pJET vector was removed using the primers FW: 5’-CGC CGA GCG CAG AAG TGG TC-3' and RV: 5’-CTG CCG GCT GGC TGG TTT ATT G-3', because *BglI* is used in further cloning. The ELP gene was cut by digestion with *Van91I* and *BglI* and run on a 1% agarose gel in TAE buffer. The band containing the ELP gene was excised from the gel and purified using a spin column purification kit (General Electric). pJET with target fragments were also digested with *Van91I* and *BglI* and dephosphorylated with Fast AP. The vectors were purified by 1% agarose gel extraction. The linearised pJET vectors and the ELP-encoding gene were ligated using T4 ligase with a molar ratio 1:3 and transformed into chemically competent *E. coli* DH5α cells. Cells were plated and colonies were picked and grown in LB medium supplemented with 100 µg/mL carbenicillin overnight, and plasmids were isolated using the GeneJET Plasmid Miniprep kit. Positive clones were verified by analytical digest with *Van91I* and *BglI* following gel electrophoresis. The DNA sequences of the inserts were verified by DNA sequencing (Microsynth Sequencing AG). Gene oligomerisation was again performed as described by

Chilkoti and co-workers. Finally, the gene fragments encoding the ELP fusion proteins were transferred into the expression vector pET25b (+) for protein expression.

Table 5.1 Information on SUP samples used in this work.

Name	Isoelectric point (pI)	Sequence (N terminal to C terminal)	Molecular weight (kDa)
eGFP	6.0	eGFP	27.4
eGFP-E36	4.57	eGFP-$(GEGVP)_{36}H_6$	46.6
eGFP-K18	9.8	eGFP-$(GKGVP)_{18}H_6$	37.9
eGFP-K36	10.3	eGFP-$(GKGVP)_{36}H_6$	46.6
GFP-K72	10.7	eGFP-$(GKGVP)_{72}H_6$	64.0
K72	11.85	$(GKGVP)_{72}H_6$	36.4
V40K72	11.85	$(GVGVP)_{40}(GKGVP)_{72}H_6$	52.8
CpsfCherry2-K72	10.15	CpsfCherry2-$(GKGVP)_{72}H_6$	62.9
Sn-K72	10.98	Sn-$(GKGVP)_{72}H_6$	44.1
mIFP-K72	10.45	mIFP-$(GKGVP)_{72}H_6$	73.0
K36-SfGFP-K36	10.7	$(GKGVP)_{36}$-SfGFP-$(GKGVP)_{36}H_6$	63.8
K36-SfCherry2-K36(K198C)	10.17	$(GKGVP)_{36}$- SfCherry2-$(GKGVP)_{36}H_6$	62.5

The number n means the repeat number of GXGVP sequence and net charge.

5.2.2 Protein expression and purification

I acknowledge Tina-Marie Thomas for the expression and purification of protein samples used in this work. The *recA*-deficient variant *E. coli.* BLR (DE3) was used for protein expression. This strain has the ability to stabilise plasmids with repetitive sequences. To produce the target proteins, an LB overnight culture was diluted in TB medium (6% (w/v) Tryptone, 12% (w/v) Yeast extract, 85 mM KH_2PO_4, 360 mM K_2HPO_4) to an OD600 of 0.1, supplemented with 100 µg/mL carbenicillin and incubated in a shaking incubator at 37°C and 200 rpm until OD600 0.6 to 0.8 was reached. The temperature was decreased to 30°C and grown over night. The cells had been centrifuged after harvesting at 4,000× g, 15 min, 4°C, resuspended in lysis buffer (50 mM sodium phosphate buffer pH 7.0, 300 mM NaCl, 20 mM Imidazole, EDTA-free Protease Inhibitor Cocktail (cOmplete™, Roche), 10 µg/mL DNaseI) and disrupted by high pressure

homogeniser (Constant Systems Ltd Multi-Shot). Insoluble cell debris were removed by centrifugation twice (14,000× g, 1 h, 4°C). The supernatant had been filtered through pore size membrane filter (0.22 µm, Millipore), before target proteins were purified under native conditions by IMAC Fast Protein Liquid Chromatography (BioRad NGCTM) and loaded onto a pre-equilibrated (Binding buffer: 50 mM sodium phosphate buffer pH 7.0, 300 mM NaCl, 20 mM Imidazole) Histrap fast flow column (5 mL, Cytiva). Subsequently, 5 column volumes were used to remove non-binding impurities. Elution was carried out over 4 column volumes (CV) with a gradient of 0 to 100% elution buffer (50 mM sodium phosphate buffer pH 7.0, 300 mM NaCl, 500 mM Imidazole) and a flow rate of 1 mL/min. The fractions were collected with a volume of 1 mL. The product was further purified by ion exchange chromatography (V=5 mL; Q HP column for glutamic acid containing SUPs; Heparin HP column for lysine containing SUPs) on the already mentioned NGC™ Chromatography System. The Product fractions of previous IMAC chromatography were pooled and 10 times diluted with ion exchange binding buffer (IEC A buffer: 50 mM Phosphate Buffer, 50 mM NaCl, pH = 7). The sample was loaded onto a pre-equilibrated ion exchange column. Unspecific binding proteins were washed out by using 4 CV IEC A. The gradient elution proceeded from 0 - 100% elution buffer (50 mM Phosphate Buffer, 2 M NaCl, pH = 7) within 4 CV with a flow rate of 1.0 mL/min. Protein purity was determined on a 12 % SDS-PAGE stained with Coomassie staining solution (30% ethanol, 20% glacial acetic acid, 0.05% Brilliant Blue G250, 0.05% Brilliant Blue R250) and destained with destaining solution (40% EtOH, 10% acetic acid).

5.2.3 Fabrication of nanopipettes

Quartz capillaries (GQF100-50-7.5, World Precision Instruments, UK) with an outer diameter of 1.0 mm and an inner diameter of 0.5 mm with an inner filament were plasma cleaned (Harrick Plasma, US) and then pulled by a laser-based pipette puller (Sutter Instrument, P-2000, USA). Nanopipettes used in all nanopore experiments were fabricated through a two-line protocol: (1) HEAT = 825, FIL = 4, VEL = 30, DEL = 130, PUL = 80; (2) HEAT = 850, FIL = 3, VEL = 20, DEL = 127, PUL = 185. It should be noted that these parameters are instrumentally specific and were optimised to yield nanopore openings of 12 ± 2 nm.

5.2.4 Nanopore measurements and data processing

The buffer used in the translocation experiments consisting of 1 M KCl and 10 mM Tris-EDTA (pH = 8) unless noted otherwise. For the binding assays, 1 nM eGFP-K72 was used and incubated with anti-GFP antibody (Thermo Fisher Scientific) at different concentrations for at least 2 h prior to nanopore experiments. Approximately 10 µL of the electrolyte was filled inside the nanopipette via a MicroFil needle (MF34G, World Precision Instruments, UK). Freshly made Ag/AgCl electrodes were then inserted into the nanopipette (*trans* chamber) and the bath (*cis* chamber), respectively. All ionic current recordings were performed using a high-bandwidth amplifier VC100 (Chimera Instruments, US). The recorded data was resampled to 1 MHz and low-pass filtered at 10 kHz. Analysis of all translocation events was performed using a custom-written MATLAB code, namely The Nanopore App, credited to Professor Joshua B. Edel. A workflow of the analysis procedure is shown in Figure 5.2.



Figure 5.2 Workflow of the Nanopore App for data analysis. (a) Data import and filter. In this step, nanopore data was loaded into the Nanopore App and then resampled and low-pass filtered dependent on the signal-to-noise ratio (e.g., 1 MHz sampling rate and 10 kHz low-pass filter). (b) Baseline tracking and threshold. The baseline was tracked to compensate for fluctuations in the current recordings. A histogram of all points was fitted by a Poisson distribution for the baseline, and a threshold (e.g., 7 σ) was used to classify events. (c) Peak selection. Events with a peak amplitude above the set threshold were selected. (d) Subpeak analysis. Multiple levels of an event were classified using cumulative sum (CUSUM) analysis, and subpeak amplitude and fractional position could be exported.

5.3 Results and Discussion

5.3.1 Design and characterisation of supercharged polypeptides

Supercharged unstructured polypeptides (SUPs) are structurally similar to natural elastin, specifically tropoelastin found in the extracellular matrix of vertebrate cells. [29, 33] The SUPs are characterised by a repetitive sequence of $(VPGXG)_n$, where each monomeric pentapeptide unit consists of Val-Pro-Gly-X-Gly (**Figure 5.1**). This sequence incorporates a highly hydrophobic backbone that allows the SUP to maintain an unstructured conformation, along with a variable residue X that determines the presence or absence of a charge. SUPs of various lengths and charges can be produced through recombinant expression in an *E. coli* system by manipulating the repeat number (n) and the amino acid X in the SUP gene. To generate SUP genes with specific lengths, a recursive directional ligation (RDL) approach was employed as shown in **Figure 5.3**. RDL is a stepwise procedure for assembling an oligomeric gene with a defined number of repeats. By adjusting the monomer length or performing multiple rounds of RDL, genes encoding SUPs of desired lengths can be obtained. In this study, SUPs with different numbers of repeat units, resulting in different net charges and chain lengths, were generated, including E36, K18, K36, and K72. The designations E and K represent the glutamic acid and lysine residues used in the X position, respectively, and the digit denotes the repeat number as well as charge number along the polypeptide backbone.

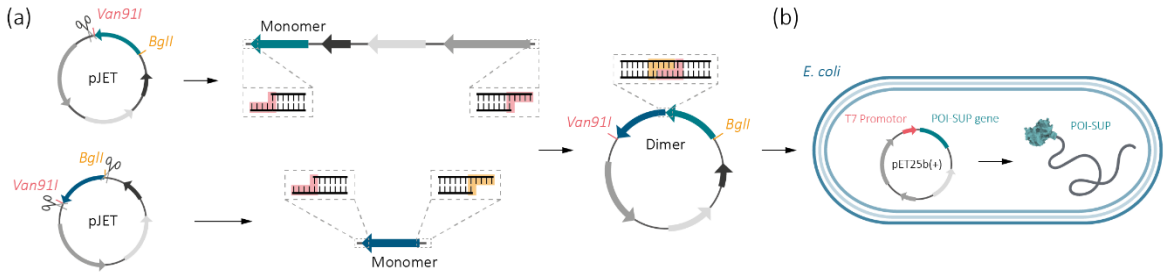


Figure 5.3 Schematic for the preparation of SUPs via recombinant DNA technology. (a) Recursive directional ligation (RDL) was used for the molecular cloning of SUP plasmid. (b) The fused SUPs were expressed in an *E. coli* system.

To fuse SUPs with proteins of interest (POI), the SUP genes and the POI genes were ligated together *via* the RDL process. The resulting fusion genes were then expressed in their native state and purified using affinity chromatography and ion exchange chromatography, resulting in fusion proteins with a purity greater than 90%. The expressed proteins were characterised using sodium dodecyl sulphate polyacrylamide gel electrophoresis (SDS-PAGE) and mass spectrometry techniques, such as matrix-assisted laser desorption/ionisation time-of-flight mass spectrometry (MALDI-TOF MS) or electrospray ionisation time-of-flight mass spectrometry (ESI-TOF MS), Figure 5.4 and Figure 5.5. This detailed characterisation ensures the integrity and quality of the SUPs and protein-SUP fusion constructs, confirming their suitability for use in controlling protein transport through nanopores. The information on the purity and identity of the expressed proteins also enables accurate interpretation of the subsequent experimental results.

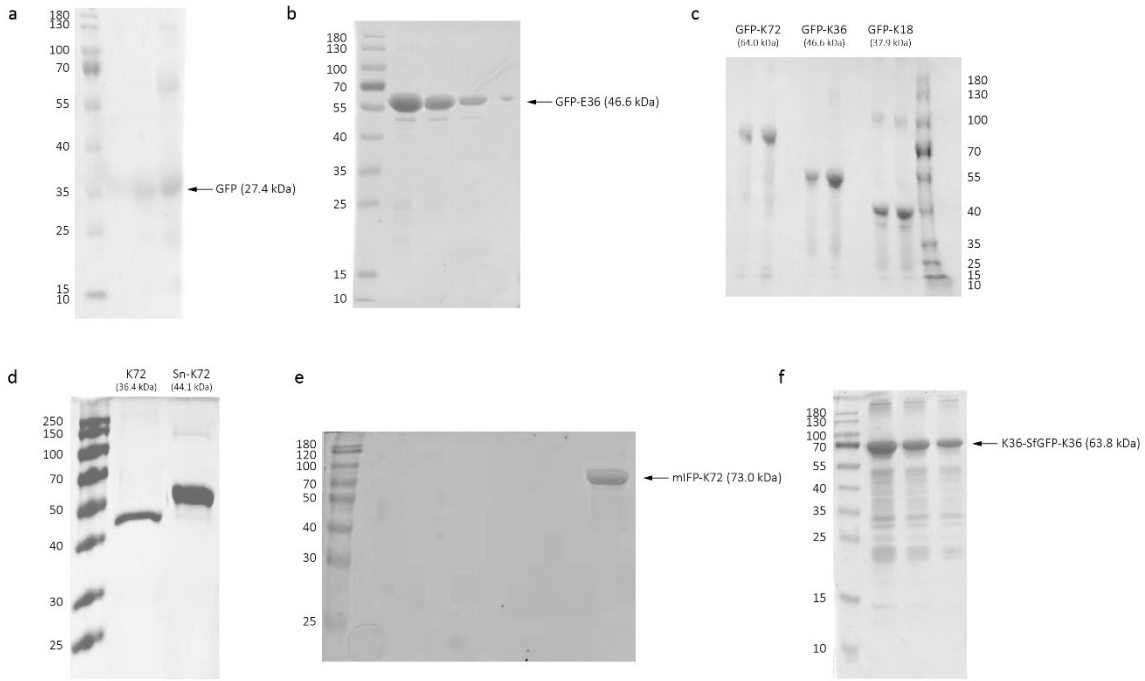


Figure 5.4 SDS-PAGE characterisation of SUP samples. Protein molecular weight markers were shown in each gel image with the protein products (a) eGFP; (b) eGFP-E36; (c) eGFP-K18, eGFP-K36, and eGFP-K72; (d) K72 and Sn-K72; (e) mIFP-K72; (f) K36-SfGFP-K36. It should be noted that the electrophoretic mobility of highly charged SUP samples is slightly different from that of folded proteins, which usually exhibit

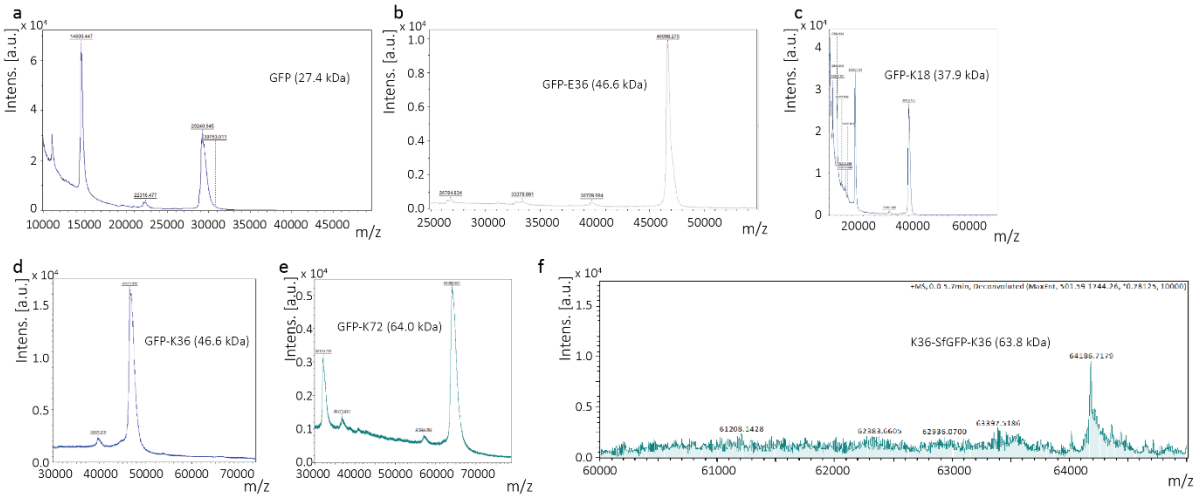


Figure 5.5 Mass spectra of SUP samples. (a) eGFP; (b) eGFP-E36; (c) eGFP-K18; (d) eGFP-K36; (e) eGFP-K72; (f) K36-SfGFP-K36.

5.3.2 Single-molecule protein sensing using nanopipettes

In the nanopore experiments, single-barrel quartz nanopipettes were utilised, which were fabricated using a laser-assisted pulling technique as previously described. [11] The resulting nanopores had a diameter of 12 ± 2 nm, as confirmed by scanning electron microscopy (SEM) imaging (**Figure 5.6**). This diameter estimation was consistent with the conductance measurements, where the open-pore conductance was determined to be 20.0 ± 1.6 nS (n = 20) in a 1 M KCl, 10 mM Tris-EDTA pH 8.0 buffer. The experimental setup involved introducing protein analytes from the outside of the nanopipette, with a ground/reference Ag/AgCl electrode placed in the *cis* chamber, and a patch Ag/AgCl electrode inserted into the pipette containing only buffer solution (*trans* chamber). Ionic current traces were recorded using a high-bandwidth amplifier (Chimera Instruments, VC100) at a sampling rate of 1 MHz and with a low-pass filter set to 10 kHz, unless otherwise specified. The power spectral density (PSD) plot confirmed that the recorded signals exhibited the typical noise levels expected for such measurements (**Figure 5.7**). This experimental setup allowed for the precise characterisation of protein transport through the nanopores using the SUP carriers, facilitating the investigation of protein translocation dynamics and interactions at the single-molecule level. The noise levels were carefully controlled to ensure accurate and reliable measurement of the ionic current signals during the experiments.

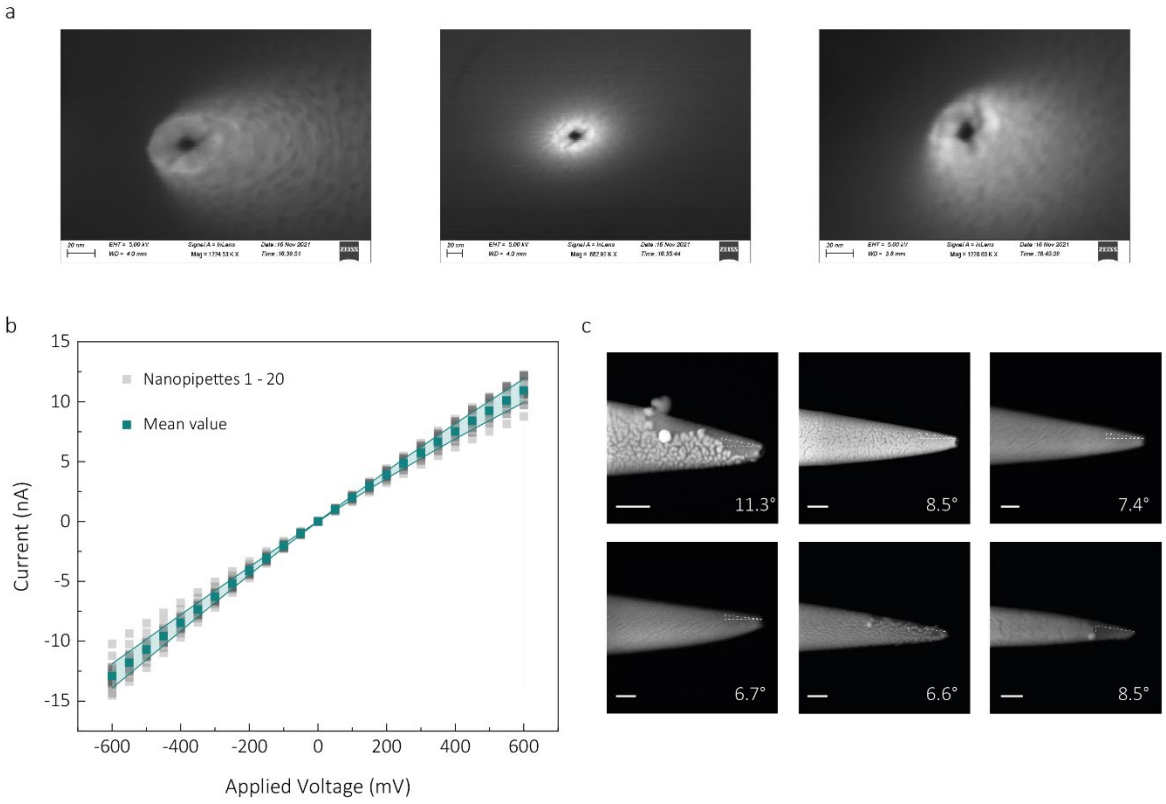


Figure 5.6 SEM and conductance characterisation of nanopipettes. The nanopipettes used in this work were fabricated from quartz capillaries (ID: 0.5 mm, OD: 1.0 mm) by a laser-assisted puller. (a) Top-view SEM images of the nanopores (scale bar: 20 nm). (b) I-V curves were measured in 1 M KCl, 10 mM Tris-EDTA, pH 8.0 buffer. The nanopore conductance was estimated to be 20.0 ± 1.6 nS fitted as a linear curve. (c) SEM images of the nanopipettes show the taper and geometry (scale bar: 100 nm). The outer half cone angle was directly measured from these side-view images. When calculating the nanopore size, the inner semi-angle was assumed to be equal to the outer semi-angle.

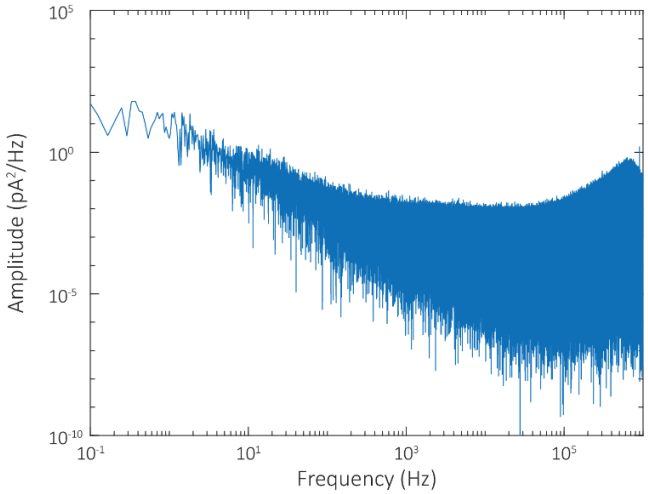


Figure 5.7 Power spectral density (PSD) plots of the nanopore platform. PSD plots were measured in 1 M KCl, 10 mM Tris-EDTA, pH 8.0 buffer, under a voltage of 500 mV and processed by The Nanopore APP.

To investigate how the SUP carrier affects protein transport through the nanopore, I focused on using enhanced green fluorescent protein (eGFP) as a model protein first. eGFP has a rigid beta-barrel structure and is relatively small (27 kDa), making it challenging to resolve using solid-state nanopores. [34, 35] In this study, I compared the transport properties of native eGFP with those of anionic eGFP-E36 and cationic eGFP-K36. In nanopore experiments, protein transport is influenced by a combination of diffusion, electrophoretic (EP) movement, and electroosmotic (EO) flow when an electric field is applied. [9] To minimise the contribution of EO flow and maximise the signal-to-noise ratio (SNR) of the measurements, the experiments were conducted under relatively high ionic strengths (1 M KCl). This high salt concentration helps to suppress EO flow while maintaining the native structure of the proteins. Under these conditions, protein molecules are captured and transported by the EP forces under the local electric field around the nanopore. [36] During protein translocation, a current blockade (ΔI_b) is generated, which is directly related to the excluded ionic volume (Λ) as described by **Equation 5.1**. [11, 12]

$$\Delta I_b \approx \sigma \psi \Lambda / H_{eff}^2 \quad (5.1)$$

Where:

σ represents the solution conductivity.

ψ is the applied potential difference.

ΔH_{eff} is the effective length of the nanopore.

By comparing the translocation properties of different eGFP variants (eGFP, eGFP-E36, and eGFP-K36), insights can be achieved into how the SUP carrier influences protein transport through the pore. This comparison, including current blockades and other relevant parameters, for different eGFP variants, is presented in **Figure 5.8** and **Figure 5.11**. These results provide detailed information on the effects of the SUP carrier on protein transport and nanopore measurements.

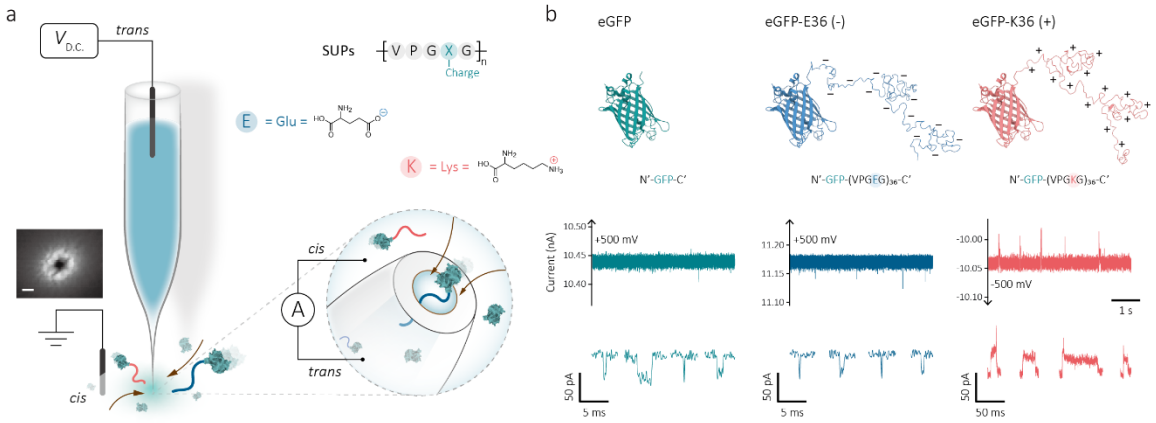


Figure 5.8 Single-molecule nanopore sensing of proteins carried by SUPs. (a) Schematic of the experimental setup of single-protein detection using nanopipettes. A SEM image of a typical 13 nm nanopore formed at the tip of a quartz nanopipette (scale bar: 20 nm). (b) Structural illustration of enhanced green fluorescent protein (eGFP, 28.6 kDa, pI of 5.58), anionic eGFP-E36 (46.6 kDa, pI of 4.57) and cationic eGFP-K36 (46.6 kDa, pI of 9.83). Representative ionic current traces and typical translocation events (filtered at 5 kHz for visualisation) in 1 M KCl, 10 mM Tris-EDTA, pH 8.0 buffer for eGFP (5 nM, +500 mV), eGFP-E36 (5 nM, +500 mV) and eGFP-K36 (5 nM, -500 mV) were shown respectively. Data was recorded at 1 MHz and fur-ther processed with a 10 kHz low-pass filter for statistics.

5.3.3 Comparison of native protein and its charged variants

In the experiments, native eGFP, which is negatively charged at pH 8.0, was driven by a positive voltage of +500 mV to translocate from the *cis* to the *trans* chamber of the nanopipette. This resulted in ionic current blockades corresponding to individual translocation events, as shown in **Figure 5.8**. The same positive voltage of +500 mV was applied to measure eGFP-E36, which has a higher net negative charge compared to native eGFP. Conversely, the voltage was reversed (-500 mV) for the translocation of eGFP-K36, which is positively charged under the same condition. By applying these voltages, the translocation of each eGFP variant could be controlled based on their charge properties.

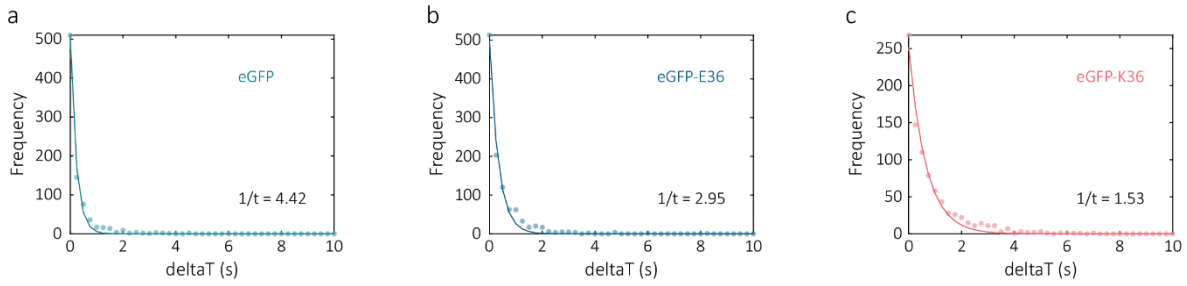


Figure 5.9 Capture rate of eGFP, eGFP-E36 and eGFP-K36. Distributions of the inter-event time (the time between two successive captured events) for (a) 750 nM eGFP, (b) 5 nM eGFP-E36, and (c) 5 nM eGFP-K36 at an applied voltage of 500 mV in 1 M KCl, 10 mM Tris-EDTA, pH 8.0 buffer. Solid lines represent single-exponential fits, from which the protein capture rate was extracted.

The capture rate of the three eGFP variants was determined by analysing the distribution of interval times (Δt) between two consecutive translocation events (**Figure 5.9**). [37] The capture rate reflects the efficiency of capturing individual eGFP molecules as they translocate through the nanopore. Due to the low capture rate of native eGFP at nanomolar concentrations, it was necessary to use a higher concentration (750 nM) to collect sufficient data for analysis (**Figure**

5.10). The normalised capture rate was compared between native eGFP and the supercharged eGFP-E36 and eGFP-K36 variants (Figure 5.11a). It was found that the introduction of SUP carriers significantly improved the capture efficiency. eGFP-E36 showed a 70-fold improvement, while eGFP-K36 exhibited a 37-fold improvement, compared to native eGFP, under the same magnitude of applied voltage. P-value analysis confirmed the statistical significance of these improvements. The enhanced capture efficiency observed with the SUP carriers can be attributed to the elevated charge density of individual eGFP molecules. This increased charge density leads to a stronger EP driving force experienced by the proteins during nanopore transport. Consequently, the SUP carriers improve the transport and capture of eGFP molecules, enhancing the performance of nanopore-based protein analysis.

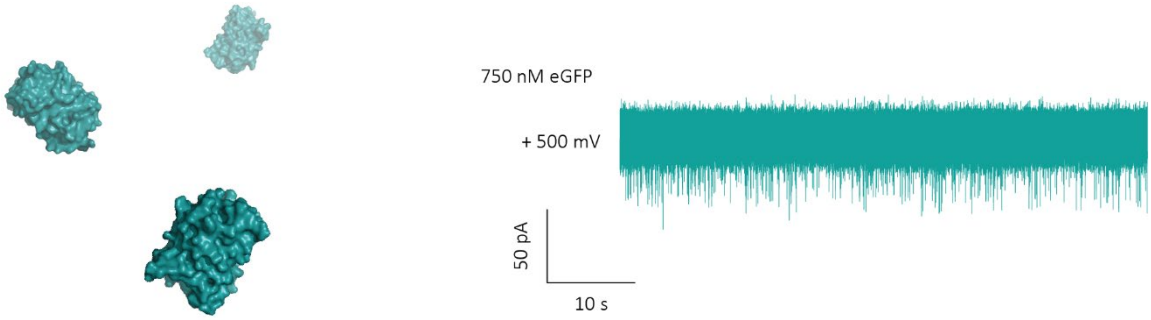


Figure 5.10 eGFP nanopore detection at a high concentration. 750 nM eGFP was used to obtain sufficient data for statistical analysis due to the low capture rate for native eGFP. Protein translocation was performed in 1 M KCl, 10 mM Tris-EDTA, pH 8.0 buffer at +500 mV.

Improving the spatiotemporal resolution of protein sensing is crucial for accurate and efficient protein detection and single-molecule protein sequencing. [16] Two key characteristics that reflect the spatiotemporal resolution of a nanopore measurement system are the dwell time and peak amplitude of translocation events. In Figure 5.11b, the scatter plots of dwell time versus peak amplitude indicate that eGFP-K36 has the highest spatiotemporal resolution

among the three eGFP variants. The dwell time is closely related to the electrokinetic transport of proteins within the local electric field and their interactions with the nanopore. For native eGFP, the mean dwell time was determined to be 1.3 ± 0.2 ms, consistent with previous studies using similar nanopore systems. [35] In contrast, eGFP-E36 molecules exhibited faster translocation with a mean dwell time of 0.3 ± 0.1 ms. However, the translocation of eGFP-K36 molecules was significantly slower, with a mean dwell time of 18.2 ± 2.6 ms (**Figure 5.11c**). The mean peak amplitude for eGFP-K36 and eGFP-E36 was similar, measuring 42 ± 3 pA and 36 ± 2 pA, respectively (**Figure 5.11d**).

This change in dwell time can be attributed to the introduction of the SUP carriers, which altered the interaction between the protein molecules and the nanopore during translocation. [31] Similar slowing-down of translocation events has been observed for DNA molecules passing through nanopores engineered with positive charges. [38] In the experimental setup, the quartz nanopore surfaces are negatively charged at pH 8.0. As a result, negatively charged eGFP-E36 experiences electrostatic repulsion from the nanopore walls, reducing its adhesion. On the other hand, positively charged eGFP-K36 is attracted to the nanopore surface, significantly slowing down its translocation and improving the temporal resolution. This increase in dwell time enhances event detection rates and facilitates accurate determination of the translocation signal amplitude. [39]

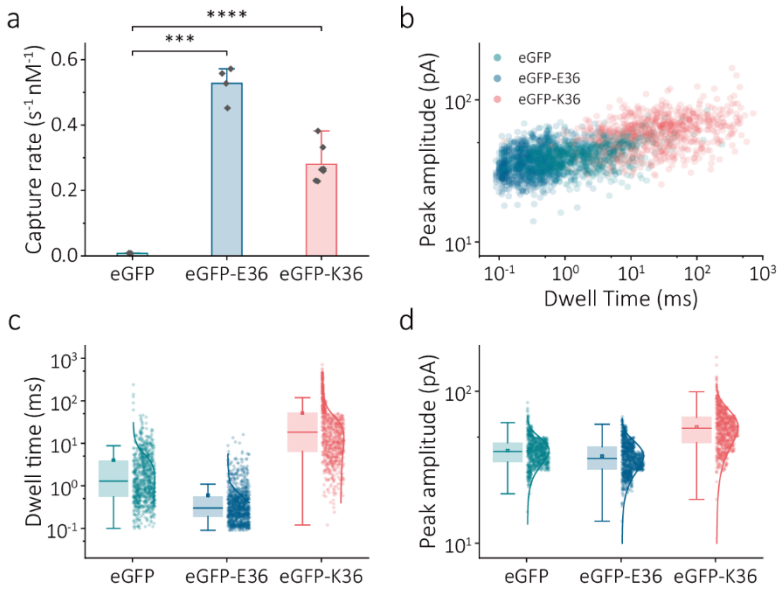


Figure 5.11 Nanopore translocation behaviours of different eGFP variants. (a) Normalised capture rate (event frequency/concentration) for eGFP, eGFP-E36, and eGFP-K36 at the same voltage magnitude (500 mV). T scores were used to test the statistical significance between eGFP and eGFP-SUPs; ***P<0.001 and ****P<0.0001. (b) Scatter plots of peak amplitude versus dwell time for eGFP (n = 845), eGFP-E36 (n = 1074), and eGFP-K36 (n = 871) at 500 mV. Box and whisker plots of (c) dwell time and (d) peak amplitude for eGFP, eGFP-E36, and eGFP-K36, along with associated statistics.

5.3.4 Length and voltage dependence of cationic SUPs on nanopore translocation

In order to confirm the mechanism of slowing down protein translocations using cationic SUPs, a series of cationic GFP-SUPs were synthesised with different positive charges, including eGFP-K18, eGFP-K36, and eGFP-K72 (typical traces are shown in **Figure 5.12**), by tuning the cycle number of recursive directional ligation (RDL). Gel electrophoresis and mass spectrometry were used to characterise these constructs (**Figure 5.4** and **Figure 5.5**). The dependence of the capture rate on the charges of the SUP carriers was first investigated. It has been previously shown that for pores larger than the analyte, the capture rate of a protein is linearly proportional to the voltage and protein concentration. [34] Consistent with this trend, **Figure 5.13b** demonstrates that the capture rate increases as more positive charges are introduced

in the cationic eGFP-SUPs. This increase is attributed to the enhancement of EP driving forces with increasing net charges. Comparing with eGFP alone, the capture rate for eGFP-K18 (with +18 net charges), eGFP-K36 (with +36 net charges), and eGFP-K72 (with +72 net charges) showed approximately 17-fold, 29-fold, and 136-fold increases, respectively.

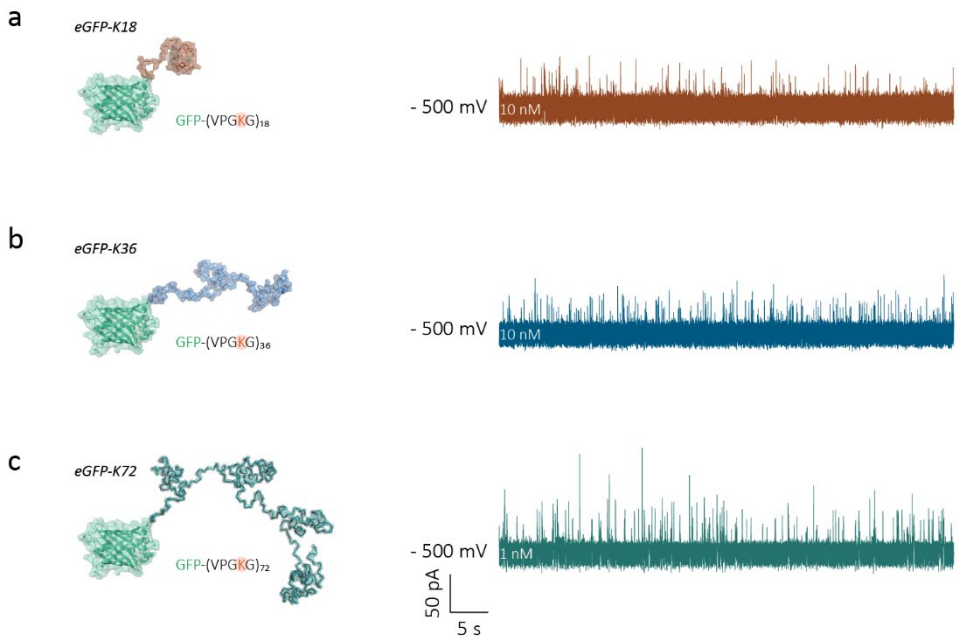


Figure 5.12 Nanopore detection of eGFP-K18, eGFP-K36 and eGFP-K72. Representative traces for the translocation of (a) 10 nM eGFP-K18, (b) 10 nM eGFP-K36, and (c) 1 nM eGFP-K72. All the translocation experiments were performed in 1 M KCl, 10 mM Tris-EDTA, pH 8.0 buffer at -500 mV. Data was sampled at 1 MHz and digitally filtered using a Bessel low-pass filter at 10 kHz.

Furthermore, the voltage showed a linear dependence on the normalised capture rate for eGFP, eGFP-K18, eGFP-K36, and eGFP-K72 (**Figure 5.13c**). However, the capture rate plots of eGFP and eGFP-K18 also exhibited an exponential trend with voltage as shown in **Figure 5.14**, indicating a barrier-limited regime that describes the capture of short molecules under a weak

EP force.[40] On the other hand, as the length and charge of the SUPs increased, both eGFP-K36 and eGFP-K72 exhibited a more strictly linear voltage dependence. This transition suggests that the effective capture mechanism shifts to a diffusion-limited regime, where long molecules experience a strong EP force during nanopore transport. These findings indicate that the introduction of more positive net charges can significantly enhance the protein capture efficiency, and a diffusion-limited regime can be achieved with longer SUPs.[41] This suggests that further increasing the positive net charges in the SUP carriers may lead to even greater improvement in protein capture efficiency.

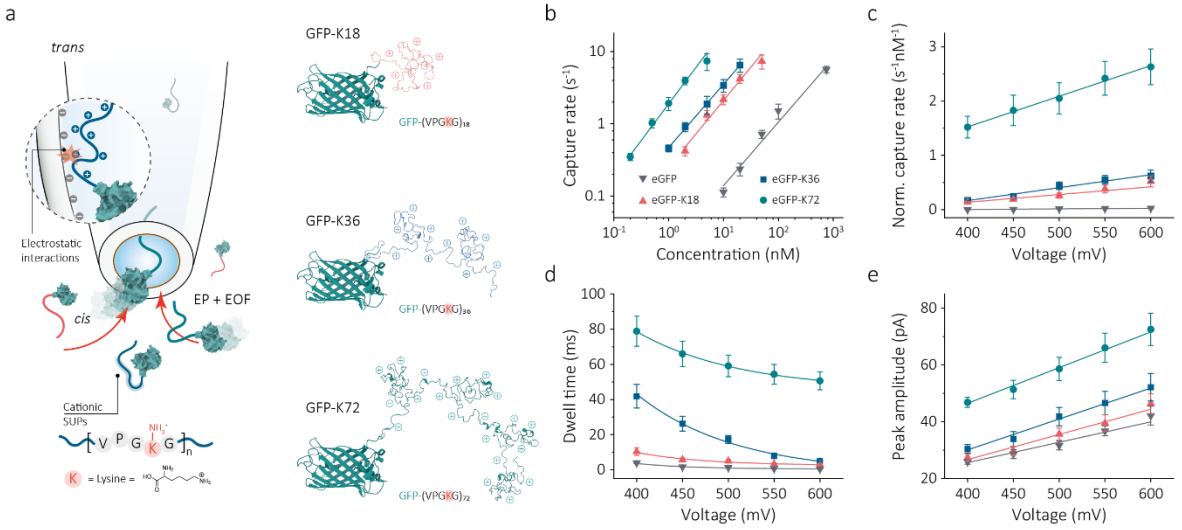


Figure 5.13 Charge- and length-dependence of nanopore translocation for eGFP-SUPs. (a) Schematic of the cationic eGFP-SUPs translocated through a nanopore. Lysine is the key compound in the repeated sequence $(VPGKG)_n$, where n represents the net charge of the SUP. Application of a negative bias to the *trans* chamber captures cationic eGFP-SUPs by both EP and EO flows. A series of eGFP-SUPs with different charges and chain lengths (K18, K36, and K72) were shown. Ionic current was recorded in 1 M KCl, 10 mM Tris-EDTA pH 8.0 buffer. Data was sampled at 1 MHz and low-pass filtered at 10 kHz. (b) Concentration dependence of capture rate for eGFP, eGFP-K18, eGFP-K36, and eGFP-72 at -500 mV. Voltage dependence of (c) normalised capture rate, (d) dwell time, and (e) peak amplitude for eGFP, eGFP-K18, eGFP-K36, and eGFP-72. The error bars represent one standard deviation of at least three independent experimental repeats.

The dwell time of each cationic eGFP variant exhibits an exponential decay with increasing voltage (**Figure 5.13d**), indicating that the applied voltage reduces the energy barrier for protein translocation. [4] This voltage dependence confirms that individual protein molecules translocate through the nanopore rather than bind and dissociate due to strong electrostatic interactions. [42] Compared to native eGFP, the mean dwell time for eGFP-K18, eGFP-K36, and eGFP-K72 was 3.7 times, 13.0 times, and 44.7 times slower, respectively, at a voltage of -500 mV. This increasing slowdown effect is not solely attributed to the increase in polypeptide contour length translocated, as the length and charge of eGFP-K36 and eGFP-K72 fusions are only doubled and quadrupled compared to eGFP-K18, respectively. It is primarily caused by the increasing electrostatic interactions within the nanopore. [43]

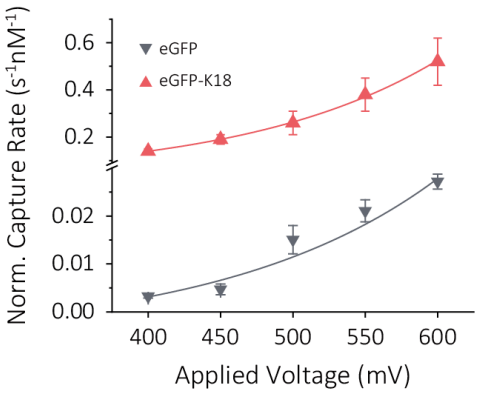


Figure 5.14 Voltage dependence of capture rate for eGFP and eGFP-K18. Normalised capture rate of cationic eGFP-SUPs was plotted as a function of the applied voltage. In particular, eGFP and eGFP-K18 show an exponential increase with the voltage, which indicates its nanopore translocation is limited by an energy barrier. Longer molecules, eGFP-K36 and eGFP-K72, present a linear increase with voltage.

The peak amplitude of the translocation signal increases with the increasing length of the SUPs (**Figure 5.15**). This increase is associated with the larger molecular weight of eGFP-SUPs, leading to greater ion exclusion within the sensing region. [12] The peak amplitude of each eGFP variant linearly increases with the applied voltage (**Figure 5.13e**), consistent with the relationship described in **Equation 5.1**. Based on these findings, it is evident that introducing more positive charges into the SUP chain significantly improves the performance of nanopore sensing. Among the cationic eGFP variants, eGFP-K72 demonstrates the highest potential as a molecular carrier for protein sensing, offering high capture efficiency and spatiotemporal resolution.

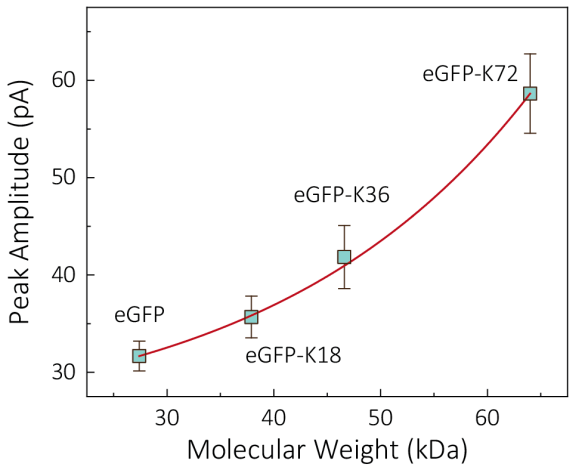


Figure 5.15 Dependence of peak amplitude on molecular weight. Peak amplitude of eGFP variants as a function of molecular weight. The current amplitude shows an exponential increase in response to the increasing length of SUPs. This experiment was repeated at least three times for each protein at 500 mV.

5.3.5 SUP carriers for improved protein detection

The use of genetically programmable SUPs offers flexibility in tuning the sign and amount of protein charge, enabling improved capture rates and detection efficiency regardless of the charge polarity. In this study, cationic SUPs were utilised to significantly slow down protein translocation, enhancing detection accuracy. This precise detection allows for highly-resolved analysis of individual translocation events, enabling the identification of structural details and binding states through subpeak analysis. This analytical method relies on the difference in excluded volume between molecular carriers and target proteins, a principle previously applied in DNA-carrier-assisted protein screening. [21, 23] However, the quick translocation of DNA through nanopores limits the effectiveness of the approach when resolving subpeak features. Long DNA carriers (several micrometres in length) are typically required, which does not effectively slow down the translocation of target proteins. In addition, the random folding of long DNA carriers can introduce interference, increasing the probability of false positives in determining protein subpeaks.

Control experiments were conducted using only SUP carriers (K72) and compared to lambda phage DNA (λ-DNA), a commonly used double-stranded DNA carrier in nanopore sensing (Figure 5.16). The mean dwell time for K72 translocation was 40.1 ± 5.0 ms at an applied voltage of -500 mV. Based on the linear conformation of K72 within the nanopore, the average translocation speed was estimated to be 3.6 nm ms^{-1}, assuming a length of 0.35 nm per amino acid. [44] This speed is approximately 4,000 times slower than that of λ-DNA under the same conditions, as shown in Figure 5.17. The amplitude distribution of lambda-DNA exhibited four distinct populations, with the first corresponding to unfolded DNA translocation and the remaining populations representing DNA molecules folded to different degrees. [45] These complex folding states could introduce interference in subpeak analysis when target proteins are bound to DNA carriers . In contrast, the density plot of K72 revealed two populations corresponding to its unfolded and folded states, respectively (Figure 5.16). Importantly, the folding conformation of K72 did not produce sharp protein-binding-like subpeaks but instead showed two stepped current levels. This indicates that the probability of false positives caused by carrier folding can be negligibly small. Thus, K72 can serve as a candidate SUP carrier for

controlling protein translocation and enabling the recognition of specific proteins through subpeak analysis.

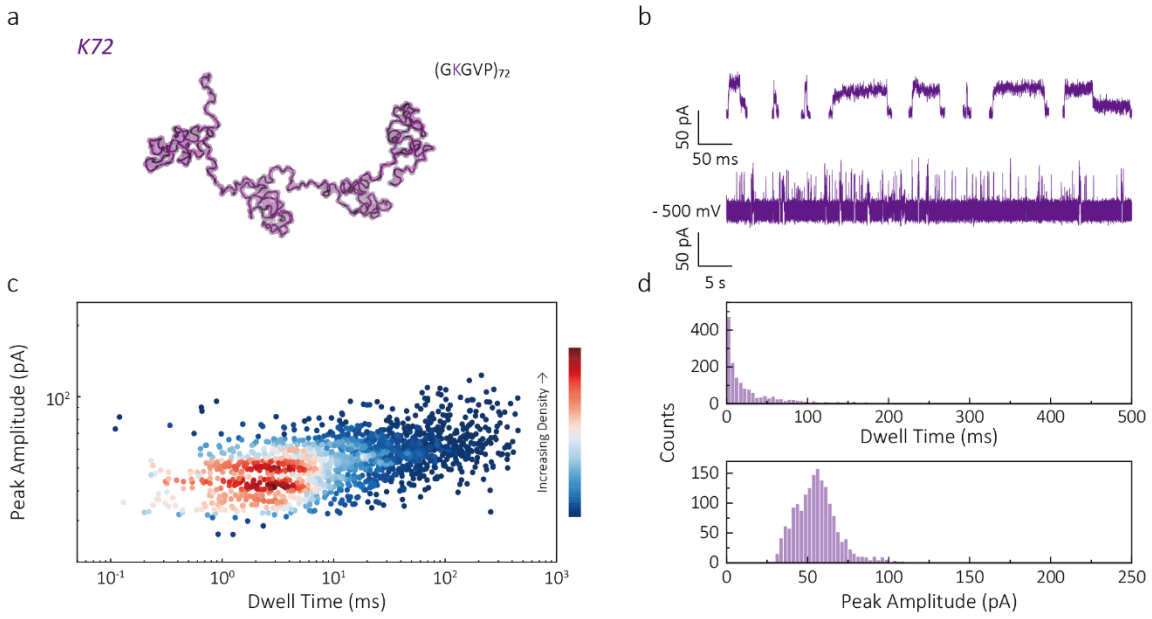


Figure 5.16 Nanopore detection of K72. (a) Protein model of K72 predicted by I-TASSER.[46] (b) Typical events and current-time traces of 1 nM K72 translocation recorded in 1 M KCl, 10 mM Tris-EDTA, pH 8.0 buffer at -500 mV. Data was sampled at 1 MHz and digitally filtered using a Bessel low-pass filter at 10 kHz. (c) Scatter plot of peak amplitude versus dwell time. (d) Distribution of the dwell time and peak amplitude for K72 translocation.

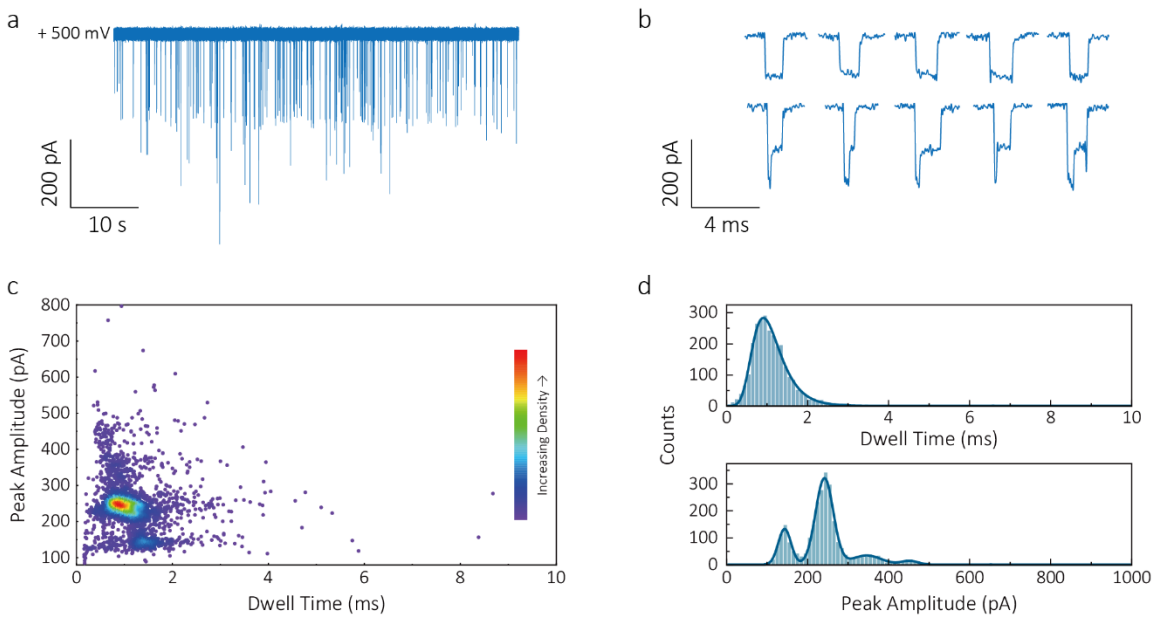


Figure 5.17 Nanopore detection of λ-DNA. (a) Representative current-time traces of 100 pM λ-DNA translocation were recorded in 1 M KCl, 10 mM Tris-EDTA, pH 8.0 buffer at +500 mV. Data was sampled at 1 MHz and digitally filtered using a Bessel low-pass filter at 10 kHz. (b) Typical events of unfolded and folded DNA molecules. (c) Scatter plot of peak amplitude versus dwell time. (d) Distribution of the dwell time and peak amplitude for λ-DNA translocation showing multiple folding levels.

In protein analysis, it is common to bind target proteins at one end of the carrier molecule. This can be achieved through covalent or non-covalent binding, allowing for the study of biophysical properties or protein screening, respectively. In this study, proteins of different sizes and shapes were covalently extended with a cationic K72 SUP to create protein-K72 structures, as shown in **Figure 5.18a**. When the fusion protein is threaded into the nanopore, a two-level current signature is expected, as depicted in **Figure 5.18b**. The first level corresponds to the translocation of the SUP carrier and has a long duration similar to that of K72 translocation without the protein fused. The second level appears at the beginning or end of the event and corresponds to the translocation of the folded target protein, which has a shorter dwell time but a greater current blockade. This increased current blockade is attributed to the larger volume exclusion per unit length of folded proteins compared to unfolded SUPs. **Figure 5.19** demonstrate the ability of K72 SUP carriers to effectively control and distinguish

target proteins of different sizes based on the subpeaks observed in individual translocation events. Four proteins ranging in size from 13.0 to 35.2 kDa were compared: antifreeze protein (Sn, 13.0 kDa), red fluorescent protein (SfCherry, 20.3 kDa), enhanced green fluorescent protein (eGFP, 28.6 kDa), and monomeric near-infrared fluorescent protein (mIFP, 35.2 kDa), as illustrated in **Figure 5.19a**.

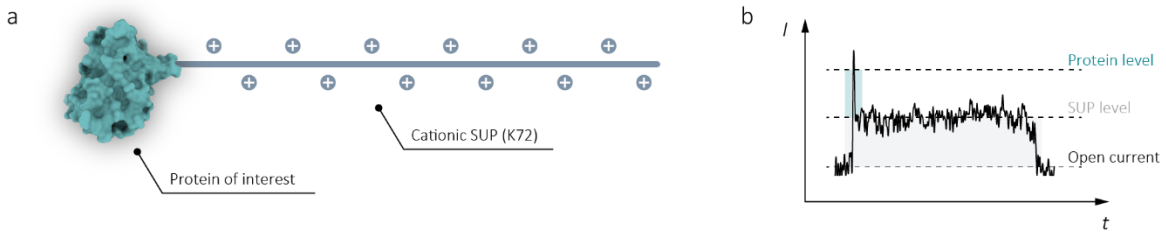


Figure 5.18 Schematic of protein detection carried by K72 carriers. (a) Structure of the protein-SUP complex, where the protein of interest was attached at one end of K72. (b) Schematic illustration of a typical event of one protein-SUP molecule during nanopore translocation. The relationship between the excluded volume (Λ) and the blockade current (ΔI_b) can be estimated using **Equation 5.1**, indicating current blockade is proportional to the excluded volume of translocated molecules. A folded protein, therefore, has a greater excluded volume per unit length than that of an unfolded, linear SUP. Individual nanopore readouts are shown with the protein level as a higher current blockade and the SUP level as a lower current blockade but longer time residence.

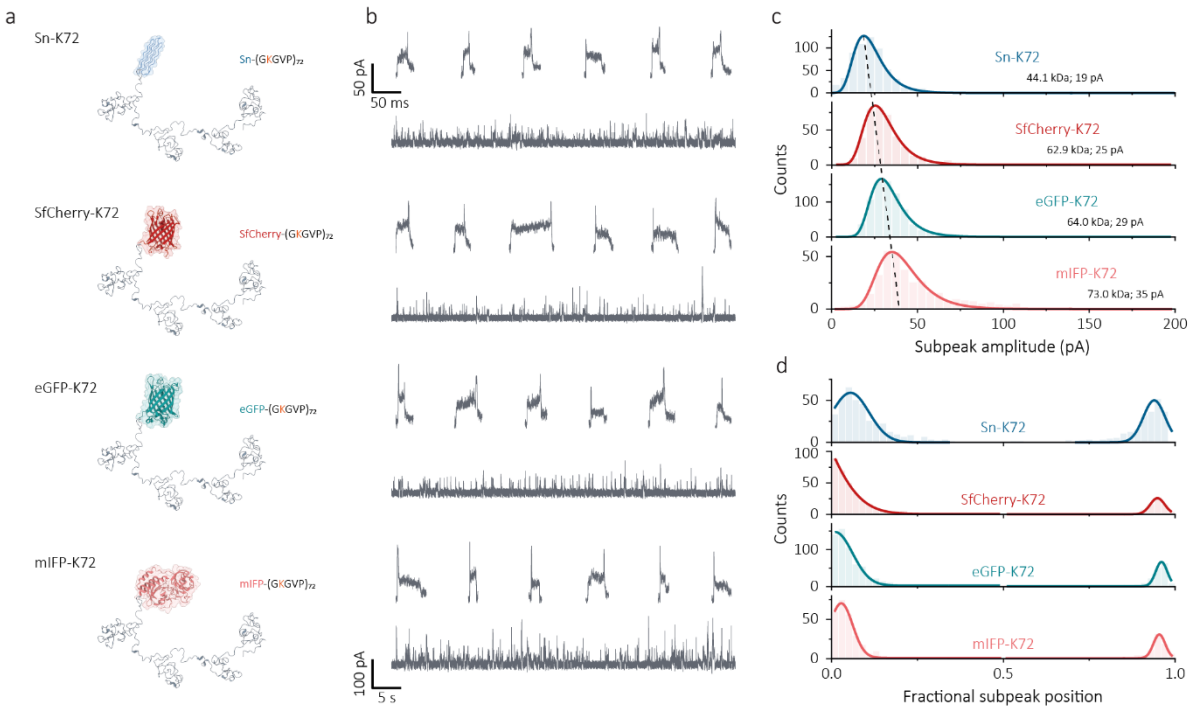


Figure 5.19 Size-dependent single-protein identification using cationic SUPs and subpeak analysis. (a) Structures of a series of proteins with different sizes, Sn (13.0 kDa), SfCherry (20.3 kDa), eGFP (28.6 kDa), and mIFP (35.2 kDa), fused in K72 carriers. (b) Representative ionic current traces (scale bar: 100 pA; 5 s) and typical individual translocation events (scale bar: 50 pA; 80 ms) for the corresponding structures were filtered to 5 kHz for better visualisation. Protein translocation was performed in 1 M KCl, 10 mM Tris-EDTA pH 8.0 buffer at -500 mV and processed with a low-pass filter of 10 kHz. (c) Distributions of the subpeak amplitude extracted from individual translocation events for Sn-K72 (n = 578), SfCherry-K72 (n = 389), eGFP-K72 (n = 765), and mIFP-K72 (n = 341). The mean amplitude of subpeaks shows an increasing trend as the size of proteins increases. Distribution is fitted by the Gumbel function. (d) Distributions of fractional subpeak position (i.e., relative location) suggest subpeaks located at either start or end of individual events, consistent with the protein-SUP structure. Protein Data Bank (PDB) codes: Sn, 3BOI; SfCherry, 4KF4; eGFP, 2Y0G; mIFP, 5VIQ.

In **Figure 5.19b**, representative current traces and individual events are shown for the four protein-K72 fusions at a low concentration of 1 nM during nanopore measurements. The current-time traces indicate that the capture rate for each protein-K72 fusion is sufficiently high for single-molecule analysis and remains consistent across all cases, suggesting that the

SUP carrier (K72) can effectively control protein transport regardless of the size and net charge of the target proteins. After performing subpeak classification, events exhibiting a two-level signature were identified, accounting for approximately 36%, 38%, 46%, and 42% of the total events for Sn-K72, SfCherry-K72, eGFP-K72, and mIFP-K72, respectively. This high proportion of subpeaks indicates the successful recognition of protein binding events. However, it is worth noting that the lack of subpeaks in some events may be attributed to insufficient temporal resolution, which could be improved by using a higher-bandwidth amplifier. [13, 14] Interestingly, the ratio of detectable subpeaks slightly increased with the molecular weight of the target proteins, likely due to increased signal-to-noise ratio and dwell time for larger proteins. The distribution of subpeak amplitudes extracted from individual events (Figure 5.19c) showed a well-defined single population for all proteins, with the mean subpeak amplitude exhibiting a linear increase with molecular weight (Figure 5.20), consistent with the behaviour expected for globular proteins. [47] This high sensitivity enables precise identification of different proteins and the detection of protein-protein interactions that may affect volume exclusion within the nanopore. Furthermore, most events for all four protein-K72 fusions displayed a single subpeak at the beginning or end of the events, with a fractional position of approximately 0.05 or 0.95, respectively (Figure 5.19d).

A control experiment using V40-K72, where an uncharged linear polypeptide (V40) is connected to the K72 carrier, showed translocation events without protein-bound-like subpeaks similar to the folded proteins in previous cases (Figure 5.21). Importantly, this subpeak recognition method also worked at a near-physiological salt concentration (100 mM KCl), where two distinct current levels were detected (Figure 5.22). However, higher voltages were required to overcome the stronger electrostatic interactions at lower ionic strengths, which sometimes resulted in irreversible blockage of the nanopore.

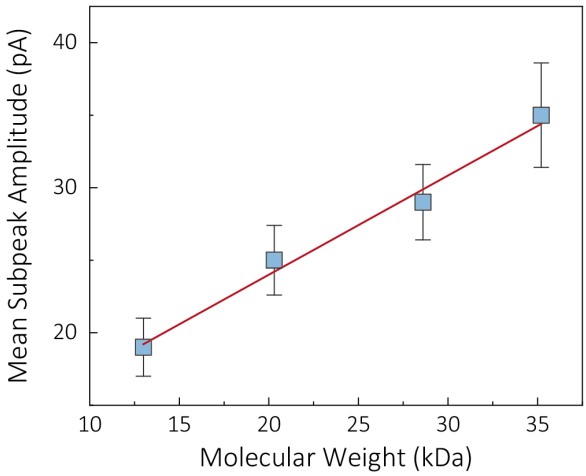


Figure 5.20 Dependence of subpeak amplitude on molecular weight. Subpeak amplitude of different proteins as a function of molecular weight. The red line represents a linear fitting through the blue markers. This experiment was repeated at least three times for each protein, showing a similar linear dependence for these globular proteins.

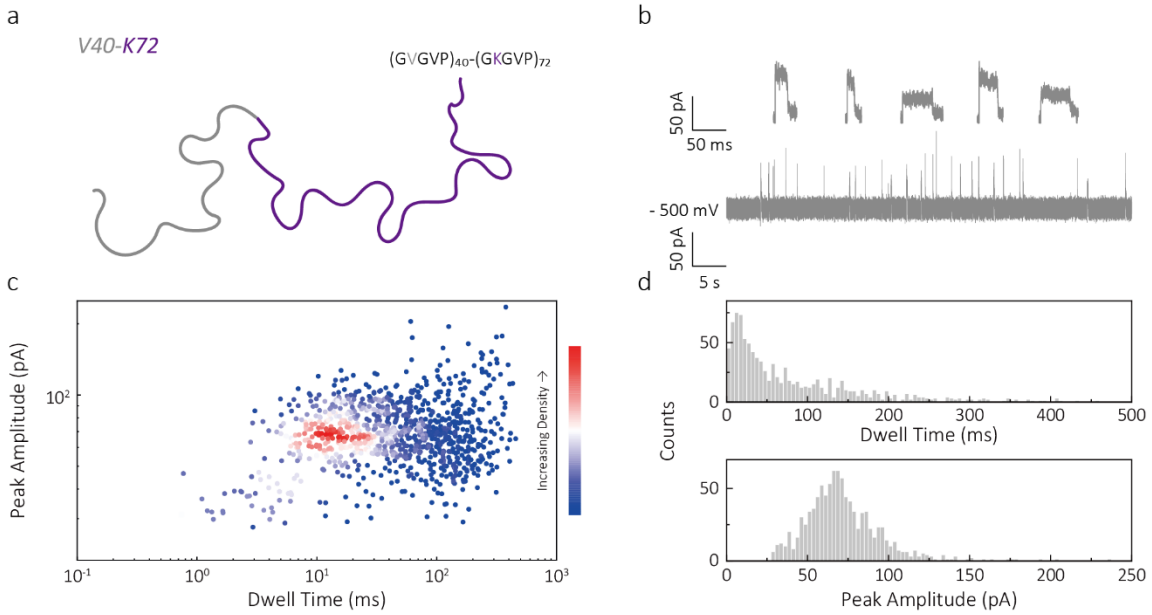


Figure 5.21 Nanopore detection of V40K72. (a) Protein model and sequence of V40K72. (b) Typical events and current-time traces of 1 nM V40K72 translocation were recorded in 1 M KCl, 10 mM Tris-EDTA, pH 8.0 buffer at -500 mV. Data was sampled at 1 MHz and digitally filtered using a Bessel low-pass filter at 10 kHz. (c) Scatter plot of peak amplitude versus dwell time. (d) Distribution of the dwell time and peak amplitude for V40K72 translocation.

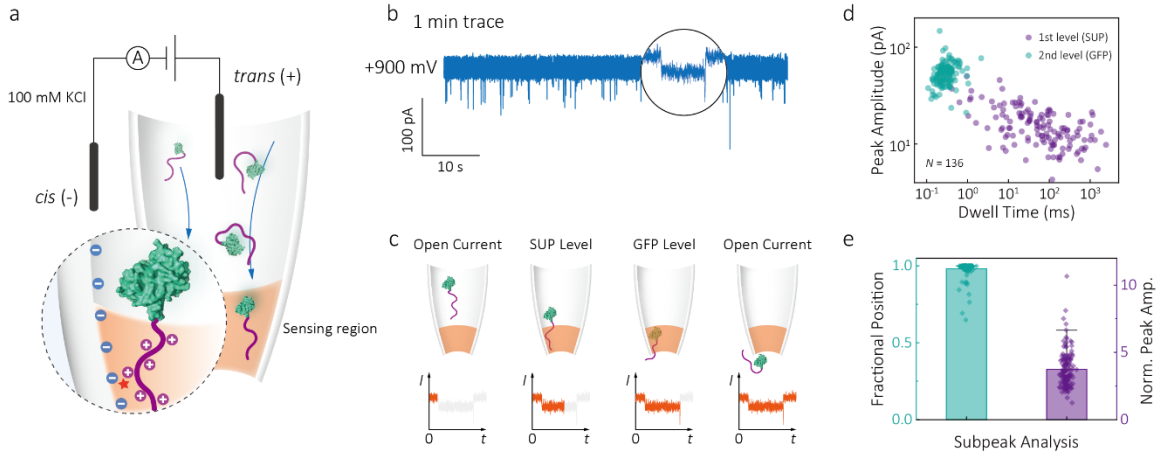


Figure 5.22 Nanopore detection of eGFP-K72 at low ionic strengths. (a) Schematic of eGFP-K72 translocation at a low salt concentration (100 mM KCl, 10 mM10 mM Tris-EDTA, pH 8.0 buffer). In this case, the protein was added inside the nanopipette (*trans* chamber), and a negative voltage was applied to drive protein molecules translocating from *trans* to *cis* side. Cationic SUPs had stronger electrostatic interaction with the nanopore inner walls at low ionic strengths. (b) Typical events and current-time traces of 10 nM eGFP-K72 show a two-level current signature with a subpeak at the end. (c) Illustration of eGFP-K72 translocation and corresponding current blockade. (d) Scatter plots of peak amplitude versus dwell time for the first level (SUP level) and second level (eGFP level). (e) Statistics for the subpeak position and subpeak amplitude.

Our sensing strategy demonstrates a well-defined consistency between protein structures and nanopore readouts. This consistency is observed not only in the subpeak position, where the target protein is located, but also in the size differentiation based on the subpeak amplitude. It has been successfully shown that this strategy is suitable for generic proteins, irrespective of their size and charge. To further enhance the accuracy of this approach, a rational carrier structure has been designed, as illustrated in **Figure 5.23a**. In this structure, the target protein is positioned at the centre of the carrier, forming a K36-protein-K36 fusion without altering the total charge of the SUP carrier. By placing the target protein at the centre, false positives caused by partial folding of the carriers were minimised, as random folding of linear biomolecules tends to occur more frequently at the ends of the molecules. [48] Furthermore,

incorporating recognition sites at various fractional positions of a single carrier allows for multiplexed high-throughput protein sensing. [21] Example events again exhibit a two-level current signature, with the subpeak shifting to the centre where the target protein is attached (Figure 5.23b).

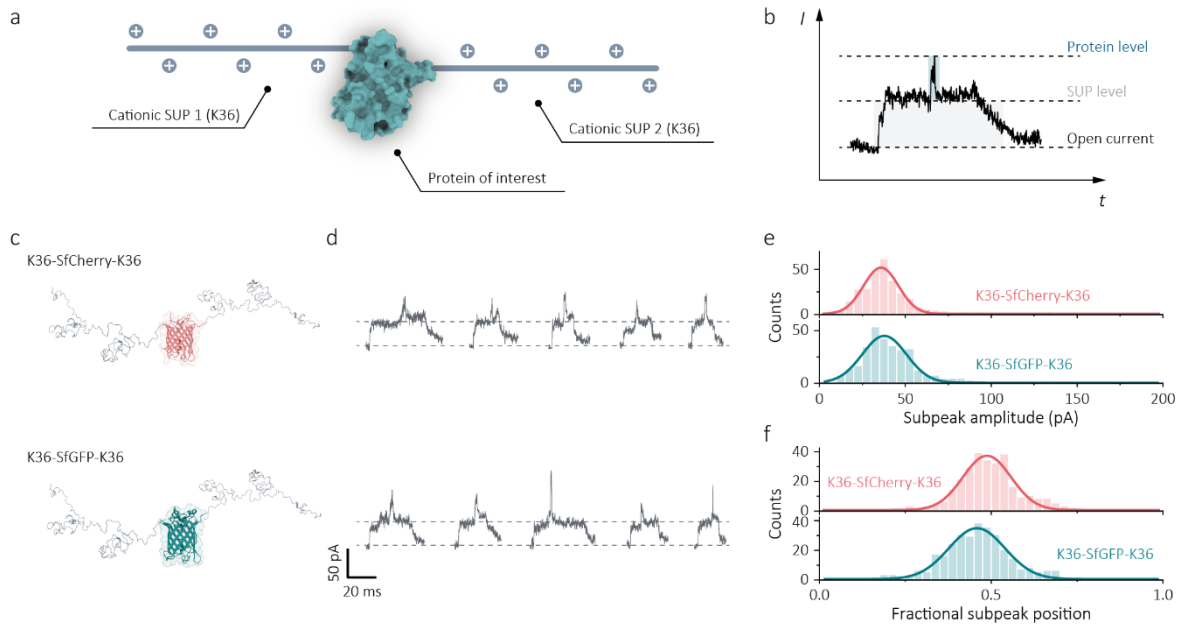


Figure 5.23 Subpeak analysis of rational design of protein-SUP constructs. (a) Schematic of the structure of K36-protein-K36, in which the net charge is equivalent to K72 carriers, but target protein is bound at the centre of the carrier. (b) An example translocation event for K36-protein-K36 shows the subpeak is shifted to the centre of the signal where the target protein is. (c) Structures of K36-SfCherry-K36 and K36-SfGFP-K36 used for single-molecule protein identification. (d) Representative translocation events (scale bar: 50 pA; 20 ms; filtered to 5 kHz) indicating nanopore signals were consistent with the protein structures with a folded protein at the centre. Nanopore experiments were performed in 1 M KCl, 10 mM Tris-EDTA pH 8.0 buffer at -500 mV with a low-pass filter of 10 kHz. (e) Distributions of the subpeak amplitude extracted from individual events for K36-SfCherry-K36 (n = 286) and K36-SfGFP-K36 (n = 307) were fitted with the Gaussian function. (f) Distributions of fractional subpeak position suggest that subpeaks are located at the centre of individual events as designed in the structure.

As a proof of concept, two commonly used fluorescent proteins, SfCherry and SfGFP (**Figure 5.23c**), were employed for the nanopore analysis due to their relatively small sizes and rigid structures. The capture rate of K36-SfCherry-K36 and K36-SfGFP-K36 was comparable to that of protein-K72 fusions at a typical concentration of 1 nM (**Figure 5.24**). Following a similar subpeak analysis, approximately 22% and 23% of the total events were observed for K36-SfCherry-K36 and K36-SfGFP-K36, respectively, displaying a distinguishable subpeak at the centre (**Figure 5.23d**). This proportion is slightly lower than that of the protein-K72 series, indicating that the rational carrier structure effectively eliminates false positives caused by carrier folding. Both samples exhibit a mean subpeak amplitude of 35 ± 3 pA and 37 ± 3 pA, respectively, which closely align with the values obtained using K72 carriers (**Figure 5.23e**). Further evidence is provided by the distribution of subpeak fractional positions for both variants, which display a single peak at 0.5, corresponding to the expected location of the target protein (**Figure 5.23f**).

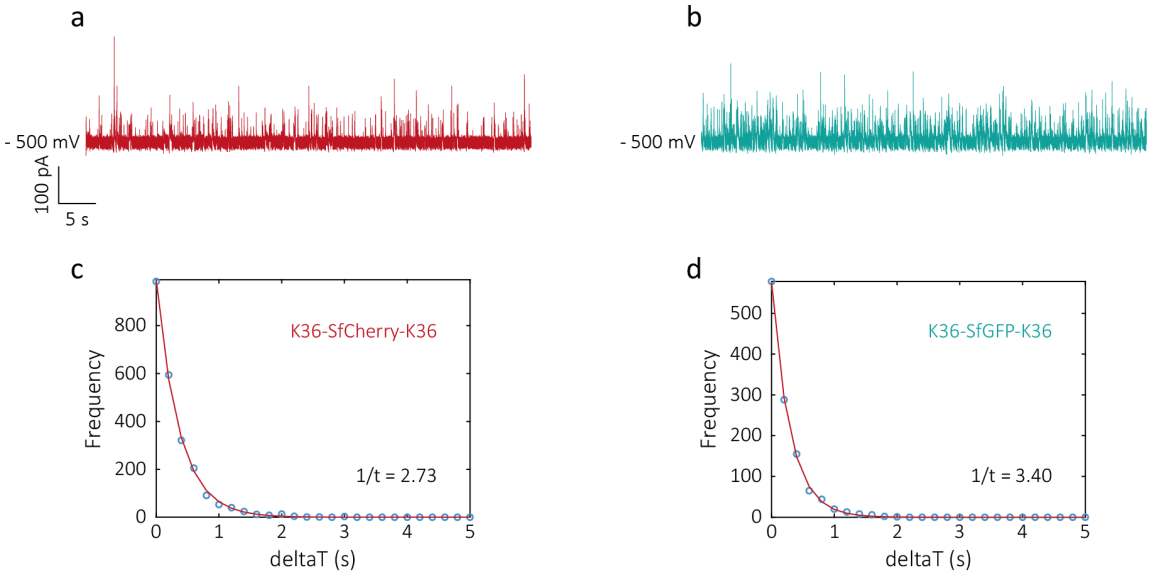


Figure 5.24 Nanopore detection of K36-SfCherry-K36 and K36-SfGFP-K36. Representative current-time traces of (a)1 nM K36-SfCherry-K36 and (b) 1 nM K36-SfGFP-K36 translocation recorded in 1 M KCl, 10 mM Tris-EDTA, pH 8.0 buffer at -500 mV. Data was sampled at 1 MHz and digitally filtered using a Bessel low-pass filter at 10 kHz. Distributions of the elapsed time between successive captured events for (c) 1 nM K36-SfCherry-K36 and (d) 1 nM K36-SfGFP-K36 with a single-exponential decay fitting.

5.3.6 Nanopore sensing of protein-protein interactions using SUP carriers

Protein-protein interactions (PPIs) play a vital role in maintaining and modulating normal cellular processes. Understanding these interactions provides valuable insights into the mechanisms of protein-related physiological processes and diseases. [49] Recent advancements in nanopore technology offer the potential for real-time recognition of PPIs at the single-molecule level. [50] However, accurately identifying PPIs remains challenging due to the lack of sufficient spatiotemporal resolution in conventional nanopore measurements, especially when dealing with minor changes in nanopore readouts. To address the resolution limitations, protein translocation assisted by cationic SUP carriers has shown superior performance in revealing biophysical information of detected proteins compared to conventional nanopore measurements. In this study, the original target protein was replaced with its protein-K72 form to enhance capture efficiency and spatiotemporal resolution without affecting its structure and function. By introducing the interacting protein partner, an increase was observed in ionic-current blockade at the protein-bound subpeak, indicating a boost in volume exclusion. This boost confirms the occurrence of the desired PPI.

To validate the feasibility of recognising PPIs using an unmodified nanopore, the antigen-antibody interaction was utilised as a model. This interaction is a fundamental reaction characterised by high specificity and affinity during the immune process. Specifically, eGFP-K72 was employed as the molecular probe to recognise anti-GFP antibody (IgG1, 146 kDa). In comparison to the standard binding assay where eGFP was bound to the antibody without the aid of SUP (K72), the experimental results are presented in Figure 5.25.

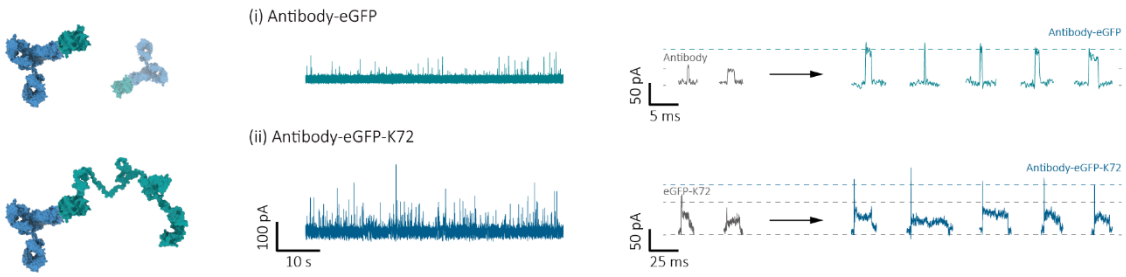


Figure 5.25 Nanopore sensing of single protein-protein interactions using cationic SUPs. A proof-of-concept demonstrated here is using eGFP-K72 as the antigen to detect anti-GFP antibody. Schematic representation of antibody-eGFP complexes and antibody-eGFP-K72 complexes. Representative ionic current traces for (i) antibody (10 nM)-eGFP (1 nM) interactions and (ii) antibody (10 nM)-eGFP-K72 (1 nM) interactions recorded in PBS + 1 M KCl, 10 mM Tris-EDTA pH 8.0 buffer (1: 9, v/v) at -500 mV. Typical individual events show an enhanced subpeak for antibody-eGFP-K72 complexes compared with eGFP-K72. Data was sampled at 1 MHz and re-filtered to 5 kHz for visualisation.

To ensure sufficient reaction efficiency for successful subpeak analysis, eGFP and its antibody were incubated in a physiological condition (PBS buffer) for 2 hours. Subsequently, 9 times the volume of 1 M KCl Tris-EDTA buffer was added to make it compatible with nanopore measurements. Under these conditions, translocation of the anti-GFP antibody was performed, as shown in **Figure 5.26**. Despite the large molecular weight of the IgG antibody, its translocation speed was still relatively fast, with a mean dwell time of 0.2 ± 0.1 ms. The distribution of peak amplitude during antibody translocation exhibited a well-defined single population with a mean value of 39 ± 2 pA. However, the antibody did not show a significantly deeper current blockade compared to previously measured proteins. This anomaly can be attributed to its Y-shape, which deviates from the typical behaviour of globular proteins. [51]

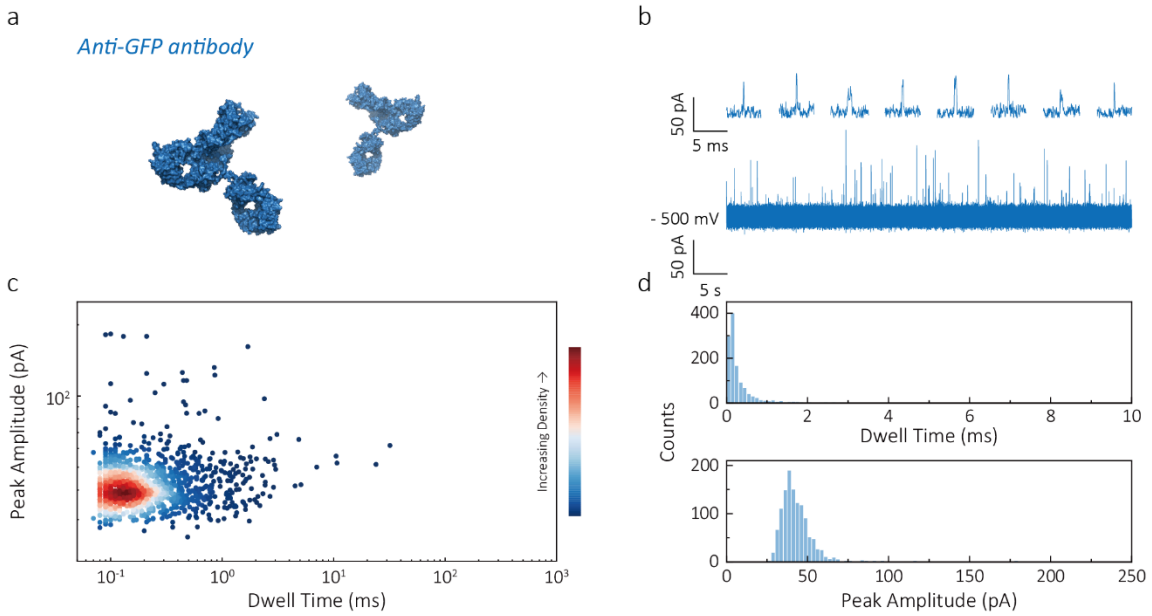


Figure 5.26 Nanopore detection of anti-GFP antibody. (a) Protein model of anti-GFP antibody (IgG1). (b) Typical events and current-time traces of 10 nM anti-GFP antibody translocation recorded in 1 M KCl, 10 mM Tris-EDTA, pH 8.0 buffer at -500 mV. Data was sampled at 1 MHz and digitally filtered using a Bessel low-pass filter at 10 kHz. (c) Scatter plot of peak amplitude versus dwell time. (d) Distribution of the dwell time and peak amplitude for anti-GFP antibody translocation.

To investigate the formation of immune complexes, 1 nM eGFP was added at a stoichiometric ratio of 1:10 between the antigen and antibody. This resulted in a wider distribution of peak amplitude, with a new but not well-separated population at approximately 55 ± 3 pA (**Figure 5.27**). These events indicated the presence of immune complexes, which led to greater volumetric exclusion during nanopore translocation. However, distinguishing these two populations solely based on dwell time proved challenging, as the true translocation speed approached or exceeded the limit of temporal resolution set by the 10 kHz low-pass filter. Thus, direct differentiation of antigen-antibody complexes from a mixture remained a challenge.

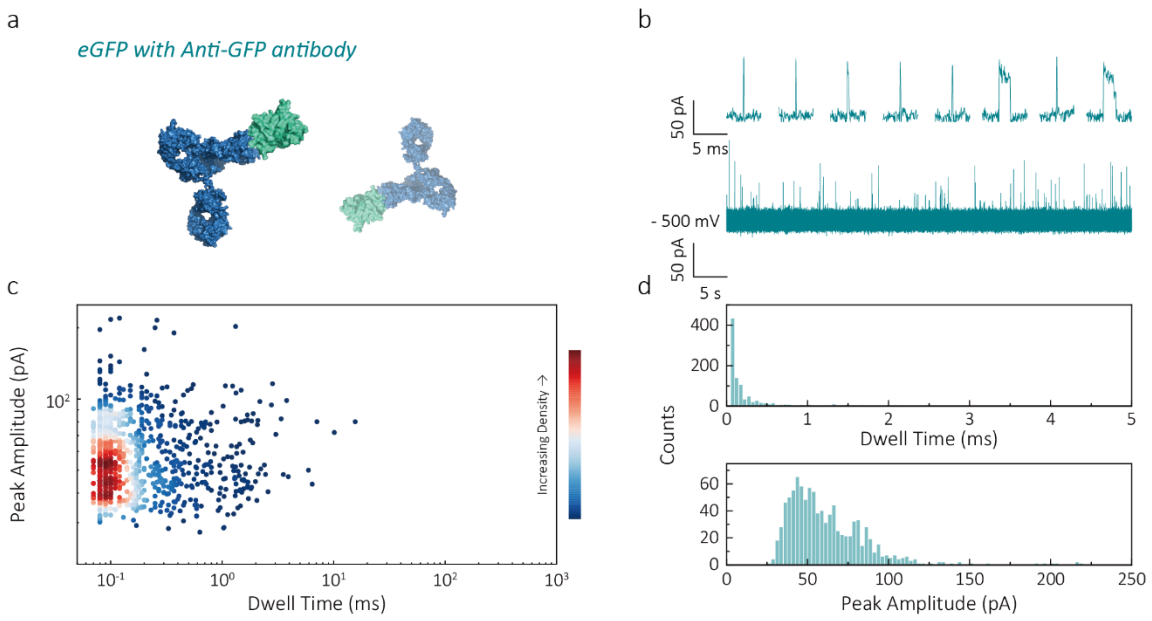


Figure 5.27 Nanopore detection of eGFP with anti-GFP antibody. (a) Protein model of eGFP-anti-GFP antibody complex. (b) Typical events and current-time traces of 1 nM eGFP + 10 nM anti-GFP antibody translocation were recorded in 1 M KCl, 10 mM Tris-EDTA, pH 8.0 buffer at -500 mV. Data was sampled at 1 MHz and digitally filtered using a Bessel low-pass filter at 10 kHz. (c) Scatter plot of peak amplitude versus dwell time. (d) Distribution of the dwell time and peak amplitude for the translocation of eGFP with anti-GFP antibody (1: 10).

Due to the charge-rich nature of the SUP carrier, nonspecific electrostatic interactions between the carrier and the target antibody can potentially compete with the desired antigen-antibody interaction. [52] Prior to investigating the interaction between eGFP-K72 and the antibody, the K72 carrier alone was first incubated with the antibody. Individual events showed minimal protein-bound-like subpeaks, as depicted in **Figure 5.28**. To confirm the successful binding of the antibody with eGFP-K72, an excess amount of antibody (10 nM) was added to a solution containing 1 nM eGFP-K72. This led to the detection of translocation events with longer dwell times and an increase in subpeak amplitude, as shown in **Figure 5.25** and **Figure 5.29**. These results indicated the successful binding of the antibody to eGFP-K72.

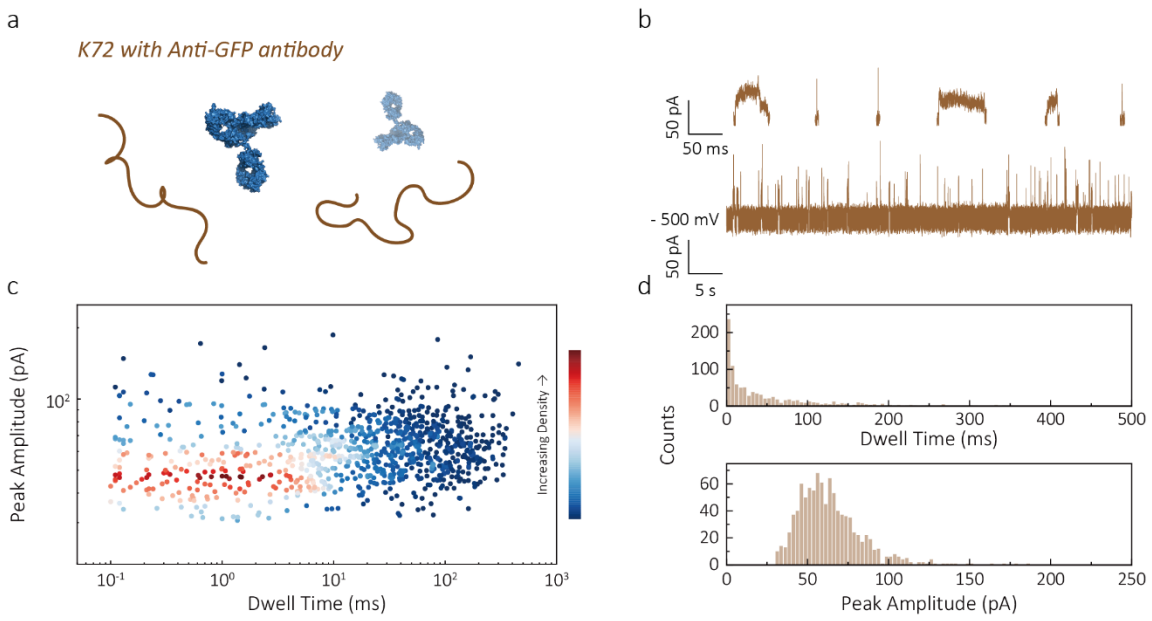


Figure 5.28 Nanopore detection of K72 with anti-GFP antibody. (a) Protein model of K72 and anti-GFP antibody. (b) Typical events and current-time traces of 1 nM K72 + 10 nM anti-GFP antibody translocation were recorded in 1 M KCl, 10 mM Tris-EDTA, pH 8.0 buffer at -500 mV. Data was sampled at 1 MHz and digitally filtered using a Bessel low-pass filter at 10 kHz. (c) Scatter plot of peak amplitude versus dwell time. (d) Distribution of the dwell time and peak amplitude for the translocation of K72 with anti-GFP antibody (1: 10).

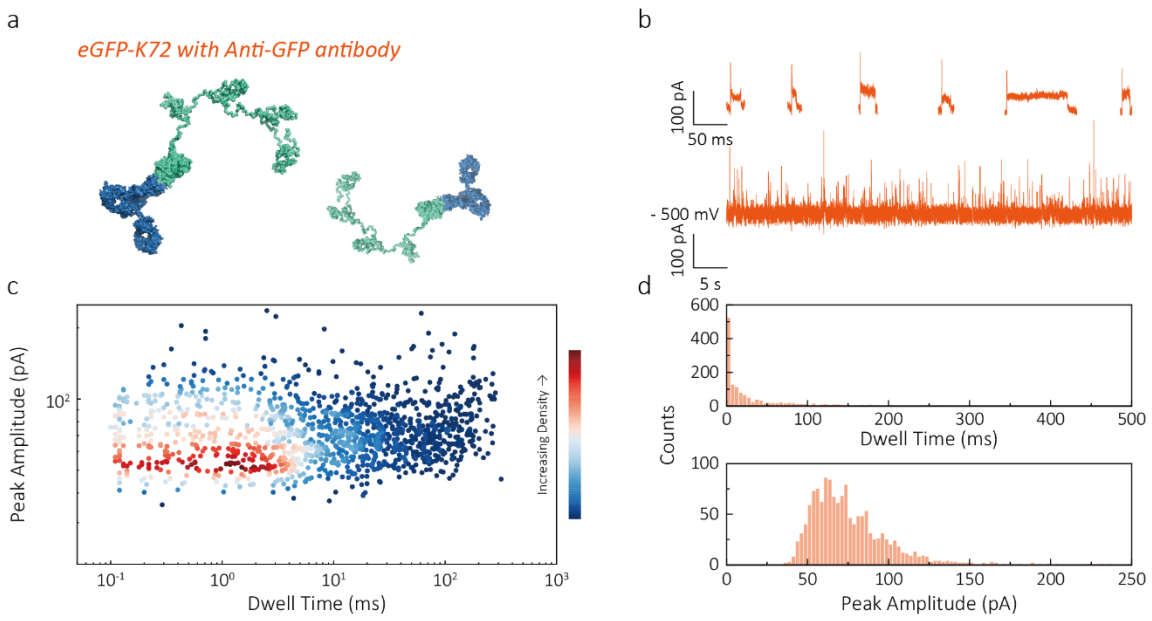


Figure 5.29 Nanopore detection of eGFP-K72 with anti-GFP antibody. (a) Protein model of eGFP-K72-anti-GFP antibody complex. (b) Typical events and current-time traces of 1 nM eGFP-K72 + 10 nM anti-GFP antibody translocation were recorded in 1 M KCl, 10 mM Tris-EDTA, pH 8.0 buffer at -500 mV. Data was sampled at 1 MHz and further low-pass filtered at 10 kHz. (c) Scatter plot of peak amplitude versus dwell time. (d) Distribution of the dwell time and peak amplitude for the translocation of eGFP-K72 with anti-GFP antibody (1: 10).

Figure 5.30 presents a comparison between density scatterplots for events attributed to eGFP-K72, antibody, antibody with eGFP, antibody with K72, and antibody with eGFP-K72. With the assistance of K72 SUPs, the signals generated by the binding of eGFP-K72 with the antibody could be clearly differentiated from free antibodies due to their distinct two-level patterns. Further details are presented in the distribution of the extracted subpeak amplitude, where two populations at 31 ± 3 pA and 66 ± 5 pA correspond to unbound eGFP and antibody-bound eGFP, respectively (**Figure 5.31a**). Therefore, a simple rule can be deduced: the current blockade of the antigen-antibody complex is approximately equal to the sum of its separate peak values. Moreover, the increase in subpeak amplitude only occurred in the presence of eGFP, indicating the specificity of antibody towards its antigen.

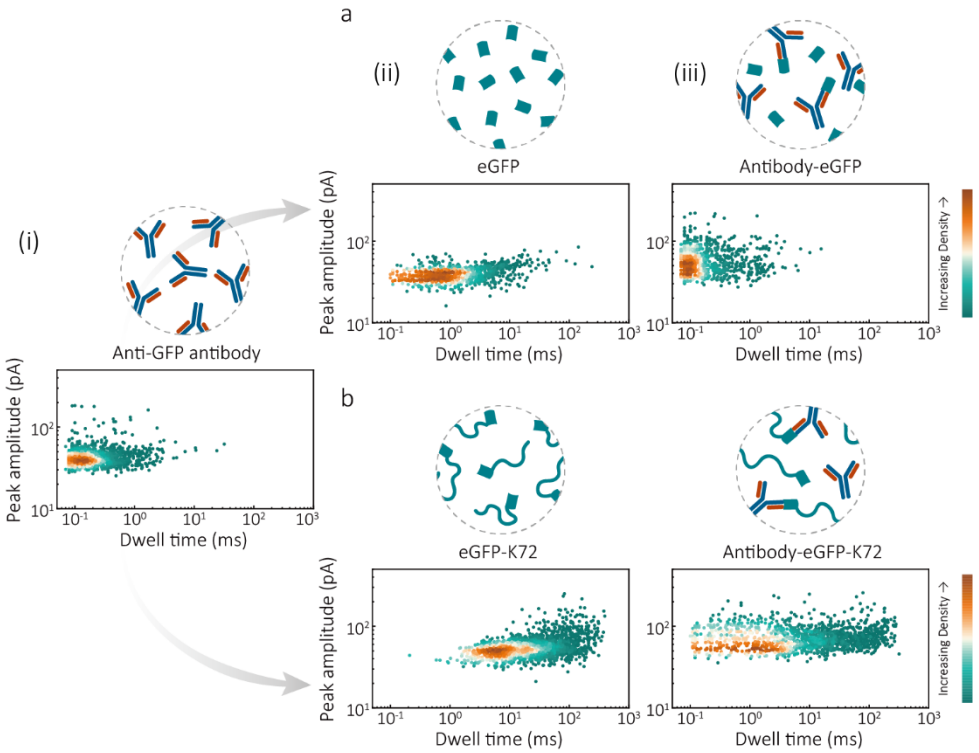


Figure 5.30 Identification of protein-protein interactions with SUP and without SUP. (a) Schematic illustration of antibody-eGFP binding and density scatter plots of peak amplitude versus dwell time for separate translocation experiments of 10 nM antibody (n = 1220), 750 nM eGFP (n = 845), and 10 nM antibody + 1 nM eGFP (n = 979). (b) Same antigen-antibody binding, but the antigen was replaced with eGFP-K72. Density scatter plots for separate experiments of 10 nM antibody (n = 1220), 1 nM eGFP-K72 (n = 1865), and 10 nM antibody + 1 nM eGFP-K72 (n = 1378).

To assess the extent of antigen-antibody complex formation at different antigen-antibody ratios, a binding assay was conducted by varying the concentration of the target antibody while keeping the concentration of eGFP-K72 constant at 1 nM. Specifically, antibody concentrations ranged from 1 pM to 50 nM. Using the distribution of subpeak amplitude presented in **Figure 5.31a**, a threshold of 50 pA was chosen to differentiate between eGFP and its antibody-bound forms. For instance, upon the addition of ten equivalents of antibody, approximately 60 ± 5% of the subpeaks exhibited an amplitude greater than 50 pA. The binding curve was fitted using the Hill-Langmuir equation, as depicted in **Figure 5.31b**, allowing estimation of the dissociation constant (K_d) to be 7.85 nM. The limit of detection (LOD), defined as three standard deviations

(3σ) above the background noise, was determined to be 74 pM by analysing the linear region within the low concentrations. The system noise primarily originates from the overlap between the distributions of eGFP-K72 and antibody-eGFP-K72 complexes. The accuracy of detection can be further improved by incorporating machine-learning algorithms into the analysis of nanopore data, as suggested in previous studies. [53]

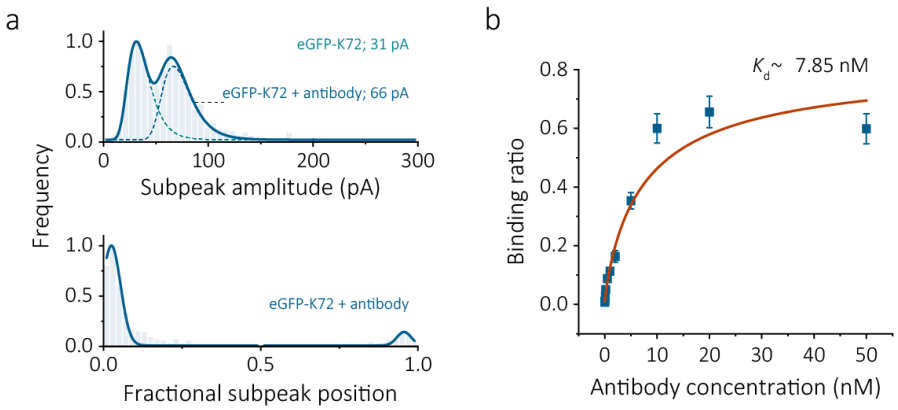


Figure 5.31 Binding assays of eGFP-K72 with its antibody. (a) Subpeak analysis of eGFP-K72 (1 nM) interacting with antibody (10 nM). Distribution of subpeak amplitude and fractional position (n =425) showed the antibody bound with eGFP at the ends of SUP carriers resulting in a boost in subpeak amplitude. Threshold: subpeak amplitude > 50 pA; dwell time > 1 ms was selected to distinguish antibody-eGFP-K72 complexes from unbound states. (e) Binding assays of 1 nM eGFP-K72 in the presence of anti-GEP antibody ranging from 1 pM to 50 nM. The binding curve was fitted using the Hill-Langmuir equation and the dissociation constant (K_d) was determined to be ~ 7.85 nM under this condition. Error bars represent one standard deviation of at least three independent experimental repeats.

5.4 Conclusions

In **Chapter 5**, I have demonstrated the effectiveness of supercharged unstructured polypeptides (SUPs) in controlling protein transport through nanopores. These SUPs can be genetically programmed to have specific charge densities, allowing for flexible tuning according to the desired application. Both cationic and anionic SUPs have shown enhanced efficiency in protein capture by increasing the electrokinetic driving force within the nanopore electric field. Notably, cationic SUPs have been particularly effective in slowing down the translocation of attached proteins, addressing a key limitation in spatiotemporal resolution for protein nanopore sensing. By investigating various cationic SUPs, it has been confirmed that the nanopore transport slowdown is a result of electrostatic forces between the SUPs and the oppositely charged nanopore. The analysis of subpeaks in the nanopore signals has allowed us to establish correlations between the signals and the composition of target proteins, enabling the recognition of protein-protein interactions at the single-molecule level. Furthermore, the subpeak position accurately corresponds to the position of the attached protein, suggesting the possibility of labelling multiple binding sites within a single SUP carrier for high-throughput multiplexed detection. The improved capture efficiency enables the analysis of rare proteins with low copy numbers involved in cellular processes, complementing the advancements in single-molecule proteomics. [15, 16]

To expand the application of the established method to other proteins, a universal approach can be developed involving chemical modification of SUPs to specific targets using linker chemistry. In addition, solid-state nanopores can be easily engineered by surface modifications[42, 54] or integration with other components such as tunnelling detectors, [55, 56] field-effect transistors (FETs), [57, 58] and dielectrophoretic (DEP) traps, [37, 55] further enhancing the performance. Moreover, amino acid-based recognition groups, such as antibodies, nanobodies, or peptide aptamers, can be readily fused with SUP carriers through rational genetic encoding, providing additional versatility and specificity to this platform. In summary, this study demonstrates the potential of SUPs as effective molecular carriers for controlling protein transport through nanopores, which facilitates a viable route for fingerprinting single proteins and mapping potential protein interomics.

5.5 References

1. Bludau I, Aebersold R. Proteomic and interactomic insights into the molecular basis of cell functional diversity. *Nature Reviews Molecular Cell Biology* **21**, 327-340 (2020).

2. Suhre K, McCarthy MI, Schwenk JM. Genetics meets proteomics: perspectives for large population-based studies. *Nature Reviews Genetics* **22**, 19-37 (2021).

3. Timp W, Timp G. Beyond mass spectrometry, the next step in proteomics. *Science Advances* **6**, eaax8978.

4. Varongchayakul N, Song J, Meller A, Grinstaff MW. Single-molecule protein sensing in a nanopore: a tutorial. *Chemical Society Reviews* **47**, 8512-8524 (2018).

5. Xue L, Yamazaki H, Ren R, Wanunu M, Ivanov AP, Edel JB. Solid-state nanopore sensors. *Nature Reviews Materials* **5**, 931-951 (2020).

6. Miles BN, Ivanov AP, Wilson KA, Doğan F, Japrung D, Edel JB. Single molecule sensing with solid-state nanopores: novel materials, methods, and applications. *Chemical Society Reviews* **42**, 15-28 (2013).

7. Wang Y, Zhao Y, Bollas A, Wang Y, Au KF. Nanopore sequencing technology, bioinformatics and applications. *Nature Biotechnology* **39**, 1348-1365 (2021).

8. Ying Y-L*, et al.* Nanopore-based technologies beyond DNA sequencing. *Nature Nanotechnology* **17**, 1136-1146 (2022).

9. Firnkes M, Pedone D, Knezevic J, Döblinger M, Rant U. Electrically Facilitated Translocations of Proteins through Silicon Nitride Nanopores: Conjoint and Competitive Action of Diffusion, Electrophoresis, and Electroosmosis. *Nano Letters* **10**, 2162-2167 (2010).

10. Bandara YMNDY, Farajpour N, Freedman KJ. Nanopore Current Enhancements Lack Protein Charge Dependence and Elucidate Maximum Unfolding at Protein's Isoelectric Point. *Journal of the American Chemical Society* **144**, 3063-3073 (2022).

11. Wang X*, et al.* Single-molecule nanopore sensing of actin dynamics and drug binding. *Chemical Science* **11**, 970-979 (2020).

12. Talaga DS, Li J. Single-Molecule Protein Unfolding in Solid State Nanopores. *Journal of the American Chemical Society* **131**, 9287-9297 (2009).

13. Plesa C, Kowalczyk SW, Zinsmeester R, Grosberg AY, Rabin Y, Dekker C. Fast Translocation of Proteins through Solid State Nanopores. *Nano Letters* **13**, 658-663 (2013).

14. Larkin J, Henley RY, Muthukumar M, Jacob, Wanunu M. High-Bandwidth Protein Analysis Using Solid-State Nanopores. *Biophysical Journal* **106**, 696-704 (2014).

15. Restrepo-Pérez L, Joo C, Dekker C. Paving the way to single-molecule protein sequencing. *Nature Nanotechnology* **13**, 786-796 (2018).

16. Alfaro JA*, et al.* The emerging landscape of single-molecule protein sequencing technologies. *Nature Methods* **18**, 604-617 (2021).

17. Ouldali H*, et al.* Electrical recognition of the twenty proteinogenic amino acids using an aerolysin nanopore. *Nature Biotechnology* **38**, 176-181 (2020).

18. Afshar Bakshloo M*, et al.* Nanopore-Based Protein Identification. *Journal of the American Chemical Society* **144**, 2716-2725 (2022).

19. Yan S*, et al.* Single Molecule Ratcheting Motion of Peptides in a Mycobacterium smegmatis Porin A (MspA) Nanopore. *Nano Letters* **21**, 6703-6710 (2021).

20. Brinkerhoff H, Kang ASW, Liu J, Aksimentiev A, Dekker C. Multiple rereads of single proteins at single–amino acid resolution using nanopores. *Science* **374**, 1509-1513 (2021).

21. Sze JYY, Ivanov AP, Cass AEG, Edel JB. Single molecule multiplexed nanopore protein screening in human serum using aptamer modified DNA carriers. *Nature Communications* **8**, 1552 (2017).

22. Cai S, Sze JYY, Ivanov AP, Edel JB. Small molecule electro-optical binding assay using nanopores. *Nature Communications* **10**, 1797 (2019).

23. Bell NAW, Keyser UF. Specific Protein Detection Using Designed DNA Carriers and Nanopores. *Journal of the American Chemical Society* **137**, 2035-2041 (2015).

24. Tian K, Decker K, Aksimentiev A, Gu L-Q. Interference-Free Detection of Genetic Biomarkers Using Synthetic Dipole-Facilitated Nanopore Dielectrophoresis. *ACS Nano* **11**, 1204-1213 (2017).

25. Lin X, Ivanov AP, Edel JB. Selective single molecule nanopore sensing of proteins using DNA aptamer-functionalised gold nanoparticles. *Chemical Science* **8**, 3905-3912 (2017).

26. Ren R*, et al.* Single-Molecule Binding Assay Using Nanopores and Dimeric NP Conjugates. *Advanced Materials* **33**, 2103067 (2021).

27. Roberts S, Dzuricky M, Chilkoti A. Elastin-like polypeptides as models of intrinsically disordered proteins. *FEBS Letters* **589**, 2477-2486 (2015).

28. Ma C, Malessa A, Boersma AJ, Liu K, Herrmann A. Supercharged Proteins and Polypeptides. *Advanced Materials* **32**, 1905309 (2020).

29. Zhou Y, Huo S, Loznik M, Göstl R, Boersma AJ, Herrmann A. Controlling Optical and Catalytic Activity of Genetically Engineered Proteins by Ultrasound. *Angewandte Chemie International Edition* **60**, 1493-1497 (2021).

30. Lee EN*, et al.* Stabilizing Peptide Fusion for Solving the Stability and Solubility Problems of Therapeutic Proteins. *Pharmaceutical Research* **22**, 1735-1746 (2005).

31. Fahie MA, Chen M. Electrostatic Interactions between OmpG Nanopore and Analyte Protein Surface Can Distinguish between Glycosylated Isoforms. *The Journal of Physical Chemistry B* **119**, 10198-10206 (2015).

32. McDaniel JR, MacKay JA, Quiroz FG, Chilkoti A. Recursive Directional Ligation by Plasmid Reconstruction Allows Rapid and Seamless Cloning of Oligomeric Genes. *Biomacromolecules* **11**, 944-952 (2010).

33. Li J*, et al.* Engineered Near-Infrared Fluorescent Protein Assemblies for Robust Bioimaging and Therapeutic Applications. *Advanced Materials* **32**, 2000964 (2020).

34. Waduge P*, et al.* Nanopore-Based Measurements of Protein Size, Fluctuations, and Conformational Changes. *ACS Nano* **11**, 5706-5716 (2017).

35. Steinbock LJ*, et al.* Probing the size of proteins with glass nanopores. *Nanoscale* **6**, 14380-14387 (2014).

36. Asandei A, Schiopu I, Chinappi M, Seo CH, Park Y, Luchian T. Electroosmotic Trap Against the Electrophoretic Force Near a Protein Nanopore Reveals Peptide Dynamics During Capture and Translocation. *ACS Applied Materials & Interfaces* **8**, 13166-13179 (2016).

37. Freedman KJ, Otto LM, Ivanov AP, Barik A, Oh S-H, Edel JB. Nanopore sensing at ultra-low concentrations using single-molecule dielectrophoretic trapping. *Nature Communications* **7**, 10217 (2016).

38. Maglia G, Restrepo MR, Mikhailova E, Bayley H. Enhanced translocation of single DNA molecules through α-hemolysin nanopores by manipulation of internal charge. *Proceedings of the National Academy of Sciences* **105**, 19720-19725 (2008).

39. Shekar S*, et al.* Wavelet Denoising of High-Bandwidth Nanopore and Ion-Channel Signals. *Nano Letters* **19**, 1090-1097 (2019).

40. Wanunu M, Morrison W, Rabin Y, Grosberg AY, Meller A. Electrostatic focusing of unlabelled DNA into nanoscale pores using a salt gradient. *Nature Nanotechnology* **5**, 160-165 (2010).

41. Charron M, Briggs K, King S, Waugh M, Tabard-Cossa V. Precise DNA Concentration Measurements with Nanopores by Controlled Counting. *Analytical Chemistry* **91**, 12228-12237 (2019).

42. Wei R, Gatterdam V, Wieneke R, Tampé R, Rant U. Stochastic sensing of proteins with receptor-modified solid-state nanopores. *Nature Nanotechnology* **7**, 257-263 (2012).

43. Wanunu M, Sutin J, McNally B, Chow A, Meller A. DNA Translocation Governed by Interactions with Solid-State Nanopores. *Biophysical Journal* **95**, 4716-4725 (2008).

44. Ainavarapu SRK*, et al.* Contour Length and Refolding Rate of a Small Protein Controlled by Engineered Disulfide Bonds. *Biophysical Journal* **92**, 225-233 (2007).

45. Kumar Sharma R, Agrawal I, Dai L, Doyle PS, Garaj S. Complex DNA knots detected with a nanopore sensor. *Nature Communications* **10**, 4473 (2019).

46. Roy A, Kucukural A, Zhang Y. I-TASSER: a unified platform for automated protein structure and function prediction. *Nature Protocols* **5**, 725-738 (2010).

47. Schmid S, Stömmer P, Dietz H, Dekker C. Nanopore electro-osmotic trap for the label-free study of single proteins and their conformations. *Nature Nanotechnology* **16**, 1244-1250 (2021).

48. Bell NAW, Keyser UF. Digitally encoded DNA nanostructures for multiplexed, single-molecule protein sensing with nanopores. *Nature Nanotechnology* **11**, 645-651 (2016).

49. Keskin O, Tuncbag N, Gursoy A. Predicting Protein–Protein Interactions from the Molecular to the Proteome Level. *Chemical Reviews* **116**, 4884-4909 (2016).

50. Thakur AK, Movileanu L. Real-time measurement of protein–protein interactions at single-molecule resolution using a biological nanopore. *Nature Biotechnology* **37**, 96-101 (2019).

51. Yusko EC*, et al.* Real-time shape approximation and fingerprinting of single proteins using a nanopore. *Nature Nanotechnology* **12**, 360-367 (2017).

52. Frutiger A, Tanno A, Hwu S, Tiefenauer RF, Vörös J, Nakatsuka N. Nonspecific Binding—Fundamental Concepts and Consequences for Biosensing Applications. *Chemical Reviews* **121**, 8095-8160 (2021).

53. Taniguchi M*, et al.* Combining machine learning and nanopore construction creates an artificial intelligence nanopore for coronavirus detection. *Nature Communications* **12**, 3726 (2021).

54. Al Sulaiman D, Cadinu P, Ivanov AP, Edel JB, Ladame S. Chemically Modified Hydrogel-Filled Nanopores: A Tunable Platform for Single-Molecule Sensing. *Nano Letters* **18**, 6084-6093 (2018).

55. Tang L*, et al.* Combined quantum tunnelling and dielectrophoretic trapping for molecular analysis at ultra-low analyte concentrations. *Nature Communications* **12**, 913 (2021).

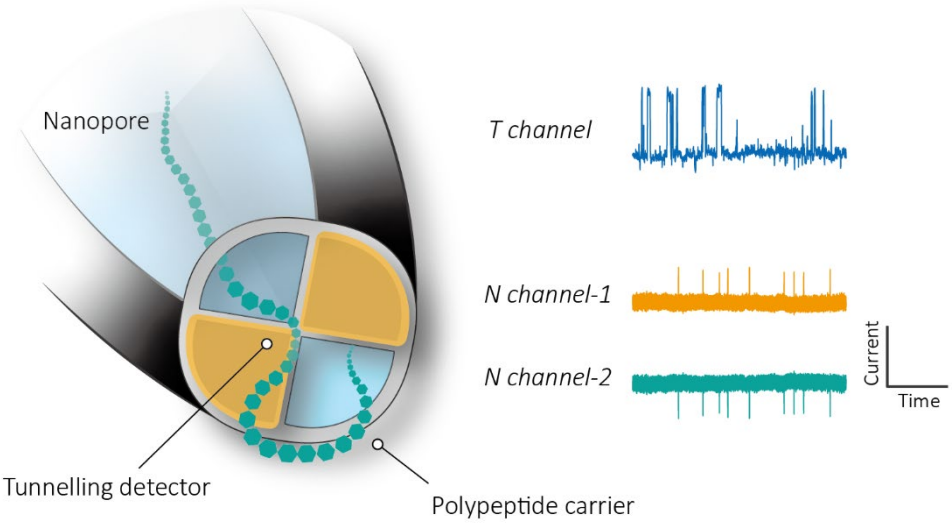
56. Tang L*, et al.* Measuring conductance switching in single proteins using quantum tunneling. *Science Advances* **8**, eabm8149.

57. Ren R*, et al.* Nanopore extended field-effect transistor for selective single-molecule biosensing. *Nature Communications* **8**, 586 (2017).

58. Ren R*, et al.* Selective Sensing of Proteins Using Aptamer Functionalized Nanopore Extended Field-Effect Transistors. *Small Methods* **4**, 2000356 (2020).

CHAPTER 6

Conclusions and future work



Synopsis

This chapter serves as the culmination of the PhD work, focusing on its key aims and conclusions. It highlights the significant findings and insights gained during the research journey. Moreover, it provides an overview of potential future work, outlining possible improvements to the device design and detection strategy. By addressing these areas, the study aims to enhance the overall efficiency and sensitivity of the nanopore sensing, with an eye towards exploring single-molecule proteomics. This conclusive section offers a roadmap for using nanofabrication and biotechnology, such as nanopores and molecular carriers, to advance protein analysis and beyond.

6.1 Aims and achievements

In summary, this thesis addresses the limitations of single-molecule protein analysis and explores novel methods to enhance the practicality of nanopore techniques for future applications, including early-stage diagnosis and single-molecule proteomics. The key conclusions from the research are as follows:

Chapter 2 provides a comprehensive overview of the experimental procedures, materials, instruments, and data analysis techniques used throughout the thesis. It lays the groundwork for the subsequent chapters, setting the stage for the results and findings.

In Chapter 3, label-free nanopore sensing of actin, a critical protein in eukaryotic cells, is demonstrated. Nanopores offer unique insights into molecular states of actin, including filamentous and globular forms, and its interactions with drug inhibitors. The technique allows real-time observation of actin unfolding processes, transient oligomers, filament growth, and drug binding at the single-molecule level. Overcoming limitations, nanopore sensing emerges as a powerful tool for studying actin and advancing drug development.

Chapter 4 introduces a novel single-molecule protein detection method using aptamer-modified DNA carriers. Unlike conventional DNA carriers, this approach utilises protein-binding-induced DNA dimerisation instead of subpeaks to detect target proteins. The clear differentiation between DNA dimers and monomers is achieved through simple charge classification. Dimeric proteins like VEGF and PDGF are effectively detected using this method with homogenous DNA carriers. The strategy can be theoretically applied to any proteins with two distinct aptamer-binding regions. Successful detection of thrombin and observation of ligand-induced dimerisation of c-Met demonstrate the versatility of this approach.

In Chapter 5, supercharged unstructured polypeptides (SUPs) are introduced as a new molecular carrier to control protein transport through a nanopore. Cationic SUPs significantly

improve protein capture and detection while slowing down protein translocation due to their electrostatic attraction with the pore. By using SUP molecular carriers, the required protein concentrations for nanopore measurements are reduced to pM levels, enabling the characterisation of low-copy-number proteins within cells. This approach facilitates size identification of small proteins and precise recognition of protein-protein interactions at the single-molecule level.

Overall, the thesis presents innovative strategies and tools that address the limitations of single-molecule protein analysis using nanopore techniques. The findings demonstrate the potential of nanopore-based biosensing for more robust and transformative applications in proteomics and early-stage diagnostics. The research opens new avenues for further exploration and development of nanopore technologies in the field of molecular analysis and medical research.

6.2 Future work

In this proposed future direction, the integration of a tunnelling detector into quad-barrel nanopipettes presents a compelling approach to overcome the challenges faced by solid-state nanopores in achieving atomic precision comparable to biological pores. Multi-barrel nanopipettes, such as dual-barrel and quad-barrel pipettes, have already demonstrated their capability to manipulate single molecules and integrate with other techniques. [1, 2, 3, 4, 5] The recent development of a tunnelling detector on a dual-barrel nanopipette by Edel group showcases the potential of this approach for ultrasensitive single-molecule detection of oligonucleotides and proteins. [6, 7, 8]

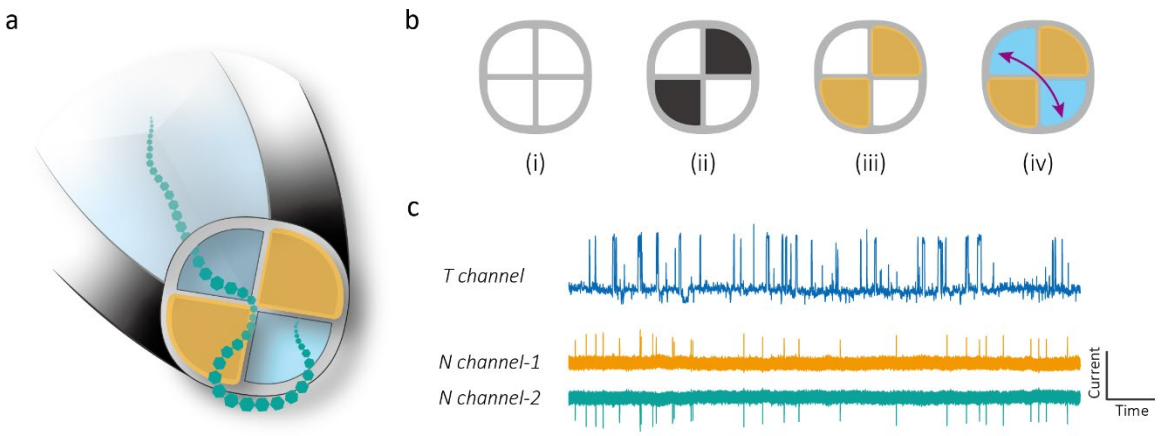


Figure 6.1 Integration of a tunnelling detector into a nanopore sensor for protein analysis. (a) Schematic of a gold tunnelling detector embedded in a quad-barrel nanopipette. (b) Fabrication of the integrated device. i. Quad-barrel nanopipettes are fabricated using the laser-assisted pulling technique. ii. Two channels of the pipettes are filled with carbon to serve as conductive nanoelectrodes. iii. Tunnelling gold electrodes with a gap less than 2 nm are formed by a feedback-controlled electrodeposition. iv. Simultaneous reading of tunnelling currents and ionic currents by the integrated detector. (c) Expected current traces of tunnelling currents (T channel) and ionic currents (two N channels).

Building upon this advanced nanofabrication technique, the design proposed in **Figure 6.1** involves the integration of a tunnelling detector into two channels across the diagonal of a quad-barrel nanopipette. The quad-barrel design offers two additional channels, which can be utilised as tools to control and manipulate molecules passing through the tunnelling junction. This integration aims to provide improved precision, sensitivity, and versatility in nanopore-based sensing platforms, particularly for single-molecule protein analysis.

6.2.1 Integration of tunnelling-based detector with nanopipettes

The fabrication process of tunnelling detector integrated nanopipettes involves four main steps, as outlined below: [8]

1) Laser-assisted pulling of nanopipettes

A laser-based pipette puller is used to pull a quad-barrel quartz capillary into two symmetrical nanopipettes. The pulling process utilises a three-line heating protocol, resulting in sharp tips for each nanopipette. The nanopipettes have four adjacent nanopores, each with a maximum dimension of about 30 nm, separated by a septum with a width of 20 nm. [2]

2) Fabrication of carbon nanoelectrodes

Two of the nanopipette channels, positioned across the diagonal, are filled with carbon by pyrolytic deposition. This forms two carbon nanoelectrodes at the tip of the nanopipettes. The remaining two channels are blocked with Blue Tack before carbon deposition to reserve them for the nanopores. [5]

3) Feedback-controlled deposition of the gold tunnelling gap

The electrodeposition process is divided into three parts as shown in Figure 6.2. First, excess carbon on the outer pipette surface is removed by electrochemical etching in a basic solution. Next, gold is electrochemically pre-deposited upon the carbon nanoelectrodes using a bipotentiostatic process. Finally, to reduce the electrode gap distance to within the tunnelling regime, a galvanostatic feedback-controlled deposition is used. By applying a constant preset current between the nanoelectrodes, the gap is gradually reduced until it enters the tunnelling regime, and the voltage jumps back to zero.

4) Device stabilisation

The fabricated devices are immersed in ultrapure DI water before measuring their I-V curves, ensuring proper stabilisation before experimentation.

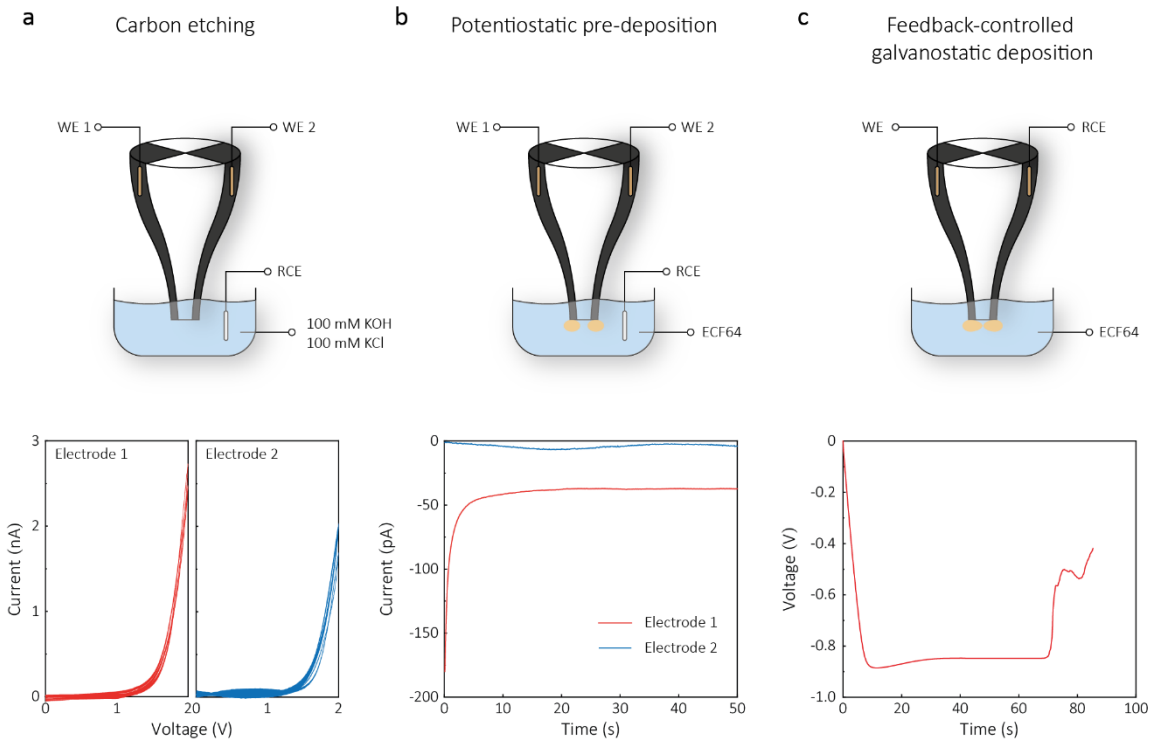


Figure 6.2 Feedback controlled electrodeposition. (a) Carbon etching. Excess carbon outside the pipette was removed by a cyclic voltammetry (CV) process (0 – 2 V, 2 cycles). (b) Gold was first pre-deposited on the carbon surface using a bipotentiostatic method. (WE 1: -0.73 V, WE 2: -0.75 V, time: 50 s). (c) Feedback-controlled galvanostatic deposition was used for fabrication of gold nanogap (I_{set} = 1 nA). The jump of V-t curve suggests the formation of a tunnelling junction.

Figure 6.3 illustrates the process of forming electromigrated nanogaps in the fabricated tunnelling detectors (performed using a custom-written LabView code on Gamry Reference 600 Potentiostat, Gamry Instruments, US). After the tunnelling junctions are created between the two gold electrodes, there is a possibility of the formation of a nanocontact, where the electrodes are in close proximity to each other. [9] This nanocontact is initially intact and may not be ideal for tunnelling measurements.

To optimise the tunnelling performance and achieve a well-defined and reproducible nanogap, a feedback-controlled electromigration process is applied. [10, 11, 12, 13, 14] Electromigration

involves applying a high voltage across the nanocontact, leading to a high-density current flow in the nanoscale region. The current density becomes concentrated at weak points within the nanocontact, causing the metal to migrate and ultimately breaking the nanocontact. This process is precisely controlled using a feedback system that monitors the electrical properties of the junction during the electromigration process. By carefully adjusting the voltage and the monitoring the electrical response, the electromigration process can be controlled to achieve a desired nanogap size.

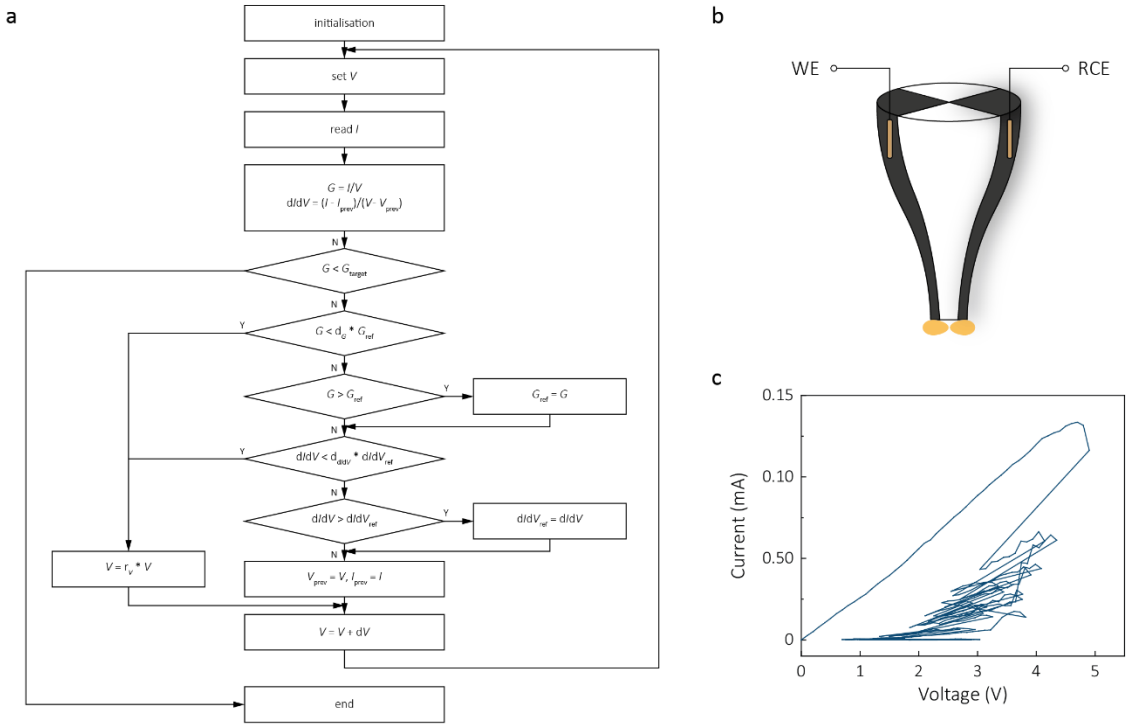


Figure 6.3 Feedback controlled electromigration. (a) Flowchart of the algorithm governing the feedback-controlled electromigration process. (b) Electrical setup for electromigration of gold nanocontacts. (c) I-V curve for feedback controlled electromigration.

Figure 6.4a and Figure 6.4b show typical SEM characterisations of a quad-barrel nanopipette before and after the fabrication of a tunnelling detector. Initially, the quad-barrel nanopipette exhibits a well-defined structure with four nanopores, each having a diameter of about 30 nm, after the pulling process. However, after the deposition of carbon and gold, the nanopores are enlarged to about 100 nm due to the thermal dilation. In the middle of the pipette, a very small gap is formed between the two gold electrodes, as expected.

Figure 6.4c presents the fabricated tunnelling detectors characterised by measuring the current-voltage (I-V) curves. These I-V curves can be fitted using the Simmons model (Equation 6.1), [15] a well-known model for describing tunnelling current. The Simmons model accounts for various factors such as the effective tunnelling barrier height, gap distance, and active tunnelling area, and it is commonly used to analyse tunnelling current data in nanoscale devices.

$$I = A\left(\frac{e}{4\pi^2\hbar d^2}\right)\left\{\left(\varphi - \frac{eV}{2}\right)\exp\left[-\frac{2(2m)^{\frac{1}{2}}}{\hbar}\left(\varphi - \frac{eV}{2}\right)^{\frac{1}{2}}d\right] - \left(\varphi + \frac{eV}{2}\right)\exp\left[-\frac{2(2m)^{\frac{1}{2}}}{\hbar}\left(\varphi + \frac{eV}{2}\right)^{\frac{1}{2}}d\right]\right\} \quad (6.1)$$

Where:

m is electron mass.

d is the gap distance.

φ is the effective tunnelling barrier height.

$h(= 2\pi\hbar)$ is Planck's constant.

V is applied bias and A is the active tunnelling area.

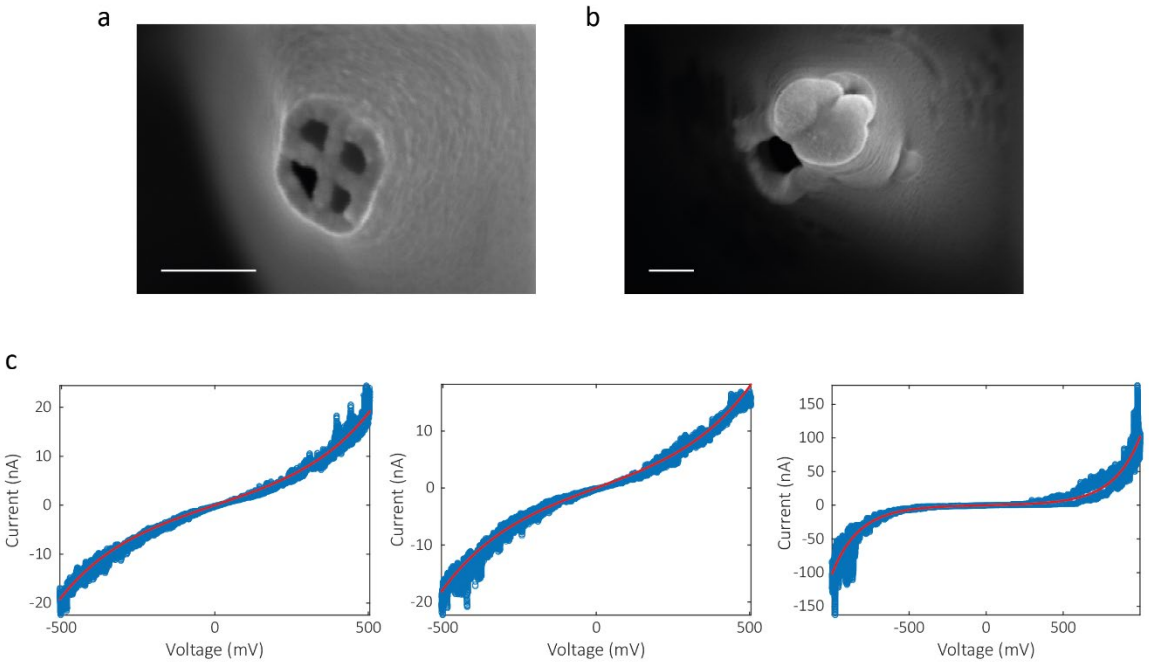


Figure 6.4 Characterisation of tunnelling detector integrated quad-barrel nanopipettes. SEM images of quad-barrel nanopipettes before (a) and after being integrated with a tunnelling detector (b). Flowchart of the algorithm governing the feedback-controlled electromigration process. (c) Typical I-V curves of fabricated tunnelling detectors.

6.2.2 Proteomic analysis using molecular carriers

To date, recognition tunnelling detectors[16] and sub-nm nanogaps[17] have demonstrated their ability to differentiate single amino acids, including post-translational modifications, with high resolution. However, these techniques often require high concentrations of analyte amino acids due to the lack of a capture compound in the device. Moreover, the differentiation is limited to single amino acids or short peptides, making sequencing of entire proteins a challenge.

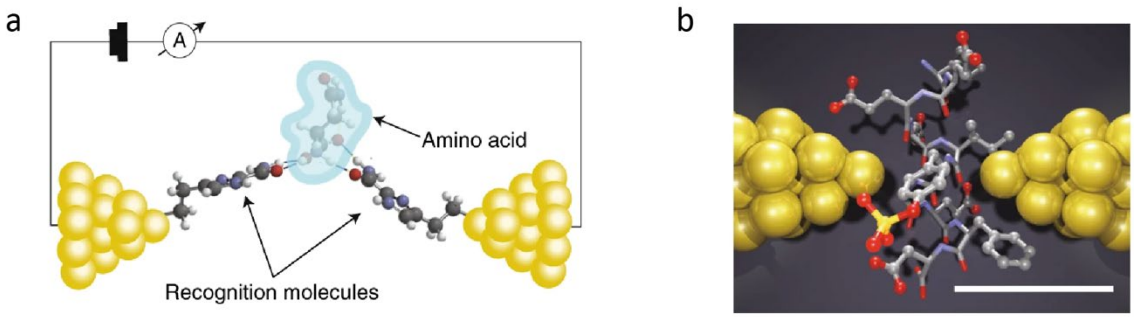


Figure 6.5 Measurements of single amino acids using a tunnelling detector. (a) Recognition tunnelling detector where the electrodes are functionalised with recognition molecules. (b) Single amino acid detection using a sub-nm nanogap. Panel (a) adapted from reference and panel (b) adapted from reference.

By integrating a tunnelling detector into a nanopore sensor and utilising molecular carriers discussed in the thesis, sequencing of whole proteins becomes a viable possibility. In this configuration, the nanopore functions more like a nanofluidic channel, allowing efficient capture of analyte samples by electrophoresis or electroosmosis at the tunnelling sensing region. The molecular carriers, such as DNA or polypeptide carriers, can significantly enhance capture efficiency and facilitate protein transport through the nanopore and tunnelling detector. For protein sequencing purposes, the analyte protein would need to be unfolded using enzymes or chemical denaturants before measurement by the device. In this case, the non-covalent binding of carriers with the protein analyte could be problematic, as the binding may be disrupted after the protein is unfolded. Therefore, a covalent binding of the protein analyte to the carrier molecule becomes necessary.

Previous attempts using a biological nanopore system involved modifying a DNA carrier to the analyte peptide using click reactions for covalent conjugation. [18, 19, 20] While this approach demonstrated single-amino-acid resolution, it was limited to very short peptides and relied on complex DNA-peptide conjugation for reproducible readings. In contrast, the SUP carriers discussed in Chapter 5 offer a promising solution for a solid-state nanopore system. They can

be easily integrated with a whole protein using native chemical ligation[21] or enzymatic reactions such as sortase ligation. [22] The interactions between the SUP carriers and the nanopore surface can control the analyte molecules, allowing sequential information to be read out by the tunnelling detector. By implementing this concept, protein sequencing or fingerprinting can be achieved using a solid-state device, promising scalability and cost-effectiveness. [23] This future direction represents a potential breakthrough in advancing single-molecule protein analysis and nanopore-based biosensing for various applications in proteomics and interomics.

6.3 Conclusions

In conclusion, this chapter presents an innovative future direction to elevate the capabilities and performance of solid-state nanopores for single-molecule protein analysis. By integrating a tunnelling detector into multi-barrel nanopipettes, we aim to surpass the current limitations and achieve atomic precision comparable to biological pores. The tunnelling detector, crafted through feedback-controlled electrodeposition and electromigration breakdown, exhibits promising reproducibility and tunability. By using molecular carriers such as DNA or polypeptides, this proposed approach enables the sequencing of entire proteins, overcoming the constraints imposed by short peptides in previous studies. The covalent binding of the protein analyte to the carrier molecule ensures stability during unfolding processes, and the integration of supercharged unstructured polypeptides (SUPs) as carriers offers a seamless solution for enhancing the performance of the nanopore system.

The integration of the tunnelling detector into the nanopore sensor unveils new possibilities for diverse applications in proteomics research. The capability for protein sequencing and fingerprinting on a solid-state device brings forth the potential for scalability and cost-effectiveness in these analyses. This future direction represents a hot topic in the development of early-stage diagnosis and single-molecule proteomics, holding the promise of significant advancements in medical research and personalised medicine. However, to fully realise this concept, it is crucial to address technical challenges in fabricating reproducible devices and

fine-tuning the nanogap formation process. Rigorous optimisation and quality control will be necessary to achieve consistent and reliable results across experiments. Nevertheless, with perseverance and continuous research efforts, the successful realisation of this concept could revolutionise the field of molecular analysis, offering novel insights into biological processes, drug discovery, and diagnostic advancements.

6.4 References

1. Cadinu P*, et al.* Double Barrel Nanopores as a New Tool for Controlling Single-Molecule Transport. *Nano Letters* **18**, 2738-2745 (2018).
2. Cadinu P, Kang M, Nadappuram BP, Ivanov AP, Edel JB. Individually Addressable Multi-nanopores for Single-Molecule Targeted Operations. *Nano Letters* **20**, 2012-2019 (2020).
3. Zhang Y*, et al.* High-resolution label-free 3D mapping of extracellular pH of single living cells. *Nature Communications* **10**, 5610 (2019).
4. Ren R*, et al.* Nanopore extended field-effect transistor for selective single-molecule biosensing. *Nature Communications* **8**, 586 (2017).
5. Nadappuram BP*, et al.* Nanoscale tweezers for single-cell biopsies. *Nature Nanotechnology* **14**, 80-88 (2019).
6. Tang L*, et al.* Combined quantum tunnelling and dielectrophoretic trapping for molecular analysis at ultra-low analyte concentrations. *Nature Communications* **12**, 913 (2021).
7. Tang L*, et al.* Measuring conductance switching in single proteins using quantum tunneling. *Science Advances* **8**, eabm8149.
8. Jiang T, Yi L, Liu X, Ivanov AP, Edel JB, Tang L. Fabrication of electron tunneling probes for measuring single-protein conductance. *Nature Protocols*, (2023).
9. Requist R, Baruselli PP, Smogunov A, Fabrizio M, Modesti S, Tosatti E. Metallic, magnetic and molecular nanocontacts. *Nature Nanotechnology* **11**, 499-508 (2016).
10. Park H, Lim AKL, Alivisatos AP, Park J, McEuen PL. Fabrication of metallic electrodes with nanometer separation by electromigration. *Applied Physics Letters* **75**, 301-303 (1999).

11. Esen G, Fuhrer MS. Temperature control of electromigration to form gold nanogap junctions. *Applied Physics Letters* **87**, 263101 (2005).

12. Ward DR*, et al.* Electromigrated Nanoscale Gaps for Surface-Enhanced Raman Spectroscopy. *Nano Letters* **7**, 1396-1400 (2007).

13. Los Santos Valladares LD*, et al.* Controlled electroplating and electromigration in nickel electrodes for nanogap formation. *Nanotechnology* **21**, 445304 (2010).

14. Ward DR, Hüser F, Pauly F, Cuevas JC, Natelson D. Optical rectification and field enhancement in a plasmonic nanogap. *Nature Nanotechnology* **5**, 732-736 (2010).

15. Simmons JG. Generalized Formula for the Electric Tunnel Effect between Similar Electrodes Separated by a Thin Insulating Film. *Journal of Applied Physics* **34**, 1793-1803 (2004).

16. Zhao Y*, et al.* Single-molecule spectroscopy of amino acids and peptides by recognition tunnelling. *Nature Nanotechnology* **9**, 466-473 (2014).

17. Ohshiro T, Tsutsui M, Yokota K, Furuhashi M, Taniguchi M, Kawai T. Detection of post-translational modifications in single peptides using electron tunnelling currents. *Nature Nanotechnology* **9**, 835-840 (2014).

18. Brinkerhoff H, Kang ASW, Liu J, Aksimentiev A, Dekker C. Multiple rereads of single proteins at single–amino acid resolution using nanopores. *Science* **374**, 1509-1513 (2021).

19. Yan S*, et al.* Single Molecule Ratcheting Motion of Peptides in a Mycobacterium smegmatis Porin A (MspA) Nanopore. *Nano Letters* **21**, 6703-6710 (2021).

20. Nova IC, Ritmejeris J, Brinkerhoff H, Koenig TJR, Gundlach JH, Dekker C. Detection of phosphorylation post-translational modifications along single peptides with nanopores. *Nature Biotechnology*, (2023).

21. Agouridas V, El Mahdi O, Diemer V, Cargoët M, Monbaliu J-CM, Melnyk O. Native Chemical Ligation and Extended Methods: Mechanisms, Catalysis, Scope, and Limitations. *Chemical Reviews* **119**, 7328-7443 (2019).

22. Mao H, Hart SA, Schink A, Pollok BA. Sortase-Mediated Protein Ligation: A New Method for Protein Engineering. *Journal of the American Chemical Society* **126**, 2670-2671 (2004).

23. Xue L, Yamazaki H, Ren R, Wanunu M, Ivanov AP, Edel JB. Solid-state nanopore sensors. *Nature Reviews Materials* **5**, 931-951 (2020).

Appendices

Appendix I: Copyright permission

Figure number	Source	Copyright holder	Permission	License number	Approval number
Figure 1.1	*Angewandte Chemie International Edition* **55**, 11354-11366 (2016).	John Wiley and Sons	Granted	5656521316050	1
Figure 1.3, 1.11c, 1.13e-f	*Nature Reviews Materials* **5**, 931-951 (2020).	Springer Nature	Granted	5656530426715	2
Figure 1.8	*Nano Letters* **10**, 2162-2167 (2010).	American Chemical Society	Granted	N/A	3
Figure 1.9a	*Nature Nanotechnology* **5**, 807-814 (2010).	Springer Nature	Granted	5656530815297	4
Figure 1.9b	*ACS Nano* **11**, 5706-5716 (2017).	American Chemical Society	Granted	N/A	5
Figure 1.10a	*Nature Nanotechnology* **7**, 257-263 (2012).	Springer Nature	Granted	5656531078464	6
Figure 1.10b	*Nature Nanotechnology* **12**, 360-367 (2017).	Springer Nature	Granted	5656531187351	7
Figure 1.11a	*Nature Communications* **8**, 1552 (2017).	Springer Nature	Open Access (under CC-BY)	N/A	8
Figure 1.11b	*Science* **374**, 1509-1513 (2021).	The American Association for the Advancement of Science	Granted	5656540991265	9
Figure 1.12a	*Nature Nanotechnology* **5**, 874-877 (2010).	Springer Nature	Granted	5656540167576	10
Figure 1.12b	*Journal of the American Chemical Society* **144**, 22540-22548 (2022).	American Chemical Society	Granted	N/A	11
Figure 1.13a-d	*Nano Letters* **22**, 869-880 (2022).	American Chemical Society	Granted	N/A	12
Figure 1.14a-b	*Nature Nanotechnology*, (2023).	Springer Nature	Granted	5656540503292	13
Figure 1.14c	*Nature Nanotechnology* **14**, 791-798 (2019).	Springer Nature	Granted	5656540625099	14
Figure 1.15a	*Nature Communications* **8**, 586 (2017).	Springer Nature	Open Access (under CC-BY)	N/A	15
Figure 1.15b	*Nature Biotechnology* **26**, 1146-1153 (2008).	Springer Nature	Granted	5656540765905	16

Approval 1

RightsLink

My Orders | My Library | My Profile | Welcome xiaoyi.wang18@imperial.ac.uk | Log out | Help | FAQ

My Orders > Orders > All Orders

License Details

This Agreement between Xiaoyi Wang ("You") and John Wiley and Sons ("John Wiley and Sons") consists of your license details and the terms and conditions provided by John Wiley and Sons and Copyright Clearance Center.

Print Copy

License Number	5656521316050
License date	Oct 26, 2023
Licensed Content Publisher	John Wiley and Sons
Licensed Content Publication	Angewandte Chemie International Edition
Licensed Content Title	Single-Molecule Sensors: Challenges and Opportunities for Quantitative Analysis
Licensed Content Author	J. Justin Gooding, Katharina Gaus
Licensed Content Date	Jul 22, 2016
Licensed Content Volume	55
Licensed Content Issue	38
Licensed Content Pages	13
Type of Use	Dissertation/Thesis
Requestor type	University/Academic
Format	Print and electronic
Portion	Figure/table
Number of figures/tables	1
Will you be translating?	No
Title of new work	Single-molecule Protein Analysis Using Nanopores
Institution name	Imperial College London
Expected presentation date	Jan 2024
Portions	Figure 1.1
Requestor Location	82 Wood Lane Molecular Sciences Research Hub White City Campus London, London W12 0BZ United Kingdom Attn: Xiaoyi Wang
Publisher Tax ID	EU826007151
Total	**0.00 GBP**

BACK

Approval 2

RightsLink

My Orders | My Library | My Profile | Welcome xiaoyi.wang18@imperial.ac.uk | Log out | Help | FAQ

My Orders > Orders > All Orders

License Details

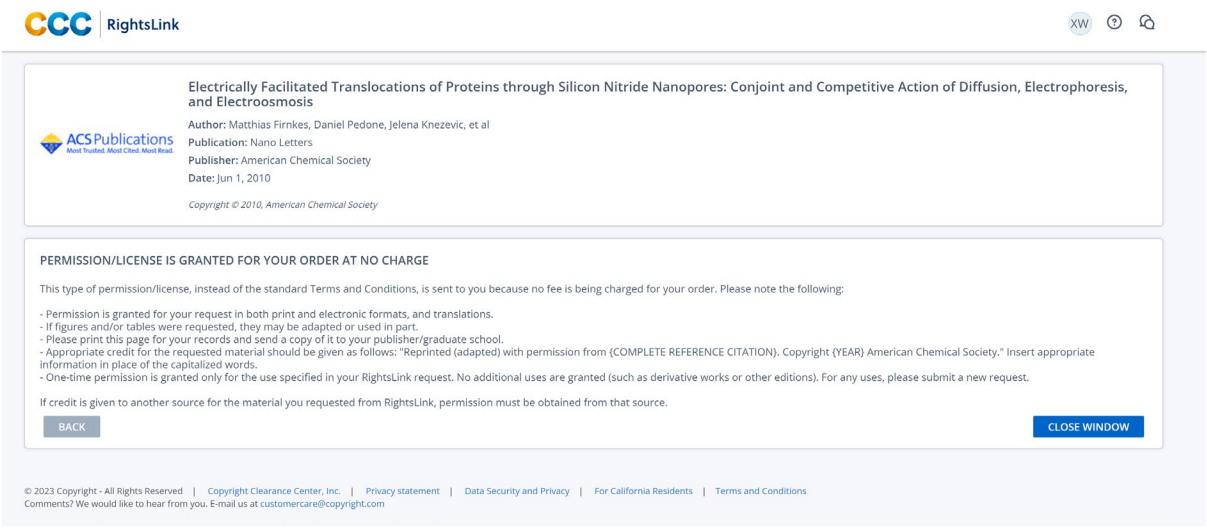
This Agreement between Xiaoyi Wang ("You") and Springer Nature ("Springer Nature") consists of your license details and the terms and conditions provided by Springer Nature and Copyright Clearance Center.

Print Copy

License Number	5656530426715
License date	Oct 26, 2023
Licensed Content Publisher	Springer Nature
Licensed Content Publication	Nature Reviews Materials
Licensed Content Title	Solid-state nanopore sensors
Licensed Content Author	Liang Xue et al
Licensed Content Date	Sep 21, 2020
Type of Use	Thesis/Dissertation
Requestor type	academic/university or research institute
Format	print and electronic
Portion	figures/tables/illustrations
Number of figures/tables/illustrations	3
Would you like a high resolution image with your order?	no
Will you be translating?	no
Circulation/distribution	30 - 99
Author of this Springer Nature content	no
Title of new work	Single-molecule Protein Analysis Using Nanopores
Institution name	Imperial College London
Expected presentation date	Jan 2024
Portions	Figure 1.3, Figure 1.11, Figure 1.13
Requestor Location	Xiaoyi Wang 82 Wood Lane Molecular Sciences Research Hub White City Campus London, London W12 0BZ United Kingdom Attn: Xiaoyi Wang
Total	**0.00 GBP**

BACK

Approval 3



RightsLink

XW

Electrically Facilitated Translocations of Proteins through Silicon Nitride Nanopores: Conjoint and Competitive Action of Diffusion, Electrophoresis, and Electroosmosis

ACS Publications
Most Trusted. Most Cited. Most Read.

Author: Matthias Firnkes, Daniel Pedone, Jelena Knezevic, et al
Publication: Nano Letters
Publisher: American Chemical Society
Date: Jun 1, 2010

Copyright © 2010, American Chemical Society

PERMISSION/LICENSE IS GRANTED FOR YOUR ORDER AT NO CHARGE

This type of permission/license, instead of the standard Terms and Conditions, is sent to you because no fee is being charged for your order. Please note the following:

- Permission is granted for your request in both print and electronic formats, and translations.
- If figures and/or tables were requested, they may be adapted or used in part.
- Please print this page for your records and send a copy of it to your publisher/graduate school.
- Appropriate credit for the requested material should be given as follows: "Reprinted (adapted) with permission from {COMPLETE REFERENCE CITATION). Copyright {YEAR} American Chemical Society." Insert appropriate information in place of the capitalized words.
- One-time permission is granted only for the use specified in your RightsLink request. No additional uses are granted (such as derivative works or other editions). For any uses, please submit a new request.

If credit is given to another source for the material you requested from RightsLink, permission must be obtained from that source.

BACK

CLOSE WINDOW

© 2023 Copyright - All Rights Reserved | Copyright Clearance Center, Inc. | Privacy statement | Data Security and Privacy | For California Residents | Terms and Conditions
Comments? We would like to hear from you. E-mail us at customercare@copyright.com

Approval 4

RightsLink

My Orders | My Library | My Profile | Welcome xiaoyi.wang18@imperial.ac.uk | Log out | Help | FAQ

My Orders > Orders > All Orders

License Details

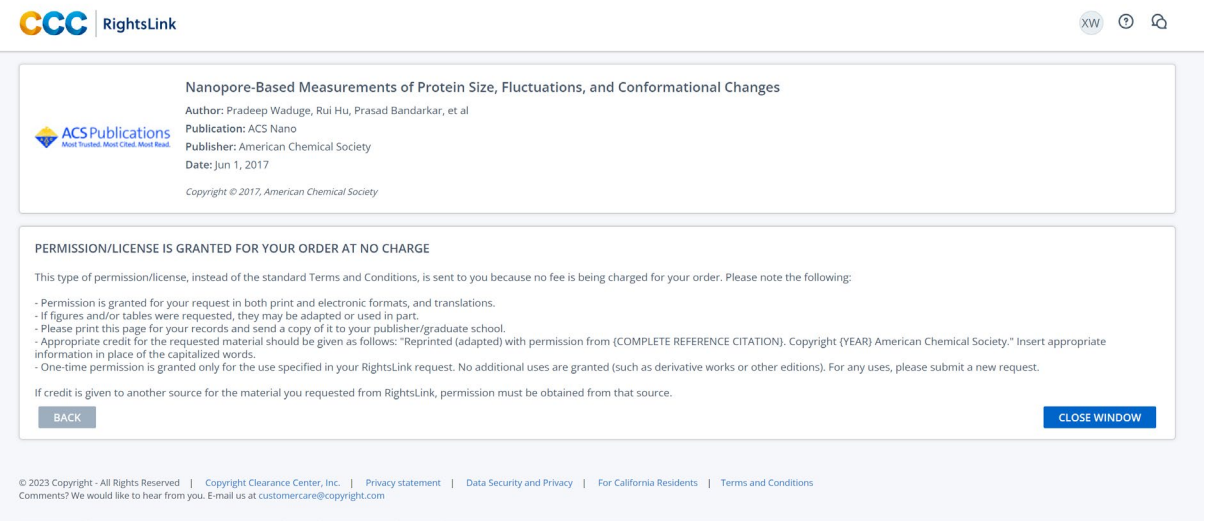
This Agreement between Xiaoyi Wang ("You") and Springer Nature ("Springer Nature") consists of your license details and the terms and conditions provided by Springer Nature and Copyright Clearance Center.

Print Copy

License Number	5656530815297
License date	Oct 26, 2023
Licensed Content Publisher	Springer Nature
Licensed Content Publication	Nature Nanotechnology
Licensed Content Title	Rapid electronic detection of probe-specific microRNAs using thin nanopore sensors
Licensed Content Author	Meni Wanunu et al
Licensed Content Date	Oct 24, 2010
Type of Use	Thesis/Dissertation
Requestor type	academic/university or research institute
Format	print and electronic
Portion	figures/tables/illustrations
Number of figures/tables/illustrations	1
Would you like a high resolution image with your order?	no
Will you be translating?	no
Circulation/distribution	100 - 199
Author of this Springer Nature content	no
Title of new work	Single-molecule Protein Analysis Using Nanopores
Institution name	Imperial College London
Expected presentation date	Jan 2024
Portions	Figure 1.9a
Requestor Location	Xiaoyi Wang 82 Wood Lane Molecular Sciences Research Hub White City Campus London, London W12 0BZ United Kingdom Attn: Xiaoyi Wang
Total	**0.00 GBP**

BACK

Approval 5



CCC | RightsLink

XW

Nanopore-Based Measurements of Protein Size, Fluctuations, and Conformational Changes

Author: Pradeep Waduge, Rui Hu, Prasad Bandarkar, et al
Publication: ACS Nano
Publisher: American Chemical Society
Date: Jun 1, 2017

Copyright © 2017, American Chemical Society

ACS Publications
Most Trusted. Most Cited. Most Read.

PERMISSION/LICENSE IS GRANTED FOR YOUR ORDER AT NO CHARGE

This type of permission/license, instead of the standard Terms and Conditions, is sent to you because no fee is being charged for your order. Please note the following:

- Permission is granted for your request in both print and electronic formats, and translations.
- If figures and/or tables were requested, they may be adapted or used in part.
- Please print this page for your records and send a copy of it to your publisher/graduate school.
- Appropriate credit for the requested material should be given as follows: "Reprinted (adapted) with permission from {COMPLETE REFERENCE CITATION}. Copyright {YEAR} American Chemical Society." Insert appropriate information in place of the capitalized words.
- One-time permission is granted only for the use specified in your RightsLink request. No additional uses are granted (such as derivative works or other editions). For any uses, please submit a new request.

If credit is given to another source for the material you requested from RightsLink, permission must be obtained from that source.

BACK

CLOSE WINDOW

© 2023 Copyright - All Rights Reserved | Copyright Clearance Center, Inc. | Privacy statement | Data Security and Privacy | For California Residents | Terms and Conditions
Comments? We would like to hear from you. E-mail us at customercare@copyright.com

Approval 6

CCC | RightsLink

My Orders | My Library | My Profile | Welcome xiaoyi.wang18@imperial.ac.uk | Log out | Help | FAQ

My Orders > Orders > All Orders

License Details

This Agreement between Xiaoyi Wang ("You") and Springer Nature ("Springer Nature") consists of your license details and the terms and conditions provided by Springer Nature and Copyright Clearance Center.

Print Copy

License Number	5656531078464
License date	Oct 26, 2023
Licensed Content Publisher	Springer Nature
Licensed Content Publication	Nature Nanotechnology
Licensed Content Title	Stochastic sensing of proteins with receptor-modified solid-state nanopores
Licensed Content Author	Ruoshan Wei et al
Licensed Content Date	Mar 11, 2012
Type of Use	Thesis/Dissertation
Requestor type	academic/university or research institute
Format	print and electronic
Portion	figures/tables/illustrations
Number of figures/tables/illustrations	1
Would you like a high resolution image with your order?	no
Will you be translating?	no
Circulation/distribution	100 - 199
Author of this Springer Nature content	no
Title of new work	Single-molecule Protein Analysis Using Nanopores
Institution name	Imperial College London
Expected presentation date	Jan 2024
Portions	Figure 1.10a
Requestor Location	Xiaoyi Wang 82 Wood Lane Molecular Sciences Research Hub White City Campus London, London W12 0BZ United Kingdom Attn: Xiaoyi Wang
Total	**0.00 GBP**

BACK

Approval 7

RightsLink

My Orders | My Library | My Profile | Welcome xiaoyi.wang18@imperial.ac.uk | Log out | Help | FAQ

My Orders > Orders > All Orders

License Details

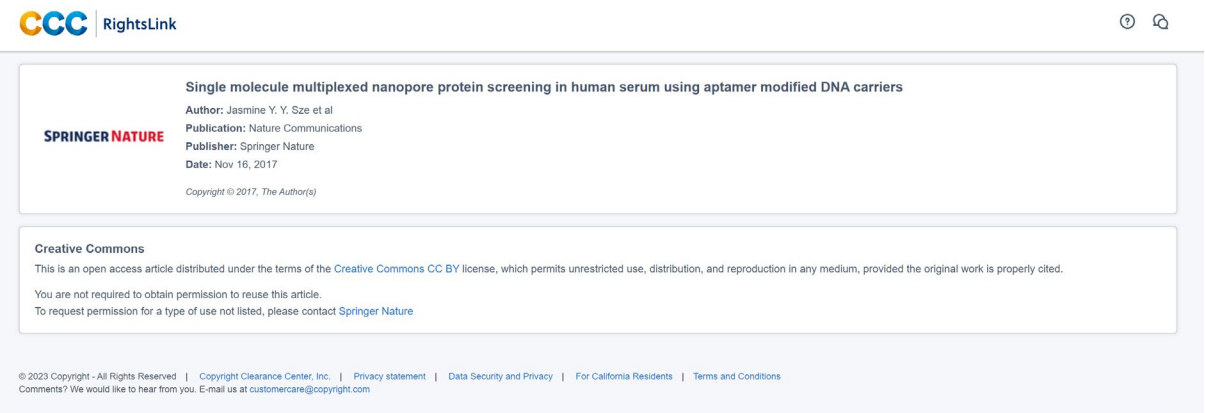
This Agreement between Xiaoyi Wang ("You") and Springer Nature ("Springer Nature") consists of your license details and the terms and conditions provided by Springer Nature and Copyright Clearance Center.

Print Copy

License Number	5656531187351
License date	Oct 26, 2023
Licensed Content Publisher	Springer Nature
Licensed Content Publication	Nature Nanotechnology
Licensed Content Title	Real-time shape approximation and fingerprinting of single proteins using a nanopore
Licensed Content Author	Erik C. Yusko et al
Licensed Content Date	Dec 19, 2016
Type of Use	Thesis/Dissertation
Requestor type	academic/university or research institute
Format	print and electronic
Portion	figures/tables/illustrations
Number of figures/tables/illustrations	1
Would you like a high resolution image with your order?	no
Will you be translating?	no
Circulation/distribution	100 - 199
Author of this Springer Nature content	no
Title of new work	Single-molecule Protein Analysis Using Nanopores
Institution name	Imperial College London
Expected presentation date	Jan 2024
Portions	Figure 1.10b
Requestor Location	Xiaoyi Wang 82 Wood Lane Molecular Sciences Research Hub White City Campus London, London W12 0BZ United Kingdom Attn: Xiaoyi Wang
Total	**0.00 GBP**

BACK

Approval 8



CCC RightsLink

SPRINGER NATURE

Single molecule multiplexed nanopore protein screening in human serum using aptamer modified DNA carriers

Author: Jasmine Y. Y. Sze et al
Publication: Nature Communications
Publisher: Springer Nature
Date: Nov 16, 2017

Copyright © 2017, The Author(s)

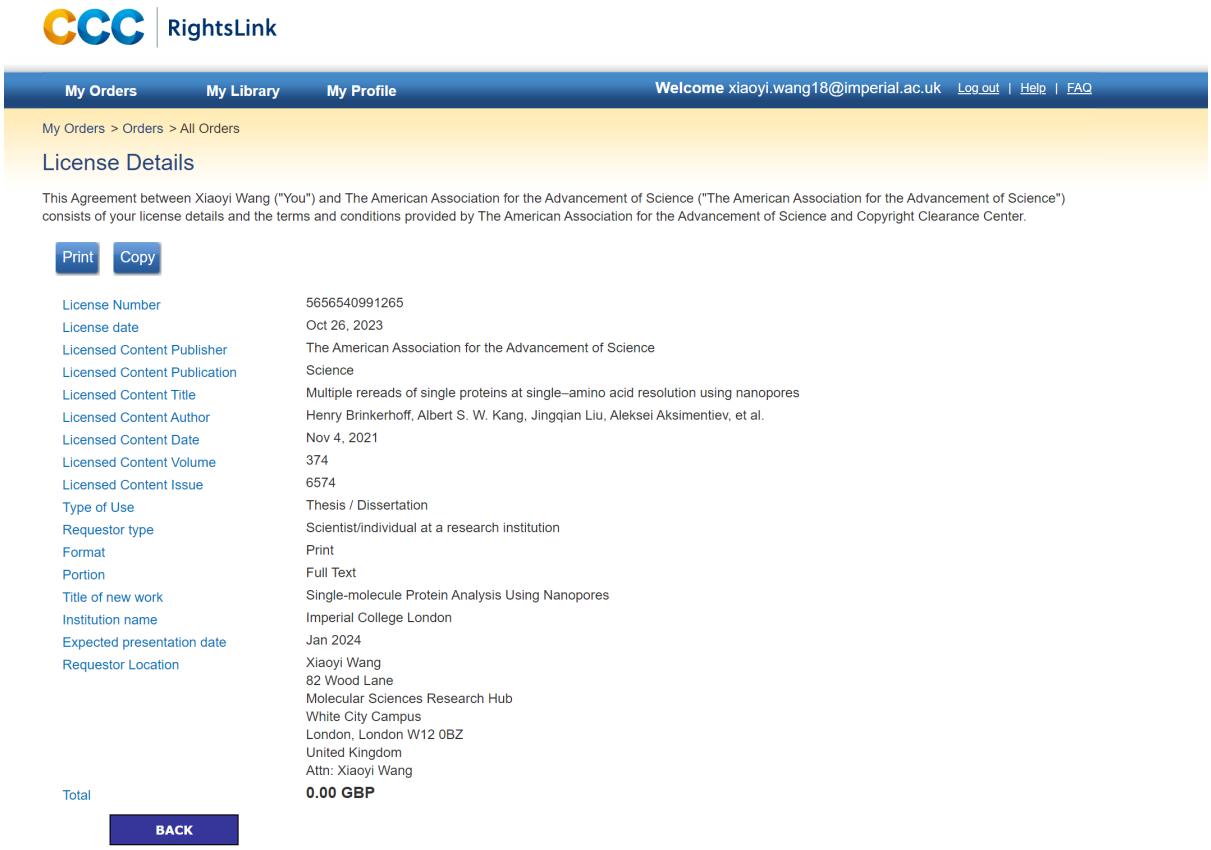
Creative Commons

This is an open access article distributed under the terms of the Creative Commons CC BY license, which permits unrestricted use, distribution, and reproduction in any medium, provided the original work is properly cited.

You are not required to obtain permission to reuse this article.
To request permission for a type of use not listed, please contact Springer Nature

© 2023 Copyright - All Rights Reserved | Copyright Clearance Center, Inc. | Privacy statement | Data Security and Privacy | For California Residents | Terms and Conditions
Comments? We would like to hear from you. E-mail us at customercare@copyright.com

Approval 9



RightsLink

My Orders | My Library | My Profile | Welcome xiaoyi.wang18@imperial.ac.uk | Log out | Help | FAQ

My Orders > Orders > All Orders

License Details

This Agreement between Xiaoyi Wang ("You") and The American Association for the Advancement of Science ("The American Association for the Advancement of Science") consists of your license details and the terms and conditions provided by The American Association for the Advancement of Science and Copyright Clearance Center.

Print Copy

License Number	5656540991265
License date	Oct 26, 2023
Licensed Content Publisher	The American Association for the Advancement of Science
Licensed Content Publication	Science
Licensed Content Title	Multiple rereads of single proteins at single–amino acid resolution using nanopores
Licensed Content Author	Henry Brinkerhoff, Albert S. W. Kang, Jingqian Liu, Aleksei Aksimentiev, et al.
Licensed Content Date	Nov 4, 2021
Licensed Content Volume	374
Licensed Content Issue	6574
Type of Use	Thesis / Dissertation
Requestor type	Scientist/individual at a research institution
Format	Print
Portion	Full Text
Title of new work	Single-molecule Protein Analysis Using Nanopores
Institution name	Imperial College London
Expected presentation date	Jan 2024
Requestor Location	Xiaoyi Wang 82 Wood Lane Molecular Sciences Research Hub White City Campus London, London W12 0BZ United Kingdom Attn: Xiaoyi Wang
Total	**0.00 GBP**

BACK

Approval 10

CCC RightsLink

My Orders | My Library | My Profile | Welcome xiaoyi.wang18@imperial.ac.uk | Log out | Help | FAQ

My Orders > Orders > All Orders

License Details

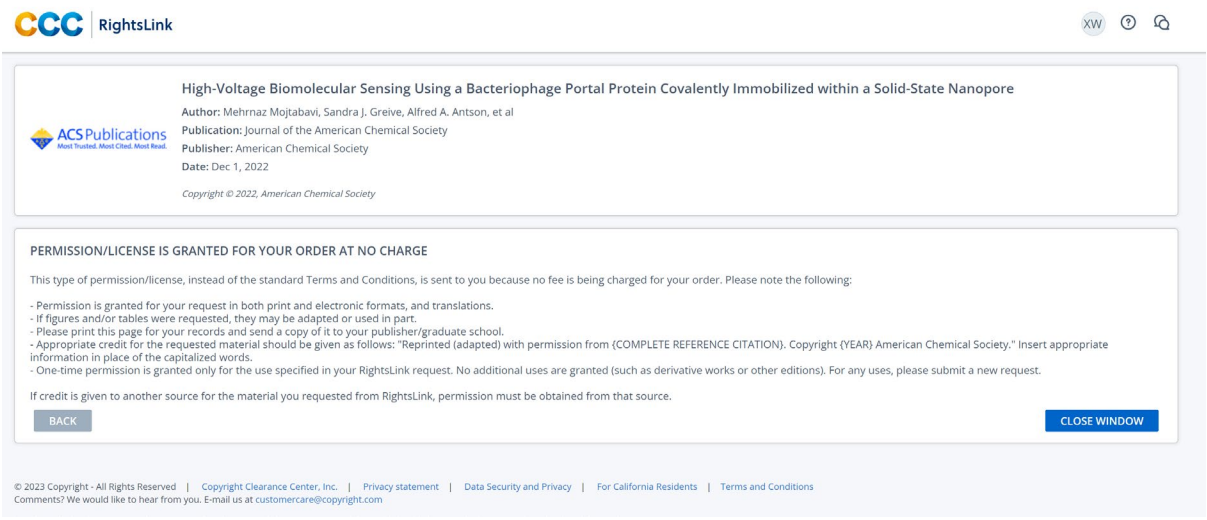
This Agreement between Xiaoyi Wang ("You") and Springer Nature ("Springer Nature") consists of your license details and the terms and conditions provided by Springer Nature and Copyright Clearance Center.

Print Copy

License Number	5656540167576
License date	Oct 26, 2023
Licensed Content Publisher	Springer Nature
Licensed Content Publication	Nature Nanotechnology
Licensed Content Title	Hybrid pore formation by directed insertion of α-haemolysin into solid-state nanopores
Licensed Content Author	Adam R. Hall et al
Licensed Content Date	Nov 28, 2010
Type of Use	Thesis/Dissertation
Requestor type	academic/university or research institute
Format	print and electronic
Portion	figures/tables/illustrations
Number of figures/tables/illustrations	1
Would you like a high resolution image with your order?	no
Will you be translating?	no
Circulation/distribution	100 - 199
Author of this Springer Nature content	no
Title of new work	Single-molecule Protein Analysis Using Nanopores
Institution name	Imperial College London
Expected presentation date	Jan 2024
Portions	Figure 1.12a
Requestor Location	Xiaoyi Wang 82 Wood Lane Molecular Sciences Research Hub White City Campus London, London W12 0BZ United Kingdom Attn: Xiaoyi Wang
Total	**0.00 GBP**

BACK

Approval 11



RightsLink

XW

ACS Publications
Most Trusted. Most Cited. Most Read.

High-Voltage Biomolecular Sensing Using a Bacteriophage Portal Protein Covalently Immobilized within a Solid-State Nanopore

Author: Mehrnaz Mojtabavi, Sandra J. Greive, Alfred A. Antson, et al
Publication: Journal of the American Chemical Society
Publisher: American Chemical Society
Date: Dec 1, 2022

Copyright © 2022, American Chemical Society

PERMISSION/LICENSE IS GRANTED FOR YOUR ORDER AT NO CHARGE

This type of permission/license, instead of the standard Terms and Conditions, is sent to you because no fee is being charged for your order. Please note the following:

- Permission is granted for your request in both print and electronic formats, and translations.
- If figures and/or tables were requested, they may be adapted or used in part.
- Please print this page for your records and send a copy of it to your publisher/graduate school.
- Appropriate credit for the requested material should be given as follows: "Reprinted (adapted) with permission from {COMPLETE REFERENCE CITATION}. Copyright {YEAR} American Chemical Society." Insert appropriate information in place of the capitalized words.
- One-time permission is granted only for the use specified in your RightsLink request. No additional uses are granted (such as derivative works or other editions). For any uses, please submit a new request.

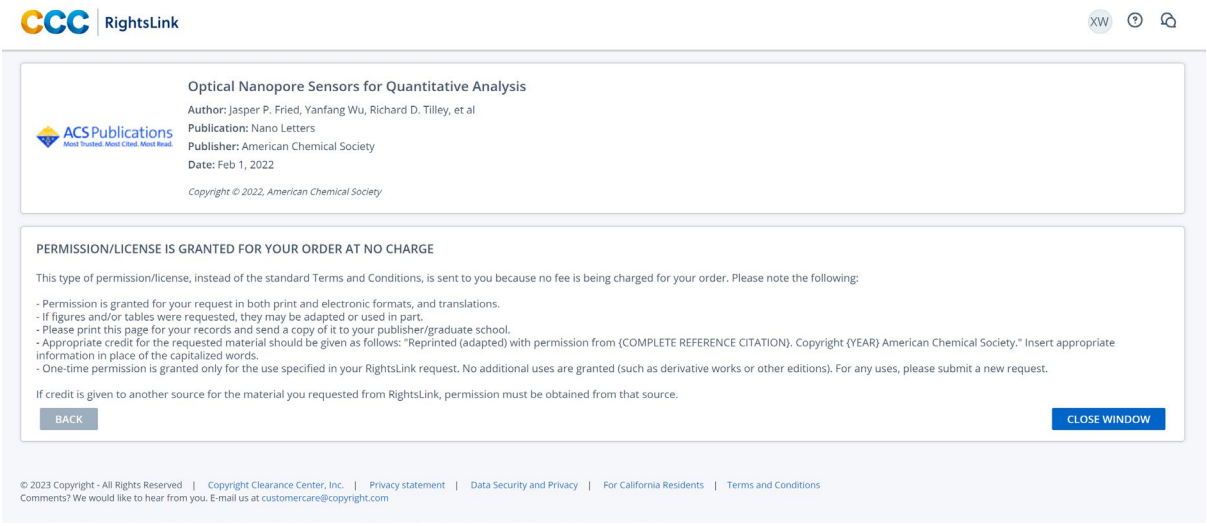
If credit is given to another source for the material you requested from RightsLink, permission must be obtained from that source.

BACK

CLOSE WINDOW

© 2023 Copyright - All Rights Reserved | Copyright Clearance Center, Inc. | Privacy statement | Data Security and Privacy | For California Residents | Terms and Conditions
Comments? We would like to hear from you. E-mail us at customercare@copyright.com

Approval 12



CCC RightsLink

XW

Optical Nanopore Sensors for Quantitative Analysis

Author: Jasper P. Fried, Yanfang Wu, Richard D. Tilley, et al

Publication: Nano Letters

Publisher: American Chemical Society

Date: Feb 1, 2022

Copyright © 2022, American Chemical Society

PERMISSION/LICENSE IS GRANTED FOR YOUR ORDER AT NO CHARGE

This type of permission/license, instead of the standard Terms and Conditions, is sent to you because no fee is being charged for your order. Please note the following:

- Permission is granted for your request in both print and electronic formats, and translations.
- If figures and/or tables were requested, they may be adapted or used in part.
- Please print this page for your records and send a copy of it to your publisher/graduate school.
- Appropriate credit for the requested material should be given as follows: "Reprinted (adapted) with permission from {COMPLETE REFERENCE CITATION}. Copyright {YEAR} American Chemical Society." Insert appropriate information in place of the capitalized words.
- One-time permission is granted only for the use specified in your RightsLink request. No additional uses are granted (such as derivative works or other editions). For any uses, please submit a new request.

If credit is given to another source for the material you requested from RightsLink, permission must be obtained from that source.

BACK

CLOSE WINDOW

© 2023 Copyright - All Rights Reserved | Copyright Clearance Center, Inc. | Privacy statement | Data Security and Privacy | For California Residents | Terms and Conditions
Comments? We would like to hear from you. E-mail us at customercare@copyright.com

Approval 13

RightsLink

My Orders | My Library | My Profile | Welcome xiaoyi.wang18@imperial.ac.uk | Log out | Help | FAQ

My Orders > Orders > All Orders

License Details

This Agreement between Xiaoyi Wang ("You") and Springer Nature ("Springer Nature") consists of your license details and the terms and conditions provided by Springer Nature and Copyright Clearance Center.

Print Copy

License Number	5656540503292
License date	Oct 26, 2023
Licensed Content Publisher	Springer Nature
Licensed Content Publication	Nature Nanotechnology
Licensed Content Title	Spatially multiplexed single-molecule translocations through a nanopore at controlled speeds
Licensed Content Author	S. M. Leitao et al
Licensed Content Date	Jun 19, 2023
Type of Use	Thesis/Dissertation
Requestor type	academic/university or research institute
Format	print and electronic
Portion	figures/tables/illustrations
Number of figures/tables/illustrations	1
Would you like a high resolution image with your order?	no
Will you be translating?	no
Circulation/distribution	100 - 199
Author of this Springer Nature content	no
Title of new work	Single-molecule Protein Analysis Using Nanopores
Institution name	Imperial College London
Expected presentation date	Jan 2024
Portions	Figure 1.14
Requestor Location	Xiaoyi Wang 82 Wood Lane Molecular Sciences Research Hub White City Campus London, London W12 0BZ United Kingdom Attn: Xiaoyi Wang
Total	**0.00 GBP**

BACK

Approval 14

RightsLink

My Orders | My Library | My Profile | Welcome xiaoyi.wang18@imperial.ac.uk Log out | Help | FAQ

My Orders > Orders > All Orders

License Details

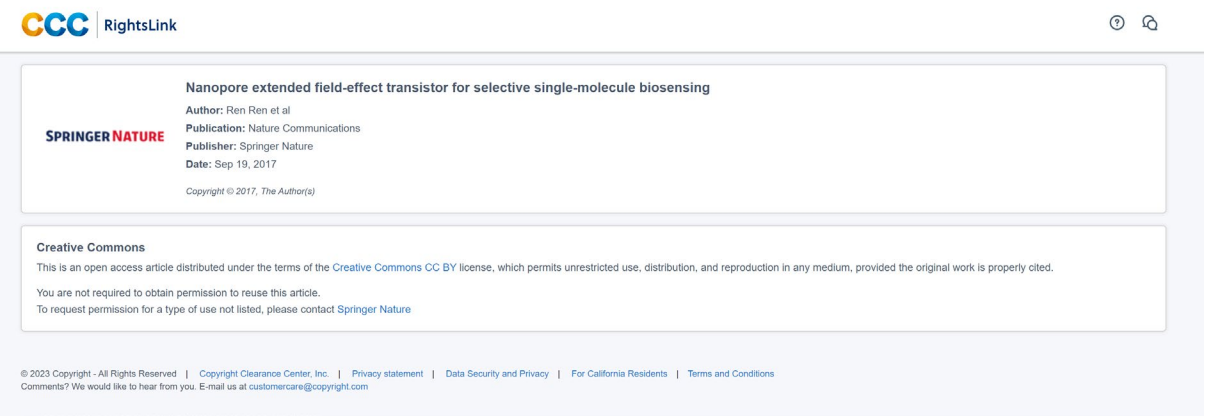
This Agreement between Xiaoyi Wang ("You") and Springer Nature ("Springer Nature") consists of your license details and the terms and conditions provided by Springer Nature and Copyright Clearance Center.

Print Copy

License Number	5656540625099
License date	Oct 26, 2023
Licensed Content Publisher	Springer Nature
Licensed Content Publication	Nature Nanotechnology
Licensed Content Title	Localized detection of ions and biomolecules with a force-controlled scanning nanopore microscope
Licensed Content Author	Morteza Aramesh et al
Licensed Content Date	Jul 15, 2019
Type of Use	Thesis/Dissertation
Requestor type	academic/university or research institute
Format	print and electronic
Portion	figures/tables/illustrations
Number of figures/tables/illustrations	1
Would you like a high resolution image with your order?	no
Will you be translating?	no
Circulation/distribution	100 - 199
Author of this Springer Nature content	no
Title of new work	Single-molecule Protein Analysis Using Nanopores
Institution name	Imperial College London
Expected presentation date	Jan 2024
Portions	Figure 1.14
Requestor Location	Xiaoyi Wang 82 Wood Lane Molecular Sciences Research Hub White City Campus London, London W12 0BZ United Kingdom Attn: Xiaoyi Wang
Total	**0.00 GBP**

BACK

Approval 15



CCC RightsLink

SPRINGER NATURE

Nanopore extended field-effect transistor for selective single-molecule biosensing

Author: Ren Ren et al
Publication: Nature Communications
Publisher: Springer Nature
Date: Sep 19, 2017

Copyright © 2017, The Author(s)

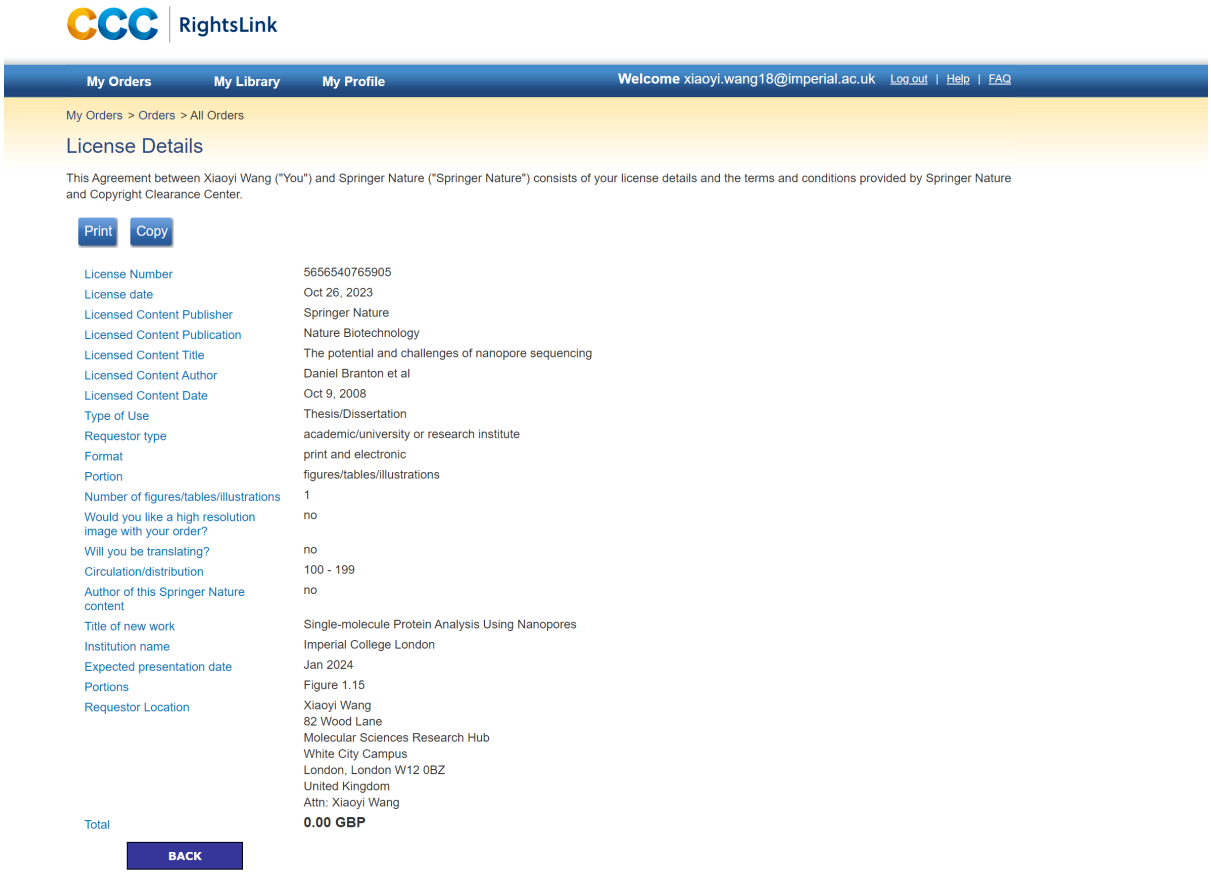
Creative Commons

This is an open access article distributed under the terms of the Creative Commons CC BY license, which permits unrestricted use, distribution, and reproduction in any medium, provided the original work is properly cited.

You are not required to obtain permission to reuse this article.
To request permission for a type of use not listed, please contact Springer Nature

© 2023 Copyright - All Rights Reserved | Copyright Clearance Center, Inc. | Privacy statement | Data Security and Privacy | For California Residents | Terms and Conditions
Comments? We would like to hear from you. E-mail us at customercare@copyright.com

Approval 16



CCC RightsLink

My Orders | My Library | My Profile | Welcome xiaoyi.wang18@imperial.ac.uk | Log out | Help | FAQ

My Orders > Orders > All Orders

License Details

This Agreement between Xiaoyi Wang ("You") and Springer Nature ("Springer Nature") consists of your license details and the terms and conditions provided by Springer Nature and Copyright Clearance Center.

Print Copy

License Number	5656540765905
License date	Oct 26, 2023
Licensed Content Publisher	Springer Nature
Licensed Content Publication	Nature Biotechnology
Licensed Content Title	The potential and challenges of nanopore sequencing
Licensed Content Author	Daniel Branton et al
Licensed Content Date	Oct 9, 2008
Type of Use	Thesis/Dissertation
Requestor type	academic/university or research institute
Format	print and electronic
Portion	figures/tables/illustrations
Number of figures/tables/illustrations	1
Would you like a high resolution image with your order?	no
Will you be translating?	no
Circulation/distribution	100 - 199
Author of this Springer Nature content	no
Title of new work	Single-molecule Protein Analysis Using Nanopores
Institution name	Imperial College London
Expected presentation date	Jan 2024
Portions	Figure 1.15
Requestor Location	Xiaoyi Wang 82 Wood Lane Molecular Sciences Research Hub White City Campus London, London W12 0BZ United Kingdom Attn: Xiaoyi Wang
Total	**0.00 GBP**

BACK

Appendix II: List of publications

1. Xiaoyi Wang, Tina-Marie Thomas, Ren Ren, Yu Zhou, Peng Zhang, Jingjing Li, Shenglin Cai, Kai Liu, Aleksandar P. Ivanov, Andreas Herrmann and Joshua B. Edel. Nanopore Detection Using Supercharged Polypeptide Molecular Carriers. *J. Am. Chem. Soc.* 2023, 145, 11, 6371–6382.

[Featured by JACS Spotlights: *J. Am. Chem. Soc.* 2023, 145, 11, 5989–5990.]

2. Xiaoyi Wang, Mark D. Wilkinson, Xiaoyan Lin, Ren Ren, Keith R. Willison, Aleksandar P. Ivanov, Jake Baum and Joshua B. Edel. Sing-molecule nanopore sensing of actin dynamics and drug binding. *Chem. Sci.* 2020, 11, 970–979.

3. Ren Ren, Xiaoyi Wang, Shenglin Cai, Yanjun Zhang, Yuri Korchev, Aleksandar P. Ivanov and Joshua B. Edel. Selective sensing of proteins using aptamer functionalized nanopore extended field-effect transistors. *Small Methods* 2020, 2000356.

4. Yaxian Liu, Xiaoyi Wang, Giulia Campolo, Xiangyu Teng, Liming Ying, Aleksandar P. Ivanov, Joshua B. Edel. Single-Molecule Detection of α-Synuclein Oligomers in Parkinson's Disease Patients Using Nanopores. *ACS Nano* 2023, 17, 22, 22999–23009.

5. Shenglin Cai, Ren Ren, Jiaxuan He, Xiaoyi Wang, Zheng Zhang, Zhaofeng, Luo, Weihong Tan, Yuri Korchev, Joshua B. Edel and Aleksandar P. Ivanov. Selective single-molecule nanopore detection of mpox A29 protein directly in biofluids. *Nano Lett.* 2023, XXXX, XXX, XXX-XXX.

6. Ren Ren, Shenglin Cai, Xiaona Fang, Xiaoyi Wang, Zheng Zhang, Micol Damiani, Charlotte Hudlerova, Annachiara Rosa, Joshua Hope, Nicola J Cook, Peter Gorelkin, Alexander Erofeev, Pavel Novak, Anjna Badhan, Michael Crone, Paul Freemont, Graham Taylor, Longhua Tang, Christopher Edwards, Andrew Shevchuk, Peter Cherepanov, Zhaofeng Luo, Weihong Tan, Yuri Korchev, Aleksandar P. Ivanov and Joshua B. Edel. Multiplexed detection of viral antigen and RNA using nanopore sensing and encoded molecular probes. *Nat. Commun.* 2023, 14, 7362.

7. Xiaoyi Wang, Yaxian Liu, Ren Ren, Aleksandar P. Ivanov and Joshua B. Edel. Single-molecule protein profiling using nanopores and dimeric aptamer-modified DNA carriers. submitted.